Universidad Autónoma de Madrid
Departamento de Física de la Materia Condensada

TOPOLOGY AND INTERACTION EFFECTS IN DIRAC QUASIPARTICLE SYSTEMS

Tesis doctoral presentada por
Adolfo González Grushin

Programa de doctorado de Física de la Materia Condensada y Nanotecnología

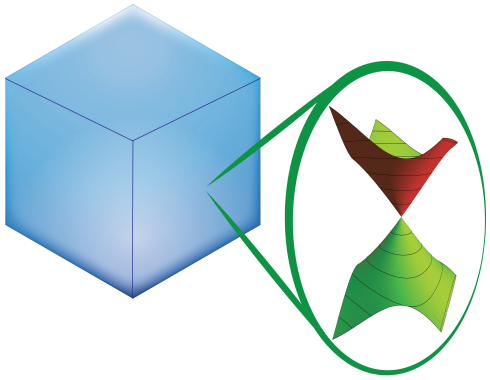

Directora:
María Ángeles Hernández Vozmediano

Codirector:
Alberto Cortijo

Tutor:
Amadeo López Vázquez de Parga

Madrid, Enero de 2013

Contents

List of Figures

Agradecimientos

Esta tesis esta muy lejos de ser un esfuerzo individual. He tenido la inmensa fortuna de contar con el apoyo incondicional de muchas personas, no sólo durante el desarrollo de este trabajo sino también desde mucho antes.

Tengo mucho que agradecer a mis dos directores de tesis. A Geli por su infinita y no siempre fácil paciencia que ha tenido para formarme como científico. Su constante dedicación y disposición para ayudarme en este y otros aspectos de la vida han sido esenciales. También a Alberto por su extraordinaria capacidad de generar ideas y motivación y saber transmitirlo con inagotable sentido del humor. Cualquier éxito que pueda cosechar de aquí en adelante será seguro gracias a ellos.

Quiero también dar las gracias a Amadeo, mi tutor en la UAM por acceder a tutelar esta tesis y su plena accesibilidad durante el desarrollo de la misma.

En estos años, he tenido el placer de aprender y colaborar con grandes científicos que resultaron ser además bellísimas personas. Influyeron mucho en mi las tardes (muchas llegaron a ser noches) trabajando mano a mano con Eduardo que es desde entonces para mi un ejemplo a seguir, y no sólo en el aspecto científico. También estaré siempre agradecido a Belén no sólo por la idea que me inició en esto sino por su permanente sonrisa y afecto haciendo que sea muy fácil trabajar a su lado. También quiero agradecer a Pablo, su paciencia y dedicación para enseñarnos los secretos del efecto Casimir. Me gustaría hacer una mención especial a Fernando. Desde el principio no dudó en dedicarme incontables horas de las que siempre le agradeceré (¡y admiraré!) su inestimable capacidad de hacerse entender en términos intuitivos. Esto unido a su claridad, su pragmatismo, su espíritu crítico y su amabilidad hacen que contar no sólo con su colaboración, sino con su amistad, sea un auténtico honor para mi.

I want to thank also Claudio Chamon at Boston University for his very kind hospitality. Witnessing his immense creativity and being able to learn from it was indeed priceless. Thanks to him I was able to meet and learn also from Luiz Santos, Christopher Mudry and especially Titus Neupert. I am indebted to all of them for their excellent guidance inside the intricate world of the fractional quantum Hall effect. I will always remember all the people

I met there, that made of Boston my second home both inside and outside the department. From BU I want to thank Diego, Cheng-Wei, Ying, Maro, Paul and of course Silvia, but especially Luca and Rebecca who I feel very lucky to have met. De las personas que conocí fuera del departamento me gustaría agradecer en especial a toda la comuna de Leland: Susana, Nick, Manu, Ana, Edu, Marta, Chari, Jan, Julia y muy particularmente a Alicia por ser todos ellos mi familia al otro lado del charco, así como a Javi y a Teresa por su inestimable ayuda e introducirme en ese magnífico mundo.

El ICMM ha sido siempre un lugar estimulante gracias a muchos de los que he aprendido física y no sólo física: Paco, Luis Brey, Pilar, Ramón, Leni, Rafa, Elsa, Pablo, Fernando, Robert, Mathias, Álvaro, David y Carlos así como a Mauricio, Emilia y Bruno con los que disfruto hablando de cualquier tema. Siempre quedará en mi memoria el magnífico viaje a Santa Barbara con Héctor y Emanulelle en el que tuve la fortuna de compartir con ellos infinitas risas y anécdotas, que hoy todavía siguen. También quiero agradecer a todos los miembros de WEE de todas las épocas por hacer que divulgar fuese tan divertido. Muy especialmente a Miguel Camblor con el que he compartido y sigo compartiendo inquietudes de todo tipo. Su amistad es sin duda una de las cosas más valiosas que me quedarán después de mi paso por el instituto. A Simone quiero agradecerle sus acertados consejos, el placer de su compañía en WEE y por supuesto el fantástico y alocado congreso de Benasque. En disfrutar de este último también contribuyo mucho Javi Sabio, del que siempre admiraré su franqueza y altura de miras de las que tanto he aprendido.

Otra mención especial va para María que hizo mucho más llevadero el día a día del despacho, especialmente, esas tardes calurosas de verano. Coincidir con ella tanto tiempo ha sido una suerte y no exagero si digo que su buen humor, compañía y sabiduría han sido fundamentales para acabar cuerdo la tesis. Gracias también a Eduardo, Deborah y más recientemente, Marta, Oliva, Jan y Mónica por hacer del despacho un sitio excepcional para trabajar.

Quiero poner en un pedestal aparte a todos mis amigos de las mesas, que día a día han hecho que pueda llevar esta y otras muchas cosas a buen puerto. A Paula quiero agradecerle especialmente, entre innumerables otras cosas, el año no menos que ideal que pasamos viviendo en Palencia. También a Miguel y Manuela por sufrirme tantos años y a pesar de ello seguir dedicándome el placer de su amistad, así como a Paloma por darme ese punto de sensatez que tanto hace falta. Imprescindible ha sido la "tedia" a distancia de Peibol, el carisma de Clara, el humor absurdo de Edu, Luis y Drino, la elocuencia de Yago, el sentido de humor de Emilio y las risas con Vicky y todos los que están o estuvieron de algún modo, a los que también agradezco su enorme paciencia y amistad durante estos años. Quiero agradecer también a Alex muchos momentos puntuales de risas y digresiones tanto en el Máster como después.

También he contado con el incalculable apoyo de toda la familia de Vistasierra que tanto me ha ayudado siempre. No menos vitales han sido todos estos años de encuentros con Ivar del que no paro de aprender y al que no paro de admirar a pesar de las distancias. Estoy en deuda también con todos los miembros de Schizzofunk por esos lunes de evasión, y en especial a Pep, con el que he disfrutado enormemente tocando en todos sus grupos.

Para terminar quiero agradecer a mis padres por ser el mejor ejemplo, así como por su incansable apoyo y siempre creer que puedo llegar a lo más alto. También a mi familia y muy en especial a mis abuelos que siempre han sabido entender y apreciar el proceso de convertirse en científico. Finalmente a Isa, la mejor persona con la que se puede compartir cualquier cosa, y en particular un viaje como este.

Por último quiero dedicar esta tesis a la memoria de Adam, su dedicación y creatividad me servirán permanentemente de inspiración y vivirán siempre conmigo.

A él y a todos vosotros, gracias.

Publications

Part of the work presented in this thesis has given rise to the following publications and preprints:

1. *"Effect of Coulomb interactions on the optical properties of graphene"*
   Adolfo G. Grushin, Belen Valenzuela y Maria A. H. Vozmediano
   Phys. Rev. B 80, 155417 (2009)
   Selected as "Editor's suggestion".

2. *"Renormalization of Coulomb interaction in graphene: computing observable quantities"*
   Fernando de Juan, **Adolfo G. Grushin**, Maria A. H. Vozmediano
   Phys. Rev. B 82, 125409 (2010)

3. *"Topological insulating phases in monolayer and bilayer graphene: An effective action approach"*
   Alberto Cortijo, **Adolfo G. Grushin**, Maria A. H. Vozmediano
   Phys. Rev. B 82, 195438 (2010)

4. *"Tunable Casimir repulsion with three dimensional topological insulators"*
   Adolfo G. Grushin, Alberto Cortijo
   Phys. Rev. Lett. 106, 020403 (2011)
   and featured in Physical Review Focus: Phys. Rev. Focus 27, 1 (2011)

5. *"Effect of finite temperature and uniaxial anisotropy on the Casimir effect with three-dimensional topological insulators"*
   Adolfo G. Grushin, Pablo Rodriguez-Lopez, Alberto Cortijo
   Phys. Rev. B 84, 045119 (2011)

6. *"Topological Fermi Liquids from Coulomb interactions in the doped Honeycomb lattice"*
   E. V. Castro, **Adolfo G. Grushin**, B. Valenzuela, Maria A. H. Vozmediano, Alberto Cortijo, Fernando de Juan
   Phys. Rev. Lett. 107, 106402 (2011)

7. *"Consequences of a condensed matter realization of Lorentz-violating QED in Weyl semimetals"*
   Adolfo G. Grushin
   Phys. Rev. D 86, 045001 (2012)

8. *"Finite frequency response of three dimensional topological insulators"*
   Adolfo G. Grushin, Fernando de Juan
   Phys. Rev. B 86, 075126 (2012)

9. *"Enhancing the stability of fractional Chern insulators against competing phases"*
   Adolfo G. Grushin, Titus Neupert, Claudio Chamon, Christopher Mudry
   Phys. Rev. B 86, 205125 (2012)

10. *"Charge instabilities and topological phases in the extended Hubbard model on the honeycomb lattice with enlarged unit cell"*
    Adolfo G. Grushin, E. V. Castro, B. Valenzuela, Maria A. H. Vozmediano, Alberto Cortijo, Fernando de Juan
    arXiv: 1212.6836 (2012)

Abstract

In this thesis we provide ways to understand and efficiently describe the physical consequences of electron-electron interactions and topology in Dirac quasiparticle systems. We study graphene and topological insulators to understand how Dirac quasiparticles in these materials behave under different circumstances. The thesis is divided into three main parts.
In the first part we study interaction effects in Dirac quasiparticle systems and how they affect observables. First, a phenomenological theory is constructed to recover features seen in the experimentally measured optical conductivity in graphene. Then, within diagrammatic perturbation theory, a microscopic, cut-off independent theory is constructed for Dirac quasiparticles in graphene from which observables can be calculated in a systematic way.
In the second part, we will study how topological phases, both in their integral and fractional versions can emerge out of short range interactions in Dirac quasiparticle systems. First, under a mean field approach we will show that novel topological phases that break translational invariance and time reversal symmetry can appear near commensurate fillings in the honeycomb lattice. These novel phases are characterized by a finite Hall conductivity and topologically non trivial bands with Chern numbers different from zero. Then, we will present a model of Dirac quasiparticles that realizes fractional Hall effect phases. It is argued that high Chern numbers and dispersive bands can stabilize these fractional states, contrary to naive expectation based on the Landau level paradigm.
In the final part of this thesis we will study different aspects of topological phases as well as novel physical phenomena that they can originate. We first provide a unified view of time reversal invariant topological phases appearing in graphene and its bilayer from an effective action approach. We then present two examples of topological phenomena that arise solely due to the fact that these materials are described by topological terms. On the one hand, the Casimir force between two topological insulator plates is proven to be repulsive at short distances and attractive at long distances, including the effects of finite temperature and uniaxial anisotropy. This will motivate the study of the finite frequency dependency of the topological term, which can strongly affect the Casimir effect and other topological phenomena. To conclude, a consistent response theory for an heterostructure of alternating ordinary and topological insulator, a Weyl semi-metal, is developed. It is shown that the effective theory of this response is a condensed matter realization of one of the possible extensions of the standard model of particle physics (Lorentz violating QED) with measurable physical consequences such as birefringence.

Resumen

En esta tesis se describen las consecuencias físicas de las interacciones electrón-electrón y la topología en sistemas de cuasipartículas de Dirac. Se estudiarán el grafeno y los aislantes topológicos que realizan dichas cuasipartículas para entender como se comportan en diferentes circunstancias. La tesis se subdivide en tres partes principales.
En la primera parte se estudiará la interacción electrón-electrón en cuasipartículas de Dirac en grafeno y su efecto en cantidades observables. Primero se construirá una teoría fenomenológica para recuperar características de la conductividad óptica de grafeno observadas experimentalmente. Entonces se describirá la teoría microscópica e independiente del cut-off para cuasipartículas de Dirac en grafeno con la que calcular observables sistematicamente.
En la segunda parte se demostrará que fases topológicas, tanto en sus versiones enteras como fraccionarias, pueden emerger de interacciones de corto alcance en sistemas de cuasipartículas de Dirac. En primer lugar, en campo medio se demostrará que es posible estabilizar nuevas fases topológicas que rompen invariancia traslacional y la simetría bajo inversión temporal cerca de llenados conmensurados en la red hexagonal. Dichas fases se caracterizarán mediante su conductividad Hall y por su estructura de bandas topológicamente no triviales. A continuación, se presentará un modelo de cuasipartículas de Dirac donde se pueden estabilizar fases Hall fraccionarias. Se demostrará que sistemas con bandas con números de Chern mayores de uno con dispersión finita pueden estabilizar estos estados, contrariamente a la intuición basada en el paradigma de niveles de Landau.
En la parte final se estudiarán nuevos fenómenos físicos que podrían originar algunas fases topológicas. Se proporcionará primero una visión unificada de estas fases mediante el formalismo de acciones efectivas en grafeno y su bicapa. A continuación se presentan dos ejemplos de fenómenos físicos asociados directamente al hecho de que estos materiales poseen respuestas topológicas. Por un lado, se calculará la fuerza de Casimir entre dos placas de aislantes topológicos demostrando que es repulsiva (atractiva) a distancias cortas (largas), incluyendo efectos de temperatura y anisotropía. Esto motivará el estudio de la dependencia en frecuencia del término topológico. Para concluir, se desarrollará una teoría de respuesta lineal a campos externos libre de ambigüedades para una heteroestructura de aislantes ordinarios y topológicos, un ejemplo de semi-metal de Weyl. Se demostrará que la forma de dicha respuesta es la realización en materia condensada de una posible extension del modelo estándar de física de partículas que viola invariancia Lorentz, con consecuencias tales como la birrefringencia.

1. Introduction

"I have an equation; do you have one too?"
-P. A. M. Dirac to R. P. Feynman (Extracted from [2])

In 1928 Dirac proposed a theory for the electron that was both consistent with quantum mechanics, described by Schroedinger's equation, and with special relativity, characterized by Lorentz transformations [3]. To that purpose he introduced an equation that should describe the motion of the electron as a relativistic quantum mechanical particle described by its wave function ψ, now known as the Dirac equation

$$i\hbar\frac{\partial\psi}{\partial t} = \left(\sum_{i=1}^{3}\alpha_i p_i c + \beta mc^2\right)\psi. \tag{1.1}$$

Here p_i is the momentum of the particle in each spatial direction and α_i, β are matrices that satisfy adequate anticonmutation relations. Although this was one of the first important steps towards our current understanding of particle physics, with the above equation being a crucial building block of quantum electrodynamics (QED) and quantum chromodynamics (QCD), it is only now when we are beginning to grasp the deep consequences of such an equation to condensed matter physics and material science. Physics described by the Dirac equation was early encountered in condensed matter physics [4–6]. However it was with the advent of graphene [7], a two dimensional hexagonal lattice of carbon atoms, and topological insulators [8, 9], band insulators classified with concepts borrowed from topology, that the Dirac equation was definitely embraced by a large part of the physics community, not only as a description of fundamental particles, but also, as a description of emergent low energy degrees of freedom in condensed matter systems conventionally known as *quasiparticles*. The astonishing connection between theories proposed to understand high energy processes, on the MeV and TeV regimes, and those describing low energy physics, on the eV regime, through the Dirac equation has elevated these theories to the status of universal and thus, it is of fundamental interest to address them in as many situations as possible.
This thesis is focused precisely on understanding the behaviour of Dirac quasiparticles under different kinds of interactions and what role topology can play on the physical properties of materials hosting such quasiparticles. Although both issues can certainly be unrelated in some situations with each one of them manifesting remarkable physical effects, in this thesis we will also find that they can engage strongly with some deep experimental and theoretical

consequences, which can open our understanding of fundamental many-body phenomena. The discussion of these aspects in this thesis will follow a continuous transition from interaction to topology. Starting with pure interaction effects, we will move on to study the interplay between interaction and topological phases to end with the experimental consequences of such topological phases and other related questions.
To begin our discussion we will find it useful to provide, in the following sections a concise but hopefully self contained introduction to the most relevant physical and mathematical concepts employed in this thesis. We will summarize the main properties of two natural systems where Dirac quasiparticles emerge, graphene and topological insulators, central to the findings presented in the main body.

1.1. Graphene

Graphene [7] is probably the single material which, on its own, has triggered the fastest and most voluptuous response of the condensed matter physics community. Despite its apparently simple lattice structure, an hexagonal lattice of carbon atoms, it has attracted a vast amount of attention since its isolation in 2004 [10] because of the collection of remarkable properties that it possesses. In particular, it is by now the most celebrated example of a system that hosts low energy Dirac quasiparticles, and thus a natural candidate for the realization of much of the work presented in this thesis. In what follows, the main electronic properties of this material will be summarized. The discussion will be partially based on the detailed description of several aspects of graphene that can be found in the collection of review articles [7, 11–16].

1.1.1. Main electronic properties

Graphene is composed of carbon atoms arranged in a honeycomb lattice as shown in Fig. 1.1 (a). The atoms bond covalently with three neighbours through σ orbitals formed out of one s and two p outer shell orbitals of each carbon atom. The remaining electron occupies the $2p_z$, or π orbital forming the conduction and valence band and will determine the electronic properties of graphene. To find such band structure first one must note that the honeycomb lattice is not a Bravais lattice; it is constructed out of two interpenetrating triangular sublattices, conventionally label A and B. The primitive vectors a triangular lattice can be chosen to be $\mathbf{a}_1 = \frac{a}{2}(3, \sqrt{3})$ and $\mathbf{a}_2 = \frac{a}{2}(3, -\sqrt{3})$ with $a \simeq 1.42$ the distance between two neighbouring atoms. There are therefore, two atoms per unit cell, each one of them connected to its three other neighbouring atoms of a different sublattice by three vectors $\boldsymbol{\delta}_i$ $i = 1, 2, 3$ (see Fig. 1.1 (a)). The corresponding Brillouin zone is shown in Fig. 1.1 (b), with reciprocal lattice vectors given by $\mathbf{b}_1 = \frac{2\pi}{3a}(1, \sqrt{3})$ and $\mathbf{b}_2 = \frac{2\pi}{3a}(1, -\sqrt{3})$.
The first calculation of the band structure of graphene was published as early as 1947 by

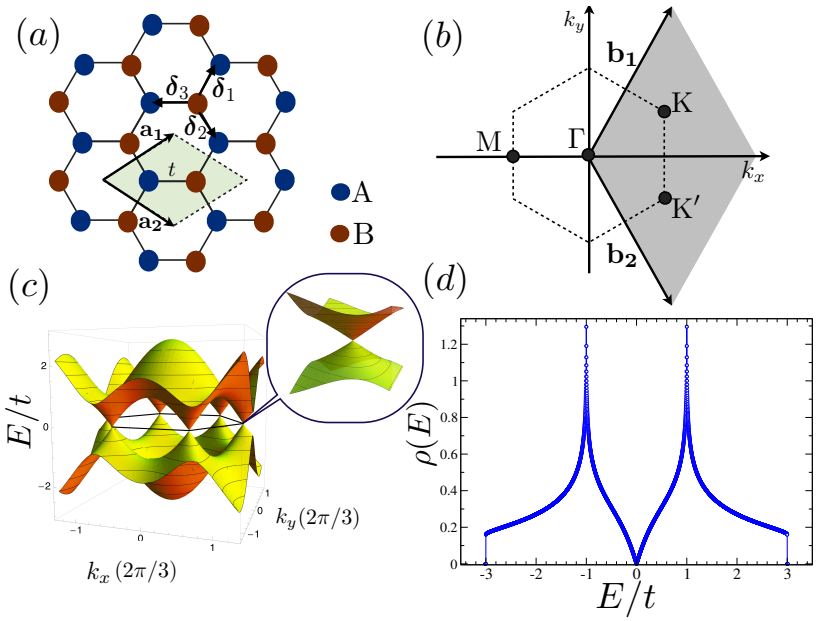

Figure 1.1.: Graphene in a nutshell: (a) graphene's honeycomb lattice in real space composed of sublattices A and B with primitive vectors are $\mathbf{a_{1,2}}$. A given carbon atom is connected to its neighbours through vectors $\boldsymbol{\delta}_i$, $i = 1, 2, 3$. The green rhombus shows the two atom unit cell. (b) The corresponding hexagonal Brillouin zone with reciprocal vectors $\mathbf{b_{1,2}}$. (c) Tight binding band structure of free standing graphene within the nearest-neighbour approximation. (d) The corresponding density of states for the band structure (c). The van Hove singularity is located at $E = \pm t$.

Wallace [17] in a tight binding approximation, which he used as a starting point to understand graphite. Assuming that electrons can hop only between nearest neighbouring atoms with an amplitude $t \sim 2.8$eV [7], the tight binding Hamiltonian of graphene can be written in second quantization as:

$$\mathcal{H} = -t \sum_{\mathbf{R}_i} a^\dagger(\mathbf{R}_i) \left[b(\mathbf{R}_i) + b(\mathbf{R}_i - \mathbf{a}_1) + b(\mathbf{R}_i - \mathbf{a}_2) \right] + \text{h.c.}, \tag{1.2}$$

where $a^\dagger(\mathbf{R}_i)$ ($a(\mathbf{R}_i)$) creates (annihilates) an electron in sublattice A (an equivalent definition holds for sublattice B). Transforming into Fourier space by the transformation $a(\mathbf{R}_i) = \frac{1}{\sqrt{N}} \sum_{\mathbf{k} \in BZ} a_{\mathbf{k}} e^{i \mathbf{R_i} \mathbf{k}}$ with N the number of unit cells, the Hamiltonian (1.2) can be written in a matrix form

$$\mathcal{H} = \sum_{\mathbf{k}} \psi^\dagger_{\mathbf{k}} H_{\mathbf{k}} \psi_{\mathbf{k}}, \tag{1.3}$$

where $\psi^\dagger = (a^\dagger_{\mathbf{k}}, b^\dagger_{\mathbf{k}})$ is a two component spinor and

$$H_{\mathbf{k}} = -t \begin{pmatrix} 0 & \gamma_k \\ \gamma_k^* & 0 \end{pmatrix}, \tag{1.4}$$

with $\gamma_k = 1 + e^{i\mathbf{k}\mathbf{a}_1} + e^{i\mathbf{k}\mathbf{a}_2}$. The two bands resulting from the diagonalization of such a Hamiltonian are given by $E_{\pm\mathbf{k}} = \pm|\gamma_\mathbf{k}|$ which explicitly are given by

$$E_{\pm\mathbf{k}} = \pm t\sqrt{3 + 2\left[\cos(ak_x) + 2\cos(ak_x/2)\cos(\sqrt{3}ak_y/2)\right]}, \tag{1.5}$$

shown in Fig. 1.1 (c), with corresponding eigenstates

$$|s\mathbf{k}\rangle = \frac{1}{\sqrt{2}}\begin{pmatrix} s\frac{\gamma_\mathbf{k}}{|\gamma_\mathbf{k}|} \\ 1 \end{pmatrix}, \tag{1.6}$$

with $s = \pm$. Since each carbon atom contributes with one electron, the lower band is completely filled and the Fermi energy lies exactly at the six band touching points, known as Fermi or Dirac points. The low energy quasiparticles are thus given by expanding around the two inequivalent points $\mathbf{K}$ and $\mathbf{K}'$ located at $(\frac{2\pi}{a3}, \pm\frac{2\pi}{a3\sqrt{3}})$ known as valleys. To linear order, the Hamiltonian around these points is nothing but the Dirac Hamiltonian defined in (1.1) which reads, for one valley

$$H_\mathbf{k} = v_F\begin{pmatrix} 0 & k_x - ik_y \\ k_x + ik_y & 0 \end{pmatrix} = v_F\boldsymbol{\sigma}\cdot\mathbf{k}, \tag{1.7}$$

where $\boldsymbol{\sigma} = (\sigma_x, \sigma_y)$ and $v_F = \frac{3at}{2}$ is the Fermi velocity ($v_F \sim 10^6 \mathrm{ms}^{-1}$) that has a linear dispersion $E_{\pm\mathbf{k}} = \pm v_F|\mathbf{k}|$ shown in the inset of Fig. 1.1 (c). The Hamiltonian for the other valley is also a Dirac Hamiltonian that can be obtained by a time reversal transformation of (1.7). The linear approximation is valid up to a cut-off energy $E_c \sim 1.0$ eV set by the energy where the dispersion relation departs from linearity.

We have therefore shown that indeed graphene hosts low energy quasiparticles described by the massless Dirac Hamiltonian defined at the right hand side of eq. (1.1), constrained to two spatial dimensions, with the Fermi velocity v_F and the Pauli matrices playing the role of c and the α_i matrices respectively. Throughout this thesis we will refer to any low energy quasiparticles that realize a version of (1.1) as *Dirac quasiparticles*. The presence of the low energy Dirac Hamiltonian in graphene is not a tight binding property, it originates from the symmetries of the lattice and the low energy expansion [18–20] which gives a sense of the robustness of such a description.

Indeed, such a model captures all the basic features observed in early experiments [21, 22], where it was shown that the spectrum of Landau levels in graphene was that of a Dirac Hamiltonian. Further confirmation was given from angle resolved photoemission spectroscopy (ARPES) [23] that showed (see Fig. 1.2) a band structure which matched well the predicted band structure in Fig. 1.1 (c). The success and robustness of such a description has been proven in various contexts [7, 11, 14, 24, 25]. The fact that the Dirac equation, in principle conceived to describe relativistic particles, also manifests as low energy degrees of freedom is remarkable and it is therefore not surprising the vast amount of attention given

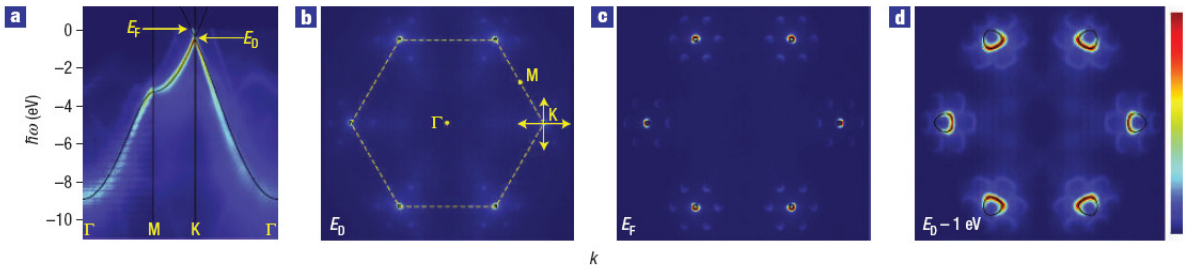

Figure 1.2.: (a) Electronic bands in graphene (b),(c),(d) through out the first Brillouin zone at different gate voltages measured with angle resolved photoemission spectroscopy (ARPES)[23].

to graphene both on the theoretical and experimental side. This has enabled beautiful analogues with high energy field theories [26] which we will partially explore in chapter 3.
Under the experimental point of view, a second remarkable property was that the carrier density n (and the sign of the carriers) in graphene was highly controllable by a gate voltage V_g through a field effect $n = C_g V_g / e$, where C_g is the gate capacitance per unit area [10]. Thus, by electrostatic doping graphene it is possible to explore the low energy sector of the band structure of graphene and its density of states, the latter shown in Fig. 1.1 (d) and given, near the Dirac point by

$$\rho(E) = \frac{g_s g_v |E|}{2\pi^2 v_F^2},$$

where $g_s = g_v = 2$ are the spin and valley degeneracies respectively. The fact that the density of states vanishes linearly with energy is a defining property of Dirac quasiparticles since as we approach zero energy, interactions between Dirac quasiparticles are poorly screened and thus the interaction among them is purely long ranged [26]. We will construct a theory to calculate physical observables around this fact in in chapter 3.
In addition, in chapter 4 we will explore the physics occurring near the van Hove singularities shown in Fig. 1.1 (d) at $E = \pm t$, which are saddle points of the band structure [27]. At these points, the diverging density of states is keen to host instabilities due to Stoner's criterion [28] which mathematically states the physical fact that an infinitesimal interaction will try to prevent the system from acquiring such a high degeneracy.

1.1.2. Bilayer graphene

For our discussion in chapter 6 we will also consider briefly the system composed of two layers of graphene known as bilayer graphene. Bilayer graphene [7, 29–32] is most commonly synthesised in two different stacking patterns. In the rarely found AA stacking, the layers are directly on top of each other, and so we will not consider it here. In Bernal stacking or AB stacking, one corner of the hexagons of the second sheet is located above the center of

the hexagons of the bottom sheet, as shown in Fig. 1.3 (a). The unit cell contains now four atoms and one can apply similar arguments to the monolayer case to obtain the low energy Hamiltonian. Following [32] one can write such a Hamiltonian in $\mathbf{k}$ space as $\mathcal{H} = \sum_{\mathbf{k}} \psi^{\dagger}_{\mathbf{k}} H_{\mathbf{k}} \psi_{\mathbf{k}}$ where now $\Psi^{\dagger}_{\mathbf{k}} = (a^{\dagger}_{1\mathbf{k}}, b^{1\dagger}_{\mathbf{k}}, b^{\dagger}_{2\mathbf{k}}, a^{\dagger}_{2\mathbf{k}})$ and

$$H_{\mathbf{k}} = \begin{pmatrix} V/2+\Delta & \zeta & t_{\perp} & -v_4\zeta^* \\ \zeta^* & V/2 & -v_4\zeta^* & v_3\zeta \\ t_{\perp} & -v_4\zeta & -V/2+\Delta & \zeta^* \\ -v_4\zeta & v_3\zeta^* & \zeta & -V/2 \end{pmatrix}, \tag{1.8}$$

The hopping parameters are defined in Fig. 1.3 (a), $\zeta(\mathbf{k}) = t\sum_i e^{i\mathbf{k}\cdot\boldsymbol{\delta}_i}$ and $v_i = \gamma_i/t$ with $i = 3, 4$. Parameter V takes into account a possible perpendicular electric field [31], which will induce a potential difference between the layers. The layers can have in addition an intrinsic charge asymmetry Δ [30]. The band structure of bilayer graphene with $\gamma_3 = \gamma_4 = \Delta = 0$ is shown in Fig. 1.3 (b)(c) for $V = 0$ and $V \neq 0$.

Importantly, the effect of parameter V is to open a gap, in sharp contrast with monolayer graphene, where a perpendicular electric field only induces charge carriers but does not open a gap. Infrared spectroscopy measurements fix the value of the parameters to be $t \sim 3$ eV, $t_{\perp} \sim 0.3$ eV, $\gamma_3 \sim 0.1 - 0.3$ eV and $\gamma_4 \sim 0.15$ eV although other values have been reported (for a representative summary see [33]). It is noteworthy that the effect of γ_3 is to split the quadratic band crossing into a four Dirac cone structure, one at the K point which is surrounded by three other points [29]. However, the original uncertainties and perhaps the search for simple models have motivated many authors often to neglect $\gamma_{3,4}$ against t and $t_{\perp}$.

In fact, as in monolayer graphene, the simple tight binding picture with only t and $t_{\perp}$ captures the essence of the electronic properties of bilayer graphene. As shown in [34] and reproduced in Fig. 1.3 (d), the band structure has been confirmed by ARPES. Important transport experiments in high magnetic fields also confirmed that the Hall effect is that of the parabolic dispersion shown in the Fig. 1.3 (b) and (c) [31]. Remarkably, both experiments are consistent with the opening of a gap when an external gate voltage V is applied.

Bilayer graphene its therefore, on its own, a very interesting material. Not only the opening of a gap with an external knob is important under the perspective of possible technological applications, but it is also a puzzling material under a more fundamental point of view. For instance, very recently, several groups have reported experimental evidence to support that the band structure is possibly strongly affected by electron-electron interactions at very low energies (see for example [35–37]). The nature of such a state is still unclear mainly because of controversies between different experimental results and also between different theoretical approaches [38–40]. Despite being a fascinating issue, in this thesis we will only consider non interacting bilayer graphene and describe it through the model (1.8).

To summarize this section, we have introduced both monolayer and bilayer graphene as

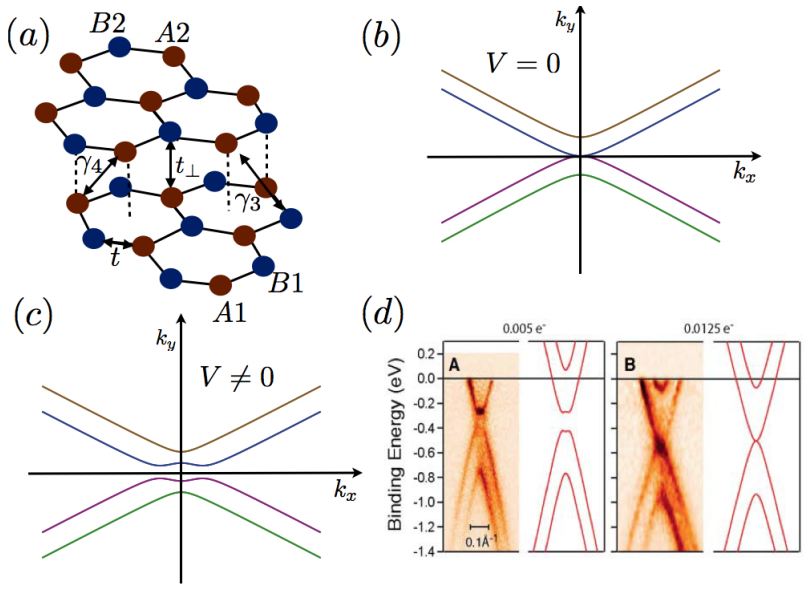

Figure 1.3.: Bilayer graphene in a nutshell: (a) bilayer graphene lattice in real space with the hoppings described in the text (b) The band structure of bilayer graphene with $\gamma_3 = \gamma_4$ is shown in Fig. 1.3(b)(c) for $V = 0$ and (c) $V \neq 0$ (d) ARPES image of bilayer graphene with and without external gate voltage (extracted from [34]).

systems that host low energy Dirac quasiparticles. We have discussed their main electronic properties that will be used throughout the thesis. We now proceed to describe a different class of materials, known collectively as topological insulators which shall also serve as an example of systems that host low energy Dirac quasiparticles.

1.2. Topological phases of matter

A fundamental part of our knowledge of physical systems gained in the 20th century gravitates around the concept of symmetry breaking [41]. With such a concept we have understood, for example, how the translational invariant Coulomb interaction can be responsible for crystalline order, that breaks such a translational invariance. This simple but profound idea has served well to understand other fundamental physical phenomena, from magnetic order [42], to the emergence of mass in sub atomic particles [43] with the celebrated discovery of the Higgs boson [44, 45]. The description of the process of symmetry breaking is given in terms of order parameters, which have vanishing expectation value if the symmetry is present, but acquire a finite expectation value via some mechanism in the symmetry broken state.

The discovery of the quantum Hall effect, both in its integer [46] and fractional [47, 48] versions could not be explained on the basis of such a symmetry breaking paradigm. In turn,

these phases of matter are described by concepts borrowed from the mathematical field of topology, namely topological invariants. In technical terms, topological invariants are used in mathematics to classify equivalence classes of homeomorfisms [49]. This is the precise mathematical way to say that, given a class of geometrical objects which can be *continuously* deformed into objects of that same class, these are classified by the same topological invariant. Objects that cannot be deformed into such a class will have a different topological invariant. The most intuitive example of a topological invariant is the genus g of a 2D surface, i.e. the number of holes it possesses. A torus, cannot be deformed smoothly into a sphere and thus they are said to belong to different equivalence classes of homeomorphisms. In general, if two classes have different topological invariants, they cannot be homeomorphic (smoothly deformed) to each other.
This apparently abstract way of classifying topological objects has emerged in condensed matter physics since the advent of the quantum Hall effect. For example, the quantized Hall conductivity can be written in terms of a product of e^2/h and a topological invariant which can only take integer values [50–52]. Physical phases that are realizations of such classifications of topological invariants are known as topological phases. In physics one can generalize the idea of deforming smoothly geometrical objects, to the idea of smoothly deforming Hamiltonians. In that case, gapped Hamiltonians which can be smoothly connected to others without closing the gap can be considered topologically equivalent, establishing a topological classification. It does not depend on details of the Hamiltonian, but rather on more general properties such its behaviour under different (discrete) symmetry operations such as time reversal or particle hole symmetry (for an exhaustive classification see [53]). It is important to stress that such a classification is not purely academic. It has some physical consequences such as the quantized Hall conductivity and the existence of extended and protected boundary states that are now understood as a consequence of such classifications[1] .

In this thesis we will focus on two topological phases of matter which we shall relate to Dirac quasiparticles, namely topological insulators with and without time-reversal symmetry. The quantum Hall effect measured in the two dimensional electron gas with an external magnetic field would fall in the second category while materials with a quantized spin Hall effect, called time-reversal invariant topological insulators would fall in the first category. The search for precise physical relationships between topological phases of matter and the physics of Dirac quasiparticles is one of the central goals of this thesis. Much work has been done in this direction already on which we will build up to extend our understanding of the interplay between Dirac quasiparticles and topological phases. To do so we will now discuss briefly some important concepts and models that will help us throughout this thesis.

[1] "Protected" here means for example that a perturbation which respects the symmetry of the Hamiltonian will not open a gap in the boundary states.

1.2.1. Time reversal breaking topological insulators

As in the case of the quantum Hall effect, the Hall conductivity of band insulators can also be associated to a topological invariant [54]. We will now review the basic concepts to understand the topological character of such a response that we shall employ in chapters 4 and 5. The intrinsic Hall conductivity of a non interacting band system can be generically calculated through the Kubo formula for any Bloch Hamiltonian with eigenstates and eigenvalues given by $\mid n, \mathbf{k} >$ and $\varepsilon_n(\mathbf{k})$ respectively through [54]

$$\begin{aligned} \sigma_{xy} &= e^2\hbar \sum_{n' \neq n} \int \frac{d\mathbf{k}}{(2\pi)^d} \left[n_f[\varepsilon_n(\mathbf{k}), \mu] - n_f[\varepsilon_{n'}(\mathbf{k}), \mu] \right] \\ &\times \ \mathrm{Im} \frac{< n, \mathbf{k} \mid \mathbf{v}_x \mid n', \mathbf{k} >< n', \mathbf{k} \mid \mathbf{v}_y \mid n, \mathbf{k} >}{(\varepsilon_n(\mathbf{k}, \mu) - \varepsilon_n(\mathbf{k}, \mu))^2}, \end{aligned} \tag{1.9}$$

where the velocity operator is defined through $\mathbf{v} = \frac{1}{i\hbar}[\mathbf{r}, H]$ and $n_F[\varepsilon_m(\mathbf{k}), \mu]$ is the Fermi-Dirac distribution. A remarkable property of this quantity is that it can be rewritten in terms of the topological properties of the wave function [55], namely the Berry connection and the Berry curvature [56, 57]

$$\sigma^{xy}(\mu) = \frac{e^2}{\hbar} \frac{1}{N\mathcal{V}} \sum_{\mathbf{k},m} \Omega_m^{xy}(\mathbf{k}) n_F[\varepsilon_m(\mathbf{k}), \mu], \tag{1.10}$$

where $\mathcal{V}$ is the volume of the unit cell, m is the band index and $\Omega_m^{ab}(\mathbf{k})$ is the Berry curvature for band m defined from the Berry connection $\mathcal{A}_m^a(\mathbf{k}) = -i \left\langle \Psi_m(\mathbf{k}) | \nabla_{\mathbf{k}}^a \Psi_m(\mathbf{k}) \right\rangle$, $\Omega_m^{ab}(\mathbf{k}) = \nabla_k^a \mathcal{A}_m^b(\mathbf{k}) - \nabla_k^b \mathcal{A}_m^a(\mathbf{k})$ with $a, b = x, y$. The remarkable parallelism between the Berry connection and Berry curvature with the electromagnetic gauge potential and the magnetic field is not casual. In order to give a brief insight to such a profound connection and interpret it under a topological perspective, consider a single band α[2]. For such a band it is possible to define the so called Chern number of the band, related to (1.10):

$$C_\alpha = \frac{e^2}{\hbar} \frac{1}{N\mathcal{V}} \sum_{\mathbf{k}} \Omega_\alpha^{xy}(\mathbf{k}), \tag{1.11}$$

This quantity is gauge invariant under a gauge transformation $\mathcal{A}_m^a(\mathbf{k}) \to \mathcal{A}_m^a(\mathbf{k}) + \partial_{\mathbf{k}}^a \chi_{\mathbf{k}}$ with $\chi_{\mathbf{k}}$ an arbitrary smooth function. This is evident if we think in terms of the electromagnetic analogy, since the integral (1.11) of Ω_α^{xy} in $\mathbf{k}$ is just the "flux" created by the "magnetic field" Ω_α^{xy} enclosed inside the Brillouin zone, which is a gauge invariant quantity. Following Berry [56] we can transform, by Stokes theorem the area integral into a line integral which is the circulation of the gauge potential on the closed path that encloses the surface. This allows for a second interpretation. The Chern number is determined by the phase the wave function acquires as it moves in a close loop in a region of "magnetic field" described by Ω_α^{xy}, which is just the analogous of the Aharanov-Bohm phase with real magnetic fields. Such a phase,

[2] For a complete review we refer the reader to Ref. [57].

is independent of the path taken. As long as it encloses a finite "flux" it will not be zero. This is thus a topological quantity, it only depends on the general properties (or topological class) of the underlying geometry of the Hilbert space. This is, in spirit, similar to the discussion above regarding the genus of a surface. If one can find a closed path that encloses one hole, then the object is in a different class than those without a hole, i.e. one surface cannot be deformed into the other. In our case, if the bands of a Hamiltonian have a non zero Chern number, it is not possible to continuously deform the Hamiltonian to one with bands of zero Chern number without closing the gap. This is equivalent to say that (1.11) is a topological invariant that classifies a topological phase of matter with non zero Hall conductivity. It is the band analogue of the invariant defined by Thouless *et al.* [50–52] for the integer quantum Hall effect.

In practice, it is possible to know from (1.10) when a given Hamiltonian will allow a finite Hall conductivity by just looking at the discrete symmetries it satisfies. The following table summarizes the conditions imposed to the Berry curvature and the Chern number whenever the Hamiltonian has either time reversal, inversion symmetry or a combination of both.

Symmetry	Berry Phase	σ_{xy} (1.10)
$\mathcal{T}$	$\boldsymbol{\Omega}_n(\mathbf{k}) = -\boldsymbol{\Omega}_n(-\mathbf{k})$	0
$\mathcal{I}$	$\boldsymbol{\Omega}_n(\mathbf{k}) = \boldsymbol{\Omega}_n(-\mathbf{k})$	non-zero*
$\mathcal{TI}$	$\boldsymbol{\Omega}_n(\mathbf{k}) = -\boldsymbol{\Omega}_n(\mathbf{k}) = 0$	0

The asterisk indicates the fact that the integral that defines the Hall conductivity might still be accidentally zero if the Chern numbers of the filled bands add up to zero, although it is generically non-zero. We shall use this table in chapter 4 to classify the possible topological phases that can appear in doped graphene from electron-electron interactions.

Having discussed time reversal broken phases, we now describe time reversal invariant topological phases.

1.2.2. Time reversal invariant topological insulators

In recent times the attempts to generalize the quantum Hall effect to time reversal invariant systems have opened new routes to realize topological phases of matter [8, 9]. The materials where these phases are realized are known as time reversal invariant topological insulators[3]. The discovery of such systems was motivated, on the experimental side, by the realization of the spin Hall effect [58–63], where the role of the Hall conductivity $\sigma_{xy} = \sigma^{\uparrow}_{xy} + \sigma^{\downarrow}_{xy}$ is played by the spin Hall conductivity defined as $\sigma^{(s)}_{xy} = \sigma^{\uparrow}_{xy} - \sigma^{\downarrow}_{xy}$.

The key step to realize a quantum spin Hall insulator with quantized spin Hall conductivity was proposed first in graphene by Kane and Mele [61, 64] partially inspired by earlier

[3] Note however that the term “time reversal invariant" is very often dropped from the name and these materials are referred to simply as topological insulators. This is usually clear from the context.

works by Semenoff and Haldane [65, 66]. A similar proposal in HgTe/CdTe quantum wells by Bernevig, Hughes and Zhang [63, 67] soon followed[4] and the remarkable experimental confirmation of such set-up [69] triggered the field of time reversal invariant topological insulators, and by extension, reinvigorated the investigation of topological phases of matter in general [8, 9].

We will now describe some general properties of two and three dimensional time reversal invariant insulators. We will focus not on particular models but rather on general properties which will be important later in the thesis. As we will now show these phases can be generically constructed and understood out of Dirac quasiparticle Hamiltonians and so, they are fundamental building blocks of the developments presented in this thesis. For further details we refer the reader to the review articles [8, 9] and references therein.

2D Topological insulators

To construct a two dimensional time reversal insulator we need to define a gapped Hamiltonian which is in a topologically non trivial class as compared to a different time reversal invariant Hamiltonian. Deforming one Hamiltonian into another is only possible by closing the gap and opening it again, going in the process through a topological phase transition. This introduces the concept of band inversion. A trivial insulator may be turned into a topological insulator through a band inversion process by closing the gap and opening it again.

As abstract as this might sound, this idea is at the heart of the proposal by Bernevig, Hughes and Zhang in Ref. [67]. The idea was to control the band inversion by an adjustable parameter which in their case was the thickness of the quantum well.

Instead of going to the details of this or other particular model, we will now describe a generic procedure to construct two dimensional time reversal topological insulator from Dirac quasiparticle Hamiltonians. This will serve us to introduce the general principles underlying such a phenomena which shall not require reference to any particular model. This is in fact is a measure of the beauty and robustness of topological phenomena. We will then make contact with the physical world by understanding under this framework the two physical models mentioned earlier, the Kane and Mele [61, 64] and the Bernevig, Hughes and Zhang [67] proposal. We will also encounter extensions of such a construction in the Kane and Mele type models which will be studied in detail in chapter 6.

Any two band Hamiltonian in two dimensions can be written in $\mathbf{k}$ space as

$$H(\mathbf{k}) = \epsilon(\mathbf{k})\mathbb{1} + d_i(\mathbf{k})\sigma_i, \tag{1.12}$$

where $i = 1, 2, 3$, σ_i are the three Pauli matrices, $\mathbf{k} = (k_x, k_y)$ and summation of repeated indices is implicit. In this case the Kubo formula for the Hall conductivity (1.9) can be written

[4] The appearance of a linear spectrum because of band inversion in semiconductor heterostructures and in particular in HgTe/CdTe quantum wells was in fact known much before that, see [68].

in the form [70]

$$\sigma_{xy} = \frac{e^2}{h}\frac{1}{8\pi^2}\int_{BZ} d\mathbf{k}\ \ \hat{\mathbf{d}}_{\mathbf{k}} \cdot (\partial_{k_x}\hat{\mathbf{d}}_{\mathbf{k}} \times \partial_{k_y}\hat{\mathbf{d}}), \tag{1.13}$$

where $\hat{\mathbf{d}}_{\mathbf{k}} = \mathbf{d}_{\mathbf{k}}/|\mathbf{d}_{\mathbf{k}}|$. This is nothing but again the topological invariant (1.11) this time explicitly written for the Hamiltonian (1.12). Its topological character is manifest by identifying the integrand as the Jacobian of a mapping defined by $\hat{\mathbf{d}}_{\mathbf{k}}$ from a two-torus T^2, the topology of the Brillouin zone, to a two-sphere S^2 spanned by the unit vector $\hat{\mathbf{d}}_{\mathbf{k}}$. Such a mapping defines the topological invariant (1.13) which is quantized to be an integer. For a massive (gapped) two dimensional Dirac Hamiltonian, i.e. $\mathbf{d}_{\mathbf{k}} = (k_x, k_y, m)$ the unit vector $\hat{\mathbf{d}}_{\mathbf{k}}$ only maps half of the unit sphere. Therefore, the contribution of a single Dirac cone to the Hall conductivity is $1/2$ in units of e^2/h. In fact, it is easy to check by direct substitution that the Hall conductivity is $\sigma_{xy} = \frac{1}{2}\frac{e^2}{h}\text{sign}(m)$.

Due to the Nielsen-Ninomiya theorem [71, 72], Dirac fermions in lattice systems always come in pairs and the Hall conductivity is the sum of the contribution of all of them as dictated by (1.13). If the system is time reversal invariant the contributions of each cone cancel out and the Hall conductivity is zero, i.e. the two cones have mass with opposite signs for each flavour of Dirac fermion (in graphene there are two flavours, one for each valley). The key idea introduced by Kane and Mele [64] and also underlying the proposal in CdTe/HgTe quantum wells in Ref. [67] is that assembling higher dimensional matrices out of 2×2 Dirac Hamiltonians, one can construct time reversal invariant Hamiltonians that have the appropriate mass signs so as to realize a finite spin Hall conductivity $\sigma^{(s)}_{xy} = \sigma^{\uparrow}_{xy} - \sigma^{\downarrow}_{xy} \neq 0$.

In graphene, the Hamiltonian (1.12) is realized for the sublattice (or pseudospin) degree of freedom. As Kane and Mele showed introducing the other valley and the spin degree of freedom it is possible to realize the quantum spin Hall phase with a quantized $\sigma^{(s)}_{xy}$. We will review and extend such a proposal in detail in chapter 6.

In the case of the CdTe/HgTe quantum wells of Ref. [67], the Hamiltonian (1.12) is realized in the spin subspace and the extra degrees of freedom are obtained by introducing the two quantum well sub-bands. The thickness of the quantum well fixes the sign of the Dirac mass for each 2×2 Hamiltonian determining whether the system is the topologically trivial or topologically non trivial spin quantum Hall state[5].

The common element of all proposals is therefore band inversion to control the sign of the mass (gap) at each Dirac node while preserving time reversal symmetry. Physically, this is achieved by a strong spin orbit interaction. In graphene, the intrinsic spin orbit interaction, proportional to the atomic number is small, and thus it is not in principle a plausible candidate to realize such a phase[6]. This is not the case of HgTe/CdTe quantum well systems,

[5] The topological invariant for a time reversal invariant phase is a $\mathbb{Z}_2$ number and not $\mathbb{Z}$ as in the quantum Hall effect [61].

[6] There are interesting proposals to enhance spin orbit interactions by external mechanisms such as flexural phonons, see for example [73].

which turned the effect observable as demonstrated in [69].
As a final note, it is possible to show that such a topological structure implies the existence of a pair of spin polarized edge states [61, 64]. At each edge there are two counter-propagating edge states that are protected from back scattering by time reversal symmetry and thus robust under non-magnetic impurities or defects. If a system realizes an even number of edge states, they will be no longer topologically protected and can localize.
With this discussion, we have highlighted the most important aspects, at least for this thesis, of $2D$ topological insulators under a general perspective. Importantly, these concepts can be generalized to three dimensional systems which we now briefly describe.

3D Topological insulators

The realization of three dimensional time reversal invariant topological insulators is determined by the same two key elements as for their two dimensional counter parts, namely time reversal symmetry and band inversion.
There are two types of time reversal invariant topological insulators, labelled weak and strong depending on the value of a $\mathbb{Z}_2$ topological invariant [74]. Although both have two dimensional boundary states only the ones of the strong type are topologically protected. The difference can be understood as follows. For example, if one constructs a three dimensional topological insulator by stacking two dimensional ones, the edge states will form a two dimensional boundary state. It is possible however to stack an even number of layers, and thus pile up an even number of edge states that can localize as discussed above. Therefore, protection is not topologically guaranteed. In this thesis however we will only refer to the strong type which have robust edge states.
As for the two dimensional case, here we will not derive a particular model but rather construct a generic theory which incorporates the most important elements of a time reversal invariant topological insulator used in this thesis. Then we will establish the connection of the presented construction with real materials that realize such phases and comment on the experimental status.
To begin, consider a Dirac quasiparticle in three dimensions defined by a four component spinor ψ. This time, we will allow it to be massive and to live in three spatial dimensions. The action which recovers the Dirac equation (1.1) by applying the Euler-Lagrange equations can be written as [75]

$$S = \int d^3x dt \;\; \bar{\psi}_x \left(i\gamma^i \partial_i - m \right) \psi_x. \tag{1.14}$$

The matrices γ_i, known as Dirac matrices, satisfy the Clifford algebra $\{\gamma_\mu, \gamma_\nu\} = 2g^{\mu\nu}$ where $g^{\mu\nu} = diag(1, -1, -1, -1)$, $\mu = 0, 1, 2, 3$ and $\bar{\psi} = \psi\gamma_0$. It is easy to check that applying Euler-Lagrange equations to (1.14) with respect to $\bar{\psi}$ one obtains $(i\gamma_\mu \partial_\mu - m)\psi = 0$ which defines,

by comparing to (1.1), the γ matrices in terms of α and β[7]. Referring to any standard quantum field theory textbook [75], it is easy to show that this action is time reversal invariant. Consider however the following global transformation:

$$\psi \rightarrow e^{ie\gamma_5\frac{\theta}{2}}\psi \tag{1.15}$$

$$\bar{\psi} \rightarrow \bar{\psi}e^{ie\gamma_5\frac{\theta}{2}}, \tag{1.16}$$

where $\gamma_5 = i\prod_{i=0}^{3}\gamma_i$ that satisfies $\{\gamma_5, \gamma_\mu\} = 0$. Under this transformation, known as a chiral transformation, the Lagrangian (1.14) is not invariant and changes to [75, 76]:

$$\begin{aligned} S &= \int d^3xdt\bar{\psi}_x\left(i\gamma^i\partial_i - me^{i\gamma_5\theta}\right)\psi_x \\ &= \int d^3xdt\bar{\psi}_x\left(i\gamma^i\partial_i - m\cos\theta - im\gamma_5\sin\theta\right)\psi_x. \end{aligned} \tag{1.17}$$

This action is not time reversal invariant. However, note that if $\theta = 0, \pi \pmod{2\pi}$ the action recovers time reversal symmetry since in that case the $\sin\theta$ term vanishes and we are only left with a term $\pm m$ for $\theta = 0, \pi$. Thus, we can classify time reversal invariant insulators in three dimensions by the sign of their mass. From the previous section, this already sounds familiar. It is only possible to connect the two with a continuous transformation while preserving time reversal symmetry by closing the gap and open it again with a different sign. Any other path, can be parametrized by a finite θ and thus breaks time reversal symmetry. We have then realized a topological classification for three dimensional time reversal invariant topological insulators[8].

In fact, this is not all one can learn from the simple action (1.14). Lets connect a topologically trivial insulator $\theta = \pi$ with an ordinary insulator with $\theta = 0$ which one can generically parametrize by space dependent mass $m(x)$ with the requirement that $\lim_{x\to-\infty} m(x) = m$ and $\lim_{x\to\infty} m(x) = -m$. This *domain wall* in the mass is what we need to prove there are edge states. Indeed, one can see that solving the Dirac equation with such a mass profile leads generically to a solution of the form [6, 79]:

$$\psi = e^{-\int_0^x dx' m(x')}\psi_{\text{surf}}(k_x, k_y). \tag{1.18}$$

The wave function at the surface $\psi_{\text{surf}}(k_x, k_y)$ satisfies a massless 2+1 dimensional Dirac equation, analogous to the one described by the Dirac Hamiltonian (1.7) although in the case of topological insulators the matrices σ_i, the Pauli matrices, represent the real spin, and not the sublattice pseudospin degree of freedom of graphene.

We have shown therefore that when two different topological phases are “glued" together

[7] The Dirac equation emerging in condensed matter systems is not Lorentz invariant. It is easy to incorporate in such action a Fermi velocity that will take that fact into account. However such a refinement will not affect our discussion and so we will omit it in what follows. We will further comment on related points in chapter 9.

[8] For a precise derivation see for example [77, 78].

a gapless zero mode boundary state appears, since we cannot go continuously from one to another without closing the gap. As we have shown, this does not depend on the profile $m(x)$. The existence of such states is fact is a topological feature, and they are gapless as long time reversal symmetry is conserved [74, 77].

The arguments discussed here are based on the simple action (1.14), but nevertheless they capture the basic key elements of topological insulators, namely band inversion (here represented by the sign of the mass) which then implies topologically protected boundary states. The mechanism for band inversion is, as in the two dimensional case a strong spin orbit coupling, and therefore one should look at materials that have such property (see Fig. 1.4 (a) and (c)).

Historically, it was first realized that some materials could hold three dimensional analogues of two dimensional time reversal invariant topological insulators by generalizing the topological invariants that describe them [74]. It was proven that strong topological insulators should have an odd number of surface states[9]. In particular, the alloy $Bi_{1-x}Sb_x$ was pointed out as a possible candidate [74]. Such a prediction was confirmed experimentally by ARPES experiments showing a five surface state structure [80]. Soon, more predictions followed for crystalline materials such as Bi_2Se_3 and Bi_2Te_3 [81] that realized the simplest of the surface models with only one surface state described, at low energy, by a two dimensional massless Dirac equation on the surface. Again, these detailed predictions were confirmed by photoemission experiments [82, 83] showing a clear gapless state at the surface (see Fig. 1.4 (d)). The topological character of such states was then deeply examined in Ref. [77] where they interpreted the findings under a field theory point of view that we used in this section. Remarkably, the list of proposed materials is rapidly increasing, while some of them are also regularly confirmed as being in the topological phase (for an up to date list see [84]).

In fact one can still go further to understand perhaps the the most striking consequence of such a state of matter, which we will repeatedly use and investigate in this thesis, namely the response of a time reversal invariant topological insulator to an external electromagnetic field. Fortunately, we can still understand such a response by using the action (1.14). Hence, and to end this section, we will highlight key aspects of the derivation of this response and some additional results that will be used in this thesis.

Consider, to this extent, coupling the simple action (1.14) to an external electromagnetic field, modelled by a gauge field A_μ. This theory is known as quantum electrodynamics (QED) in three spatial and one temporal dimensions ($D = 3+1$) and it is obtained with the formal replacement $\partial_\mu \to \partial_\mu + ieA_\mu$ which minimally couples the gauge field A_μ to the fermion ψ

[9] We note that the simple model (1.14) cannot account for this fact and only has one surface state, but it is in general possible to generalize such construction to incorporate these facts [77].

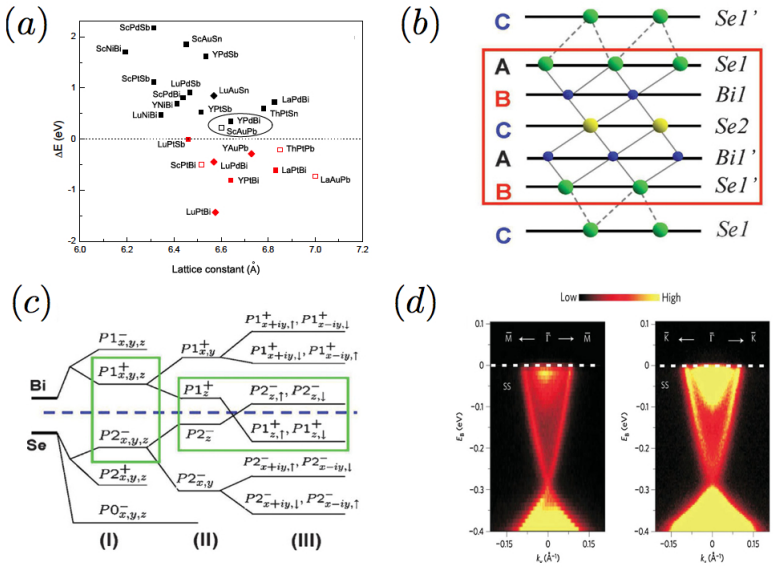

Figure 1.4.: 3D Topological insulators in a nutshell: (a) The search for a band inversion involves calculating band gaps with numerical methods which can map candidates to topological insulating phases (adapted from [84]). (b) The quintuple layer unit cell of Bi_2Se_3 (adapted from [81]) (c) The mechanism of inversion step (I) represents the chemical bonding, step (II) represent the crystal field and step (III) represents the spin orbit coupling correction which inverts the bands (adapted from [81]). (d) ARPES image for the surface in Bi_2Se_3 showing the predicted gapless surface state (adapted from [82]).

giving

$$\mathcal{S} = \int d^3x dt \;\; \bar{\psi}(i\not{D} - m)\psi - \frac{1}{4}F^{\mu\nu}F_{\mu\nu}, \tag{1.19}$$

where $\not{D} = \not{\partial} + ieA$ and the second term is the kinetic energy for the electromagnetic field with $F_{\mu\nu} = \partial_\mu A_\nu - \partial_\nu A_\mu$. Such an action will be discussed in detail in chapter 3 and we will take it here as a definition. If we want to know how the material responds to an external perturbation it is possible to integrate out the electrons and encode their effect into the functions ε and μ the electric permittivity and the magnetic permeability, which will in general be functions of the momentum and the frequency in an action of the form[10]:

$$\mathcal{S}_{EM} = \int d^3x dt \;\; \varepsilon \mathbf{E}^2 - \frac{1}{\mu}\mathbf{B}^2. \tag{1.20}$$

This is the end of the story for conventional dielectric materials. However, it is possible to show following Fujikawa [85] that the theory is not invariant under the local version of the

[10] On a more technical note, this is done by noting that the path integral of the action (1.19) is quadratic in the fermions and thus we can integrate them out, finding a theory for A_μ that encodes the effect of the fermions in a function $\Pi^{\mu\nu}$ the details of such a procedure will be described in detail in chapter 6.

chiral transformation (1.15)[11]. This adds a term to (1.20) of the form:

$$\mathcal{S}_\theta = \int d^3x dt \;\; \theta \frac{e^2}{8\pi h} \tilde{F}^{\mu\nu} F_{\mu\nu} = \int d^3x dt \;\; \theta \frac{e^2}{2\pi h} \mathbf{E} \cdot \mathbf{B}, \tag{1.21}$$

where $\tilde{F}^{\mu\nu} = \epsilon^{\mu\nu\rho\sigma} F_{\rho\sigma}$, also known as the *theta*-term or axionic term. One may be tempted to think that this term is unimportant since it is a surface term, and surface terms do not enter the equations of motion. This is true only for a constant θ which is readily seen by writing the Maxwell's equations

$$\begin{aligned}
\nabla \cdot \mathbf{D} &= 4\pi\rho + \frac{\alpha}{\pi} \boldsymbol{\nabla}\theta \cdot \mathbf{B}, && (1.22)\\
\nabla \cdot \mathbf{B} &= 0, && (1.23)\\
\nabla \times \mathbf{E} &= -\frac{1}{c}\frac{\partial \mathbf{B}}{\partial t}, && (1.24)\\
\nabla \times \mathbf{H} &= \frac{4\pi}{c}\mathbf{j} + \frac{1}{c}\frac{\partial \mathbf{D}}{\partial t} - \frac{\alpha}{\pi}\boldsymbol{\nabla}\theta \times \mathbf{E} - \frac{\alpha}{\pi}\frac{1}{c}\frac{\partial \theta}{\partial t}\mathbf{B}, && (1.25)
\end{aligned}$$

where $\alpha = \frac{e^2}{\hbar c}$ is the fine structure constant. Since in a time reversal invariant insulator $\theta = 0, \pi$ we recover the usual Maxwell equations. However if θ changes in space, for example across the topological insulator boundary, the new terms enter and we realize Wilczek's axion electrodynamics [86] known in the topological insulator literature as the topological magneto-electric effect. This type of electrodynamics has very exotic consequences, such as an induced image monopole when a charge is close to a the surface [87]. In chapter 7, we will explore the consequences that such a response has on the Casimir effect.

It is important to note that the assumption that θ changes across the boundary *implies* that we have broken by some physical mechanism time reversal symmetry at the surface. This can be seen by taking (1.21) and integrating it by parts for a step-like profile in $\theta(x)$. For θ going from π to 0 one may write the action at the boundary as

$$\mathcal{S}_\mathrm{b} = \int d^2x dt \;\; \sigma_{xy} \epsilon^{\mu\nu\rho} A_\mu \partial_\nu A_\rho, \tag{1.26}$$

where $\sigma_{xy} = \frac{e^2}{2h}$. In such case, the action turns to be a Chern-Simons action [77] at the boundary. As we saw for the two dimensional topological insulators this is exactly the Hall contribution of a single gapped (massive) Dirac cone, which in this case is at the surface. This explicitly breaks time reversal symmetry since a Hall response can only arise when time reversal symmetry is broken as discussed in section 1.2.1. Therefore, one has to conclude that for the equations (1.22)-(1.25) to be valid, time reversal symmetry should be broken.

Experimentally, such a breaking of the symmetry was proposed to be realized by a magnetization arising either from coating the topological insulator with a ferromagnetic material or by the presence of magnetic impurities. The resulting Zeeman field is, for the massless 2+1 Dirac fermions at the surface exactly a mass term that opens a gap at the surface, giving

[11] Technically, it is the path integral measure which is not invariant under such a transformation.

rise to (1.26). Note that the sign of the mass (which can be translated to the sign of θ) is determined by the sign of the magnetization at the surface, a fact we will use in chapter 7. It was shown [88] that for the topological insulator Bi_2Se_3, the magnitude of the surface gap increases with the (magnetic) impurity density and can be as large as 60meV for a concentration of 0.12 Fe impurities per Bi atom. Recent works also show the opening of a gap due to manganese impurities [89]. Theoretically, it was also shown in [90] that breaking time reversal symmetry with antiferromagnetic and ferrimagnetic orders at the surface may also lead to the opening of a surface gap. Despite several proposals, the realization of such axion electrodynamics defined by (1.22)-(1.25) remains elusive although the experimental progress is fast towards this direction [89].

We now end this section with some concluding remarks. The construction presented here based on (1.14) can be refined, as it will be in chapter 8, where we will construct a lattice model that realizes different magnitudes of the surface gap, among other details. Nonetheless, since we discussed topological properties, the conclusions presented here are very general, and do not depend on the particular lattice model that describes a topological insulator, as long as it is in the topological phase.
In the above discussion we have come across different topological phases in both two and three spatial dimensions. A very important and general aspect of such topological phases which we did not mention explicitly, is that the low energy response theory of such phases can be very generically written in terms of a topological field theory [49, 91]. We have already encountered two examples of such topological field theories, the first one being S_θ (1.21), which is a topological term known as the θ-term. This type of terms can be constructed in even dimensions and have, in D space time dimensions, a Lagrangian of the form $\mathcal{L} \sim \theta \epsilon^{\mu_1,\mu_2\cdots\mu_D} \partial_{\mu_1} A_{\mu_2} \partial_{\mu_3} A_{\mu_4} \cdots \partial_{\mu_{D-1}} A_{\mu_D}$. In odd space-time dimensions, the corresponding topological field theory is a Chern Simons theory of the form of S_b given by the generalization to odd space-time dimensions of (1.26) with Lagrangian $\mathcal{L} \sim \theta \epsilon^{\mu_1,\mu_2\cdots\mu_D} A_{\mu_1} \partial_{\mu_2} \cdots \partial_{\mu_{D-1}} A_{\mu_D}$. Both theories can be connected by a dimensional reduction procedure or compactification. Although much more can be said about such theories and their generalizations [2, 49, 91–93], in this thesis we will only briefly comment on them as they appear.

To summarize, in this chapter we have established the preliminaries on which this thesis is based. In the following section, we will review the general organization of the thesis.

1.3. Organization of the thesis

This thesis is divided into three different parts. The first two chapters deal with interactions in Dirac quasiparticle systems. The two central chapters aim to investigate how topological phases may arise from interactions. Finally in the last four chapters, several properties of

topological phases will be studied under a fundamental perspective, as well as also presenting novel physical effects which this phases help to realize. We will end the thesis with the overall conclusions. Building up on this, the findings presented in this thesis are structured as follows.

In chapter 2 we propose a phenomenological model to explain some relevant features of the optical response of graphene. We will propose a phenomenological *ansatz* for the self-energy inspired on a marginal Fermi liquid hypothesis which has support from a microscopical model of electron-electron interactions in graphene. We will see that it is possible to recover some features of the optical conductivity that are not explained by traditional approaches. We will also present the calculation, under such assumptions, of the electronic Raman response, related to the optical conductivity.

In chapter 3, we will introduce the concept of renormalization to determine observable quantities in the low energy model of neutral graphene. We will first extensively review past results for completeness and see that, in order to have a consistent, cut-off independent theory of interactions to calculate observables in graphene, one should introduce what are known as renormalization conditions. We will see that one can explicitly write cut-off independent quantities, which shall serve to calculate corrections to observables such as the conductivity.

In chapter 4, we propose a model to find time reversal breaking topological phases arising from extended Hubbard interactions in the doped honeycomb lattice. We will show that enlarging the unit cell stabilizes such phases. We will study the corresponding mean field phase diagram and understand the properties of the emerging topological phases using properties of Dirac quasiparticles such as the Hall conductivity. We will see generically, that these phases are analogues to the integer quantum Hall effect in lattice systems that we shall compare to other phases in the literature.

In the same spirit, we will look for fractional Hall phases in Dirac quasiparticles under strong interactions in chapter 5. We will characterize the so called *fractional Chern insulator* phases with tools borrowed from the vast knowledge gained in the understanding of the Fractional Hall effect. We will see that, perhaps contrary to naive expectation, such phases can be stabilized away from the Landau level intuition, i.e. a mathematically flat band with Chern number one. To do so, we will study models which realize non flat bands with higher Chern number (C=2) and characterize the emergent phases through numerical exact diagonalization methods.

After this, we will analyse some physical properties of topological phases and their experimental consequences. In chapter 6 we will review different mechanisms to realize two dimensional time reversal topological insulators under the unified perspective of the effective action formalism. This will generate a global framework to understand such phases. We will study as a model system time reversal topological phases in graphene and its bilayer.

In chapter 7 we will show that a repulsive Casimir effect is possible in a system of topological insulators, unlike in conventional dielectric systems. We will describe the conditions

under which two topological insulators, when close enough, may repel each other due solely to quantum effects. The topological nature of the electromagnetic response of these systems shall turn to be crucial to understand why repulsion appears in this system. The topological part of the response mixes the two light polarizations, unlike ordinary dielectrics, enabling the possibility of repulsion.

The study of the Casimir effect will raise the previously unanswered question of how the topological magnetoelectric response is generalized to finite frequency and finite chemical potential, a common situation in any current experimental set-up. We will shed light on this question in chapter 8 showing that the response is in general not quantized as soon as finite frequency and finite chemical potential are included.

As a final discussion, in chapter 9, we will use a previously reported system that realizes the three dimensional Dirac equation to resolve an ambiguity found in theories beyond the standard model of particle physics that violate Lorentz symmetry. In particular, this system realizes a version of Lorentz violating quantum electrodynamics which we shall use to formulate a consistent theory to describe the response of such system to an external field.

Finally, we will end with the concluding chapter 10 that will summarize and put into perspective the general findings of the thesis, followed by the bibliography.

Part I.

Interactions

2. Effect of Coulomb interactions on the optical conductivity of graphene

"Your ideas are so confusing that I cannot say whether they are nonsense or not"
-Wolfgang Pauli to L. D. Landau.

2.1. Introduction

Interesting physical phenomena often stem from acting on a system with an external perturbation. If such a perturbation has small strength compared to some characteristic scale in the system it is possible to expand the response in a power series in the interaction. To linear order in the interaction strength the response is simply proportional to the external field. Calculating the physical properties of the proportionality function between the field and the physical response is the aim of linear response theory [94, 95].
Consider the response of a system of electrons to an applied external electromagnetic field. In linear response theory, the current density induced in the system is proportional to the applied field. The proportionality function is known as the conductivity and it is in general a non-local in space-time tensor $\sigma^{\alpha\beta}(t', \mathbf{r}'; t, \mathbf{r})$[42, 96]. As will be argued below, this function carries information about interactions in the system under study and in particular about electron-electron interactions. It is therefore plausible to use this function as a measure of interactions between Dirac quasiparticles.
To this extent, the aim of the forthcoming sections is to characterize the conductivity in graphene from a phenomenological point of view, which will highlight some important aspects that characterize interactions between Dirac quasiparticles. Thus, in this chapter we will propose a simple model motivated by the experimental measured conductivity functions which will capture, up to some extent, the effect of electron-electron interactions in graphene.
The subject of interactions in graphene, at the time of writing, is still a very active and intense area of research [15]. Most commonly this issue is divided into two separate cases: the problem of interactions when the chemical potential lies exactly at the Dirac points, known

as undoped or intrinsic graphene, and the problem of interactions where extrinsic charge carriers are introduced in the system, for example with an external gate voltage, turning it into the so called doped or extrinsic graphene. An essential difference between these two cases is the dimensionality of the Fermi surface, being zero dimensional in the undoped case (two Dirac points) and one dimensional in the doped case (a line). This difference is profound since the general theory that describes interactions in solid state physics, the Landau-Fermi Liquid [94, 97], is based on the existence of a finite Fermi surface. For example, this theory fails when trying to describe an interacting one dimensional system where a new form of electron liquid emerges, the Tomonoga-Luttinger Liquid [98], whose fundamental degrees of freedom are described by a bosonic theory. Graphene is thus an interesting example of a two dimensional electronic system that has, in its intrinsic state, a zero dimensional Fermi surface. It is thus not surprising that the ordinary Landau-Fermi liquid theory for interacting electron systems is not completely applicable to graphene and new interesting physics can appear, a part of which we will discuss in some detail below. In fact, intrinsic graphene shares some properties of what is known as *marginal* Fermi liquid, a kind of electronic liquid that was first phenomenologically proposed to describe some experimental features of High-T_c superconducting cuprates, including the optical conductivity [99, 100].
One of the intriguing aspects of interactions in graphene is the crossover between these two seemingly contradictory behaviours, the Fermi-liquid, applicable to doped graphene, and the marginal Fermi liquid that describes intrinsic graphene. Through the optical conductivity, in this chapter we will argue that it is possible that the undoped physics of the marginal Fermi liquid can have experimental signatures at finite doping where the Landau-Fermi liquid should be still applicable.
The chapter is structured as follows. First, for completeness, we will review some basic concepts of the linear response theory and its application to graphene as a tool to calculate the optical conductivity and the related Raman spectra. Then the relevant aspects of the Fermi Liquid theory and the marginal Fermi liquid theory will be discussed to motivate the phenomenological model. After the particulars of the model have been introduced the results will be presented and discussed ending with a summary of the main conclusions of the chapter.

2.1.1. Linear response theory: The optical conductivity

As mentioned in the introduction, the conductivity is the function that relates an applied electromagnetic field to the induced current density. Mathematically, the induced current density is the expectation value of the current operator $\langle \mathbf{j} \rangle$ inside the system due to the external perturbation. To define such a quantity we first couple the Hamiltonian to the electromagnetic field which is achieved through the Peierls substitution [101]. To first order this is equivalent to a minimal coupling of the electromagnetic field, which amounts to the sub-

stitution $\mathbf{k}$ for $\mathbf{k} - \frac{e}{c}\mathbf{A}$, where $\mathbf{A}$ is the electromagnetic vector potential. The current operator is defined through the functional derivative of the Hamiltonian with respect to $\mathbf{A}$

$$\delta\mathcal{H} = -\frac{1}{c}\int d\mathbf{r}\,\mathbf{j}\,\delta\mathbf{A}. \tag{2.1}$$

For a generic Hamiltonian, the current operator $\mathbf{j}$ involves two types of terms to first order in $\mathbf{A}$, one proportional to $\mathbf{A}$ known as the diamagnetic contribution, and the $\mathcal{O}(\mathbf{A}^0)$ order contribution, known as the paramagnetic term [42]:

$$\mathbf{j} \;=\; \mathbf{j}_{para} + \mathbf{j}_{dia}. \tag{2.2}$$

These two terms can be understood as arising from the first to terms of the functional derivative with respect to $\mathbf{A}$ of an expansion in powers of $\mathbf{A}$ of the minimal coupled Hamiltonian $H(\mathbf{k} - e/c\mathbf{A})$. Thus the paramagnetic (diamagnetic) term is proportional to the first (second) derivative of the Hamiltonian with respect to the momentum $\mathbf{k}$.
For an ordinary parabolic dispersion, the case for example of a two dimensional electron gas (2DEG), the expectation value of the diamagnetic term is proportional to $\mathbf{A}$ and the equilibrium density $n(\mathbf{r}) = \langle\varrho(\mathbf{r})\rangle_0$, where the expectation value is calculated at equilibrium [42].
On the other hand, to first order in $\mathbf{A}$, the expectation value of the paramagnetic term is proportional to the the current-current correlation function, also known as polarizability:

$$\Pi^{\alpha\beta}(\mathbf{r},\mathbf{r}',\omega) = -i\int_\infty^\infty dt\theta(t-t')e^{i\omega(t-t')}\left\langle\left[j_\alpha(\mathbf{r},t), j_\beta(\mathbf{r}',t')\right]\right\rangle, \tag{2.3}$$

for $\alpha,\beta = 1,2,3$. Choosing a gauge where $\mathbf{A}(\mathbf{r},\omega) = -i/\omega\mathbf{E}(\mathbf{r},\omega)$ (the final result is of course independent of this choice) the expectation value of the α component of the current operator is:

$$\langle j^\alpha\rangle \;=\; \left\langle j^\alpha_{para}\right\rangle + \langle j^\alpha_{dia}\rangle \tag{2.4}$$

$$\;=\; \left[\frac{ie^2}{\omega}\Pi^{\alpha\beta}(\mathbf{r},\mathbf{r}',\omega) + \frac{e^2 n(\mathbf{r})}{i\omega}\delta(\mathbf{r}-\mathbf{r}')\delta^{\alpha\beta}\right]\mathbf{E}_\beta(\mathbf{r},\omega). \tag{2.5}$$

The conductivity $\sigma^{\alpha\beta}(\mathbf{r},\mathbf{r}',\omega)$ is by definition the function inside the square brackets. Making use of translational invariance:

$$\sigma^{\alpha\beta}(\mathbf{q},\omega) = \frac{ie^2}{\omega}\Pi^{\alpha\beta}(\mathbf{q},\omega) + \frac{e^2 n}{i\omega m}\delta_{\alpha\beta}. \tag{2.6}$$

This last expression is known as the Kubo formula for the conductivity [1] where $\Pi^{\alpha\beta}(\mathbf{q},\omega)$ is the Fourier transform to momentum space of (2.3) .
Before proceeding to the calculation of this quantity for graphene, a few comments are in order. Firstly, note that for a linear dispersion relation, which is of interest to describe the

[1] We have assumed a parabolic dispersion relation. For a general expression of the conductivity without any assumption on the dispersion relation see [101].

low energy physics of graphene, the diamagnetic term will not contribute to the conductivity, since it is formally proportional to the second derivative of the Hamiltonian with respect to $\mathbf{k}$. As a second point is that, in this chapter, we will be interested only in the real part of the conductivity which, gives information about the absorption of the material, and thus

$$\mathrm{Re}\sigma^{\alpha\beta}(\mathbf{q},\omega) = -\frac{e^2}{\omega}\mathrm{Im}\Pi^{\alpha\beta}(\mathbf{q},\omega). \tag{2.7}$$

This function is in general a complicated function of both $\mathbf{q}$ and ω. However, in most cases the wavelength of the incoming radiation is large compared to the atomic distance (excluding for example high energy light sources such as synchrotron radiation). Thus we can focus on the long wavelength limit and set $\mathbf{q} \to 0$. Mathematically, this limit presents no problem since $\Pi^{\alpha\beta}(\mathbf{q},\omega)$ is usually well behaved in this limit. The frequency dependent conductivity which is left is referred to as the optical conductivity since the typical energies are below the eV scale.

We have therefore reduced the problem of how the material responds to an external electric field to the calculation of a single quantity, the polarizability function $\Pi^{\alpha\beta}(\mathbf{q},\omega)$. However, our initial goal was to understand effects of electron-electron interactions between Dirac quasiparticles. In the remaining part of this section, we will address how interaction effects enter the polarization function. In order to do so, it is convenient to rewrite it in the Green's function formalism. For a generic interacting system, the electronic Green's functions have the form [42]:

$$G(\mathbf{k},\omega) = \frac{1}{\omega - \xi_{\mathbf{k}} - \Sigma(\mathbf{k},\omega)}, \tag{2.8}$$

where $\xi_{\mathbf{k}}$ are the non-interacting Hamiltonian eigenvalues and $\Sigma(\mathbf{k},\omega)$ is the self energy. All the effects of interactions are contained in the self-energy function. The non interacting Green's function (which has $\Sigma(\mathbf{k},\omega) = 0$) is modified in such a way that the free particles are now "dressed" by the interaction with other particles.

It is also useful to define another auxiliary function, the spectral function, which has a full physical meaning. The spectral function can be defined as [42]:

$$\mathcal{A}(\omega,\mathbf{k}) = -2\mathrm{Im}G(k,\omega) = \frac{-2\mathrm{Im}\Sigma(\omega,\mathbf{k})}{(\omega - E(\mathbf{k}) - \mathrm{Re}\Sigma(\omega,\mathbf{k}))^2 + (\mathrm{Im}\Sigma(\omega,\mathbf{k}))^2}. \tag{2.9}$$

It can be interpreted as the probability density that an electron has a momentum $\mathbf{k}$ and energy ω. It gives an idea of how well defined are the interacting states. For a non interacting system the spectral function is a Dirac delta centred at the energy of the particle which is equivalent to the fact that an excitation with energy ω can only happen by adding an electron to the state $\mathbf{k}$ that follows the non interacting dispersion relation $\omega = E(\mathbf{k})$. Typically, the effect of interactions will broaden the Dirac delta function peak turning the spectral function $\mathcal{A}(\mathbf{k},\omega)$ into a Lorentzian. In the presence of a scattering mechanism -disorder or interaction- the low energy excitations of the system are dressed particles or quasiparticles and these

states will now have a finite lifetime. The width of the Lorentzian is determined by the imaginary part of the self-energy and hence, it is associated with the inverse quasiparticle lifetime. From (2.9), the real part of the self-energy renormalizes the dispersion relation [2]. Following standard many-body theory, [96, 101] it is possible to show that the polarizability function is given by an integral of the product of two Green functions given by (2.8) and a vertex function. For the case in which there is no $\mathbf{k}$ dependence in the self-energy, one can see that the vertex correction is proportional to the derivative of the dispersion relation with respect to $\mathbf{k}$, due to the form of the Ward identities[3], and we are left with the expression:

$$\mathrm{Im}\Pi^{\alpha\beta}(\Omega) = \frac{g_s}{V}\sum_{\mathbf{k}} a_{\mathbf{k}} b_{\mathbf{k}} \int_{-\infty}^{\infty} \frac{d\omega}{\pi} \mathrm{Im}G(\mathbf{k},\omega)\mathrm{Im}G(\mathbf{k},\omega+\Omega) \times \left[n_F(\omega) - n_F(\omega+\Omega)\right], \quad (2.10)$$

where $a_{\mathbf{k}}, b_{\mathbf{k}} = \partial_{\mathbf{k}}\varepsilon_{\mathbf{k}}$ and we have taken already the external momentum to zero ($\mathbf{q} \to 0$). Note that, in the simple case of a 2DEG $a_{\mathbf{k}}, b_{\mathbf{k}}$ are simply proportional to $\mathbf{k}$. The function $n_F(\omega) = [\exp(\beta(\omega-\mu))+1]^{-1}$ is the Fermi distribution function and g_s is the spin degeneracy. It is now evident that this function carries information about interactions of quasiparticles through the self-energy function. Since the main goal of this chapter is to study Dirac quasiparticles in graphene we now proceed to discuss the particulars of the calculation for this system.

2.1.2. Conductivity of graphene

When calculating the optical conductivity of graphene one comes across two essential differences between this system and a 2DEG. The first one, already mentioned is that graphene has a linear dispersion relation. The second difference, not discussed previously, is related to the fact that graphene has two bands, making the Green's function a matrix which can be diagonalised in order to simplify calculations. This introduces some basis dependent factors in the formula for the conductivity which are expected when treating multiple band system. The first step is to find graphene's non interacting Green's function. In the diagonal basis, defined by the eigenvectors $|s\mathbf{k}\rangle$ in (1.6), it takes the form

$$G(\mathbf{k}) = \sum_s G_{ks} \left|s\mathbf{k}\right\rangle \left\langle s\mathbf{k}\right|, \quad (2.11)$$

where $G_{k,\pm} = 1/(ik_n \mp v_F|\vec{k}|)$ is the Green's function for each band is written in the Matsubara frequency representation, where $k_n = 2\pi(2n+1)/\beta$ are the fermionic Matsubara frequencies which can take into account temperature dependence through $\beta = k_B T$. The

[2] Renormalization is used in a broad sense, which is not to be confused with the renormalization method presented in the next chapter.

[3] Using loose notation, the vertex function $\mathbf{T}$, due to the Ward identities, satisfies when $\mathbf{q} \to 0$, $\mathbf{T} = \partial_{\mathbf{p}}\varepsilon(\mathbf{p}) + \partial_{\mathbf{p}}\Sigma(\mathbf{p})$ (see [96] Sec.7.1.D) and thus if $\Sigma(\mathbf{p},\omega) \sim \Sigma(\omega)$ it follows that $\mathbf{T} = \partial_{\mathbf{p}}\varepsilon(\mathbf{p})$. Note that this form of the Ward identities is not the general form of the Ward identities and it is stated in a different (although equivalent) form compared to particle physics or high-energy text books.

effect of interaction can be taken into account by introducing the self-energy as it was explained previously.
The next step is to find the current operator in graphene. The low energy Hamiltonian, making use of the minimal coupling is

$$\mathcal{H} = \int d\mathbf{r}\, \Psi^{\dagger}(\mathbf{r}) v_F \boldsymbol{\sigma} \left[i\boldsymbol{\partial} - \frac{e}{c}\mathbf{A} \right] \Psi(\mathbf{r}).$$

As anticipated in the previous section, it follows from (2.12) that in the low energy approximation the diamagnetic term of the Kubo formula is necessarily absent. From the definition of current operator (2.1) made earlier it is straightforward to obtain that

$$\mathbf{j}(\mathbf{k}) = e v_F \Psi^{\dagger}(\mathbf{k}) \boldsymbol{\sigma} \Psi(\mathbf{k}).$$

This defines the vertices in (2.10) as $a_{\mathbf{k}} = e v_F \boldsymbol{\sigma}$. Considering all of the above the conductivity can be expressed as (in units where $\hbar = 1$)

$$\mathrm{Re}\sigma(\omega) = g_s g_v \frac{e^2 v_F^2}{4\omega} \sum_{s,s'} \int \frac{dkk}{(2\pi)^2} \int d\epsilon \left[n_F(\epsilon) - n_F(\epsilon + \omega) \right] \mathcal{A}_s(k,\omega) \mathcal{A}_{s'}(k, \epsilon + \omega), \tag{2.12}$$

where $n_F(\epsilon) = [\exp(\beta(\epsilon - \mu)) + 1]^{-1}$ is the Fermi distribution function and $\mathcal{A}_s(k,\omega)$ is the spectral function of band s. The constants g_s and g_v are the spin and valley degeneracies respectively. At zero temperature, the Fermi distribution functions are step functions which determine the limits of the energy integral. In the rest of this chapter, no temperature effects will be considered and thus we set $T = 0$ above, although expression (2.12) is valid for finite T.
These are all the necessary ingredients to calculate the optical conductivity in graphene. Before doing so, it is illustrative however to consider the non interacting DC conductivity limit of expression (2.12) which is obtained by making the self-energy vanish $\Sigma(\omega) = 0$. It is not difficult to show that for vanishing chemical potential the polarizability function takes the form [26]

$$\mathrm{Im}\Pi^{xx} = -\frac{\pi}{8}\frac{\omega}{2\pi}. \tag{2.13}$$

When introduced in (2.7) a frequency independent conductivity is obtained (with valley and spin degeneracies included) [102]

$$\mathrm{Re}\sigma^{xx}(\omega) = \frac{\pi}{2}\frac{e^2}{h} \equiv \sigma_0, \tag{2.14}$$

where h is Planck's constant. This is a remarkable result on its own. The optical conductivity of graphene is not only constant in the low energy approximation, but determined only by fundamental constants and independent of any material parameters. Early experiments measured a conductivity somewhat larger than σ_0 [22, 103, 104] which triggered a vivid debate on the possible corrections to the conductivity due to electron-electron interactions

in the undoped case [15] which we will discuss in the next chapter. If the intensity of light is sufficiently strong (typically bigger than 1eV) then there higher order corrections must be included since the linear effective model (2.12) ceases to be valid. We will henceforth use σ_0 as the natural units for the optical conductivity of graphene, and therefore express all results relative to this quantity. For the case where there is a finite chemical potential the conductivity takes the form

$$\mathrm{Re}\sigma(\omega) = \sigma_0\theta(\omega - 2\mu). \tag{2.15}$$

The step function functional dependence of the conductivity indicates that no interband transitions are allowed for energies under 2μ which is schematically shown in Fig. 2.1 (a).
The optical conductivity is not the only optical experiment which can probe the effect of electron-electron interactions in graphene. Inelastic electronic Raman scattering is a photon in photon out process with energy transferred to a target material, thus being a phenomenon of inelastic scattering of light. There are many types of scattering sources such as phonons, magnons and of course electrons. In graphene, phononic Raman spectroscopy is used to distinguish monolayer graphene from its bilayer (or multilayer) counterparts since they have characteristic Raman spectra [105].
Electronic Raman spectroscopy however focuses on the electronic signature on Raman spectroscopy. The electronic contribution is due to modifications of charge density in the illuminated region of the sample (see Fig. 2.1). One of the key aspects in Raman is that both the incoming and the outgoing photon can be manipulated to align them in a certain polarization direction. With the help of symmetry arguments (selection rules) one can map charge excitations to projections of different regions in the Brillouin zone. This technique has therefore momentum and energy resolution.
For a system with a $\mathbf{k}$ independent self-energy it is possible to show that the inelastic electronic Raman intensity $\chi_{\gamma,\gamma}(\omega)$ satisfies the useful relation [106, 107]

$$\omega\mathrm{Re}\sigma(\omega) \propto \mathrm{Im}\chi_{\gamma,\gamma}(\omega), \tag{2.16}$$

Below, we will motivate these assumptions for the self energy of graphene making (2.16) a very useful expression to calculate the electronic Raman intensity from the optical conductivity (2.12). Inelastic electronic Raman response has been calculated for graphene in the presence of a magnetic field [108].

2.2. Self energy in graphene

In the last sections the main idea was, in a nutshell, that given a dispersion relation, the properties of the optical conductivity and the Raman intensity are determined by the self-energy. Therefore, once derived or proposed a self-energy these properties of the system

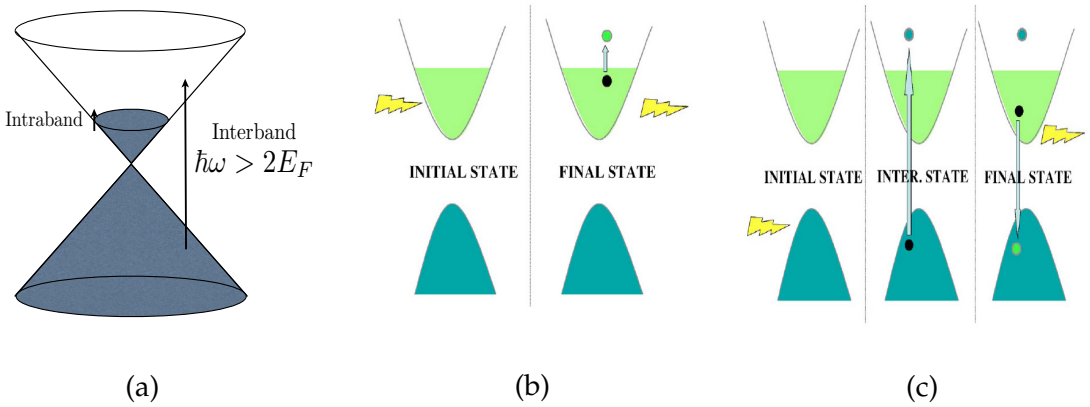

Figure 2.1.: (a) Schematic view of the allowed transitions for the optical conductivity. Interband transitions at $\mathbf{q} = 0$ are only allowed, by Pauli's exclusion principle, for energies larger than 2μ. In (b),(c) different types of Raman processes are shown: (b) Intraband and (c) Interband. Extracted from [107]

follow. Calculating self-energies in graphene, as in most systems, is not a simple task and usually different approximations have to be made. Due to the different dimensionality of the Fermi surface in doped and undoped graphene, it is reasonable to expect that the self energy in this two situations are very different. Disorder and impurities can also induce a finite density of states at the Fermi level in the system and thus change the self energy function.
Before discussing particular models for these cases it is illustrative to discuss first the experimental properties related to the self-energy, and their relation with the mentioned momentum independent approximation.

2.2.1. Measuring the self-energy: the momentum independent approximation

Many of the phenomenological calculations of observables using the self-energy, and, in particular, the ones that we will present in this chapter are based on the assumption that the self-energy can be considered momentum independent. This approach can be justified by the use of angle resolved photoemission spectroscopy (ARPES) experiments, where a direct measure of the spectral function (2.9), and hence the self energy can be performed.
To interpret the data out of this probe one can proceed as follows [109, 110]. The ARPES intensity is proportional to the spectral function (2.9). Examples of these spectra for graphene are shown in Fig. 2.2 which clearly resemble the characteristic linear dispersion relation with a Dirac point. At this stage, one can define the momentum distribution curves (MDC) which are simply $\mathrm{MDC}(\mathbf{k}) = A(\mathbf{k})|_{\omega=\mathrm{const}}$. From the definition of the spectral function these have a maximum at a certain $\mathbf{k}_m$ determined by the condition $\omega - E(\mathbf{k}_m) - \mathrm{Re}\Sigma(\omega) = 0$. Given the dispersion relation $E(\mathbf{k}_m)$ we can read from the experiment the difference $\omega - E(\mathbf{k}_m)$ and hence obtain the real part of the self-energy. Notice that we have already made the assumption that the self energy has a weak momentum dependence. This assumption will

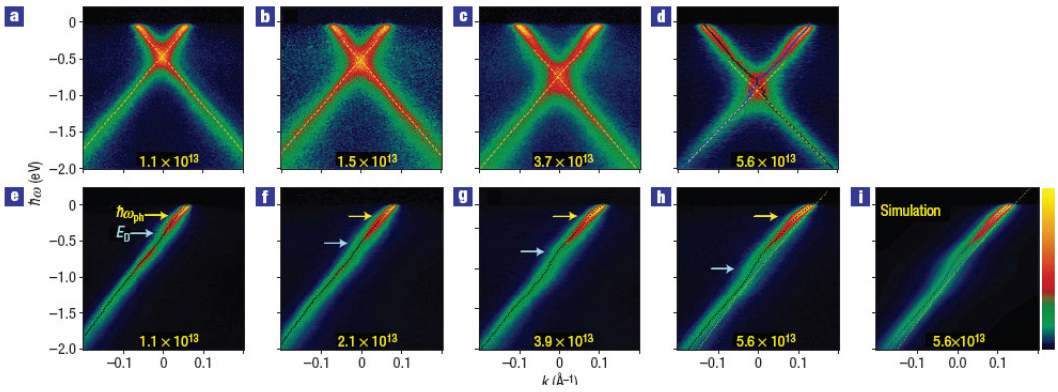

Figure 2.2.: Dispersion relation as seen by ARPES in [23].

be proven correct in a self-consistent manner only if at the end we find no contradiction with this assumption.

The next step is to plot the MDC against momentum. These will have typically a Lorentzian shape if the quasiparticle picture is reasonable inside the system under consideration. The Lorentzian curves have an omega dependent width which is proportional to the inverse quasiparticle lifetime, as it was discussed above. Hence from this measurements it is possible to obtain independently both the real and imaginary parts of the self energy. The consistency check comes from the Kramers-Kronig relations which relate the real and the imaginary parts of the self energy. Calculating the Kramers-Kronig counterpart of the real part of the self-energy and comparing it with the measured imaginary part gives the final test for the momentum independent approximation and its the validation of the hypothesis.

Reported experiments in graphene [23] show that this hypotheses is reliable. In Fig.2.2 it is shown how the simulated spectral function, calculated with real part obtained by a Kramers-Kronig check is coincident with the measured one, making the momentum independent assumption valid. We now review the different approaches used to calculate the self energy of graphene in the doped and undoped cases.

2.2.2. Self energy in doped graphene

Although ultra clean suspended graphene samples can now be grown relatively easily to achieve excellent mobilities ($\sim 10^6 cm^2 V^{-1} s^{-1}$) and very low carrier concentrations ($\sim 10^8 cm^{-2}$) [111], graphene can be doped easily, either intentionally with a gate voltage or unintentionally by a substrate and so the self energy in this context is of great experimental interest. This situation has been addressed in [23, 112] where it was argued that in the Random Phase Approximation (RPA) [112], the self-energy of graphene in the doped case is given by

$$\mathrm{Im}\Sigma_{FL}(\omega) = \frac{8E_F}{\pi}\left(\frac{\omega}{8E_F}\right)^2\left[\ln\left(\frac{\omega}{8E_F}\right)+\frac{1}{2}\right], \tag{2.17}$$

where $E_F = v_F k_F$. From the imaginary part, one can calculate the real part from a Kramers-Kronig transformation (see appendix A) This self-energy is that of a two dimensional Landau-Fermi Liquid. The Landau-Fermi Liquid theory, developed in the context of superfluid He^3, is one of the most successful paradigms in condensed matter physics [95, 97]. Essentially, it describes the low energy excitations of an interacting electronic system by filling the states of the non interacting system with dressed quasiparticles. The interaction is then hidden in some parameters such as the effective mass m^* (in the case of a 2DEG) and the wave function renormalization $Z(\omega, \mathbf{k})$. The value of this last parameter at the Fermi surface is often used to determine the Fermi liquid nature of an electron system. It contains information on the weight of the quasiparticles relative to the total spectral weight. In terms of these quantities, the Green's function has the form:

$$G(\omega, \mathbf{k}) = \frac{Z(\omega, \mathbf{k})}{\omega - \hat{\varepsilon}(\mathbf{k}) + i\mathrm{Im}\Sigma(\omega, \mathbf{k})} + G_{\mathrm{incoh}}. \tag{2.18}$$

$Z(\omega, \mathbf{k})$ determines the residue of the pole of the quasiparticles. It ranges in the interval $0 < Z \leq 1$, having a magnitude of one for the non interacting case. When this parameter vanishes at the Fermi energy, the Landau Fermi Liquid breaks down and other models have to be used. This is the case of the one dimensional electron systems or Luttinger liquids [42] and the Marginal Fermi Liquid proposal [100], which we will discuss in the next section.
Within this context, one can calculate [95] the scattering rate (the inverse quasiparticle lifetime) for the Landau Fermi Liquid theory, which is associated with the imaginary part of the self-energy, and see that for a two dimensional system it has the form (2.17). Therefore, doped graphene is a conventional Landau Fermi Liquid. The applicability of this theory in this case has been also supported by ARPES experiments [23].

2.2.3. Self energy of undoped graphene

Even before its synthesis, the low energy properties of interacting graphene were explored in [26] within a quantum field theory model similar to quantum electrodynamics (this model will be rigorously presented in the next chapter). The self energy, computed up to two loops in the presence of long range Coulomb interactions, revealed that the properties of the system departed from those of the 2DEG. In particular the inverse quasiparticle lifetime at low energies was shown in [113] to behave linearly with the energy:

$$\mathrm{Im}\Sigma(\omega) = \frac{1}{48}\left(\frac{e^2}{\epsilon_0 \hbar v_F}\right)^2 |\omega|. \tag{2.19}$$

This energy dependence is precisely the one expected in a Marginal Fermi Liquid [100]. This is an exotic case in condensed matter physics where a departure from the Landau-Fermi Liquid case is rare. The systems where this kind of behaviour is thought to be present include high-T_c superconductors where a linear dependence of the scattering rate was observed in

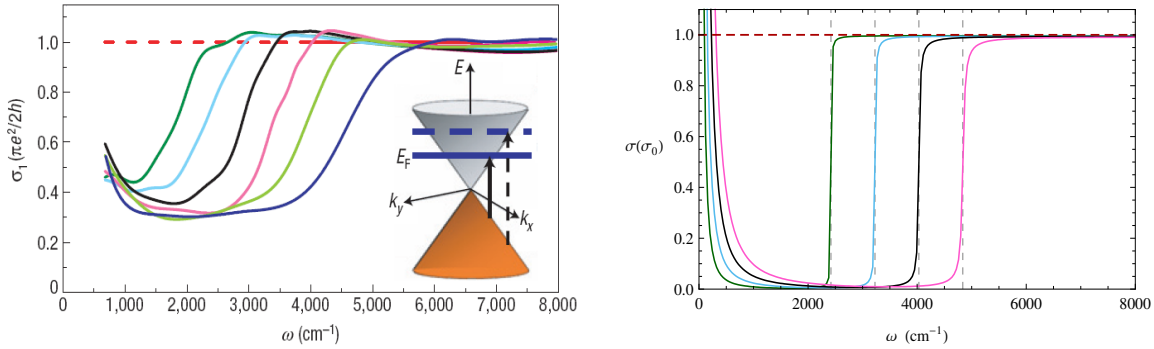

(a) (b)

Figure 2.3.: (a) Measured optical conductivity of graphene for different gate voltages (from right to left V_g = 71, 54, 40, 28, 17 and 10 V). The red horizontal line is measured at zero voltage. (b) Optical conductivity for a 2D Fermi Liquid self-energy given by (2.17) for different chemical potentials. From left to right: μ = 0.15, 0.20, 0.25, 0.30 eV. The horizontal red dashed line is for $\mu = 0$ eV. The vertical dashed lines are at $2E_F$.

the "normal" state [99]. Therefore, the fact that in graphene there is a marginal Fermi Liquid behaviour is itself remarkable.

2.3. Optical conductivity of graphene

2.3.1. Failure of the Landau-Fermi Liquid?

As it was previously discussed, the effect of electron electron interactions can be probed by measuring the optical conductivity of graphene. Recently reported experiments in graphene on a SiO_2 substrate, reproduced in Fig. 2.3(a) from [114] show several striking features regarding the observed infra-red conductivity with respect to the band picture presented above. In this experiments, the transmittance and reflectance of a graphene sample was measured at $T = 45$ K which was then related to the real part of the conductivity. There are three distinct features. The first one is localised around zero frequency, where there is a narrow peak which is due to the scattering of quasiparticles near the Fermi level, also known as the intraband transitions. This peak is associated to a Drude type conductivity of carriers at the Fermi energy which are excited with an infinitesimal amount of energy. Secondly a step function centred around $2E_F$ is observed. This is also expected from looking at equation (2.15) since it is the same step function that accounts for interband transitions although broadened by self energy effects which we will discuss below. The typical broadening is near 1400 cm^{-1}.
The third feature deserves more attention. It is a finite remanent conductivity between the Drude peak close to zero frequency and the interband step function at $2E_F$. In principle, the

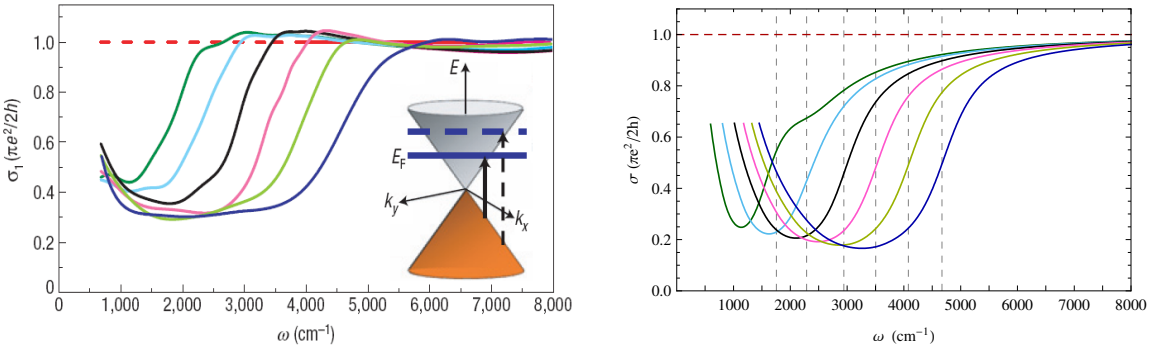

(a) (b)

Figure 2.4.: (a) Measured optical conductivity of graphene for different gate voltages (from right to left $V_g = 71$, 54, 40, 28, 17 and 10 V). The red horizontal line is measured at zero voltage. (b) Conductivity for a the piecewise self energy (2.22) for parameters $a = 0.2$, $b = 0.001$ eV, $\Lambda = 0.15$ eV and for the same gate voltages. The vertical dashed lines indicate the $2E_F$ threshold at each chemical potential.

appearance of such a finite conductivity in this region is in contradiction with the non interacting argument based on Pauli's exclusion principle descried above (see Fig. 2.1 (a)), where no quasiparticle can absorb energy within this region and with transferred momentum $\mathbf{q} = 0$. This remanent conductivity has an absolute value of approximately 30 percent and has the additional feature of being independent of the doping (although a slight dependence can be observed in lower doped curves).

Can all these three features be accounted for within the Landau-Fermi liquid picture? Strictly speaking since it is a doped sample, the self energy (2.17) introduced in (2.12) should explain most if not all of the features in Fig. 2.3(a). Calculating the real part of the self energy through the Kramers-Kronig relations (see appendix A) one obtains the optical conductivity shown in Fig. 2.3(b). It is evident that there is no remanent conductivity between zero frequency and $2E_F$ and thus the Landau-Fermi liquid self energy seems to fail when explaining the observed features. In fact, the large broadening in Fig. 2.3(a) is also too significant to neglect other possible contributions in the self energy. All of these observations need an explanation outside, or at least, complementary, to a Fermi Liquid picture.

In the next section, and motivated by the experimental results in Fig.2.3 (a), a phenomenological model for the self-energy is proposed and studied. The model, and the consequences it has on the transport properties of graphene will also be discussed. We will leave for section 2.5 the discussion of other experimental measurements of the optical conductivity.

2.3.2. Marginal Fermi Liquid hypothesis

Explaining the features of Fig. 2.3(a) needs of some other physical input in particular the remanent conductivity background. It is possible that one could account for this feature by considering the effect of impurities trapped between the substrate and the graphene sheet. This is indeed a possibility which was explored in detail in [115, 116]. The authors found that including Coulomb type scatterers indeed generated spectral weight inside the prohibited window between zero an $2E_F$. However, this remanent conductivity was strongly dependent of the chemical potential μ which is not in agreement with the reported experiments [4]. Excitonic effects [118] were shown to explain the kink above σ_0 near $2E_F$ but again fail to provide an explanation for the intermediate spectral weight.

The enhancement in the mid-infrared of the optical conductivity has been observed in high-T_c cuprates [119]. In this context, Varma *et al.* [99] proposed a self-energy hypothesis which had the effect of transferring spectral weight to higher frequencies, and in particular, from the Drude peak to the mid-infrared frequency region, thus explaining the unexpected enhancement [5]. This phenomenological self energy, the so called marginal Fermi Liquid self energy, takes the form

$$\Sigma(\omega) = \frac{2a}{\pi}\left[\omega \ln\left(\frac{\omega_c}{\omega}\right) + i\frac{\pi}{2}|\omega|\right], \tag{2.20}$$

where a is an adjustable phenomenological parameter and ω_c is an ultra-violet cut-off frequency. Notice that this self-energy hypothesis is of the form of the obtained self-energy in section 2.2 for intrinsic graphene, at zero temperature and zero chemical potential. Therefore the main idea of this chapter is that the marginal Fermi Liquid self energy might explain the observed background in Fig. 2.4(a) and so electron-electron interaction effects might account for some of the observed experimental features. It must be also noted that the linear dependence on ω of the imaginary part of the self energy can have an origin on other effects such as phonons [115, 116]. However, for the purpose of this chapter, we will forget the microscopic origin of the self energy and try to motivate it phenomenologically. Reported scanning tunnelling microscope (STM) experiments in graphene on graphite, at high magnetic field and at low temperatures were able to measure the quasiparticle lifetime from the width of the peaks of the Landau levels [120]. They concluded that the inverse quasiparticle lifetime had the form:

$$\frac{1}{\tau} = \frac{|\omega|}{\gamma} + \frac{1}{\tau_0}, \tag{2.21}$$

observed up to at least $\omega < 150$ meV. In this same experiment, parameter $\frac{1}{\gamma}$ was measured to be, in units where $\hbar = 1$, $\frac{1}{\gamma} \sim 0.07$. The parameter $\frac{1}{\tau_0} \equiv b$ is associated to extrinsic scat-

[4] A strong dependence on the chemical potential is however in agreement with the follow up experiment [117].

[5] The real part of the conductivity must satisfy the *f-sum rule* given by $\int_0^\infty d\omega \mathrm{Re}\sigma(\omega) \propto n$ where n is the electron density. Thus the total spectral weight is conserved and suppression of the spectral weight at some region must be compensated by an enhancement elsewhere.

tering mechanisms and in this particular experiment was measured to be $b \sim 0.01$ eV. One can argue that the self energy under the presence of a high magnetic field such as the one creating Landau levels in [120] can be very different to the one without a magnetic field. This is indeed true and thus the reasonable probe to measure the quasiparticle lifetime is, as argued above, the ARPES experiment. Recent measurements [121] have confirmed the picture represented by (2.21) where they measured parameters one order of magnitude bigger.
A crucial difference between the Marginal Fermi liquid behaviour of high-T_c superconducting cuprates and graphene is that a linear behaviour of the inverse quasiparticle lifetime with energy in graphene only stands for a narrow range of energies which we will take to be the measured $\Lambda < 150$ meV in [120] although higher cut-offs for this behaviour have been measured [121]. Hence, and in virtue of these observed experimental evidences, one can propose the following phenomenological model for the self-energy:

$$\mathrm{Im}\Sigma(\omega) = \begin{cases} a|\omega| + b & ,|\omega| < \Lambda \\ a\Lambda + b & ,|\omega| > \Lambda \end{cases}. \tag{2.22}$$

This phenomenological self-energy takes into account the effect of the Marginal Fermi Liquid hypothesis at lower energies under a cut-off frequency Λ and through the parameter a. The parameter b takes into account, in a phenomenological way the effect of impurities giving a constant lifetime to the quasiparticles.

2.4. Results

2.4.1. Optical conductivity

In this section, the effect of different self-energies in the optical conductivity is presented. Before analysing the properties of the conductivity obtained with (2.22), it is useful to consider the effect of both parameters in the optical conductivity. This is easily achieved by introducing in (2.12) the self-energy

$$\mathrm{Im}\Sigma(\omega) = a|\omega| + b. \tag{2.23}$$

Figs. 2.5 (a) and (b) show the optical conductivity when $b = 0$ and $a \neq 0$ while Figs. 2.5 (c) and (d) consider the case $b \neq 0$ and $a = 0$ with (2.23). Both parameters a and b produce a finite conductivity between intra ($\omega \sim 0$) and interband ($\omega \sim 2E_F$) transitions, around the mid-infrared frequencies. As discussed above, the effect a is to shift spectral weight to higher frequencies, in particular from the Drude peak at $\omega \sim 0$ to the mid-infrared region. The transferred spectral weight affects the saturation value at high frequencies which is not exactly σ_0, implying that at higher frequencies this hypothesis fails to reproduce the observed dynamics. For parameter a (b) the remanent conductivity is very insensitive (sensitive) to a change in chemical potential. Finally it is noteworthy that the width of the step is broadened

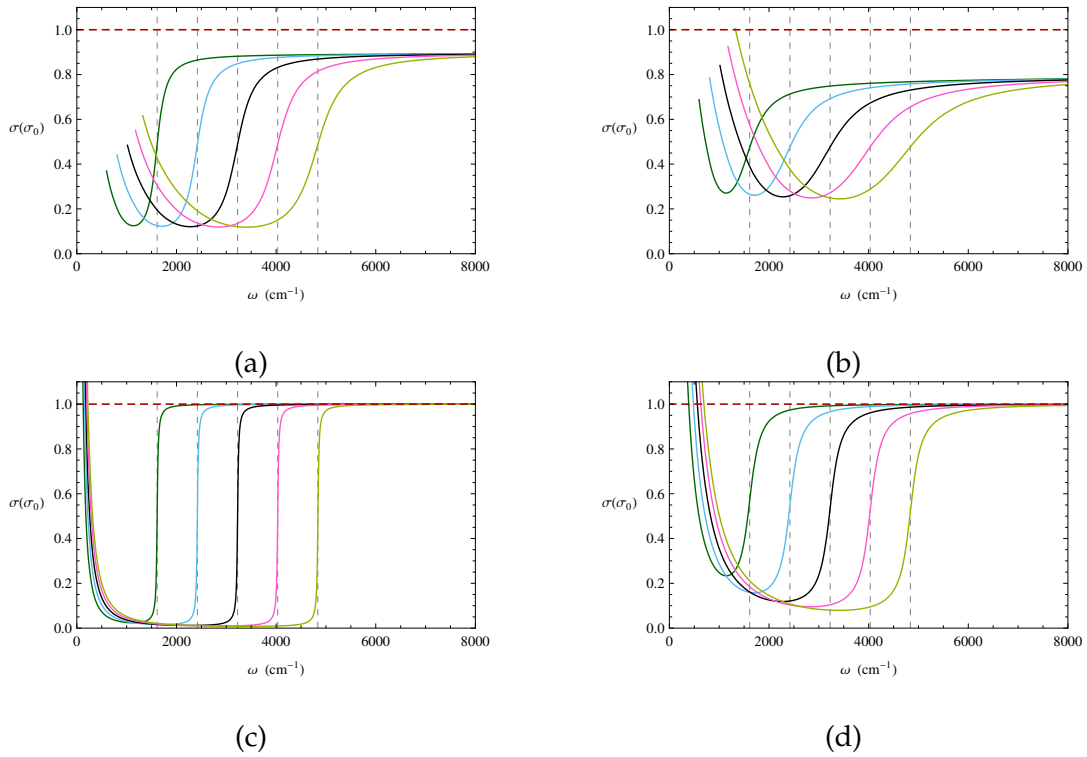

Figure 2.5.: Optical conductivities calculated from the self-energy (2.23) for different parameters and chemical potentials: (a) $a = 0.07$, $b = 0$ eV, (b) $a = 0.14$, $b = 0$ eV (c) $a = 0$, $b = 0.001$ eV (d) $a = 0$, $b = 0.01$ eV for chemical potentials (from left to right) $\mu = 0.10 - 0.30$ eV in steps of 0.05eV. The horizontal red line is the optical conductivity at zero doping. Dashed vertical lines are situated at the $2E_F$ threshold.

with respect to the Fermi Liquid case. The case of $b \neq 0$ and $a = 0$ qualitatively agrees with results obtained by [122] using a model of charged impurities and phonons.

After understanding the separate effects of parameters a and b one can start to analyse the self-energy (2.22). In this scheme a Marginal Fermi Liquid hypothesis for the imaginary part of the self energy is assumed up to a cut-off frequency Λ after which a constant self-energy, presumably caused by impurities, dominates. Its corresponding real counter part can be calculated using the usual Kramers-Kronig relation (see appendix A). Following the arguments explained in section 2.3 we have implemented the self-energy (2.22) in the optical conductivity expression (2.12) for $a = 0.2$, $b = 0.001$ eV and $\Lambda = 0.15$ eV. The results are shown in Fig. 2.4(b). The general features are the following.

Firstly, the magnitude of the residual conductivity for the parameters defined in the last paragraph is around 20 percent. Although the chemical potential dependence is noticeable, the absolute variation of the remanent conductivity for these parameters is $\sim 0.1\sigma_0$, consistent with the experimental curves in Fig. 2.4 (a). Increasing parameter a lifts the absolute value of the remanent conductivity, although moderately, maintaining its small doping de-

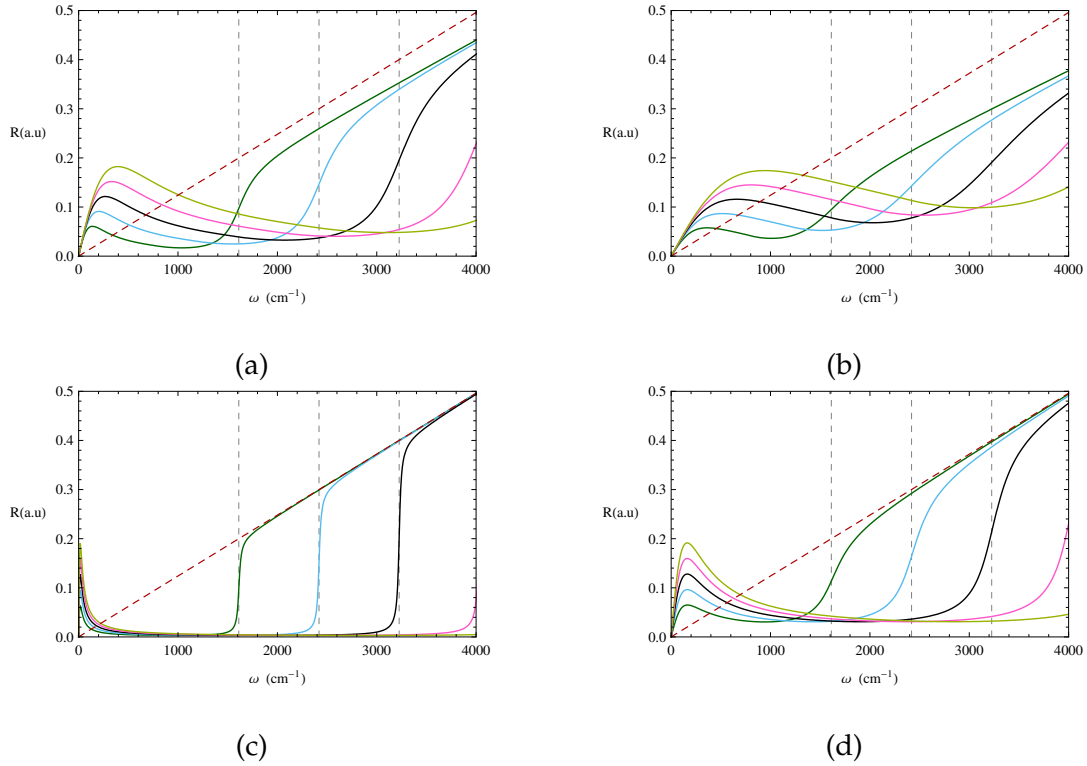

Figure 2.6.: Raman intensities calculated from the self-energy (2.23) for different parameters and chemical potentials: (a) $a = 0.07$, $b = 0$ eV, (b) $a = 0.14$, $b = 0$ eV (c) $a = 0$, $b = 0.001$ eV (d) $a = 0$, $b = 0.01$ eV for chemical potentials (from lower to higher) $\mu = 0.10 - 0.30$ eV in steps of 0.05 eV. The red dashed line corresponds to zero doping. The vertical dashed lines show the $2E_F$ interband jump.

pendence. On the other hand, increasing parameter b makes this value to increase making it doping dependent. When both parameters are included, the change with doping becomes increasingly noticeable since the effect of impurities are now considered with two different contributions: the first one given by b in the first region defined in (2.22) and the second one given by $a\Lambda + b$ in the second region.

Secondly, in the reported experiments the observed broadening of the $2E_F$ threshold was ~ 1400 cm^{-1} (approximately 0.17 eV), fairly constant with doping. In the curved shown in Fig.2.4 (b) the broadening is around 0.2 eV. The broadening is directly related to parameter a. When this parameter increases the threshold becomes significantly wider.

Finally in Fig. 2.4 (b) a slight valley appears in the low doping curve at a frequency $\omega = 2\Lambda$. It is a consequence of the piecewise form of the self energy (2.22). It originates in the interplay between the effect of impurities to saturate at the correct value $\sigma = \sigma_0$ and the effect of the linear energy dependence of the scattering rate, which tries to move spectral weight to higher frequencies. The curves with $2E_F \gtrsim 2\Lambda$ are not disturbed by the kink as observed in Fig. 2.4 (b).

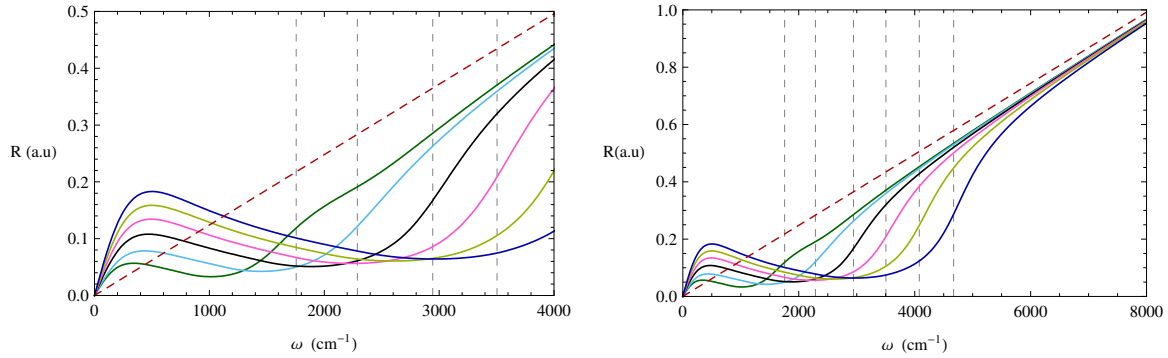

(a) (b)

Figure 2.7.: Raman intensity for the piecewise self-energy (2.22) for parameters $a = 0.2$, $b = 0.001$ eV, $\Lambda = 0.15$ eV for two different scales and for different gate voltages (corresponding to those of the measured conductivity). From higher to lower $V_g = 71$, 54, 40, 28, 17 and 10 V. The red dashed line is at a gate voltage $V_g = 0$ V and the vertical dashed lines show the $2E_F$ interband transitions for each chemical potential value.

2.4.2. Raman signature

The anomalous features observed in the infra-red conductivity of graphene should be also transferred to other optical measurements in particular an inelastic Raman experiment. Following the arguments presented in section 2.1.2, it is possible to determine the Raman spectrum from expression (2.16) and from the phenomenological self energy (2.22).
The separate effect of parameters a and b is analogous to the infra-red conductivity and are summarised in Fig. 2.6. In general there is a characteristic peak at $\omega = 2b$ and a saturation at higher energies to the line corresponding to zero doping which is a direct consequence of the saturation of the optical conductivity to the universal value σ_0.
The Raman signature for the phenomenological model (2.22) is shown in Fig. 2.7 for parameters $a = 0.2$, $b = 0.001$ eV and $\Lambda = 0.15$ eV. There are several remarkable features. The first one is that the mid-infrared peaks are not centred all in one value. In fact, the lower two peaks seem to be displaced to the left with respect to the rest. This is a feature of the self-energy with a linear dependence with energy. There is also an observable increase of the local minimum Raman intensity with doping. This increase is significantly reduced above a certain value of μ, indicating that in this region, the constant impurity part is dominant. Finally it is worth to mention that as in the case of the infra-red conductivity, the saturation is only reached at high energies and that a kink is observed due to the bipartite nature of the self-energy (2.22).

2.5. Discussion and Conclusions

In this chapter we have characterized the conductivity of graphene from a phenomenological point of view. Motivated by the fact that Dirac quasiparticles have an imaginary self-energy that depends linearly in energy, a phenomenological model was proposed that accounts for part of the experimental features observed in optical measurements regarding the infra-red conductivity in graphene that were reported in [114]. In particular, these measurements show a peculiar background between the intra and interband scattering transitions which cannot be explained in terms of the Fermi Liquid picture dominant in doped graphene or in terms of the effect of impurities trapped between the substrate and the graphene sheet [115, 116]. As in the case of high-T_c superconductors [99, 100, 119], the proposed marginal self energy has the effect of transferring spectral weight from the Drude peak to higher frequency regions and in particular to the region where electronic transitions are forbidden based on the non interacting picture. It was also shown that due to this type of self energy, both the optical conductivity and the electronic Raman spectrum showed similar anomalous features. This can motivate electronic Raman measurement in graphene, which has until now been focused only to the response of phonons. These measurements might provide, as in as in the case of high-T_c superconductors, useful information about correlations in graphene.

Besides interactions, there are other mechanisms which could account for this linear behaviour. Thus, to try to understand deeply interactions between Dirac quasiparticles, it is necessary to take a microscopic approach and build a consistent theory of interacting Dirac quasiparticles in graphene that involves the crossover between finite and zero chemical potential, which unfortunately is still lacking. We have to also consider the possibility that these anomalous features are sample dependent which will point towards an extrinsic mechanism.

To end this chapter we comment on other experimental measurements of the optical conductivity. It is important to point out that at the time of writing there are no independent confirmation of the doping independent background between the intra and interband scattering transitions observed in Ref. [114]. The optical spectroscopy experiment performed in Ref. [117] soon after Ref. [114] showed a strong doping dependence of such background, which can be accounted for by a phenomenological broadening of the quasiparticle lifetime (the b parameter) due to impurities for example. This is the case as well for the more recent experiments reported in Ref. [123]. Finally, the ultraclean experiments [124] showed a very small background in the mid-infrared region which very mildly doping dependent. All of these measurements were performed in samples of graphene on a silicon oxide substrate. It will be interesting to see if suspended samples can rule out extrinsic effects and manifest intrinsic properties of interacting electrons in graphene.

3. Renormalization of the Coulomb interaction in graphene: Computing observable quantities

Figure 3.1.: Renormalization as seen by J. F. Cartier (extracted from [1])

3.1. Introduction: Renormalization of quantum field theories

Understanding how interactions between electrons affect the behaviour of a many-body system is in most situations an extremely hard task, if not impossible at all. Of course it is always possible to postulate, as it was done in the last chapter, a phenomenological model to recover some experimental results. However, it is desirable to formulate a consistent microscopic theory which includes electron-electron interactions in a fundamental way so as to describe as many measurable phenomena as possible. It is in this context where quantum field theory [42, 125–127] emerged as a natural framework for such description, both in particle physics and many-body physics. In the context of particle physics, it was soon realized [126] that quantum field theories dealing with infinite degrees of freedom were often plagued with infinities when calculating observables in perturbation theory. In many-body physics, this can

be reinterpreted as a dependence of the low energy theory of the higher degrees of freedom through the explicit dependence on a cut-off above which the theory ceases to be valid.
Renormalization (see [75, 126, 128–130] for example) is a tool which makes possible to track consistently, in some specific situations, the effect of interactions in a field theory at the quantum level. In simple terms, the fundamental principle of this method is that the effects of degrees of freedom at energies larger than the cut-off on the low energy physics can be hidden in the finite number of parameters (coupling constants) that define the theory at low energies. In the process, these parameters are redefined or *renormalized* to an arbitrary but cut-off independent value, that is then fixed with a finite number of measurements, as many as parameters in the theory. Once these are fixed, all observables can be calculated to a given order in perturbation theory. Therefore the prescription is by construction, independent of the higher energy degrees of freedom beyond the high energy cut-off. The price to pay however is that now, the coupling constants, and through them, the observables become functions of the energy at which they are measured, and can "flow" to different values as one explores different energetic regimes.
Unfortunately, for a given field theory, this scheme is not always possible to implement. Those theories for which this scheme works as prescribed above are known as renormalizable field theories, as opposed to non-renormalizable theories where an infinite number of measurements would be needed, making this method useless in practice [1].
In its various forms, these ideas have been applied successfully to a variety of problems, ranging from statistical physics [129, 130] to particle physics [75, 128], thus turning it into one of the cornerstones of modern physics. In this chapter we will try to put together a self-contained review of the basic principles of renormalization in various contexts including Dirac quasiparticles in graphene. In the process we will highlight the main contributions of this thesis to this well established paradigm, namely the construction of finite, cut-off independent observables in graphene.

3.1.1. Renormalizable, super renormalizable and non renormalizable theories

To the describe a physical system up to an energy Λ, the cut-off, it is useful to define its Lagrangian $\mathcal{L}$, a functional which will in general depend on the fields involved $\{\psi, \phi, \cdots\}$, their derivatives and some finite set of coupling constants $\{g_i\}$. Once this functional is known, it is possible to define the Green's functions of the fields involved and following the quantum field theory (QFT) scheme described in standard textbooks [42, 125–127], one can construct out of this any observable under a perturbative expansion on the coupling constants, which

[1] To be precise, the modern approach to renormalization of field theories is framed in the notion of effective field theory. In this framework, a renormalizable field theory is a theory describing physical processes with energy less than a given energy scale E. Close to that scale, non renormalizable terms become important in the Lagrangian signalling new physics and thus a new renormalizable effective field theory should be constructed valid up to an energy E' [131].

we declare to be small [2], i.e. $g_i \ll 1$. Given this expansion there are several equivalent ways to know if a theory is renormalizable or not. As a general principle, it is necessary that all cut-off dependent terms appearing in the perturbative expansion can be absorbed by parameters in the Lagrangian, ensuring that all unknown cut-off dependent effects can be exchanged by a finite number of physical measurements that will enable the calculation of physical observables up to a certain order in perturbation theory. Fortunately there is a way, given a Lagrangian, to know whether this is the case or not.

To be more specific, we will here illustrate the renormalization procedure on a particular example, pointing out along the way which results are general. Due to its similarities to graphene a natural choice is the Lagrangian describing electrons interacting with an electromagnetic field in 3+1 dimensions, known generically as quantum electrodynamics (QED). A comprehensive description of this theory, including renormalization aspects can be found virtually in all QFT textbooks due to its historical significance [75, 126, 128, 129] and its simple structure compared to other theories such as quantum chromodynamics (QCD). The QED Lagrangian can be written as

$$\mathcal{L}_{QED} = \bar{\psi}(i\not{D} - m)\psi - \frac{1}{4}F^{\mu\nu}F_{\mu\nu}. \tag{3.1}$$

This Lagrangian describes the interaction between electrons, described by the spinor field ψ, and photons, described by the gauge field A^μ hidden in the definitions of $\not{D} = \not{\partial} + ie\not{A}$ and $F_{\mu\nu} = \partial_\mu A_\nu - \partial_\nu A_\mu$. For this chapter we adopt Feynman's "slashed" notation $\not{a} = \gamma^\mu a_\mu$ where γ_μ are Dirac matrices satisfying the Clifford algebra $\{\gamma^\mu, \gamma^\nu\} = 2g^{\mu\nu}$, with $g^{\mu\nu} = diag(1, -1, -1, -1)$ and a is an arbitrary four-vector.

Any observable of the quantum field theory can be built, in perturbation theory out of the electron and photon Green's functions $G(\omega, \mathbf{k})$ and $D_{\mu\nu}(\omega, \mathbf{k})$ (sometimes we will use $(\omega, \mathbf{k}) = k$ as a shorthand notation). This is most commonly done in terms of Feynman diagrams which are a pictorial representation of the integrals that appear at each order in perturbation theory. In practice constructing each order in perturbation theory is done by sticking together the different pieces that compose the theory, in this case the electronic and photonic Green's function and the interaction vertex shown in Figure 3.1 (a), (b) and (c) respectively [3].

The renormalization procedure is to be done order by order in perturbation theory. It is not difficult to convince oneself that the perturbative parameter in QED is, in Gaussian units, $\alpha_{QED} = \frac{e^2}{4\pi\hbar c}$ and thus to first order in perturbation theory, we must include all diagrams up to order α. The three diagrams that contribute at this order are shown in Fig. 3.2.

Consider for instance the diagram in Fig. 3.2 (c), the first order contribution to the photon

[2] That the coupling constant satisfies $g_i \ll 1$ is an assumption to be validated *a posteriori* via the flow of the coupling constants under the renormalization group equations, to be described in detail in section 3.3.5.

[3] It is only necessary to consider the diagrams known as one particle irreducible diagrams, which are those that cannot be cut into a sum of diagrams

(a) $= \quad G(k) = \frac{i}{\not{k} - m}$

(b)  $= \quad D_{\mu\nu}(k) = \frac{ig_{\mu\nu}}{k^2}$

(c) 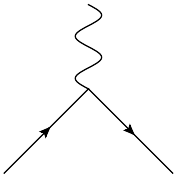 $= \quad \Gamma^{\mu} = -ie\gamma^{\mu}$

Table 3.1.: Main building blocks of QED: (a) Electronic Green's function (b) Photon Green's function (c) Interaction vertex

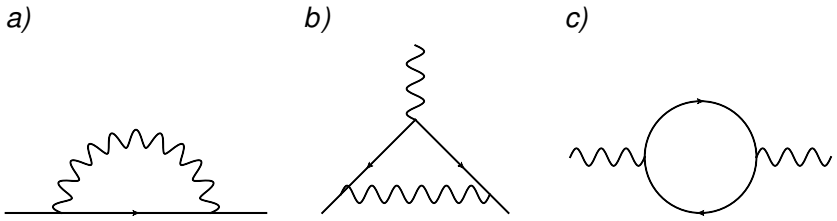

Figure 3.2.: Potentially divergent diagrams at first order in α_{QED} (a) First order correction to the electron propagator with superficial degree of divergence $M = 1$, (b) Correction to the vertex function with $M = 0$ and (c) the correction to the photon propagator with $M = 2$.

self energy, which when translated to the integral notation is given by

$$\Pi^{\mu\nu}(p) = -e^2 \int \frac{d^4k}{(2\pi)^4} \mathrm{Tr} G(k+p)\gamma^{\mu} G(k)\gamma^{\nu} \tag{3.2}$$

For the limit of large external momentum, this diagram diverges quadratically if the cut-off is sent to infinity

$$\Pi^{\mu\nu} \sim \int^{\Lambda} d^4k \frac{1}{k^2} \sim \Lambda^2 \tag{3.3}$$

This immediately posses some questions on the predictive power of such a theory. Whenever such a cut-off dependence appears explicitly it is an indication that the unknown high energy degrees of freedom are entering the theory in an uncontrolled fashion. In this sense, renormalization is a way of getting rid of these ambiguities. In what follows we outline the

method, referring the interested reader to standard textbooks and reviews [75, 126, 128–130]. However, before going into the particulars of renormalization it is worth pointing out the following technical detail. In the original formulation, renormalization was developed to cure the divergences appearing in diagrams such as (3.2), since there were thought to be truly divergent once the cut-off Λ was sent to infinity. However, the perspective gained from applications to condensed matter as well as the lack of a renormalizable theory describing gravity has led to a modification of the interpretation of the paradigm in terms of effective field theories [76] (see footnote 1). In this chapter we will often refer, for the sake of clarity, to divergent amplitudes or diagrams that one should renormalize. This should be understood as cut-off (or more generally, regularization) dependent quantities which one must eliminate in order to formulate a cut-off independent theory with predictive power.

Given that in certain QFT and in QED in particular one encounters divergences when calculating Feynman diagrams, it is possible then to define a useful quantity which quantifies the divergence of a particular diagram. The *superficial degree of divergence* M of a diagram is the power law with which the diagram grows in the ultraviolet. For example for (3.2) this corresponds to $M = 2$. For renormalizable theories (defined precisely below) the superficial degree of divergence can also be defined for n-point functions (or amplitudes) since it can be written in a way that it is independent on the number of vertices inside a diagram.

We can therefore classify the different theories corresponding to the number and type of superficially divergent diagrams that the theory generates in perturbation theory. A theory in which there are a finite number of divergent diagrams is known as super-renormalizable. However, if the theory has an infinite number of divergent amplitudes (n-point functions) whose divergences arise only due to the presence of a finite set of superficially divergent subdiagrams inserted in them the theory is known as strictly renormalizable. If all amplitudes are divergent at sufficiently high order in perturbation theory then the theory is known as non-renormalizable.

This is not at all a trivial classification. For renormalizable theories all the divergences can be cured by adding a finite number of terms to the Lagrangian known as counterterms, which precisely cancel the divergent terms. If the theory is a non-renormalizable, one is forced to add infinite types of terms to the Lagrangian to cancel the divergences, loosing completely the predictive power of the theory [4]. In fact, the renormalizability of a theory is directly related to the dimensions of the coupling constant. It is not difficult to prove [75] that the superficial degree of divergence is determined solely by the dimensions of the fields and the coupling constants since they are in fact related due to the constraint that the action must itself be a dimensionless constant in units of $\hbar = 1$. Thus, for a given theory, the dimensions of the coupling constant determine the renormalizability and the following rigorous classification emerges (see Fig. 3.3):

[4] In the effective field theory picture, non renormalizable terms appear as powers of $1/\Lambda$ in renormalizable theories and thus strict renormalizability will hold only at sufficiently low energy [76, 131]

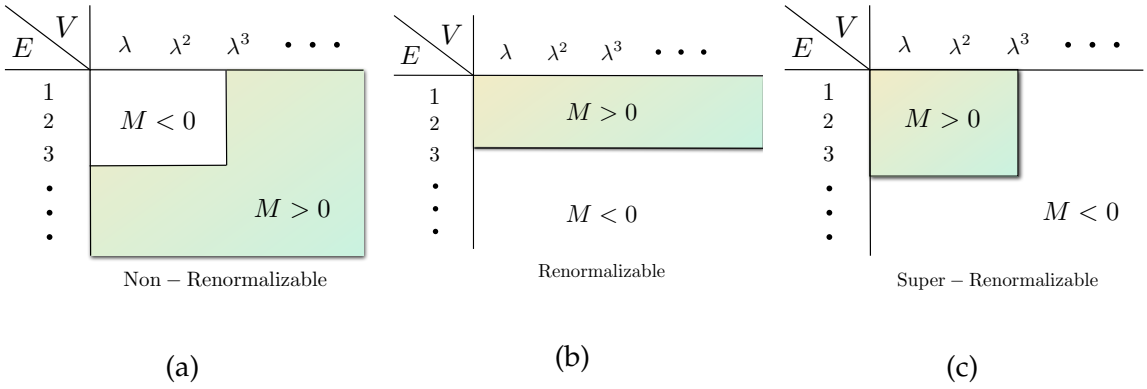

Figure 3.3.: Pictorial representation of the renormalizability of a theory in terms of the number of external legs E and vertices V for each order in perturbation theory in powers of a generic coupling constant λ. M is the superficial degree of divergence of a given diagram.

Super-renormalizable theories:
Those theories that have a finite number of divergent Feynman diagrams or equivalently a coupling constant with positive power of energy

Strictly renormalizable theories:
Those theories that have a finite number of divergent Feynman amplitudes but divergences at all orders in perturbation theory. Equivalently, it is a theory with a dimensionless coupling constant.

Non-renormalizable theories:
Those theories that have a infinite number of divergent Feynman diagrams or equivalently a coupling constant with negative power of energy.

Note therefore that whether a given theory is renormalizable or not depends on the dimension of space-time D which determines the dimensionality of the coupling constant. For a fixed space-time dimension, and due to the fact that these definitions apply directly to each of the interactions in a given Lagrangian it is possible to classify each term in the theory accordingly [76, 132]. Thus, a theory can have both renormalizable, and non-renormalizable interaction terms. However, since the dimensions of the coupling constant are a negative power of energy in the non-renormalizable ones, when one is interested in the low energy degrees of freedom there is always a sufficiently low energy where the renormalizable *operators* become more important than the non-renormalizable ones. Therefore, the operators with a dimensionless coupling constant are known as *marginal* operators. Operators with a coupling constant with units of negative (positive) power of energy are known as irrelevant

(relevant) because of their behaviour at low energies as compared to marginal operators [5].

3.2. Renormalized perturbation theory at work: The case of QED

3.2.1. Building blocks

To illustrate the process of renormalization we now briefly review below how to renormalize QED theory as a warm up for electrons in graphene. We will illustrate it as a stepwise process, order by order in perturbation theory which begins with the introduction of counterterms to hide the ambiguous infinities of the theory inside a redefinition of the field and coupling constants. Then, we will discuss how to fix the arbitrariness through a finite number of measurements known as the renormalization conditions, which can be of several sorts, ending with a brief comment on the renormalization group scheme as a whole.
Consider first the QED Lagrangian, which we now write explicitly:

$$\mathcal{L}_{QED} = \bar{\psi}(i\partial\!\!\!/ - m - eA\!\!\!/)\psi - \frac{1}{4}F^{\mu\nu}F_{\mu\nu}. \tag{3.4}$$

It is easy to check by dimensional analysis that QED in four dimensions has a dimensionless coupling constant e and thus we are guaranteed that if we are able to cure the finite set of divergent diagrams, the theory will be well defined to each order in perturbation theory since any divergence that we encounter will be inherited from these divergent terms.
At this point we can label the coupling constants and fields with the attribute *bare*, meaning that they, as parameters in a Lagrangian are unmeasurable. Now, with the help of the path integral formalism for example [75] we can construct all the possible amplitudes of the theory, for instance $\langle\bar{\psi}\psi\rangle$, $\langle\bar{\psi}\gamma^{\mu}\psi A_{\mu}\rangle$, $\langle A_{\mu}A_{\nu}\rangle$ and so on. To renormalize the theory we look at how many of these amplitudes may generate divergences, which is equivalent to calculating the superficial degree of divergence.
In QED only three diagrams are superficially divergent at first order in α_{QED} shown with their superficial degree of divergence in Fig. 3.2 which correspond to the first order correction to the electron propagator, the photon self energy together and to the vertex function[6]. Note that, as mentioned above, renormalizable theories, and QED in particular have the property that the n-point functions corresponding to these diagrams have the same degree of superficial divergence at any order in perturbation theory (see Fig. 3.3 (b)) as this quantity does not depend on the number of internal vertices. At this point, it is possible to note that the three divergent correlators are of the same form as each of the terms in (3.4),

[5] Note that the relevance or irrelevance depends on whether we are interested in the low energy or infrared limit important for condensed matter or in the high energy or ultraviolet limit, usually considered in particle physics.

[6] There are, in fact, three other superficially divergent n-point functions which are the one, three and four photon correlators. The first two can be shown to be zero due to charge conjugation symmetry (Furry's theorem) and the third one turns out to be finite due to gauge invariance.

namely $\langle\bar{\psi}\psi\rangle$, $\langle\bar{\psi}\gamma^{\mu}\psi A_{\mu}\rangle$ and $\langle A_{\mu}A_{\nu}\rangle$. If this was not so, the theory would be by definition non-renormalizable. Thus, if we encounter any divergence in the diagrams in Fig. 3.2, it is possible to absorb them by a redefinition of the *bare* quantities that appear in the Lagrangian (3.4): the bare charge e, the bare mass m and the two bare fields ψ and A_{μ}.

Let us, anticipating to the appearance of divergences, define a more efficient strategy. We will compute all correlation functions with the Lagrangian written in terms of the *renormalized parameters*, to be defined below, in what is known as renormalized perturbation theory [75, 128]:

$$\mathcal{L} = \Big[\bar{\psi}_R(i\gamma^{\mu}\partial_{\mu} - m_R)\psi_R - e_R\bar{\psi}_R\gamma^{\mu}\psi_R A_{R\mu} + \frac{1}{4}(F_R^{\mu\nu})^2 + \\ \delta_{\psi}\bar{\psi}_R\gamma^{\mu}\partial_{\mu}\psi_R + \delta_m\bar{\psi}_R\psi_R - \delta_e e_R\bar{\psi}_R\gamma^{\mu}\psi_R A_{R\mu} + \delta_A\frac{1}{4}(F_R^{\mu\nu})^2\Big], \tag{3.5}$$

The unknown parameters δ_i, known as counterterms, are to be adjusted to absorb all the divergences that appear in perturbation theory. Thus, to the Feynman rules in Fig. 3.1, which are now to be computed with the renormalized parameters $\{e_R, m_R, \psi_R, A_R^{\mu}\}$ one should add three counterterms shown in Fig. 3.2. Then all amplitudes are to be calculated with these rules to a particular order in perturbation theory. It is necessary however to define precisely the renormalized parameters e_R, m_R, ψ_R and A_R^{μ} through what is known as the renormalization condition (also referred to as renormalization prescription or renormalization scheme) which relates these quantities to a set of measurements, as will be shown precisely in the next section. After we fix these parameters, all correlation functions can be computed to an arbitrary order in perturbation theory. Thus the complete procedure of renormalization is carried out as follows. First, given a renormalizable Lagrangian, the set of divergent correlation functions are identified. Then, the quantum corrections are calculated through perturbation theory, which will in general diverge. The divergences, which will be of different form depending on the regularizator used [7], are to be absorbed in the counterterms which are then finite but arbitrary and fixed by the renormalization conditions.
Thus, to fully describe and apply this program we will now elaborate on some of the different renormalization schemes.

3.2.2. Renormalization prescriptions

At first glance it seems that the Lagrangian (3.5) is not a predictive theory. Although we have solved the problem of infinities arising in perturbation theory by introducing the coun-

[7] A technical point is in order here. There are several ways to regularize a divergent integral such as dimensional regularization, a sharp cut-off, Pauli-Villars regularization etc. When computing an observable one should be careful since some of these regularizations break symmetries of the theory (among other non trivial effects) leading to unphysical spurious terms that could break the symmetries of the classical Lagrangian at the quantum level. This phenomenon is known as the appearance of an *anomaly* in the theory.

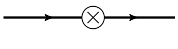

$= \quad i(\delta_\psi \gamma^\mu k_\mu - \delta_m)$

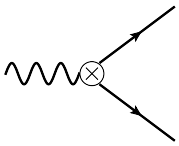

$= \quad -ie_R \delta_e \gamma^\mu$

$= \quad -i\delta_A (g^{\mu\nu} k^2 - k^\mu k^\nu)^2$

Table 3.2.: Counterterm rules in QED corresponding to δ_i in (3.5).

terterms δ_i, the statement that the renormalized parameters have to be defined by a set of measurements or renormalization conditions reminds more the picture Fig. 3.1 at the beginning of the chapter than to a predictive physical theory.
The key point to realize is that in renormalizable theories, unlike what happens in non-renormalizable ones, the number of conditions to be imposed is finite. Once they are fixed, it is possible to calculate any observable to any order in perturbation theory. For the Lagrangean (3.5) it is possible to rewrite it as:

$$\mathcal{L} = Z_\psi \bar{\psi}_R i\gamma^\mu \partial_\mu \psi_R + Z_m m_R \bar{\psi}_R \psi_R - Z_e e_R \bar{\psi}_R \gamma^\mu \psi_R A_{R\mu} + Z_A \frac{1}{4} (F_R^{\mu\nu})^2. \tag{3.6}$$

where the parameters $Z_i = 1 + \delta_i$ are to be fixed. In QED gauge invariance relates Z_A to Z_ψ and Z_e and thus we need only to fix three independent parameters. Choosing the renormalization scheme is, of course, arbitrary. However this choice is unphysical, and one at the end chooses a particular prescription if it is of practical or mathematical convenience since, as we will argue later, observables do not depend on this choice. It is therefore possible to choose several renormalization schemes that can be found in the literature. Here we review and comment the advantages and drawbacks of most frequently used prescriptions.
One of the most common prescriptions, is the physically motivated on-shell scheme. In this case, one chooses that the renormalized mass is the physical mass, defined as the pole of the electron propagator $G(k)$. The wave function renormalization is set to be unity and the value of the vertex at zero momentum is set to be the physical charge. This is equivalent to impose

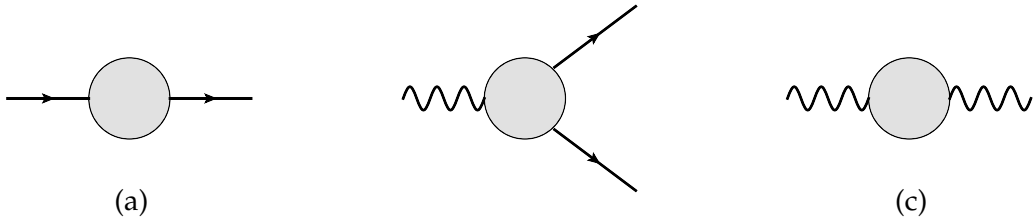

Figure 3.4.: Divergent n-point functions for QED: (a) Electron self energy $\Sigma(\not{p})$ (b) vertex function $\Gamma^{\mu}(p,p')$ and (c) photon self energy $\Pi^{\mu\nu}(p)$. The renormalization prescriptions can be imposed to the vertex and the electron self energy by (3.7) or (3.8) for example, fixing three out four parameters, since the last condition follows from gauge invariance (Ward identities).

the following mathematical conditions:

$$\Sigma(p^2 = m_{os}^2) = 0, \quad \left.\frac{\partial \Sigma(p^2)}{\partial p^2}\right|_{p^2=m_{os}^2} = 1, \quad \Gamma^{\mu}(q=0) = e\gamma^{\mu}. \tag{3.7}$$

The conditions are imposed through the full electron self-energy $\Sigma(\not{p})$ defined in the last chapter and the full vertex function $\Gamma^{\mu}(p,p')$ which are shown schematically for QED in Fig. 3.4 and where $q = p' - p$. The advantage of this particular scheme is that it is directly related to physical measurements since the measurement is performed at the physical charge and mass, and for this reason it is also known as physical scheme. Note also that the second condition in (3.7) sets the wave function renormalization to 1. In high energy physics this condition is chosen as a convention since Z_{ψ} cancels when computing S matrices [75]. In condensed matter systems in general and in graphene in particular, more care must be taken. It must be noted indeed that Z_{ψ} is the quasiparticle residue discussed in the last chapter, which determines the Fermi liquid character of the system which is observable for example in ARPES experiments. The implications of renormalization on this quantity will deserve a more detailed discussion and thus we postpone it to sections 3.3.5 and 3.4.
The next example of renormalization scheme is the off-shell scheme, defined by:

$$\Sigma(p^2 = M^2) = M^2 + m_2^2, \quad \left.\frac{\partial \Sigma(p^2)}{\partial p^2}\right|_{p^2=M^2} = 1, \quad \Gamma^{\mu}(q^2 = M^2) = e_M\gamma^{\mu}. \tag{3.8}$$

This scheme employs an arbitrary scale M introduced to avoid possible infrared (low momenta) divergences of massless theories and therefore the relation to the a physical measurement is less evident.
The last scheme we will discuss is the minimal subtraction scheme introduced independently by t'Hooft and Weinberg [133, 134]. It takes its name from the fact that it is constructed to subtract only the non-divergent part of the diagrams. It is commonly used together with the regularization known as dimensional regularization where the divergent integrals are

evaluated in d dimensions of space-time setting d to its original value n at the end of the calculation. Divergences then appear as poles $1/\epsilon^k$ where $\epsilon \to 0$ is related to the original space-time dimensionality $\epsilon = d - n$. In this case the scales M and m_{os} in the previous schemes are replaced by an arbitrary scale μ which is, like in the off-shell case, not associated to any particular measurement in a transparent way although it has the advantage of simplifying considerably the renormalization group equations, a construction that will be introduced below.
Choosing different renormalization schemes does not affect the physics once we sum up the leading divergent terms of the perturbative series. Since in practice we are only able to calculate a finite number of diagrams in perturbation theory up to a given order in the coupling constant g^n, different renormalization prescriptions can lead to results that differ to the next order $\mathcal{O}(g^{n+1})$ [135].
The explicit independence of observables on the renormalization scale is to be understood through a construction known as the renormalization group (RG) (see for example [128]) which shows that a variation in the measuring scale is compensated by a variation of the coupling constants which now "run" with energy. We will return to this remarkable property for the renormalized theory of graphene where Dirac quasiparticles naturally arise which we now address in detail.

3.3. Renormalized perturbation theory of interactions in graphene

Renormalized QED has proven to be one of the most precise theories in physics, although the exact way in which the comparison to experiments is performed was left out of the above analysis. In a nutshell, one extracts α_{QED} from a measurement of the anomalous magnetic moment of the electron [136]. Then a comparison with theory is performed by calculating the same quantity up to the eighth order correction in QED [137] inserting some other value for α_{QED} measured in an independent way, for example from the transitions between two atomic levels in a cesium atom [138]. Remarkably, the comparison agrees up to the seventh significant figure.

Given this glorious achievements, can we use the renormalization program to to learn about interactions in Dirac quasiparticles? To try to answer this question we will focus on the case of the low energy theory of graphene and try to construct a renormalizable field theory out of electron-electron interactions within Dirac quasiparticles.
Disentangling the effect of electron-electron interactions on the Dirac quasiparticles in graphene is not at all trivial, and its study is a common issue of debate in the graphene literature, very meticulously summarized in the recent review [15]. Here, we will not attempt to summarize the vast amount of relevant findings on this issue but limit the discussion to the relevant

aspects of the renormalizability and renormalization aspects of Dirac electrons in graphene. The first step towards building a consistent theory of interactions in graphene were performed in the 90s [26, 113], much earlier than the actual synthesis of the material itself in 2004 [10, 21].

Our starting point will be the massless Dirac Lagrangian in two spacial dimensions which is justified by the discrete point group symmetry of the hexagonal lattice [18–20]. The corresponding action is

$$\mathcal{S}_{kin} = \int dt d^2x \bar{\psi} i(\partial_0 \gamma^0 - v\gamma^i \partial_i)\psi, \tag{3.9}$$

where $i = 1, 2$, $\bar{\psi}(\mathbf{r}) = \psi^+(\mathbf{r})\gamma^0$, and the gamma matrices can be chosen as $\gamma_x = \sigma_2, \gamma_y = -\sigma_1, \gamma^0 = \sigma_3$ where σ_i are the Pauli matrices. It is not necessary to consider separately the two species of Dirac fermions (i.e. the two valleys in graphene) present in any lattice system with time reversal invariance as dictated by the Nielsen-Ninomiya theorem [71, 72] since we will not consider interactions which mix the two. As explained in the last section, the Lagrangian parameters Ψ and v are the *bare* parameters of the theory, to be fixed by the renormalization procedure.

At this point we must insert a term that accounts for Coulomb interactions between electrons in graphene. Short range interactions can be shown to be irrelevant by power counting in the renormalization group sense, and thus do not affect the physical observables at low energies, the regime for which (3.9) is valid. However, the unscreened Coulomb interaction is a marginal (renormalizable) interaction with Hamiltonian:

$$\mathcal{H}_{int} = \int d^2x d^2x' \frac{e^2}{4\pi\varepsilon} \frac{\bar{\psi}_{\mathbf{x}}\psi_{\mathbf{x}}\bar{\psi}_{\mathbf{x}'}\psi_{\mathbf{x}'}}{|\mathbf{x} - \mathbf{x}'|}, \tag{3.10}$$

where ε is the dielectric constant, which can be different from one if the graphene sample is placed on top of a substrate for example. The statement that the interaction is marginal is equivalent to the statement usually found in the literature to justify the use of the unscreened Coulomb interactions at the Dirac point instead of some screened model, namely the vanishing of the electronic density of states at the Fermi level.

In graphene, there is an addition peculiarity due to the dimensionality of the system. It is essential to notice that contrary to what happens in QED, in this theory the photon field propagates in one extra dimension compared to the electrons and so, in its propagator the k_z component can be integrated out to be left with a theory in three space-time dimensions [26]. Owing to this fact, the kinetic term for the gauge field is given by [26, 139].

$$\mathcal{S} = \int d\omega d\mathbf{k} \;\; A_0 |\mathbf{k}| A_0. \tag{3.11}$$

Although similar in aspect to QED in three space-time dimensions (QED_{2+1}), this fact alone makes the renormalization in graphene, as we will see, very different. The theory is closely related, although not the same to what is known as reduced QED or $RQED$ [140] where

the electrons live in a dimension $d_e < d_\gamma$ where d_γ is the dimension where the gauge field is defined. The second crucial difference from QED_{3+1} is of course the appearance of the Fermi velocity as a bare parameter in the theory. Lastly, note also the important difference that when treating many-body phenomena in condensed matter the photon propagator is instantaneous ($\sim 1/|\mathbf{k}|$) rather than retarded ($\sim 1/|\omega^2 - c^2\mathbf{k}^2|$).
Equations (3.9) and (3.10) define the dimensionless coupling constant

$$\alpha_g = \frac{e^2}{4\pi\varepsilon v}, \tag{3.12}$$

that measures how important are electron-electron interactions in this system are with respect to the kinetic term. This quantity is the equivalent in graphene to α_{QED} and we will see in the next section how to determine this quantity following the renormalization program presented above.

3.3.1. Building blocks: superficially divergent diagrams and Feynman rules

As was argued in the last section, long range interactions in graphene are governed by a dimensionless coupling constant, and thus we expect the theory to be renormalizable. This theory is represented by the renormalized action:

$$\mathcal{S} = \int d\omega d^2k \;\; \bar{\psi} Z_\psi \left[\gamma^0\omega - v Z_v \vec{\gamma}\vec{k}\right] \psi - Z_e e \bar{\psi}\gamma^0\psi A_0 + Z_A A_0 |\vec{k}| A_0, \tag{3.13}$$

where the counterterms are thus defined as:

$$\delta_\psi = Z_\psi - 1, \quad \delta_v = Z_\psi Z_v - 1, \quad \delta_e = Z_e - 1, \quad \delta_A = Z_A - 1. \tag{3.14}$$

These are to be treated as extra vertices of the theory and, as discussed above, they should be fixed according to some renormalization condition. In this Lagrangian, and for the rest of the chapter, we will drop the subindex R and thus A_μ, ψ, v and e are to be understood as the physical parameters. The Feynman rules can be derived proceeding in analogy with the QED case described above and they are shown, together with their mathematical equivalent in Figs. 3.4 and 3.3.
The next step is two construct the superficially divergent n-point functions which turn out to have, as shown in Fig. 3.5 the same structure as those of QED. Note however that the degree of divergence is different from QED in $3+1$ dimensions, a consequence of the different dimensionality of the theory and the gauge field propagator.
To define the counterterms exactly we must also provide a renormalization condition. There are apparently four quantities that we need to fix which in practice reduce to three due to gauge invariance, just as in the QED example above. However, as we will find out explicitly in the next section, a crucial difference is that the vertex function is finite and thus the electric charge is not renormalized in this model (we will return to this subtle issue in section 3.3.4). This implies that we only need to fix the counterterms associated to parameter v and to the

	=	$\frac{i(\gamma^0 k_0 + v\vec{\gamma}\vec{k})}{-k_0^2 + v^2k^2 - i\epsilon}$
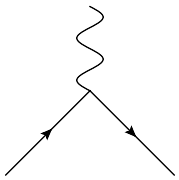	=	$-ie\gamma^0$
	=	$\frac{i}{2\left\|\vec{k}\right\|}$

Table 3.3.: Feynman rules for the graphene model (3.13)

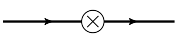	=	$-i\delta_\psi\gamma^0 k_0 - iv_R\delta_v\vec{\gamma}\vec{k}$
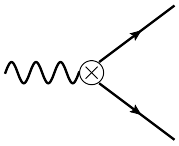	=	$-ie_R\delta_e\gamma^0$
	=	$-i\delta_A\|k\|$

Table 3.4.: Counterterm rules for graphene corresponding to δ_i in (3.13).

wave function normalization which amounts to impose a single condition to the electronic Green's function.
Choosing the on-shell prescription for this case amounts to imposing the condition

$$G^{-1}(E_R, k_R) = \gamma^0 E_R + v_F \boldsymbol{\gamma}\mathbf{k}_R, \tag{3.15}$$

with $v_R \equiv v_F = E_R/k_R$. Direct measurements of the dispersion relation such as ARPES are natural probes to define v_F. Henceforth we will use v and v_{os} interchangeably to emphasize

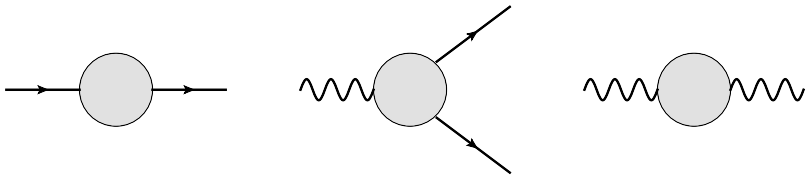

$M = 1$ $M = 0$ $M = 1$

Table 3.5.: Divergent n-point functions for the graphene model together with their superficial degree of divergence M. Diagrams that vanish by electron hole symmetry are not shown

the prescription when necessary, but both are to be understood as the renormalized Fermi velocity.
These are the basic tools to pin down which diagrams we have to fix. Since we must renormalize the theory order by order in the interaction we now center the discussion on the first order in perturbation theory (sometimes referred to as *one loop* order since the vertex diagram contains an extra e factor).

3.3.2. Renormalization of interactions in graphene at one loop order

To one loop order there are three superficially divergent diagrams represented in Fig. 3.2 which we now proceed to compute:

The electron propagator:

The one loop correction to the electron propagator is given by the diagram in Fig 3.2 (a). Using the Feynman rules in Fig. 3.3 it can be written mathematically as

$$\Sigma^{(1)}(p) = -ie^2 \int \frac{d^3k}{(2\pi)^3} \frac{\gamma^0 \left[\gamma^0(k_0+p_0) + v\vec{\gamma}(\vec{k}+\vec{p})\right] \gamma^0}{\left(-(k_0+p_0)^2 + v^2(\vec{k}+\vec{p})^2\right)(\vec{k}^2)^{1/2}}. \tag{3.16}$$

Regularizing the diagram with a sharp cut-off Λ, the integral can be evaluated to give

$$\Sigma^{(1)}_{\Lambda}(p) = \frac{e^2}{32\pi v} v\vec{\gamma}\vec{p}\left[\log\frac{p^2}{\Lambda^2} - 4\log 2 + \delta_v\right]. \tag{3.17}$$

Note that there is no divergent term proportional to $\gamma^0 p_0$ and thus there is no wave function renormalization at this order. Accordingly we can set $\delta_\psi = 0 + \mathcal{O}(\alpha_g^4)$. The divergent term is proportional to $\gamma^i p_i$ $(i = 1, 2)$ which we must cancel fixing δ_v through the renormalization

conditions. Using the on-shell condition (3.15) at an arbitrary point (E_R, k_R) we fix δ_v to be

$$\delta_v^{(os)} = \frac{e^2}{32\pi v_{os}} \left(4\log 2 - \log \frac{k_R^2}{\Lambda^2} \right) + O(e^4). \tag{3.18}$$

Adding this to (3.17) defines the electron propagator to be, at this order

$$G^{-1}(p) = -i \left[\gamma^0 p_0 + v_{os} \vec{\gamma}\vec{p} (1 - \frac{e^2}{32\pi v_{os}} \log \frac{p^2}{k_R^2}) \right]. \tag{3.19}$$

In the last expressions $\delta_v^{(os)}$ is the on-shell measurement of the Fermi velocity which fixes the electron propagator which satisfies (3.15) by construction. It is possible to recast the propagator in a more suggestive form

$$G^{-1}(k) = -i \left[\gamma^0 \omega + \bar{v}(k) \gamma^i k_i \right], \tag{3.20}$$

where

$$\bar{v}(k) = v_{os} \left[1 - \frac{e^2}{32\pi v_{os}} \log \frac{k^2}{k_R^2} \right] \tag{3.21}$$

is known as the running Fermi velocity. The depth of these results will come clear from the definition of the renormalization group equations, which show how the propagators behave under a change in the arbitrary scale k_R. For the sake of clarity we postpone the discussion to section 3.3.5.

Had we regularized the diagram with dimensional regularization and minimal subtraction ($\overline{MS}$) scheme we would have obtained

$$\Sigma_\epsilon^{(1)}(p) = v \vec{\gamma}\vec{p} \left[\frac{-e^2}{32\pi v} (\frac{1}{\epsilon} - \gamma + \log 4\pi - \log \frac{p^2}{\mu^2} + 4\log 2) + \delta_v \right], \tag{3.22}$$

where μ is an arbitrary scale with dimensions of momentum and γ is in this case Euler's constant (not to be confused with γ^μ). For this scheme, the counterterm $\delta_v^{(\overline{MS})}$ is fixed to

$$\delta_v^{(\overline{MS})} = \frac{e^2}{32\pi v_{\overline{MS}}} \left(\frac{1}{\epsilon} - \gamma + \log 4\pi \right), \tag{3.23}$$

which cancels all the finite terms and divergences. Thus, in this prescription the propagator is given by

$$G^{-1}(p) = -i \left[\gamma^0 p_0 + v_{\overline{MS}} \vec{\gamma}\vec{p} (1 - \frac{e^2}{32\pi v_{\overline{MS}}} \log \frac{p^2}{16\mu^2}) \right]. \tag{3.24}$$

Note that this propagator is of the form of (3.19) although the connection to a physical scale is not as direct as in the latter case. The important novel conceptual point here is that one has to note that both (3.20) and (3.24) are formulated only in terms of k_R, the renormalization point. Although formal, this issue will be important when we discuss the corrections to the optical conductivity since it is this fact that will enable to construct any observable in terms of k_R only.

Having illustrated the different schemes and regulators we proceed to sketch the calculations for the other two divergent diagrams which arise at one loop with a cut-off Λ and using the on-shell prescription.

The vertex function

The vertex function at one loop order is given by diagram in Fig 3.2 (b)

$$\Gamma^0(p,p+q) = e^3 \int \frac{d^3k}{(2\pi)^3} \frac{\gamma^0[\gamma^0 k_0 + v\vec{\gamma}\vec{k}]\gamma^0[\gamma^0(k_0+q_0)+v\vec{\gamma}(\vec{k}+\vec{q})]\gamma^0}{[-k_0^2+v^2\vec{k}^2][-(k_0+q_0)^2+v^2(\vec{k}+\vec{q})^2]|\vec{p}-\vec{k}|}. \tag{3.25}$$

Although being a superficially divergent diagram, this is an example where the naive power counting does not succeed in predicting its ultraviolet behaviour. An explicit calculation under a chosen regularization method, reveals that in this diagram all divergences cancel thus leaving a finite correction to the charge e which is also independent of regularization, a fact checked explicitly for a hard cut-off and dimensional regularization [8]. In virtue of this result it is again trivial to fix $\delta_e = 0 + O(e^4)$. This is in fact a check, at this order, of the Ward identities which relate the vertex with the electron propagator [75].

The photon propagator

The last diagram at this order is the one loop correction to the photon propagator given by the diagram in Fig. 3.2 (c). The fact that this diagram and the corresponding higher order diagrams to be discussed in the next section determine the corrections to the optical conductivity make this calculation particularly meaningful in graphene. The explicit form of the diagram is given by

$$\Pi^{00}(q) = e^2 \int \frac{d^3k}{(2\pi)^3} \frac{\gamma^0\left(\gamma^0 k_0 + v\vec{\gamma}\vec{k}\right)\gamma^0\left(\gamma^0(k_0+q_0)+v\vec{\gamma}(\vec{k}+\vec{q})\right)}{(-k_0^2+v^2k^2)(-(k_0+q_0)^2+v^2(\vec{k}+\vec{q})^2)}. \tag{3.26}$$

Evaluating the integral it is possible to obtain [26]

$$\Pi^{00}(q) = -\frac{e^2}{16}\frac{\vec{q}^2}{\left(-q_0^2+v^2\vec{q}^2\right)^{1/2}}, \tag{3.27}$$

which is also finite and physically represents the polarization function of graphene at half-filling. Note that since this one loop diagram contains no photon propagator, the result is the same as in QED_{2+1}. The fact that it is finite is again consistent with the results of the γ_0 part of the electron propagator and the vertex [9]. Furthermore, because of the Ward identities $Z_A^{1/2} = Z_e$ and thus, e is not renormalized at this order.

Having renormalized the theory up to the one loop level, we now show how the renormalization procedure is carried out up to two loops to illustrate some other points not encountered yet at this level.

[8] This last point is not at all trivial. There are examples of theories which have finite corrections but yield to ambiguous results depending on the regularization method. Some aspects of this theories will be discussed in Chapter 9

[9] The vertex is finite up to $\mathcal{O}(\alpha_g^2)$, which implies that the product $Z_A^{1/2}Z_\psi Z_e$ is finite up to order $\mathcal{O}(\alpha_g^2)$. In addition, the electron self-energy Z_ψ up to $\mathcal{O}(\alpha_g^2)$ is zero, it is possible to conclude that Z_A must also be finite at least up to order $\mathcal{O}(\alpha_g^2)$, which is consistent with a non divergent photon propagator at this order.

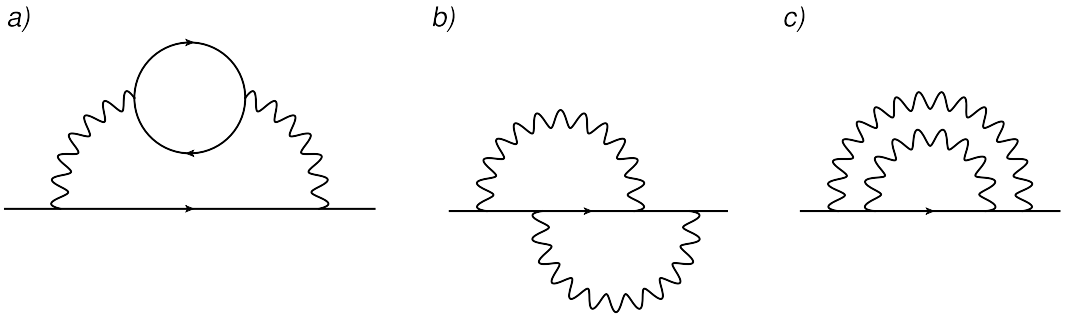

Figure 3.5.: Superficially divergent diagrams contributing to the electron self energy at two loop order.

3.3.3. Renormalization of interactions in graphene up to two loops order

The electron propagator:

There are three diagrams one can construct up to two loops that contribute the electron self energy (see Fig. 3.5). Their contributions to Z_ψ and Z_v have been calculated by several authors [26, 141] and shown to be divergent, both in the $\omega\gamma^0$ and $\vec{\gamma}\vec{k}$ parts. Thus the running of the Fermi velocity and the wave function renormalization will have two different divergent contributions at this order which one should fix using the renormalization conditions to each order in perturbation theory. The most remarkable property of these calculations is the absence of $\log^2(\Lambda)$ type of divergence. This is a very important difference with respect QED_{3+1} which does have in general a $\log^n(\Lambda)$ term to order α^n_{QED}. The appearance of such terms, known as the series of leading logarithms is important due to the fact that if they appear, they form a geometric series that can be summed up, giving the structure of the renormalized coupling constant. In graphene this resummation seems to be absent, a point we leave to section 3.3.5.

The vertex function

The vertex function is a very complicated function to calculate. Since its divergences are related through the Ward identities to the correction Z_ψ coming from the (γ_0 part) of the electron self-energy, we will not comment on this function further.

The photon propagator

The diagrams that contribute up to two loops order to the photon self energy are shown in Fig. 3.6 where also the counterterm diagram is shown. As mentioned above, these diagrams determine the optical conductivity of graphene and therefore are experimentally relevant. It

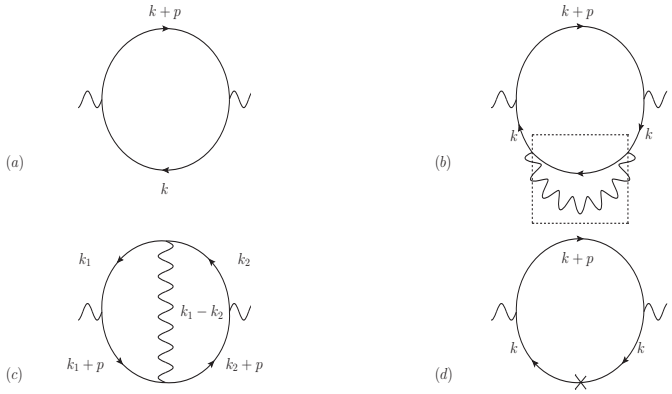

Figure 3.6.: First (a) and second (b), (c) order corrections to the photon propagator. Diagram (d) shows the two loop counter term diagram

is convenient to calculate diagrams (b) and (d) together since they can be written as

$$\Pi_{3b+3d}(q) = -e^2 \int \frac{d^3k}{(2\pi)^3}\gamma^0 G(k) \left[\Sigma_{CT} - ie^2 \int \frac{d^3p}{(2\pi)^3}\gamma^0 G(k+p)\gamma^0 \frac{1}{|\vec{p}|}\right] G(k)\gamma^0 G(k+q). \tag{3.28}$$

Notice that out of the two loop integrals one is exactly the renormalized one loop electron self energy already calculated in (3.19). Therefore, one can proceed to the calculation of the second integral

$$\frac{e^4}{32\pi v_F}\int \frac{d^3k}{(2\pi)^3} \frac{tr\gamma^0\left(\gamma^0 k_0 + v\vec{\gamma}\vec{k}\right)\vec{\gamma}\vec{k}\left(\gamma^0 k_0 + v\vec{\gamma}\vec{k}\right)\gamma^0\left(\gamma^0(k_0+q_0) + v\vec{\gamma}(\vec{k}+\vec{q})\right)\log\frac{k^2}{\mu^2}}{(-k_0^2 + v^2\vec{k}^2)^2(-(k_0+q_0)^2 - v^2(\vec{k}+\vec{q})^2)}. \tag{3.29}$$

Although an explicit calculation of all finite and divergent terms is cumbersome, it is possible to check by isolating the divergent contributions that these explicitly cancel, leaving a finite correction coming from these two diagrams. The final diagram shown in Fig. 3.6 (c) is the vertex correction to the photon propagator. Its integral form reads

$$\Pi_{3c}(q) = \int \frac{d^3k_1 d^3k_2}{(2\pi)^6}\frac{-ie^4}{v}\frac{tr\gamma^0 G(k_1+q)\gamma^0 G(k_2+q)\gamma^0 G(k_2)\gamma^0 G(k_1)}{|\vec{k_2}-\vec{k_1}|}. \tag{3.30}$$

Again, it is easy to see that one of the integrals is exactly the one loop vertex correction (3.25) which is finite. Proceeding in an analogous way as in diagrams (b) and (d) it is possible to show rigorously that the divergences of the remaining integral cancel explicitly, which is the central results of this chapter. This proves that it is possible to construct finite, cut-off

independent observables in graphene that depend only on k_R, the renormalization point.
As a summary, we have found that the electronic charge is not renormalized up to two loops order and all the divergences to this order can be reabsorbed in the wave function normalization Z_ψ and the running Fermi velocity defined by Z_v.

3.3.4. Higher loop structure

At this point we have argued how to renormalize the theory of long range interactions in graphene up two to loops. We have encountered that the only renormalized quantities in the theory are the Fermi velocity v and the electron wave function ψ. The electric charge e is not renormalized up to two loops order but, how general is this result?
In principle, we are not guaranteed that the electron charge is finite in this model up to all orders in perturbation theory. It has been argued [15, 139] that in two dimensional theories the charge e does not flow because it appears as a coefficient of a non-analytic term in the action. Although there is no formal proof of this statement, through explicit calculation [15, 26, 141] it is known to be true only up to two loops through calculations done by several groups. The complete proof of the renormalizability of the theory has been attempted also through the ladder approximation [142], which amounts to a resummation of diagrams to get insight of the full structure of the theory. Although this is not a complete proof, the results found by [142] are consistent with a charge that does not renormalize. It was shown that in this approximation the theory is free of infrared divergences and all the ultraviolet divergences can be absorbed exclusively in Z_v and Z_ψ, leaving $Z_e = 0$.

3.3.5. The renormalization group in graphene

As a final remark on the renormalization procedure we comment briefly on the construction known as the renormalization group. In the modern perspective, the renormalization group is a construction that ensures that the choice of renormalization scheme does not affect the prediction on observable quantities. Through the Callan-Symanzik equation [128] a change in the renormalization scales is compensated by a change in the coupling constants a result which is often referred to as the 'flow' of the coupling constants under a change in energy scale. Although a complete derivation of the equation is outside the scope of the present chapter, we will begin by introducing the function which characterizes this flow, the β function

$$\beta(g_i) = \mu \frac{\partial g_i}{\partial \mu}, \tag{3.31}$$

where $\{g_i\}$ are the set of coupling constants of the theory and μ is a parameter that characterizes the energy scale of the theory. For graphene the relevant β functions are defined

through the differential equations [26, 143]

$$\beta_v = \mu \frac{\partial v}{\partial \mu}, \quad \beta_e = \mu \frac{\partial e}{\partial \mu}, \quad \gamma_\psi = \mu \frac{\partial \log Z_\psi}{\partial \mu}. \tag{3.32}$$

As discussed above $Z_e = 0$ implying that $\beta_e = 0$ at least up to second order in perturbation theory. From the one loop self-energy (3.24) we have that

$$\beta_v = \frac{e^2}{16\pi}, \tag{3.33}$$

By a simple integral in an arbitrary interval $[\mu, \mu']$ one obtains

$$v(\mu') = v(\mu) - \frac{e^2}{16\pi} \log\left(\frac{\mu'}{\mu}\right). \tag{3.34}$$

which is exactly (3.21) with the identification $\mu' = k$. A remarkable physical consequence of this result is that the Fermi velocity grows as one approaches zero energy due to the effect of long range electron-electron interactions in graphene. This means that the coupling constant α_{QED} is smaller as one goes to smaller energies, which makes perturbation theory more and more reliable if we flow to lower energies and turns graphene into an asymptotically free theory (see footnote 2).

A further important comment is in order. Although (3.34) is a one loop result, it contains information about the structure of the theory. In fact it can be shown [144] through the recursive form of the RG equations that due to fact that that the one loop β_v is independent of v there is no $log^n \Lambda$ term at order n. This is a highly non trivial result since it differs substantially from QED_{3+1} where we find this kind of terms at each order in perturbation theory for the $\beta_{\alpha_{QED}}$. In that case, the renormalized parameter is the electron charge e (the velocity of light c is fixed by Lorentz invariance) and thus it is possible to perform a resummation of the leading logarithms to obtain the running coupling constant

$$\alpha_{QED}(q) = \frac{\alpha_{QED}(\mu)}{1 - \frac{2\alpha}{3\pi} \log \frac{q^2}{\mu^2}}, \tag{3.35}$$

Note that in QED the renormalization of α_{QED} is given entirely by the photon self energy in virtue of the Ward identities [75], which have $log^n(\Lambda)$ term at order n. The electron propagator both in QED and in the case of graphene does not have $log^n(\Lambda)$ term at order n. In QED, this is not a problem for the renormalization of α_{QED} since α_{QED} is entirely determined by Z_A (defined by the photon propagator), but in graphene this determines Z_v and since e is not renormalized, this fact permeates in the renormalization of α_g preventing the perturbative series to be resummed, as opposed to QED.

An explicit calculation at two loops of the electron self energy indeed shows that no $log^2(\Lambda)$ appears [141, 145]. The β_v function acquires now the form [145]

$$\beta_v = \frac{1}{4}\left(\frac{e^2}{4\pi}\right) - \left(\frac{N}{12} - \delta\right)\left(\frac{e^2}{4\pi} v\right)^2 v, \tag{3.36}$$

where $\delta \sim 0.03$ is a numerical constant and N is the number of fermionic species (for graphene $N = 4$). This structure enables the appearance of a non trivial fixed point of the renormalization group flow at $\alpha_g^* \sim 0.8$. It is easy to show by differentiation of (3.36) that this point is infrared unstable, meaning that for $\alpha_g < \alpha_g^*$ the theory is asymptotically free, and when $\alpha_g > \alpha_g^*$ the theory flows to strong coupling. Note however that the fact that $\alpha_g^* \sim 1$ prevents us from drawing any reliable conclusions since we have assumed that perturbation theory ($\alpha_q \ll 1$) is valid. We will leave a brief discussion of the possibility of a strong coupling theory for section 3.5.2.

There is also important physical information in the structure of δ_ψ. The way Z_ψ behaves as we change the energy determines the nature of the electron when interactions are introduced. As it was discussed in the previous chapter, this quantity can signal a break down of the Fermi liquid theory if it vanishes at the Fermi energy. Importantly, since the electron self-energy scales linearly in energy resembling that of marginal Fermi liquid behaviour it is often argued that graphene is a marginal Fermi liquid. One therefore might expect that Z_ψ vanishes as we approach lower energies consistent with the linear behaviour of the self energy. This however, is not the case, as was shown in [143], where they computed in RPA the flow of this quantity as the energy decreases showing that it saturated at a finite value. Thus, in this sense, graphene is a Fermi liquid. It is in fact the running of the coupling constant which prevents Z_ψ from reaching zero in the infrared.

In light of this results, we have seen that the renormalization program, ending in the renormalization group provides answers to fundamental questions of the nature of Dirac quasiparticles in graphene. We now consider how renormalization can be used to compute physical observables taking as an example the optical conductivity of graphene.

3.4. Computation of observables: the optical conductivity

In the last chapter, the optical conductivity of graphene was derived in detail and calculated through a phenomenological model of the self-energy. In this section, we will be only interested in the corrections to the optical conductivity at zero doping arising from electron electron interactions considered from the microscopic model renormalized in the preceding sections [10].

There is still an ongoing debate on the exact correction to second order in perturbation theory to the optical conductivity of graphene [11, 13, 15, 141, 146–151]. In this section we will see how the previous construction can affect such an observable. As was discussed in Chapter 2, the real part of the conductivity is given by (2.7)

$$\mathrm{Re}\sigma^{ij}(\mathbf{q},\omega) = -\frac{e^2}{\omega}\mathrm{Im}\Pi^{ij}(\mathbf{q},\omega), \tag{3.37}$$

[10] We will only focus on the theory at zero chemical potential although see section 3.5 for a comment on this issue.

where $\Pi^{\alpha\beta}(\mathbf{q},\omega)$ is the current-current correlation function. For the model (3.13) the real part of the optical conductivity is thus

$$\mathrm{Re}\sigma^{ij}(\omega) = -\lim_{q\to 0} Z_\psi^2 Z_v^2 v^2 \frac{1}{\omega}\mathrm{Im} < \bar{\psi} e\gamma^i \psi \bar{\psi} e\gamma^j \psi >, \tag{3.38}$$

where $j^\mu = (Z_\psi \bar{\psi}\gamma^0\psi, Z_\psi Z_v v \bar{\psi}\gamma^i\psi)$ is the current operator and $i,j = 1,2$. Using the continuity equation $\partial^\mu j_\mu = 0$ it is possible to recast (3.38) into the equivalent form

$$\mathrm{Re}\sigma(\omega) = -\lim_{q\to 0} Z_\psi^2 \frac{\omega}{q^2}\mathrm{Im} < \bar{\psi} e\gamma^0 \psi \bar{\psi} e\gamma^0 \psi >= -\lim_{q\to 0} \frac{\omega}{q^2}\mathrm{Im} < A_0 A_0 > . \tag{3.39}$$

The last equality, which can be proven by direct computation, shows that the optical conductivity is related to photon propagator calculated in the last sections.
To first order in perturbation theory, the optical conductivity is obtained by inserting (3.27) (see Fig. 3.6(a)) in (3.39) and considering valley and spin degeneracies

$$\sigma_0(\omega) = -\frac{4}{\hbar}\lim_{q\to 0}\frac{\omega}{q^2}\mathrm{Im}\left[-\frac{e^2}{16}\frac{\vec{q}^2}{(-\omega^2 + v^2\vec{q}^2)^{1/2}},\right] = \frac{e^2}{h}\frac{\pi}{2}. \tag{3.40}$$

which exactly coincides with the definition of σ_0 in (2.14).
The next correction arises from adding the contributions of the diagrams shown in Fig. 3.6 (b),(c) and the counterterm diagram (d), which, as we showed before ensures that the final result is finite, but dependent on the renormalization point k_R. This correction calculated by several authors [141, 146–151] is given by

$$\mathrm{Re}\sigma(\omega) = \sigma_0\left(1 + \alpha_g \tilde{C}\right). \tag{3.41}$$

where $\tilde{C} \sim 0.01$ is a small constant (due to the near cancellation of the self energy and vertex corrections) [11]. At this order, the only effect of the renormalization procedure enters through the dependence of the coupling constant α_g on k_R, and its value is to be determined by the renormalization condition on v, which is the important conceptual point of this chapter as compared to previous calculations. The fact that there is no intrinsic renormalization effect associated to the optical conductivity through the constant $\tilde{C}$ is a consequence of the fact that the real part of the counterterm diagram cancels when taking the $\vec{q} \to 0$ limit. Nevertheless, other less trivial renormalization corrections will in general arise when computing observables at finite $\vec{q}$, the imaginary part of the conductivity or higher orders in perturbation theory.

[11] There has been an ongoing controversy on the value of $\tilde{C}$ [141, 146–151] on the most suitable regularization method to calculate the required integrals, in particular the rigorous implementation of a hard cut-off. Although no consensus was reached, it is agreed and also confirmed by experiments that the effect of interactions is small. We will see in Chapter 9 that some ill defined theories can have corrections which depend on the regulator used.

To summarize our findings, we have shown, through the example of the optical conductivity, that one can construct for graphene cut-off independent observables by imposing renormalization conditions determined by the renormalization point k_R. Different choices of k_R are to be related by the renormalization group equations which guarantees the consistency of the theory with respect to changes of k_R.

3.5. Discussion

3.5.1. Experimental evidence for the renormalization picture of interactions in graphene

In the renormalization procedure, experimental probes are essential to determine the renormalization point (E_R, k_R) and also can give experimental confirmation of the whole construction. There have been a number of experimental probes used to tackle the problem of electron-electron interactions in graphene from the experimental side which we will now shortly review focusing on the mentioned aspects.

Angle resolved photoemission spectroscopy (ARPES)

Having direct access to the dispersion relation of graphene this is a natural experiment for probing the renormalization construction as well as providing a renormalization point for the renormalization program. Thus, if the precision is good enough this measurement can be used to choose a renormalization point (E_R, k_R) which will then fix the electronic Green's function $G^{-1}(E_R, k_R)$.
Although there have been several ARPES experiments [23, 152, 153] it was only recently claimed [154] that there exists experimental evidence for the renormalization of the Fermi velocity due to electron interactions. This particular experiment compared three different substrates (SiC, hBN and quartz) which will change the value of the coupling constant in virtue of its definition $\alpha_g = \frac{e^2}{4\pi\varepsilon_g v}$ and although the observed effect certainly goes in the right direction, it is still not clear whether it is due to an extrinsic property related to the substrate.

Quantum oscillations

Perhaps one of the most compelling proofs of renormalization was achieved by studying Shubnikov-de Haas oscillations in ultraclean suspended graphene samples [155]. In these set of experiments a strong Fermi velocity renormalization as a function of electron density was observed. However, before making any direct comparison with the presented renormalization procedure it must be noted that the observations of this experiment are not, strictly speaking, the same phenomenon since all the results of this chapter are to be understood at the Dirac point. Nevertheless, an analogous construction can be developed for interactions

in graphene with finite carrier density close to the Dirac point *á la* Wilson by integrating out high-energy degrees of freedom where the same logarithmic renormalization in the Fermi velocity as the one obtained in (3.21) is obtained, where the 'running' is now to be understood in terms of the carrier density n (or Fermi momentum k_F).

Local probes

A number of works have studied graphene through scanning tunnelling spectroscopy measurements (STS) that can also be useful to determine the renormalization point v_R since it has access to the local density of states (LDOS) (see for example [156]). This however, would only be an indirect measurement of the Fermi velocity since one should calculate and adjust the LDOS with the free parameter v, which will fix $G^{-1}(E_R, k_R)$, as discussed for the case of ARPES experiments above.

Landau levels

When a strong magnetic field perpendicular to the graphene sheet is applied, a series of Landau levels appear [7, 21] with energies given by $E_n = v_F\sqrt{2eBn}$ where $n = 0, 1, 2\cdots$ [7]. Thus, naively one can think that this can also be a probe of renormalization effects or the establishment of the renormalization point (E_R, k_R). However, in this case, the high magnetic fields constrained the electrons to Landau levels and this massive degeneracy complicates the problem of assessing the effect of electron-electron interactions. On the contrary, magnetic fields needed for the quantum oscillations discussed above are much lower than those needed for the appearance of Landau levels and thus keen to be understood by the treatment presented in [155], where the magnetic field is only assumed to be responsible of the quantum oscillations.

Optical probes

The optical experiment presented in Ref. [114] of graphene on SiO_2 discussed in Chapter 2 was also suggested to give a measure of the Fermi velocity renormalization. This experiment however, suffers from extracting the Fermi velocity from an indirect measurement at high doping levels (much bigger than in [155] for instance) which can certainly be subject to extrinsic effects. Anyhow, only a construction similar to Ref. [155] can explain a renormalization of the Fermi velocity due to electron electron interaction at high doping which is fundamentally different from the construction that was here developed.

3.5.2. No gap puzzle: strong coupling versus weak coupling

All the renormalization program is based on the fact that $\alpha_g \ll 1$. Recalling its definition

$$\alpha_g = \frac{e^2}{4\pi\varepsilon_g v}, \tag{3.42}$$

it is often argued that when ε_g is large enough perturbation theory is valid. In principle this assumption can be justified by situating the graphene sample on top of a substrate. However, this can induce extrinsic effects such local doping of the graphene through electron hole puddles in the case of SiO_2 or an imbalance of the two sublattices of graphene, resulting in the opening of a gap, which could mask intrinsic interaction effects.
On the other hand, for suspended graphene $\varepsilon_g = 1$ and $\alpha_g \sim 2$ hence invalidating perturbation theory. There is an extensive literature on the strong coupling problem of graphene (see [15] for an exhaustive set of references) with the overall consensus that a spontaneous metal-insulator transition (or chiral symmetry breaking in the field theory language) will occur after a certain α_g^* resulting in the opening of an excitonic gap. There are several theoretical estimations for the critical value, most of them of the order $\alpha_g^* \sim 1$ if not bigger [15]. The fact that the cleanest graphene samples [111, 155] do not show the presence of such a gap, with an upper bound of $m \lesssim 1$meV poses therefore the question of why the strong coupling approach is not explaining the observed gapless behaviour. A plausible explanation is that the critical coupling is indeed bigger, and thus, the predictions of perturbation theory will still be valid since no other critical point exists as the coupling increases, although formally the perturbation theory breaks down. However, this possibility is, at the time of writing, only speculative and no rigorous proof exists.

3.5.3. Infrared constraints

The running of the Fermi velocity to higher values in the infrared posses other fundamental questions. Causality should prevent the renormalization of this quantities to values $v > c$ although, for the model (3.13) this property is not included. As soon as v is comparable to c relativistic effects should be accounted for starting from the bare Lagrangean. Of course, these corrections will only appear at very low energies, inaccessible in practice to experiments. One can estimate when such corrections should be taken into account which will impose an infrared cut-off δ for the theory of order

$$\delta = k_R \exp\left[-\frac{16\pi(c - v(k_R))}{e^2}\right], \tag{3.43}$$

which depends on the renormalization point k_R. Choosing any realistic renormalization point such as $v(125\text{meV}) = 1.093 \cdot 10^6 \text{m/s} \equiv v_F$extracted for example from Ref. [157] imposes no bounds in practice to the theory presented in this chapter. Nonetheless, the 'retarded' model that arises from the inclusion of a finite speed of light c in the theory is closely

related to the Reduced QED (RQED) that has been studied in high energy physics [140]. The basis of the renormalization of the 'retarded' theory for graphene was established in [26] which has a somewhat richer structure in terms of divergences. In particular, in this theory, the vertex diverges at one loop although the charge still evades renormalization just as in QED_{2+1}. Remarkably, there is a fixed point at one loop for the Fermi velocity at $v = c$ where the Lorentz symmetry is restored due to renormalization.

3.6. Conclusions

In this chapter we have described the theoretical construction known as renormalization. Due to the form of the low energy description of electronic excitations in graphene we have been able to apply this tool to describe interactions among these Dirac quasiparticles in the regime of weak coupling. The description in terms of interacting Dirac fermions resembles the structure of quantum electrodynamics, and suffers from similar problems: perturbation theory gives divergent (cut-off dependent) results which have to be treated in order to make comparisons to experiment.

In this context, we have first reviewed earlier work to show that the renormalization procedure can be carried out order by order in perturbation theory giving finite results that depend on the renormalization point, a scale which is used to fix the parameters of the Lagrangian. This conceptual ingredient, usually overlooked in graphene, enabled us to calculate corrections to any observable of the theory at any order in perturbation theory without requiring any finite cut-off. The independence of the theory on different renormalization points is ensured by the renormalization group equations where changes in the renormalization scale are absorbed by running coupling constants that change depending on the energetic scale where we wish to calculate an observable. The procedure for calculating observables was exemplified with the optical conductivity and any other observable can be computed following analogous steps to the ones presented in this chapter.

Finally different experimental results related to the renormalization of interactions in graphene were presented and discussed. Although there is still further experimental and theoretical work to be done in order to clarify the absence of an excitonic gap in suspended samples, the present experimental status of the field suggests the compelling picture that interactions in graphene are successfully addressed via the renormalization construction. The present experimental situation has justified the construction presented here, as we secretly expected from the beginning of the chapter where we argued that perturbation theory was only to be justified *a posteriori*, taking into account the running of the coupling constants.

Part II.

Topology and Interactions

4. Time reversal breaking topological phases in highly doped graphene

"Nature does not count nor do integers occur in nature."
-Percy William Bridgman, 'The Way Things Are'.

4.1. Introduction

In previous chapters we have understood different aspects of Dirac quasiparticles, first by proposing a phenomenological model, followed by the construction of the low energy quantum field theory description for such quasiparticles, enabling us to construct well defined observables in perturbation theory. The latter approach relied upon the fact that low energy Dirac quasiparticles close to the Dirac point have a density of states which vanishes linearly with energy and is exactly zero at the Dirac point [7]. This justifies the use of the long range Coulomb interaction employed extensively in the last chapter [26]. However, at higher fillings, graphene has a finite density of states and thus a screened model of interactions is better suited to describe the system.
Arguably, the standard model of repulsive Coulomb interactions in solids is the Hubbard model [158]. In this model, Hubbard assumed that out of all the complicated matrix elements of the long range Coulomb interactions $\langle ij|1/r|kl\rangle$ (Latin letters indicate the position of the electron in the lattice) the most relevant term is that where the two interacting electrons are situated at the same site, $\langle ii|1/r|ii\rangle$, i.e. the on-site repulsion, followed by the repulsion between nearest neighbours and so on. This assumption can be justified under several physical scenarios, in particular when the Coulomb interaction is expected to be strongly screened, such as in the situation which will concern the findings in this chapter.
In particular, we will see how strongly screened Coulomb interactions described by the Hubbard model will give rise to novel electronic phases in doped graphene. In this case, our attention will be focused on the emergence of topological phases, phases which are classified through topological invariants introduced in Chapter 1. Remarkably, despite the fact that the system is highly doped, some properties of these phases such as the anomalous Hall conductivity will be understood in terms of Dirac quasiparticle physics, among other

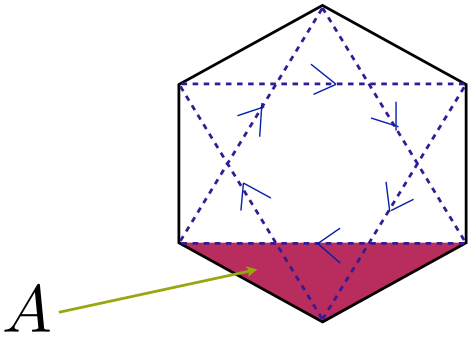

Figure 4.1.: Complex hopping structure for the Haldane phase [66].

physical paradigms regarding discrete symmetries and topological invariants. We will find that the doped honeycomb lattice can host examples of topological Fermi liquids introduced by Haldane [55] and classified by Sun and Fradkin [159] which are Fermi liquids that host low energy excitations that have a topological structure.
The key new element that we will be introduced in this chapter in order to stabilize novel topological phases is the relaxation of translational symmetry to allow phases with enlarged unit cells. In the particular case of the honeycomb lattice considered in this chapter, the enlarged unit cells will be tripled unit cells as compared to the usual two atom unit cell used to describe the honeycomb lattice. To understand exactly why this method is effective in bringing up new topological phases, let us briefly review the history of time reversal breaking topological phases in graphene.

4.1.1. Topological phases in graphene

Long before graphene was isolated [21], and building up on an earlier work by Semenoff [65], Haldane [66] proved that an integer version of the Hall effect could be realized without an external magnetic field in the honeycomb lattice. He considered the tight binding model in such a lattice with real first neighbours hoppings but complex second nearest neighbours hoppings. Complex hoppings break time reversal symmetry and emulate the effect of the magnetic field. This is so because a magnetic field, introduces a phase factor to the wave function of the electron known as the Peierls phase [160] which is the unimodular phase factor $\exp(ie/\hbar \int \mathbf{A} \cdot d\mathbf{r})$ that an electron acquires when hopping in a magnetic field from one atom to another. In the tight binding language, this is equivalent to a complex hopping. Note that by choosing an appropriate form for the complex hoppings it is possible to have zero magnetic flux in the unit cell and thus, zero external magnetic field, but still break time reversal symmetry.
In his original work, Haldane argued that these complex phase factors could arise from lo-

calized magnetic dipoles at the center of each hexagon ordered ferromagnetically, although we will soon argue that they can be spontaneously generated by interactions. Either way, choosing an appropriate gauge which will of course not modify the final physical properties, these phase factors can be written in terms of the fluxes that each closed circuit of hoppings enclose.

The particular choice of Haldane is shown in Fig. 4.1 where the real hoppings t_1 are denoted by solid lines and the complex hoppings $t_2 e^{\pm i\phi}$ are denoted by dashed lines with arrows. The sign of the phase depends on whether the electron is jumping clockwise or anti-clockwise. The arrows in Fig. 4.1 represent how an electron hops to acquire the positive sign of the phase, where ϕ is the flux enclosed in region A chosen to satisfy that the total flux per unit cell is zero.

It is not difficult to show, for example by calculating the low energy theory, that at half filling the Haldane model is gapped and has a quantized Hall conductivity $\sigma_{xy} = \frac{e^2}{h}$ arising from the contribution of two massive Dirac fermion to the Hall conductivity [1]. This constitutes a realization of the quantum Hall effect without external magnetic fields. As the band is filled, the Hall conductivity takes non quantized values which are, in the low energy limit given by $\sigma_{xy} = \frac{e^2}{h}\frac{m}{|\mu|}$ where μ is the chemical potential, an example of a non quantized quantum Hall effect known as the anomalous quantum Hall effect [54].

As anticipated, an analogous phase can arise from interactions. Raghu *et al.* [161] studied the emergence of such topological phases within a nearest neighbour tight binding model and the extended Hubbard model, including the on-site repulsion U, first nearest neighbours, V and second nearest neighbours V' repulsive interactions. For the spinless case, and due to the Pauli principle, two electrons cannot sit on the same site an thus the on-site interaction U is not necessary. In this case, a topological phase as the one considered by Haldane emerges at half-filling with a total flux per unit cell of zero. Note in particular that if only nearest neighbours are considered there is no way to generate a self consistent pattern of currents with zero flux, and thus, no time reversal breaking phase can be generated. Therefore, it is not coincidental that Raghu *et al.* considered next to nearest neighbouring interactions, since precisely these allows the necessary second nearest neighbour hopping structure which, in some region of parameters generates the time reversal broken phase.

Does this mean that there is no way to generate a topologically non trivial phase out of nearest neighbours interactions in the honeycomb lattice? The current argument above prevents us from using only nearest neighbouring hoppings and a model which includes third nearest neighbours might be even more contrived.

In this chapter we will explore a way out of this problem. It is in fact possible to realize

[1] In fact, this contribution can also be understood as a topological invariant arising as the coefficient of the topological term in the effective action of the external electromagnetic field. This approach to the Hall conductivity will be described in subsequent chapters.

time reversal breaking, and within these, topologically non trivial states with only nearest neighbour hoppings and interactions by allowing phases that have tripled unit cells. In principle, bigger unit cells allow for different self consistent intra-cell current patterns with only nearest neighbour interactions. In fact, it will be shown that these phases arise in doped graphene and its properties might be understood in terms of emergent Dirac quasiparticles. To this extent, we will employ a variational mean field approach to know at which point inside the parameter space defined by the interaction strength and the electronic density these phases are stabilized. Once isolated, we will classify them through their topological properties through the study of the Hall conductivity of each phase and study the order of the relevant phase transitions. In the final part, the effect of introducing second nearest neighbours and the spin degree of freedom will be addressed.
In the following section we introduce the variational mean field method. In order to gain an intuition for the complicated case of the enlarged unit cell, we will first apply it the simpler two atom unit cell.

4.2. Variational mean field method in graphene

The mean field approach is a powerful tool to study emergent many body phases in condensed matter [42]. In this paradigm, we transform, under some mean field *ansatz*, the complicated interacting Hamiltonian into an effective, diagonalizable one body Hamiltonian. Such a Hamiltonian describes a system where each quasiparticle feels an average field created by the rest of the particles, its form determined precisely by the chosen mean field *ansatz*.
Usually, several phases compete to realize the ground state of the system and thus it is useful to take a variational approach on the mean field method [162, 163] which relies on the inequality

$$\Omega \leq \langle \mathcal{H} \rangle_{MF} - T\mathcal{S}_{MF} - \mu \langle \mathcal{N} \rangle_{MF} , \tag{4.1}$$

where Ω is the grand canonical potential of the system, T is the temperature, μ is the chemical potential, and $\langle \cdots \rangle_{MF}$ and $\mathcal{S}_{MF}$ are respectively the thermal average and the entropy for any thermal distribution $\rho_{MF} = \exp(-\beta \mathcal{H}_{MF})$. These quantities are defined through a trial family of mean field Hamiltonians $\mathcal{H}_{MF}[\xi_i]$ parametrized by a set of parameters $\{\xi_i\}$.
In this expression, $\mathcal{N}$ is the operator for the total number of particles which, by assumption satisfies $[\mathcal{H}, \mathcal{N}] = 0$. The equality in (4.1) is realized when the mean field Hamiltonian $\mathcal{H}_{MF} = \mathcal{H}$ and thus the inequality can be used as a variational principle to obtain, out of the family defined by $\mathcal{H}_{MF}[\xi_i]$ the set of $\{\xi_i\}$ that minimizes the right hand side of (4.1).
To this extent, it is useful to rewrite (4.1) as

$$\Omega \leq \Omega_{MF} + \langle \mathcal{H} - \mathcal{H}_{MF} \rangle_{MF} , \tag{4.2}$$

with $\Omega_{MF} = \langle \mathcal{H}_{MF} \rangle_{MF} - T\mathcal{S}_{MF} - \mu \langle \mathcal{N} \rangle_{MF}$. In the following sections we will ask our system to conserve the number of particles under the requirements of Luttinger's theorem [164] and thus the average number of fermions in the system will be always N_e, the total number of fermions in the system i.e. $\langle \mathcal{N} \rangle = N_e$. Hence, it is in practice more useful to work in the canonical ensemble that works with a constant number of particles, volume and temperature. In the thermodynamic limit, we have that $\Omega = \mathcal{F} - \mu \langle \mathcal{N} \rangle$ where $\mathcal{F}$ is known as the free energy and we can express (4.2) as

$$\mathcal{F} \leq \mathcal{F}_{MF} + \langle \mathcal{H} - \mathcal{H}_{MF} \rangle_{MF} \equiv F[\xi_i], \tag{4.3}$$

with $\mathcal{F}_{MF} = \Omega_{MF} + \mu N_e$ with μ is fixed through the condition $\langle \mathcal{N} \rangle = N_e$. The right hand side of inequality (4.3) defines the functional $F[\xi_i]$ that we should minimize with respect to a variation of $\{\xi_i\}$ through the variational condition $\delta F = 0$. In other words, the minimization procedure obtains the set of $\{\xi_i\}$ for which the grand canonical potential Ω_{MF} is closest to the real Ω.

Before relaxing translational invariance to obtain a set of topological phases in graphene through this method, it is illustrative to elaborate on a simpler example that shall illustrate the procedure.

4.2.1. An illustrative example: Pomeranchuk instability in graphene

To discuss how the variational procedure works in practice, we will now try to recover the result that was put forward some time ago [165] that graphene can host a Pomeranchuk instability when it is doped up to a filling known as the *van Hove* filling [27]. In the next section we will allow for phases that break translational invariance and have a periodicity of three times that of ordinary graphene i.e. a tripled unit cell which shall host novel topological phases but for the moment we will work with the conventional two atom unit cell.

As was discussed superficially in the introduction (see Fig. 1.1(d)), within the tight binding model of graphene, the van Hove filling is a saddle point in the band structure where the non interacting density of states diverges. At this filling, which in graphene lies exactly at $\pm t$ the nearest neighbour hopping, it is not unexpected that interactions might rearrange the spectrum to lift the degeneracy, an intuition which is established based on the Stoner criterion [28]. In this example, we will show how the Fermi surface reshapes itself breaking its original point group of sixfold rotations to a smaller point group symmetry of twofold rotations. This less symmetric state will be denoted as Pomeranchuk phase in honour of the first instabilities of the Fermi surface first studied by Pomeranchuk [166].

Our starting point is the tight binding model description (1.3) of graphene discussed in chapter 1, which, considering only nearest neighbour hopping reads

$$\mathcal{H}_{TB} = -t \sum_{\mathbf{k}} \psi^{\dagger}_{\mathbf{k}} \begin{bmatrix} 0 & \gamma_{\mathbf{k}} \\ \gamma^{*}_{\mathbf{k}} & 0 \end{bmatrix} \psi_{\mathbf{k}}, \tag{4.4}$$

where $\gamma_{\mathbf{k}} = 1 + e^{\mathbf{k}\cdot\mathbf{a}_1} + e^{\mathbf{k}\cdot\mathbf{a}_2}$, $\psi^\dagger_{\mathbf{k}} = (a^\dagger_{\mathbf{k}}, b^\dagger_{\mathbf{k}})$ and t is the nearest neighbor hopping. The lattice vectors can be chosen to be $\mathbf{a}_1 = \frac{a}{2}(\sqrt{3}, 3)$ and $\mathbf{a}_2 = \frac{a}{2}(-\sqrt{3}, 3)$. Since we are interested in the highly doped system, let us now introduce a term which will account for a screened Coulomb interaction between nearest neighbours,

$$\mathcal{H}_{int} = V \sum_{\mathbf{r},\boldsymbol{\delta}} a^\dagger_{\mathbf{r}} a_{\mathbf{r}} b^\dagger_{\mathbf{r}+\boldsymbol{\delta}} b_{\mathbf{r}+\boldsymbol{\delta}} + h.c. \tag{4.5}$$

This is an extended version of the Hubbard Hamiltonian [28] and since we shall only consider spinless fermions, no on site interaction U will be included. By Fourier transforming this last term one obtains

$$\mathcal{H}_{int} = V \sum_{\mathbf{q},\mathbf{k},\mathbf{k}'} \gamma_{\mathbf{q}} a^\dagger_{\mathbf{k}} a_{\mathbf{k}-\mathbf{q}} b^\dagger_{\mathbf{k}'} b_{\mathbf{k}'+\mathbf{q}} + h.c. \tag{4.6}$$

As argued above, to solve this Hamiltonian under a variational mean field approach it is necessary to come up with a mean field Hamiltonian *ansatz* $\mathcal{H}_{MF}$. We might choose it of the form

$$\mathcal{H}_{MF} = \mathcal{H}_{TB} + V \sum_{\mathbf{k}} \psi^\dagger_{\mathbf{k}} \boldsymbol{\sigma} \cdot \boldsymbol{\Delta}_{\mathbf{k}} \psi_{\mathbf{k}} \tag{4.7}$$

Here $\boldsymbol{\sigma} = (\sigma_x, \sigma_y)$ and $\boldsymbol{\Delta}_{\mathbf{k}} = (\mathrm{Re}(\Delta_{\mathbf{k}}), \mathrm{Im}(\Delta_{\mathbf{k}}))$ are the parameters that characterize $\mathcal{H}_{MF}$. Note that this particular form of the mean field Hamiltonian is already disregarding some possible phases such as a superconducting phase or a charge density waves. The system shall realize the allowed phase with lowest free energy. In addition, since the momentum dependence of the proposed mean field Hamiltonian satisfies that $\mathcal{H}_{MF}(\mathbf{k}) = \mathcal{H}_{MF}(\mathbf{k}+\mathbf{G})$, where $\mathbf{G}$ is a vector of the reciprocal lattice, the order parameter $\Delta_{\mathbf{k}}$ must fulfil $\Delta_{\mathbf{k}} = \Delta_{\mathbf{k}+\mathbf{G}}$. Thus, the $\Delta_{\mathbf{k}}$ can be decomposed into

$$\Delta_{\mathbf{k}} = \xi_1 + \xi_2 e^{i\mathbf{a}_1\mathbf{k}} + \xi_3 e^{i\mathbf{a}_2\mathbf{k}}. \tag{4.8}$$

Transforming back to real space or by direct comparison with $\gamma_{\mathbf{k}}$ in (4.4), it is not difficult to understand the physical meaning of the (possibly complex) parameters $\{\xi_i\}$ to be determined by solving the mean field equations. They correspond to each of the three hopping amplitudes that stem from each site and thus correct the value of t in each direction.
In the variational approach the functional $F[\xi_i]$ defined by inserting (4.7) in (4.3) is minimized with respect to $\{\xi_i\}$ at a given point in (V, n) space where n is the electronic density which is fixed by Luttinger's theorem [164]. This will define a set of mean field equations, one for each parameter ξ_i, and their solution will result in the phase diagram of the model in the mentioned (V, n) space.
To derive the mean field equations one imposes that $\delta F[\xi_i] = 0$. Although the procedure is straight forward we leave the detailed derivation for the appendix B.1.1. For this case the mean field equation reads

$$\Delta_{\mathbf{k}} = -\frac{2}{N} \sum_{\mathbf{k}'} \gamma_{\mathbf{k}-\mathbf{k}'} \left\langle b^\dagger_{\mathbf{k}'} a_{\mathbf{k}'} \right\rangle_{MF}, \tag{4.9}$$

where N is the number of unit cells. As explicitly shown in appendix B.1.1, and consistent with the assumptions encoded in the mean field Hamiltonian (4.7), in the derivation of such mean field equations we only keep terms which are hopping-like decouplings that are proportional to $\langle b_{\mathbf{k}}^{\dagger} a_{\mathbf{k}} \rangle_{MF}$. The discussion of the effect of different decouplings (that allow for example charge density waves) is left for section 4.4.

Considering the functional form (4.8) of $\Delta_{\mathbf{k}}$ it is possible to split this equation into three momentum independent mean field equations which, using a compact notation, can be written as

$$\xi_i = -\frac{2}{N} \sum_{\mathbf{k}} \gamma_{\mathbf{k}}^{(i)} \left\langle b_{\mathbf{k}}^{\dagger} a_{\mathbf{k}} \right\rangle_{MF} \tag{4.10}$$

as long as we define $\gamma_k^{(i)} = (1, e^{-i\mathbf{k}\cdot\mathbf{a}_1}, e^{-i\mathbf{k}\cdot\mathbf{a}_2})$. Calculating the complex parameters ξ_i permits to distinguish between different phases. The symmetric phase is a situation where $\xi_1 = \xi_2 = \xi_3$, which is an homogeneous renormalization of the hoppings and thus all the symmetries of the band structure remain unchanged. The uniaxial phase, which we will define latter as a Pomeranchuk phase, has two equal hoppings different from the third (e.g. $\xi_1 = \xi_2 \neq \xi_3$). As will be explicit below, in this case the final Fermi surface will have a different symmetry compared to that of the non interacting system. Trivially, there is also a phase where all hoppings are different that one can label as a reduced symmetry phase. Note that, if these hoppings were to develop an imaginary part, the time reversal symmetry ($\mathcal{T}$) would be broken.

To solve the mean field equation it is necessary to calculate $\langle b_{\mathbf{k}}^{\dagger} a_{\mathbf{k}} \rangle_{MF}$. To do so one can introduce a unitary transformation which diagonalizes the Hamiltonian

$$\mathcal{U}^{\dagger} \mathcal{H}_{MF} \mathcal{U} = \sum_{\mathbf{k}} \sum_{\alpha=\pm} \varepsilon_{\alpha}(\mathbf{k}) c_{\mathbf{k},\alpha}^{\dagger} c_{\mathbf{k},\alpha} \tag{4.11}$$

The matrix $\mathcal{U}$ relates the operators a, b with $c_{\pm}$ through $a_{\mathbf{k}} = \frac{1}{\sqrt{2}} \frac{\tilde{\gamma}_{\mathbf{k}}}{|\tilde{\gamma}_{\mathbf{k}}|} (c_{\mathbf{k},+} - c_{\mathbf{k},-})$ and $b_{\mathbf{k}} = \frac{1}{\sqrt{2}} (c_{\mathbf{k},+} + c_{\mathbf{k},-})$ where $\tilde{\gamma}_{\mathbf{k}'} \equiv -t\gamma_{\mathbf{k}} + V\Delta_{\mathbf{k}}$. Finally, we obtain

$$\left\langle b_{\mathbf{k}}^{\dagger} a_{\mathbf{k}} \right\rangle_{MF} = \frac{1}{2} \frac{\tilde{\gamma}_{\mathbf{k}}}{|\tilde{\gamma}_{\mathbf{k}}|} (n_f[\varepsilon_{\mathbf{k},+}, \mu] - n_f[\varepsilon_{\mathbf{k},-}, \mu]), \tag{4.12}$$

where $n_f[\varepsilon_{\mathbf{k},\alpha}, \mu]$ is the Fermi distribution function for the band $\alpha = \pm$. Substituting this last result into (4.10) the mean field equation takes the form

$$\xi_i = -\frac{1}{N} \sum_{\mathbf{k}} \gamma_k^{(i)} \frac{\tilde{\gamma}_{\mathbf{k}}}{|\tilde{\gamma}_{\mathbf{k}}|} (n_f[\varepsilon_{\mathbf{k},+}, \mu] - n_f[\varepsilon_{\mathbf{k},-}, \mu]), \tag{4.13}$$

This equation is to be solved self consistently. Luttinger's theorem [164] imposes that the number of particles is conserved in each step which fixes the chemical potential through the equation (up to logarithmic corrections)

$$1 + n = \frac{1}{N} \sum_{\mathbf{k},\pm} n_f[\varepsilon_{\mathbf{k},\pm} \mu] \tag{4.14}$$

where $n = \frac{N_e}{N}$ is the density of electrons and half filling is defined to be at $n = 0$. This establishes the procedure to follow. At a certain (V, n) one fixes a starting $\mathcal{H}_{MF}$ defined through the initial $\xi_i^{(0)}$, fixing the chemical potential through (4.14). Then the new parameters are calculated using (4.13) and inserted back in $\mathcal{H}_{MF}$. This self consistent procedure is carried out until convergence is achieved. The final parameters ξ_i^f are interpreted as the correction to t, the hopping, for each neighbouring carbon atom thus identifying the phase.

The phase diagram resulting from solving eq. (4.9) is shown in Fig. 4.2 (a). The first thing to note is that at all points in the (V, n) diagram the hoppings $\{\xi_i\}$ turn out to be real so there are no $\mathcal{T}$ breaking phases. From the van Hove filling $n \sim 0.25$ a Pomeranchuk phase appears. As discussed above, the Pomeranchuk instability has its origin in the divergent density of states at this filling. As we move away from the van Hove filling to a region with a finite density of states, a finite interaction V is needed to activate the phase. A typical Fermi surface for the Pomeranchuk phase together with the band structure is depicted in Fig. 4.2 (c) which should be compared with the non interacting case in Fig. 4.2 (b). The breaking of the point group C_6 to a C_2 symmetry is clearly apparent in the Fermi surface shown in Fig. 4.2 (c). This phase is characterized by two hoppings that are equal and thus it can be though of as a uniaxial (or nematic) distortion of the hoppings along a certain direction (see the hopping structure in the inset of Fig. 4.2 (a)). This distortion deforms the underlying band structure, and in particular, the Fermi surface, changing its symmetry and defining the Pomeranchuk phase.

As we will now argue, when translational symmetry is relaxed to contain six atoms per unit cell novel phases shall appear enriching the phase diagram. This will enable us to obtain novel time reversal breaking topological phases analogous to the Haldane phase but with only nearest neighbour hoppings.

4.3. Variational mean field for graphene with a tripled unit cell

Now that we have illustrated the method and some particulars of the calculation we can introduce the main point of the chapter which is the use of the variational mean field method to allow phases that have translational symmetry with an enlarged unit cell which has six atoms i.e. it is three times larger than in conventional treatments of graphene. From this approach one may or may not recover the two atom unit cell case of 4.2 since novel phases might appear.

For example, one new allowed phase is the Kekulé phase shown in Fig. 4.3 (b) which cannot be fitted inside a two atom unit cell. The uniaxial distortion, i.e. the Pomeranchuk phase obtained previously and shown in Fig. 4.3 (a) can also be described in this larger unit cell and so, in the following, these and other phases will compete to enrich the phase diagram

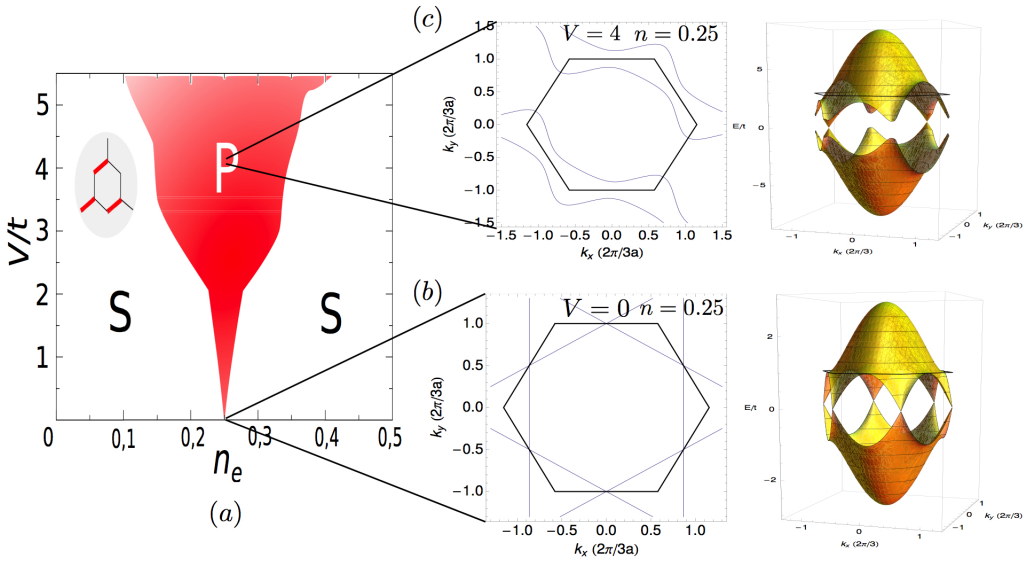

Figure 4.2.: (a) Phase diagram obtained from a nearest neighbours Coulomb interaction in the doped honeycomb lattice using a 100x100 mesh for the Brillouin zone. The inset in (a) shows one of the three degenerate hopping configuration of the Pomeranchuk phase that resembles a uniaxial distortion that has $\xi_1 \neq \xi_2 = \xi_3$. The symmetric phase has $\xi_1 = \xi_2 = \xi_3$. Figure (b) shows the unperturbed Fermi surface and band structure at the van Hove filling with the chemical potential denoted by a black line that intersects the band structure. Figure (c) show a typical Fermi surface and band structure at the Van Hove filling $n = 0.25$ for the Pomeranchuk phase. In this case, the black line in the band structure corresponds to the renormalized chemical potential resulting from solving the mean field equations.

of Fig. 4.2 and realize time reversal breaking topological phases.

To obtain the phase diagram from the variational method we need to propose a mean field Hamiltonian. As before we will consider spinless fermions, and, aiming for electronic topological phases, we will also neglect possible charge density wave orders, i.e. possible charge imbalance between the six sites of the enlarged unit cell. The effect of allowing for charge density wave order, spin wave order, as well as other mean field decouplings on the mean field *ansatz* will be discussed in section 4.4, after we have established the phase diagram.

Within these assumptions and with a two atom unit cell, the most general mean field Hamiltonian has three parameters corresponding to the three hoppings to nearest neighbouring atoms. With a tripled unit cell there are six atoms and nine independent hoppings which correspond to nine independent order parameters $\{\xi_i\}$ shown in Fig. 4.3 (c).

We start with the extended Hubbard Hamiltonian for spinless fermions in the honeycomb lattice

$$H = -t\sum_{\mathbf{r},\boldsymbol{\delta}} a^\dagger_{\mathbf{r}} b_{\mathbf{r}+\boldsymbol{\delta}} + V\sum_{\mathbf{r},\boldsymbol{\delta}} a^\dagger_{\mathbf{r}} a_{\mathbf{r}} b^\dagger_{\mathbf{r}+\boldsymbol{\delta}} b_{\mathbf{r}+\boldsymbol{\delta}} + h.c., \tag{4.15}$$

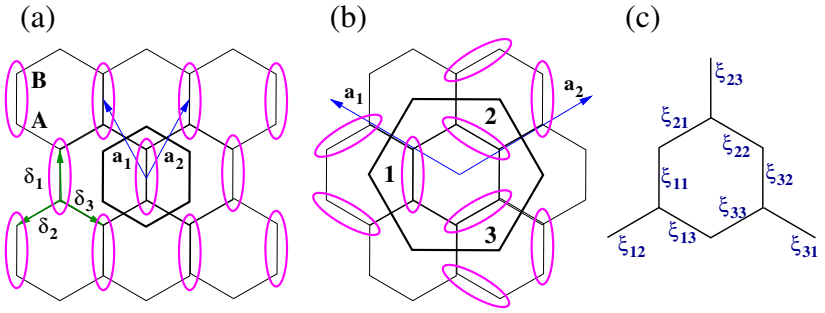

Figure 4.3.: (a) Two-atom unit cell and an example of uniaxial distortion. The links enclosed by a circle are bigger (or smaller) than the rest. (b) Six atom unit cell and Kekulé distortion, allowed in the enlarged unit cell. (c) A pictorial representation of the nine complex order parameters considered in the mean field decoupling of the Hamiltonian.

where t is the nearest neighbor hopping and V the nearest neighbor Coulomb repulsion. The vectors $\boldsymbol{\delta}$ refer to the three vectors connecting nearest neighbor sites, as shown in Fig. 4.3(a). The basis vectors of the enlarged cell in real space are $\mathbf{a}_1 = \frac{3a}{2}(-\sqrt{3}, 1)$ and $\mathbf{a}_2 = \frac{3a}{2}(\sqrt{3}, 1)$ (see Fig. 4.3 (b)), and the respective unit cell vectors in reciprocal space are $\mathbf{b}_1 = \frac{2\pi}{3\sqrt{3}a}(-1, \sqrt{3})$ and $\mathbf{b}_2 = \frac{2\pi}{3\sqrt{3}a}(1, \sqrt{3})$. With this choice the unit cell in direct space is three times bigger while in reciprocal space the Brillouin zone becomes folded, i.e. it is three times smaller. The tight binding model now is defined in terms of a wave function which is a six component spinor of the form

$$\psi^\dagger_{\mathbf{k}} = [a^\dagger_1(\mathbf{k}), b^\dagger_1(\mathbf{k}), a^\dagger_2(\mathbf{k}), b^\dagger_2(\mathbf{k}), a^\dagger_3(\mathbf{k}), b^\dagger_3(\mathbf{k})], \tag{4.16}$$

in contrast with the usual two component wave function used to describe graphene. In analogy with the two atoms per unit cell case, we label the nine complex parameters as ξ_{ij} and we group them in a 3×3 matrix instead. The explicit form of the variational mean field ansatz $\mathcal{H}_{MF}$ can be found in appendix B.1.2.

An analogous calculation as the one described in appendices B.1.1 and B.1.2, shows that the mean field equations can be written in terms of the mean field averages of the form $\langle b^\dagger_j(\mathbf{k}) a_i(\mathbf{k})\rangle_{MF}$ as

$$\xi_{ij} = -\frac{2}{N}\sum_{\mathbf{k}} \gamma^{ij}_{\mathbf{k}} \langle b^\dagger_j(\mathbf{k}) a_i(\mathbf{k})\rangle_{MF}, \tag{4.17}$$

where N is the number of unit cells, $\gamma_{\mathbf{k}}$ is a 3×3 matrix given by

$$\gamma_{\mathbf{k}} = \begin{bmatrix} 1 & e^{-i\mathbf{a}_2\cdot\mathbf{k}} & 1 \\ 1 & 1 & e^{i(\mathbf{a}_1+\mathbf{a}_2)\cdot\mathbf{k}} \\ e^{-i\mathbf{a}_1\cdot\mathbf{k}} & 1 & 1 \end{bmatrix},$$

and the momentum sum runs over the folded Brillouin zone. As in the previous section, the derivation of these equations only includes hopping-like terms proportional to $\langle b^\dagger_j(\mathbf{k}) a_i(\mathbf{k})\rangle_{MF}$

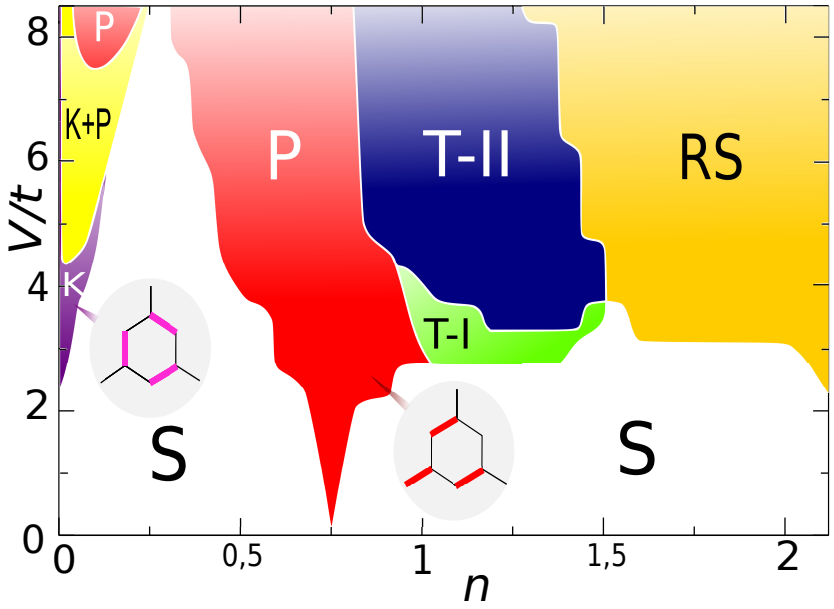

Figure 4.4.: Mean field phase diagram of the tripled unit cell system. Legend: (S) symmetric phase, i.e. bare graphene with a uniform renormalization of the hopping; (K) Kekulé distortion with hopping renormalization as shown in the inset; (P) Pomeranchuk (uniaxial) distortion of the Fermi surface and hopping renormalization as shown in the inset; (K+P) coexistence of Kekulé and Pomeranchuk distortions; (T-I) and (T-II) anomalous Hall phases discussed at length in the text; (RS) broken symmetry state with real hopping parameters, the distortion is neither Kekulé type nor Pomeranchuk (reduced symmetry).

(see appendix B.1.1).

The procedure to solve the equations (4.17) is analogous to the one presented above. This time, the unitary transformation used to calculate $\langle b_j^\dagger(\mathbf{k})a_i(\mathbf{k})\rangle_{MF}$ is not analytic, but otherwise the procedure is exactly the same. That being said we now proceed to discuss the resulting phase diagram.

4.3.1. Phase diagram

The phase diagram arising from the solution to (4.17) is shown in Fig. 4.4. The Kekulé like distortion, shown in the left inset of Fig. 4.4, appears close to the neutrality point $n = 0$ [2] with three electrons per unit cell. This result is in fact in agreement with a previously reported mean field treatment in Ref. [167] that also suggests that only at a finite V this phase can appear at half filling.

As we increase n we find that the Pomeranchuk phase (a uniaxial distortion in real space)

[2] We choose $n = 0$ to be the half-filled lattice as in the two atom per unit cell case. In the folded case, for $n = 0$ there are three electrons per unit cell.

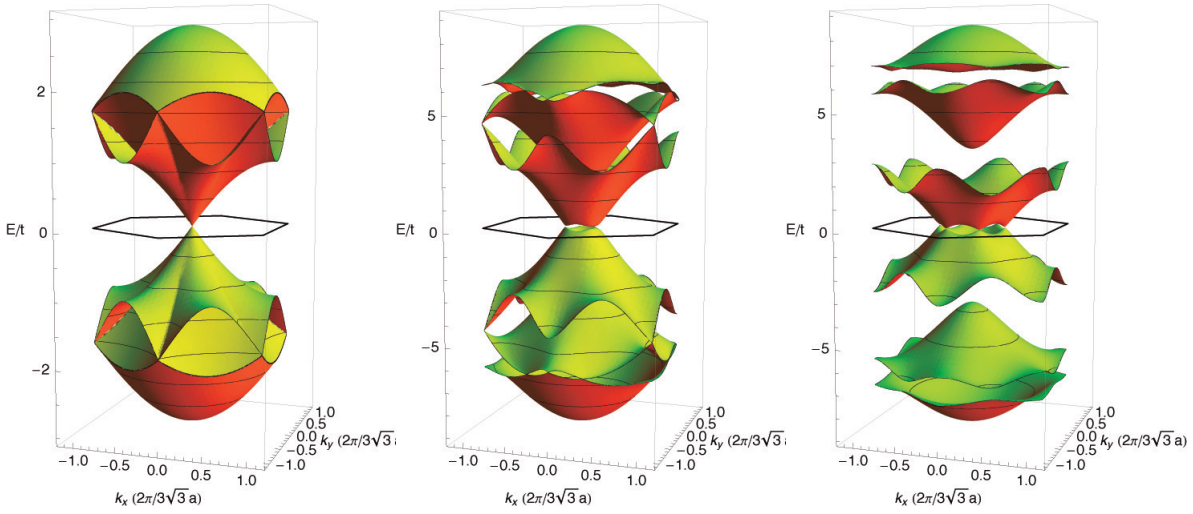

(a) (b) (c)

Figure 4.5.: (a) Folded band structure for the case without interactions ($V = 0$) and a typical band structure for the two $\mathcal{T}$-breaking phases (b) T-I and (c) T-II.

appears close to the van Hove filling, with a coexistence region at intermediate fillings. This nicely recovers the result of the previous section regarding the unfolded case acting as a consistency check, as well as indicating that it is hard, at least with spinless fermions, to remove such a phase near the van Hove filling.
The main result of this chapter is the appearance of the T-I and T-II phases, to be discussed shortly. The other phases that are realized are the symmetric phase which is, as before, an equal correction to all of the hoppings and a reduced symmetry phase that cannot be associated to none of the above with apparently uncorrelated hoppings.
We now proceed to discuss in detail the novel phases labelled T-I and T-II.

T-I phase

This phase is the first of the two time reversal breaking phases that appear in the phase diagram. The exact pattern of hoppings inside the unit cell is shown in Fig. 4.6 (a) where the arrows indicate the sign of the phase of the hopping in the case where it is complex and the thickness indicates its modulus. The first thing we might notice is the emerging Kekulé pattern that is realized on top of the complex hoppings. In addition it is not difficult to see either by direct inspection of the hoppings or by mathematically applying discrete symmetry operations to the Hamiltonian that this phase breaks both time reversal $\mathcal{T}$ and spatial inversion $\mathcal{I}$ but preserves its product $\mathcal{TI}$. As we will discuss in the next section,

this shall imply that the Hall conductivity is zero in this phase and thus it is topologically trivial. Before that, consider a typical band structure corresponding to this phase, shown in Fig. 4.5 (b), that should be compared to the non-interacting folded band structure in Fig. 4.5 (a). Firstly note that, before considering interactions, folding the two original graphene bands into a Brillouin zone which is three times smaller produces a total of six bands and the two Dirac K and K' points fold into the Γ point. In the T-I phase, no gap opens, since the invariance of the Hamiltonian under the combined symmetry $\mathcal{TI}$ prevents the opening of a gap [24] which is confirmed by inspecting Fig. 4.5 (b). This however, is not the case of the following phase.

T-II phase

As with the T-I phase the T-II phase breaks time reversal symmetry through the realization of the pattern of complex hoppings shown in Fig. 4.6 (b). The moduli of these hoppings also follows a Kekulé-like pattern although this time the phase breaks time reversal $\mathcal{T}$ but preserves inversion $\mathcal{I}$ without being invariant under $\mathcal{TI}$. A typical band structure for this phase is shown in Fig. 4.5 (c) showing explicitly that in the absence of $\mathcal{TI}$ gaps can open at Γ. Therefore and in sharp contrast with the above phase, the Hall conductivity can be generically non-zero in this phase and we shall therefore classify it as topological under the considerations we will discuss in the next section.
This phase appears close to $n = 1$, a commensurate filling which allows an intuitive interpretation of such phase. At this filling we fill the six lattice sites with four particles. At strong V this state can be thought to appear to minimize nearest neighbour interaction energy. Since the system is in this sense frustrated (one has to pay at least V to fit four particles in six sites), it can resonate between different states, and thus as soon as some kinetic energy is present, and the current loops in Fig. 4.6 (b) appear.
Note also from Fig. 4.6 (b) that such current loops are connected by real hoppings. It is possible to see directly from the numerical mean field solution, that as one increases V, the real hoppings are suppressed and the current loops become increasingly isolated. It is tentative to say that this could lead eventually to localized currents and thus perhaps topological flat bands. However it is easy to see that in that case these bands have necessarily Chern number zero. This topological phase transition, which closes and opens the gap, can be expected from the fact that a finite Chern number cannot arise from completely localized wave functions [168, 169]. If present, this trivial current loop phase is expected to be closely confined to $n \sim 1$ since it is this commensurate filling that favours the formation of self consistent current loops at strong coupling.

These two time reversal broken phases are the only independent phases which can appear

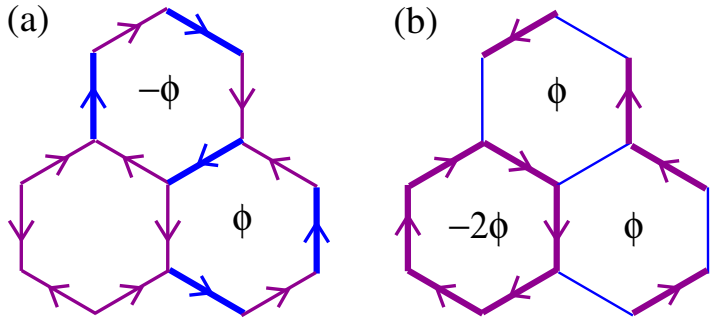

Figure 4.6.: Schematic representation of the order parameters corresponding to the $\mathcal{T}$ broken phases T-I (a) and T-II (b) discussed in the text. The thickness of the bonds represent the modulus of the hopping parameter and the direction of the arrows represents the sign of the phase when it has a complex value. A bond without an arrow means a real hopping.

given current conservation at each vertex and zero flux over the unit cell [3]. In what follows we will characterize them further by studying their Hall conductivity and band structure to which we will relate topological properties that will serve to classify them. To end this section, we will discuss the nature of the phase transitions to these topological phases.

4.3.2. Hall conductivity

To calculate the Hall conductivity we now recall that, in section 1.2.1, the intrinsic Hall conductivity of a band system was rewritten, from the usual Kubo formula, in terms of the topological properties of the wave function, namely the Berry connection and the Berry curvature [55, 57]. The exact expression is

$$\sigma^{xy}(\mu) = \frac{e^2}{\hbar}\frac{1}{N\mathcal{V}}\sum_{k,m}\Omega_m^{xy}(\mathbf{k})n_F[\varepsilon_m(\mathbf{k}),\mu], \tag{4.18}$$

where $\mathcal{V}$ is the volume of the unit cell, m is the band index and $\Omega_m^{ab}(\mathbf{k}) = \nabla_k^a\mathcal{A}_m^b(\mathbf{k}) - \nabla_k^b\mathcal{A}_m^a(\mathbf{k})$ is the Berry curvature for band m defined from the Berry connection $\mathcal{A}_m^a(\mathbf{k}) = -i\left\langle\Psi_m(\mathbf{k})|\nabla_{\mathbf{k}}^a\Psi_m(\mathbf{k})\right\rangle$. Thus, in this context, topological phases are those which allow this quantity to be non zero. It can be shown generically that the Hall conductivity (4.18) has a quantized contribution independent of the chemical potential, the Chern number, and a non quantized, or anomalous contribution arising from filling a topologically non trivial band [55] a fact that we will later encounter explicitly.

From section 1.2.1 we also recall the table summarizes the conditions imposed to the Berry curvature and the Hall conductivity whenever the Hamiltonian has either time reversal, inversion symmetry or a combination of both

[3] For similar time reversal breaking phases in the context of high-T_c cuprates see [170]

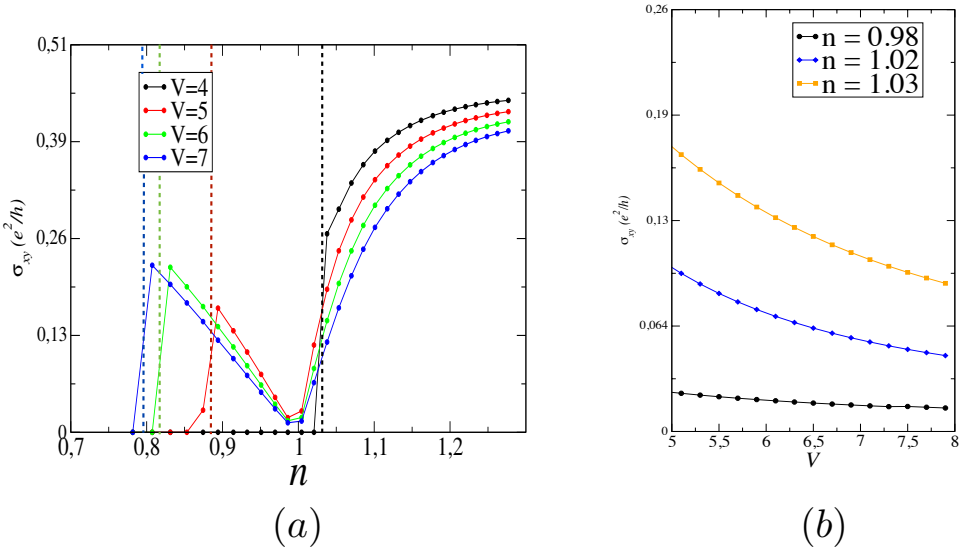

Figure 4.7.: (a) Hall conductivity as a function of n for different values of V. The vertical lines indicate the transition from a trivial phase to the topological phase with finite Hall conductivity. (b) Hall conductivity as a function of V for different values of n.

Symmetry	Berry Phase	σ_{xy}
$\mathcal{T}$	$\boldsymbol{\Omega}_n(\mathbf{k}) = -\boldsymbol{\Omega}_n(-\mathbf{k})$	0
$\mathcal{I}$	$\boldsymbol{\Omega}_n(\mathbf{k}) = \boldsymbol{\Omega}_n(-\mathbf{k})$	non-zero*
$\mathcal{TI}$	$\boldsymbol{\Omega}_n(\mathbf{k}) = -\boldsymbol{\Omega}_n(\mathbf{k}) = 0$	0

Applying these analysis to the phases described earlier it is now clear why the T-I phase has $\sigma_{xy} = 0$. Despite breaking time reversal symmetry $\mathcal{T}$ and inversion $\mathcal{I}$ it preserves its product $\mathcal{TI}$ implying $\sigma_{xy} = 0$. On the other hand the T-II phase only preserves inversion, and thus it might have a non-zero Hall conductivity which is calculated using (4.18). The integral might still be zero at some particular fillings (which is denoted by the asterisk in the above table) but for arbitrary filling it is generically non-zero. In this sense, T-I is topologically trivial while T-II is not. All of the other phases of Fig. 4.4 do not break time reversal symmetry and thus have $\sigma_{xy} = 0$, i.e. they are topologically trivial.

To test this analysis it is possible to calculate numerically the Hall conductivity for each phase by the use of (4.18). To this extent we choose cuts in the phase diagram of Fig. 4.4 at constant V (n) and calculate the Hall conductivity as a function of n (V). This is shown in Fig 4.7. Consider first a cut along constant V shown in Fig. 4.7 (a). For $V = 5, 6, 7$ as we increase n we intersect the Pomeranchuk and then the T-II phases. For $V = 4$ also the T-I phase is crossed (see Fig. 4.4). Inside the Pomeranchuk phase and from the table presented above, the Hall conductivity is zero since these phase is, in real space, a uniaxial distortion with real hoppings that preserves time reversal symmetry consistent with the numerics. As

soon as we increase n to enter T-II the Hall conductivity is finite and non quantized, given by the anomalous contribution of the fourth band which evolves with n. The phase transition between zero and finite Hall conductivity for each V is represented by the vertical dashed line in Fig 4.7 (a).

To interpret the results inside the T-II phase it might be tentative to think in terms of a fixed band structure that is filled as we increase n but this is not correct, since both the band structure and the (final) chemical potential are modified as one increases n and calculates the new ground state. Nevertheless, the form of Fig. 4.7 (a) admits an interpretation in terms of the Hall conductivity arising from filling the Dirac cone between bands four and five of Fig. 4.5 (c). We again emphasize that since the bands change this is not exactly so for Fig. 4.7 (a), but close to the commensurate filling $n \gtrsim 1$, for each (V, n) it is possible to check that the obtained Hall conductivity corresponds to

$$\sigma_{xy} = \frac{e^2}{2h} \frac{M(n,V)}{|\tilde{\mu}(n,V)|}, \tag{4.19}$$

where $M(n,V)$ is the gap at the Γ point between bands four and five and $\tilde{\mu}(n,V)$ is the renormalized chemical potential relative to the middle of the gap, both of which depend strongly on the parameters of the phase diagram.
As we will discuss in chapter 6, the form (4.19) corresponds to the non quantized part of the anomalous Hall conductivity of a Dirac cone filled up to a chemical potential $\tilde{\mu}(n,V)$.
In fact, it is possible to calculate the Chern number of the bands corresponding to the T-II phase in Fig. 4.5 (c) that are, from top to bottom $C = 1, -1, 0, 0, -1, 1$ by using expression (1.11) which is nothing but (4.18) for each filled band. When the chemical potential falls inside a band gap, the quantized Hall conductivity is given by the sum of the Chern numbers of the filled bands. Thus the gap between the fourth and fifth bands has a quantized response of $\sum_i^{i_{max}} C_i = -1 + 1 + 0 + 0 = 0$, explaining the dip in Fig. 4.7 (a) and the later increase.
As a final remark for this plot, note that at $V = 4$ (the black curve in Fig. 4.7 (a)) the Hall conductivity also crosses the T-I phase, which has, as predicted by the symmetry analysis, $\sigma_{xy} = 0$.

Lastly, in Fig. 4.7 (b) the Hall conductivity is shown for a fixed n as a function of V. This gives insight of how the chemical potential behaves in this phase. Modifying (4.19) to include the quantized part [55] we have that $\sigma_{xy} = \frac{e^2}{2h}\left(\frac{M(n,V)}{|\tilde{\mu}(n,V)|} - 1\right)$ where the -1 is the quantized part, that takes into account that the Hall conductivity vanishes between bands four and five. At fixed V it is easy to see that the gap $M(n,V)$ increases with V. If we take $\tilde{\mu} \sim M + x$ where x is a small finite filling of the fifth band, $\sigma_{xy} \sim \frac{e^2}{2h}\frac{x}{\tilde{\mu}}$ and thus since the conductivity decreases with V, the filling of the band increases slower than the chemical potential which can be traced back to the bands getting flatter as V increases.

To summarize this section, we have found the variational mean field phase diagram for the doped honeycomb lattice filled with spinless fermions allowing for hopping-like decouplings. We have found, among various phases consistent with other works [165, 167], two novel phases that break time reversal symmetry. One of them, the T-II phase, is a topologically non trivial phase where some of its bands have acquired a non zero Chern number which endows the system with a finite Hall conductivity for a generic value of the electronic density n and interaction V. At the commensurate filling $n \sim 1$ the system is insulating and has a vanishing Hall conductivity due to the cancellation of Chern numbers of the filled bands below the chemical potential.
These results, provide a way of realizing topological phases in lattice systems. Nevertheless, they might still not be realized since neither spin, nor charge density wave ordering has been taken into account. The effects of such perturbations are discussed in the following sections, but before including these, we briefly comment on the order of the relevant phase transitions.

4.3.3. Order of the phase transitions

We conclude this section with a preliminary analysis of the order of the phase transitions in the phase diagram of Fig. 4.4 delimiting the topological phases. We will study therefore phase transitions between the T-I, T-II and Pomeranchuk phase.
It is possible to study the order of a phase transition by studying the behaviour of the free energy as one varies the electron density for each phase. A crossing between two phases will be an indication of a first order phase transition, while a continuous evolution of one phase into the other will be reminiscent of a second order phase transition. The numerical study of the free energy for each phase shows that all the transitions are of first order (for the Pomeranchuk to T-II, T-I to T-II and Pomeranchuk to T-I phase transitions, see appendix B.2).
In order to get a further insight, we will introduce Maxwell's construction as a tool to study first order phase transitions [41, 171, 172] based on constraints regarding the stability of the different phases that manifest themselves through jumps or crossings in the different thermodynamical potentials. A prototypical example is the first order liquid-vapour phase transition where the pressure-volume diagram, which in our case will translate into a chemical potential μ versus density n diagram, has a region of instability which the system avoids by separating into two coexisting phases.
In our case, as shown in the appendix B.2, there exist a region of phase separation that modifies the phase diagram of Fig. 4.4 and transforms it into the phase diagram shown in Fig. 4.8 . The border of the phase separation region indicates what are the densities of the two phases at the coexisting scenario. It is interesting to note that on the time reversal breaking side of the separation, the density is very close to the commensurate one $n \sim 1$. This seems to indicate, consistent with the semi-classical arguments of the above section, that below the

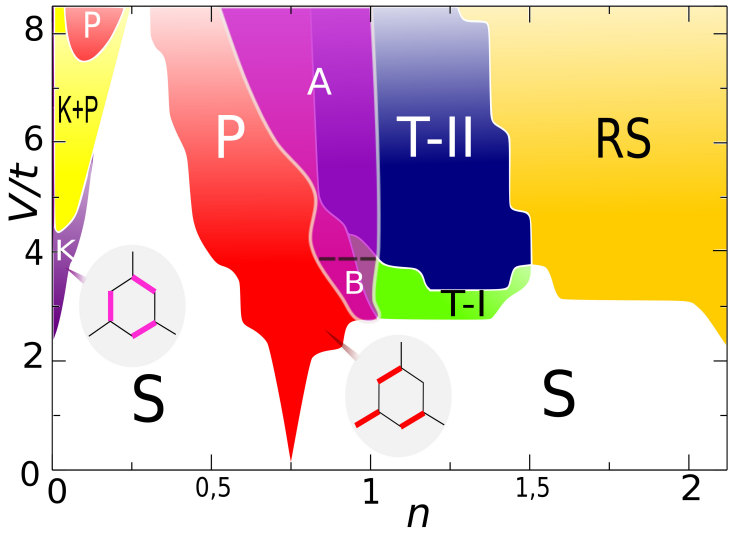

Figure 4.8.: Mean field phase diagram of the tripled unit cell system including phase separation. Region A indicates that the phase separation involves the Pomeranchuk phase and the T-II phase while region B involves the Pomeranchuk phase and the T-I phase.

commensurate filling the formation of the self consistent current loops is not possible.

4.4. Discussion

In this section we will briefly discuss how further mean field decouplings might change the picture presented in the previous analysis.

4.4.1. Charge decoupling and second nearest neighbour interaction

In what follows, we include possible charge density wave order and investigate its effect on the time reversal breaking phases T-I and T-II. Anticipating the result, we will see that these phases are washed out by such ordering to appear again if a finite next to nearest neighbour interaction (V') is included. Therefore, our starting point is the Hamiltonian

$$H = -t\sum_{\langle ij\rangle} c_i^\dagger c_j + V\sum_{\langle ij\rangle} n_i n_j + V'\sum_{\langle\langle ij\rangle\rangle} n_i n_j. \tag{4.20}$$

As usual $\langle\cdots\rangle$ and $\langle\langle\cdots\rangle\rangle$ represent summation over nearest and next nearest neighbours respectively. To derive the mean field equations, we choose a mean field Hamiltonian which includes the nine ξ_{ij} terms of the form $\langle b_j^\dagger(\mathbf{k})a_i(\mathbf{k})\rangle_{MF}$. The charge density order is taken into account by allowing in the mean field Hamiltonian terms proportional to $\langle a_i^\dagger(\mathbf{k})a_i(\mathbf{k})\rangle_{MF}$ and $\langle b_i^\dagger(\mathbf{k})b_i(\mathbf{k})\rangle_{MF}$ where $i = 1,2,3$. The coefficients i.e. the order parameters, that appear in front of such terms are the densities at each lattice site in the unit cell ρ_i^A, ρ_i^B with $i =$

1, 2, 3. Due to charge conservation, only 5 out of the six parameters are independent. In addition, we include the next to nearest neighbours mean field decoupling. In analogy to the nearest neighbours, these represent corrections to the second neighbours hoppings and are parametrized by two 3×3 matrices, $\chi_{ij}^{A,\delta}$ and $\chi_{ij}^{B,\delta}$ which are corrections in the A and B sublattices respectively. The indices ij indicate which two atoms are connected and $\delta = u, d, h$ runs over the upper, lower and horizontal next nearest neighbours.

Once the mean field Hamiltonian is set and using the variational mean field approach in analogy with the above analysis one finds the mean field equations which read

$$\xi_{ij} = -\frac{V}{N}\sum_{\mathbf{k}} \gamma_{\mathbf{k}}^{ij} \langle b_j^\dagger(\mathbf{k}) a_i(\mathbf{k})\rangle_{MF}, \tag{4.21}$$

$$\chi_{ij}^{A,\delta} = -\frac{V'}{N}\sum_{\mathbf{k}} \lambda_{\mathbf{k},ij}^{A,\delta} \langle a_j^\dagger(\mathbf{k}) a_i(\mathbf{k})\rangle_{MF}, \tag{4.22}$$

$$\chi_{ij}^{B,\delta} = -\frac{V'}{N}\sum_{\mathbf{k}} \lambda_{\mathbf{k},ij}^{B,\delta} \langle b_j^\dagger(\mathbf{k}) b_i(\mathbf{k})\rangle_{MF}, \tag{4.23}$$

$$\rho_i^A = V n_B + 3V' n_A - 3V' n_i^A, \tag{4.24}$$

$$\rho_i^B = V n_A + 3V' n_B - 3V' n_i^B, \tag{4.25}$$

where $\lambda_{\mathbf{k},ij}^{A,\delta}$, $\lambda_{\mathbf{k},ij}^{B,\delta}$ are 3×3 matrices that take into account the phase factors in an analogous way as γ_k^{ij} defined in the same way as before, $n_i^c = \frac{1}{N}\sum_k \langle c_i^\dagger(\mathbf{k}) c_i(\mathbf{k})\rangle_{MF}$ and $n_c = \sum_{i=1}^3 n_i^c$ with $c = A, B$. Details of these matrices as well as the explicit form of $\mathcal{H}_{TB}$ are given in the appendix B.1.3.

Since we are interested on the fate of the T-I and T-II phases under these new possible orders, we solve the mean equations for the parameter space spanned by (V, V') f$n \sim 1$, the commensurate filling close to which these phases appeared. First, in Fig. 4.9 (a) the original mean field phase diagram with $V' = 0$ and no charge density wave order is compared with the $V' = 0$ including charge inhomogeneities Fig. 4.9 (b). Then a cut at $n \sim 1.2$ is taken to show the effect of V' on the T-II, T-I phases shown in Fig. 4.9 (c).

The first thing to notice is that the inclusion of charge order washes out both the Kekulé and the $\mathcal{T}$-broken phases in favour of a phase with charge modulation (CM) of the form $(\rho_1^A, \rho_1^B, \rho_2^A, \rho_2^B, \rho_3^A, \rho_3^B) = (\rho, -\rho, \rho, -\rho, \rho, -\rho)$, also known as a staggered potential in the graphene language. Remarkably, as shown in Fig. 4.9 (c) the $\mathcal{T}$-broken phases T-I and T-II are recovered for a finite next to nearest neighbours interaction $V' < V$.

Similar results where obtained in Ref. [161] where they analysed the same model at half filling and found time reversal broken phases in a region with V'>V. In our case the larger filling allows a new configuration of charge decoupling that favours the re-emergence of time reversal broken phases at more physical values of the interaction.

For $V' < V$ the appearance of such a staggered charge modulation can be understood from the fact that such a charge density wave can reduce the nearest neighbour hopping cost and thus minimizing the energy. When $V' > V$ it can be energetically more favourable to have

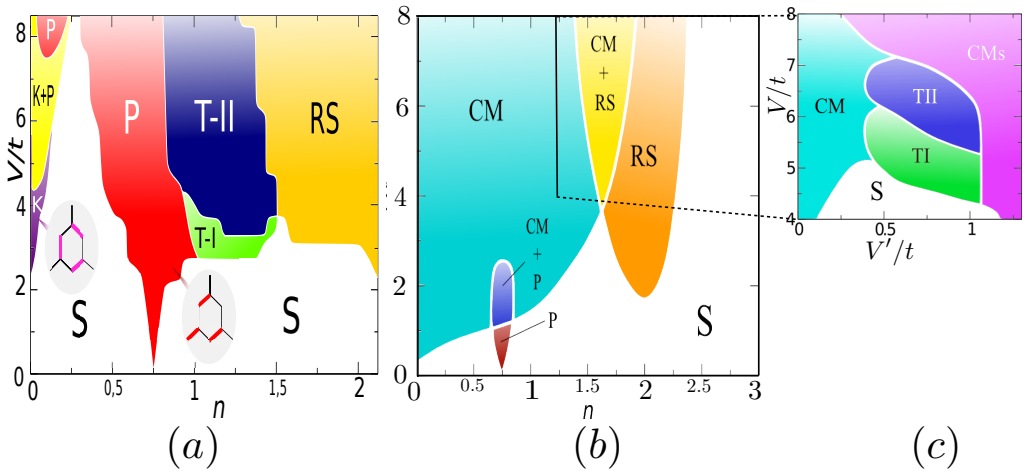

Figure 4.9.: (a) Phase diagram with only next nearest neighbour interaction V and no charge density wave order (b) The effect of including charge density order in the phase diagram (a). Legend: CM is the charge modulation phase described in the text, P is the Pomeranchuk phase, RS is a reduced symmetry phase and S is the symmetric phase. (c) Effect of V'. A cut along $n \sim 1.2$ is taken represented by the dashed line in (b) where CMs indicates a charge modulation within the sublattice.

similar charge modulation phase although with an additional modulation in the sublattice (CMs) where the density pattern is of the form $(\rho_1^A, \rho_1^B, \rho_2^A, \rho_2^B, \rho_3^A, \rho_3^B) = (\rho, -\rho, \rho, -\rho, -\rho - \Delta, \rho + \Delta)$. In this case it is energetically more favourable to sacrifice one of the dimers paying an amount proportional to V which can be compensated by the gain from the bigger next to nearest neighbour contribution V'.

Finally, the symmetries and band structure of the time reversal broken phases arising for a finite V' are similar to the ones discussed in the previous section. As an important difference, the commensurate filling $n \sim 1$ is not insulating. All the charge modulated phases encountered are metallic away from half filling.

4.4.2. Spinful fermions

A more realistic model for lattice fermions is to include possible spin orders. In this case one should introduce the leading on-site interaction, the Hubbard U. A complete analysis of this type including the possible spinful orders considered above becomes more cumbersome and so we will here try to gain perspective on the possible fate of the topological phases. Regarding the latter a generic intuition can be gained from Ref. [161]. In that case, the authors analyse the extended Hubbard model with U, V, and V' interactions at half filling. They allowed spin and charge density wave and searched for topological phases. The quantum

anomalous Hall phases that appeared in the spinless case were in that case substituted, in a very similar region of parameters by spin Hall phases, that carry a spin Hall conductivity $\sigma_s^{xy} = \sigma_\uparrow^{xy} - \sigma_\downarrow^{xy}$ as opposed to the Hall conductivity $\sigma_H^{xy} = \sigma_\uparrow^{xy} + \sigma_\downarrow^{xy}$ found in this chapter. These phases are also topologically non trivial and realize, at half filling, a time reversal invariant topological insulator.

Although an explicit calculation has to be performed for the model discussed in this chapter, the intuition gained from the above and similar examples [165, 173] suggests that the T-II phase might turn out to be a spin Hall phase carrying a finite spin Hall conductivity when the Hubbard U is included.

To conclude, it is interesting to note that other very recent works suggest the formation of an eight-atom unit cell spin density wave close to the van Hove filling ($n \sim 0.75$ in our notation) [174], or topological superconducting order exactly at $n \sim 0.75$ [173]. Whether or not these phases dominate close to $n \sim 1$ or rather a spin Hall effect is energetically more stable remains to be seen.

4.5. Conclusions

The main conclusion of this chapter is that non trivial topological phases can be spontaneously generated from interactions in systems of Dirac quasiparticles when translational symmetry is relaxed, i.e. when phases with enlarged unit cells are allowed. This simple conceptual element, the employment of enlarged unit cell, which certainly can be generalized to any lattice system, allows for novel structures of self consistent intra-cell current patterns emerging from interactions, and thus novel topological phases.

In more concrete terms, for the particular case of the honeycomb lattice we have used the variational mean field approach to spot the region in parameter space where non trivial topological phases occur. For the two atom unit cell, we argued that no topological phase can arise without including second nearest neighbour interactions V' to allow for the formation of the necessary self consistent current loops that break time reversal symmetry. Even including V', a larger second nearest neighbour interaction than the nearest neighbour interaction was needed to stabilize topological phases [161].

It was proven that allowing phases with tripled unit cells in a system of spinless fermions in the honeycomb lattice with only nearest neighbour hopping and interaction favours the emergence of two time reversal breaking phases emerge close to the commensurate filling with four atoms per unit cell. One of this phases constitutes an example of a topological Fermi liquid [55, 159] at fillings away from the commensurate filling. Exactly at $n \sim 1$, the system realizes spontaneously a topological insulator.

Charge density wave order washes out these topological phases that can be recovered by introducing a finite next to nearest neighbour interaction which need not be larger than the

nearest neighbour interaction, improving the physical scenario for the appearance of these phases compared to what was found in Ref. [161] (which was also constrained to half-filling). Nonetheless, the inclusion of U might drive the system to a spin Hall insulator, or to a spin density wave with enlarged unit cell in the spirit of [173].
As final remark, note that we have left out the possibility of superconducting phases out of this analysis. Very recently it was put forward that d-wave superconductivity could be realized at the van Hove filling $n \sim 0.75$ [173]. Considering superconducting order parameters embedded in enlarged unit cells might make novel topological superconducting phases emerge [9] opening new routes to realize these, sometimes elusive, phases of matter.

5. Fractional Hall effect in Dirac quasiparticle systems

"A man is like a fraction whose numerator
is what he is and whose denominator is what he thinks of himself.
The larger the denominator, the smaller the fraction."
-Leon Tolstoy.

5.1. Introduction

It is now manifest from the preceding chapter that Dirac quasiparticles can be a building block for topological phases in materials that host such low energy quasiparticles. Even when these systems are highly doped, the topological nature can emerge from interactions as we investigated in chapter 4. It is enlightening to recall that the motivation to find such topological phases in lattice systems was driven by the goal to achieve the integer quantum Hall effect [46] without magnetic field [66]. We have seen that within an interacting system of Dirac quasiparticles, it is possible to generate bands with non-trivial Chern numbers, a property which translates into a finite Hall conductivity. If the chemical potential lies within a gap, the Hall conductivity is quantized and given by $\sum_i C_i e^2/h$ where C_i is the Chern number of the completely occupied band i. In this sense, the system becomes a generalization of the integer Hall effect without magnetic field.

In the early 80's, and shortly after the integer quantum Hall effect was discovered in MOSFET devices [46], a second striking result was announced: the quantization of the Hall conductivity in simple fractions [47, 48]. The fact that this phenomena was only observable at very low temperatures in ultraclean samples suggested that electron-electron interactions could play a crucial role in driving the system into this novel insulating state. The fractional quantum Hall effect was thought to be an emergent, gapped (incompressible) many-body state of a strongly interacting two-dimensional electron liquid under a large magnetic field. Its defining property was a quantized Hall conductance which in units of e^2/h was equal to a quotient p/q where p and q are relative primes.

Soon after the discovery of the first fraction, appearing when the first integer Landau level was one third filled ($\nu = 1/3$), Laughlin [175] proposed a wave function to explain fractions of the form $1/m$ where m is an odd integer. The Laughlin wave function was explicitly constructed so that the relative angular momentum between any two particles was of at least m, minimizing Coulomb repulsion by spatially separating cyclotron orbits further than in the integral case. The requirement of an odd m was a direct consequence of the constraint that a fermionic wave function must be antisymmetric. This theoretical breakthrough established that the fractional Hall state had a uniform density through the plasma analogy (i.e. it was an electron liquid), as well as the fractional nature of the quasiparticle excitations [175]. Its success was tested by exact numerical diagonalization showing high numerical overlap between the Laughlin and numerical pair correlation functions [176, 177]. Following these advances, more fractions were understood under the hierarchical construction of Haldane [178] and Halperin [179] as cleaner samples were available, until the composite fermion construction was proposed (see for example [180] and references therein). In this elegant paradigm, the fractional quantum Hall effect is to be understood as the integer quantum Hall effect of the new quasiparticles labelled composite fermions.
Importantly, the quantum Hall effect was soon understood as a topological state of matter, in fact the first topological state of matter ever discovered. This means that one cannot describe such a state in terms of broken symmetries, but only in terms of topological concepts. For example, as it was mentioned in the preceding chapter, the Hall conductivity of the integral quantum Hall effect can be associated to a topological invariant [50, 51]. In turn, the fractional quantum Hall effect can be described in terms of topological field theories through the Chern-Simons-Landau-Ginzburg formalism [91, 181] which has a manifestly topological origin.

Therefore, and with the above considerations in mind, it is natural to ask if it is possible to generalize the fractional quantum Hall state to a situation without external magnetic fields, just as it happens for the integer case. Remarkably, three groups [182–184] argued independently that it might be possible to generate fractional quantum Hall states out of interaction in systems with topologically non trivial flatbands. In other words, fractionally filled bands with high degeneracy and non-zero Chern number could give rise to these fractional states. This intuition was built on the knowledge of the fractional Hall effect. They argued that the flatness of the band would mimic the high degeneracy of a Landau level which should be broken by the presence of strong electron-electron interactions. The Chern number would be required for the band to have a finite Hall conductivity through the Berry curvature, perhaps acting as a seed for the fractional Hall state [1].
In this picture, the search of materials that realize these *fractional Chern insulators* requires

[1] We note however that, at the time of writing, there is no consensus of whether this last requirement is necessary to generate a fractional Hall conductivity out of interactions.

the hierarchy of energy scales $W \ll V \ll m$. Here m is the gap separating the non trivial flatband from other bands and W is its bandwidth, being the largest and smallest energy scale respectively, while the intermediate energy scale V is the characteristic interaction energy. In this scenario, one of the groups [182] showed that for a band with Chern number one at $\nu = 1/3$ filling, a state with $\sigma_{xy} = \frac{1}{3}\frac{e^2}{h}$ emerged which, as we will discuss below, can be interpreted as the analogue of the fractional Hall effect without external magnetic fields. Soon after these results, a state consistent with a fractional Chern insulator state at filling $\nu = \frac{1}{5}$ was stabilized [185]. One year later, there are numerous examples consistent with different bosonic and fermionic fractional Hall states in different physical systems [186–199].

In this chapter we will use a lattice model that hosts low energy Dirac quasiparticles to help us realize bands with Chern number up to two in order to understand the fate of fermionic fractional states in such a situation. We will connect the emerging phases to paradigms of the fractional quantum Hall effect and we will discuss a way to characterize these states in order to distinguish them from a different competing order which is possible in lattice systems, the charge density wave. Furthermore it will be argued that fractional states can be stabilized in a band structure which is not perfectly flat, bringing the physical realization of such fractional topological phases closer.

The chapter is structured as follows. We will first present a model that will allow us to interpolate between topologically non trivial flat bands with Chern number $C = 0, \pm 1, \pm 2$. In section 5.3 we will present and discuss different physical properties which characterize the fractional Chern insulator phases that may arise when interactions are taken into account in such a model. This will include a procedure to construct real space density maps that will help to distinguish the fractional Chern insulator phase from a charge density wave state. In section 5.4 we will illustrate these tools at work by making use of the numerical technique known as exact diagonalization, from which we are to obtain the energy spectra and wave functions of finite systems with both $C = 1, 2$. We will argue from the information extracted that the realized phases are compatible with fractional Hall states. Finally, in 5.5 we will relax the flatband condition and show that the most stable state (that with the largest many body gap) is not obtained in the mathematically flatband limit but for a finite bandwidth.

5.2. The model

In this chapter, our starting point is a non-interacting tight-binding model for fermions on the two-dimensional square lattice of $L_1 \times L_2$ sites and spanned by the orthonormal primitive lattice vectors $\hat{e}_1$ and $\hat{e}_2$ under periodic boundary conditions. The fermions have two internal degrees of freedom per site, which we denote as a spin degree of freedom $s = \uparrow, \downarrow$ that can

also be interpreted as two orbitals per site. The resulting non-interacting Bloch Hamiltonian supports two bands and reads in momentum space

$$\begin{aligned} H_0 &= \sum_{\boldsymbol{k}\in \mathrm{BZ}} c_{\boldsymbol{k}}^\dagger \boldsymbol{B}_{\boldsymbol{k}} \cdot \boldsymbol{\sigma}\, c_{\boldsymbol{k}}, && \text{(5.1a)} \\ B_{\boldsymbol{k};1} + \mathrm{i} B_{\boldsymbol{k};2} &= t(\sin k_1 + \mathrm{i} \sin k_2), && \text{(5.1b)} \\ B_{\boldsymbol{k};3} &= h_1 \cos k_1 + h_2 \cos k_2 + h_3 && \text{(5.1c)} \\ &+ \frac{h_4}{2}\left[\cos(k_1+k_2) + \cos(k_1-k_2)\right], \end{aligned}$$

where $c_{\boldsymbol{k}}^\dagger \equiv (c_{\boldsymbol{k},\uparrow}^\dagger, c_{\boldsymbol{k},\downarrow}^\dagger)$ and $c_{\boldsymbol{k},s}^\dagger$ creates a fermion at momentum $\boldsymbol{k}$ in the Brillouin zone with spin $s = \uparrow, \downarrow$ while $\boldsymbol{\sigma} = (\sigma_1, \sigma_2, \sigma_3)$ are the three Pauli matrices acting on spin space. The parameters t and h_μ, $\mu = 1, \cdots, 4$ are real. The role of the hopping parameters t and h_μ, $\mu = 1, \cdots, 4$ can be illustrated by fixing $t > 0$ and expanding the Hamiltonian around the four inversion-symmetric momenta in the Brillouin zone $\boldsymbol{k}^{(ij)} = \pi(i, j)$, $(i, j = 0, 1)$. To linear order in the deviation $\boldsymbol{p}^{(ij)} = \boldsymbol{k} - \boldsymbol{k}^{(ij)}$, from each of these four momenta, the Hamiltonian takes a Dirac form $H_k^{ij} = \mathbf{k} \cdot \boldsymbol{\sigma} + m_{ij}\sigma_z$ with masses given by

$$m^{(ij)} = (-1)^i h_1 + (-1)^j h_2 + h_3 + (-1)^{i+j} h_4. \tag{5.2a}$$

The model thus allows to independently control the sign and magnitude of the mass at each of the four Dirac points via the parameters h_μ, $\mu = 1, \cdots, 4$. Recalling the discussion in 4.3.2, if all the Dirac points have a non-vanishing gap, the Chern number of each of the two bands is well defined. Each Dirac point contributes $\pm 1/2$ to the Chern number, with the sign depending on the chirality $\exp(\mathrm{i}k_1^{(ij)} + \mathrm{i}k_2^{(ij)})$ of the kinetic part of the Dirac Hamiltonian and the sign of the mass gap. The total Chern number of the lower band is then given by (1.11)

$$C = \frac{1}{2} \sum_{i,j=0,1} (-1)^{i+j} \operatorname{sgn} m^{(ij)}, \tag{5.2b}$$

and therefore can assume the values $C = \pm 2, \pm 1, 0$ in our two-band model (see Fig. 5.1). In what follows, we study this model in presence of density-density interactions between fermions on the same lattice site (U) and between fermions on neighbouring sites (V)

$$H_{\mathrm{int}} = \frac{U}{2} \sum_{\boldsymbol{r}\in\Lambda} \sum_{s\neq s'} \rho_{\boldsymbol{r},s}\, \rho_{\boldsymbol{r},s'} + \frac{V}{2} \sum_{(\boldsymbol{r},\boldsymbol{r}')} \sum_{s,s'} \rho_{\boldsymbol{r},s}\, \rho_{\boldsymbol{r}',s'} \tag{5.3}$$

upon partial filling the lower band. Here, $(\cdot,\cdot)$ denotes nearest-neighbor lattice sites and $\rho_{\boldsymbol{r},s} = c_{\boldsymbol{r},s}^\dagger c_{\boldsymbol{r},s}$ is the density of fermions with spin $s = \uparrow, \downarrow$ at site $\boldsymbol{r}$. Both U and V are measured in units of t throughout the chapter.

As discussed in the introduction, we are interested in the situation where the following hierarchy of energy scales applies

$$W \ll U, V \ll m, \tag{5.4}$$

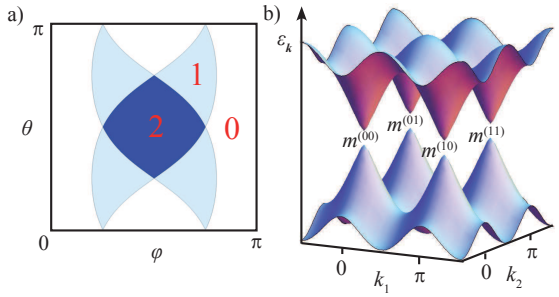

Figure 5.1.: (a) Any one of the two Chern numbers of the two bands of the noninteracting Hamiltonian (5.1) depends on the direction of the four-component mass vector $h = (h_\mu)$. When restricted to the form $h = |h|(\cos\varphi, \sin\varphi\,\cos\theta, \sin\varphi\,\sin\theta/\sqrt{2}, \sin\varphi\,\sin\theta/\sqrt{2})$, the Chern number phase diagram is obtained as shown (white: $|C| = 0$, light: $|C| = 1$, dark: $|C| = 2$). b) Band structure of the noninteracting Hamiltonian (5.1) with mass terms $m^{(ij)}$, $i, j = 0, 1$, defined in Eq. (5.2a).

with W and m being the bandwidth and the band gap of the noninteracting band structure, respectively. The fact that m is the largest energy scale is taken into account by constraining the single-particle Hilbert space to the subspace spanned by the states in the lower band. We therefore project this interaction to the Fock space built out of the single-particle subspace of the lower band

$$H_{\text{int}}^{\text{pro}} = \frac{-1}{L_1 L_2} \sum_{\boldsymbol{k},\boldsymbol{k}',\boldsymbol{q}} \gamma_{\boldsymbol{k},\boldsymbol{k}',\boldsymbol{q}}\, \chi_{\boldsymbol{k}+\boldsymbol{q}}^\dagger \chi_{\boldsymbol{k}'-\boldsymbol{q}}^\dagger \chi_{\boldsymbol{k}} \chi_{\boldsymbol{k}'} \tag{5.5a}$$

$$\gamma_{\boldsymbol{k},\boldsymbol{k}',\boldsymbol{q}} = \sum_{s,s'} \left[\frac{U}{2}(1 - \delta_{s,s'}) + V(\cos\, q_1 + \cos\, q_2) \right] u_{\boldsymbol{k}+\boldsymbol{q},s} u_{\boldsymbol{k}'-\boldsymbol{q},s'} u_{\boldsymbol{k},s}^* u_{\boldsymbol{k}',s'}^*, \tag{5.5b}$$

where $u_{\boldsymbol{k},s}$ is the eigenvector of the lower band of the 2×2 Bloch Hamiltonian $\boldsymbol{B}_{\boldsymbol{k}} \cdot \boldsymbol{\sigma}$ in (5.1) at momentum $\boldsymbol{k}$, while $\chi_{\boldsymbol{k}}^\dagger$ is the second quantized operator that creates the corresponding state in the lower band.

Furthermore, we can impose that W is the smallest energy scale by a spectral flattening of the lower band of the single-particle Hamiltonian (5.1) [182]

$$H_0^{\text{flat}} = \sum_{\boldsymbol{k} \in \text{BZ}} c_{\boldsymbol{k}}^\dagger \frac{\boldsymbol{B}_{\boldsymbol{k}} \cdot \boldsymbol{\sigma}}{|\boldsymbol{B}_{\boldsymbol{k}}|} c_{\boldsymbol{k}}, \tag{5.6}$$

which in effect maps all states in the lower band to the energy -1 and all states in the upper band to energy $+1$. It is possible to show by studying the Fourier transform to position space that this deformation of the Hamiltonian induces arbitrary-range hopping amplitudes that decay exponentially with distance (see [182] for details.). Interpolating between H_0 and H_0^{flat}, via

$$H_0(\lambda) = (1 - \lambda) H_0^{\text{flat}} + \lambda H_0 \tag{5.7}$$

with $0 \leq \lambda \leq 1$, will allow us to choose the bandwidth at will. After discussing the characterization of possible phases within exact diagonalization, we will start with the study of the

case $\lambda = 0$, using the Hamiltonian

$$H(\lambda) = H_0(\lambda) + H_{\text{int}}^{\text{pro}} \tag{5.8}$$

by carrying out exact diagonalization studies of small systems. We will always restrict the single-particle Hilbert space to that of the lower band in our calculations, i.e., we assume the limit $W/m \ll U/m, V/m \to 0$ in Eq. (5.4).

5.3. Characterization of fractional Chern states via exact diagonalization

Before studying the emergent phases of the particular model described above, in this section we will try to put forward tools that will help us to distinguish between fractional Hall states and other competing phases such as charge density waves for example. These tools will extract information from the eigenvalues and eigenfunctions of the system that can be obtained exactly only for small system sizes via the technique of exact diagonalization.

Exact diagonalization [200] is in essence a “brute" force numerical method which solves the Schroedinger equation by diagonalizing the Hamiltonian expressed in some convenient basis. Of course, the size of the Hilbert is a crucial limiting factor and thus only small system sizes are accessible in practice. Nonetheless, this method has proven very useful in various fields ranging from spin systems to the fractional quantum Hall effect [200]. Concerning the latter, it provided numerical support in the early days of the fractional quantum Hall effect for the Laughlin wave function which showed high overlaps with numerical eigenstates obtained for finite size systems and different geometries [177, 201].

In practice, the diagonalization is performed over subspaces of the Hilbert space that conserve some quantum number, which saves important computational time. For our purposes we will subdivide the Hilbert space into subspaces with a given total momentum $\boldsymbol{Q} = \boldsymbol{k}_1 + \cdots + \boldsymbol{k}_N$ where $\boldsymbol{k}_i$ $i = 1, \cdots, N$ are the N single particle momenta of an N-particle state. Because of translational invariance, the Hamiltonian does not couple states with different $\boldsymbol{Q}$ and thus the Hamiltonian is block diagonal, one block for each $\boldsymbol{Q}$. Therefore, from the exact diagonalization of small lattice systems one obtains the eigenstates and eigenvalues for each momentum sector $\boldsymbol{Q}$. These encode the properties of the many-body state realized at the particular filling we have diagonalized the system. We now review the formal aspects of several properties that can be extracted from the spectrum and eigenstates in order to elucidate whether the many body state we obtain is of the fractional Chern insulator type or, on the contrary, some other trivial state. These shall be later illustrated in section 5.4 with two concrete examples in the $C = 1$ and $C = 2$ cases.

5.3.1. Degeneracy of the ground state

A very profound fact regarding the fractional quantum Hall states in two dimensional electron gases is that the appearing fractional states can be classified by their ground state degeneracy [91]. The ground state degeneracy of the fractional quantum Hall state depends only on the geometry of the space in which they are defined, and does not change with small perturbations. For example, the Laughlin $1/m$ state has m^g degeneracy on a surface of genus g [202]. Instead of giving more elaborate topological arguments (for those see [91] and references therein) we will try to convey a simple way to understand this fact for the case of the torus in which the degeneracy is simply m.
Consider the $\nu = 1/3$ Laughlin wave function on a disc. It has the form [175] $\Pi_{i<j}(z_i - z_j)^3$ up to an exponential factor, irrelevant for the present argument. The variables z_i label the position of particle i defined as $z_i = x + iy$. By expanding this polynomial it is easy to see that it has generically terms of the form $z_1^0 z_2^3 z_3^6 \cdots + \cdots$. One can recall from solving the problem of the two dimensional electron gas in a magnetic field in the symmetric gauge that z^m (we again forget about the exponential factor) is an eigenstate of the angular momentum with eigenvalue m that forms rings of radius $r_m \sim \sqrt{m}$ around $z = 0$ (see for example [91, 203]). If we take the term of the wave function proportional to $z_1^0 z_2^3 z_3^6 \cdots$ we see that it creates a particle in orbital 0 then a particle in orbital 3 and so on, which corresponds to a wave function of the sort $[100100100\cdots]$ in occupation space, filling one every three rings. With periodic boundary conditions, corresponding to the geometry of a torus with genus $g = 1$, we can generate also the structure $[010010010\cdots]$ and $[001001001\cdots]$ which gives the three fold degeneracy of the ground state $m^g = 3$.

There is a systematic way to calculate the degeneracy of a fractional quantum Hall state through the description of fractional states in terms of the hierarchical Chern-Simons theory of the fractional quantum Hall effect. This description is nothing but the attempt of writing a field theory action that captures the essence of the Laughlin wave functions. The internal degrees of freedom coming from the many body interaction are hidden into new gauge fields known as *statistical* gauge fields a_μ. In principle, one may need not one but a family of such fields which we will refer to as flavours. The power of such an approach, besides that all the quantum field theory computational tools can be applied as usual, is that it is a unifying view of all hierarchical fractional quantum Hall states. In one simple effective action one captures, among other things, the ground state degeneracy, the Hall conductivity of the fractional quantum Hall states as well as the generalization to layered systems where two or more two dimensional electron gases are coupled. The detailed motivation of such a theory is out of the scope of this chapter and so we refer the reader the reviews [181, 204] and Wen's book [91] as well as references therein for further details. Here we will use it only as a systematic recipe to calculate both the degeneracy and the Hall conductivity for a given

fractional quantum Hall state, which will help us to relate the appearing fractional Chern states in our lattice system to known fractional quantum Hall states.
The action for such a theory reads

$$S_{\mathrm{CS}} = \frac{\varepsilon_{\mu\nu\lambda}}{4\pi} \int \mathrm{d}^2\boldsymbol{r}\,\mathrm{d}t\, \left(-K_{ij}\, a_i^\mu \partial^\nu a_j^\lambda + 2eQ_i a_i^\mu \partial^\nu A^\lambda\right) \tag{5.9}$$

in the continuum limit. Here, a_i^1, a_i^2, and a_i^0 are the spatial and temporal components of $i = 1, \cdots, N_{\mathrm{f}}$ flavours of the statistical gauge fields. As mentioned before, these statistical gauge fields represent internal degrees of freedom that capture the physics of the Laughlin wave functions. They couple to $A^\mu, \mu = 0, 1, 2$, the external electromagnetic gauge field, and K is a symmetric $N_{\mathrm{f}} \times N_{\mathrm{f}}$ matrix with integer entries, Q is the N_{f} component charge vector, in analogy with the ordinary electromagnetic coupling with integer entries (not to be confused with the momentum sector $\boldsymbol{Q}$). The summation over the repeated indices is implied.
It can be proven [2, 91, 204, 205] that the topological ground state degeneracy on the torus and the Hall conductivity are given by $\det[K_{ij}]$ and

$$\sigma_{\mathrm{H}} = \frac{e^2}{h}\, Q_i\, K_{ij}^{-1}\, Q_j, \tag{5.10}$$

respectively [2]. Thus, given a fractional Chern state arising form exact diagonalization, it can be classified by its degeneracy and Hall conductivity through the effective Chern-Simons theory above by defining as many species as necessary, which shall relate to the existing fractional Hall states known in the conventional two dimensional electron gas. Let us shortly discuss an example of the latter case to give a feeling of how this theory is to be formulated. For instance, the properties of the $\nu = \frac{1}{m}$ Laughlin state are properly captured by a single gauge field. This is easily seen if we choose the matrix K_{ij} to have a single entry $K = m$ with $Q = 1$ that necessarily recovers a degeneracy m and a Hall conductivity of $\sigma_{xy} = \frac{1}{m}\frac{e^2}{h}$. A second example is that of a bilayer state, where two layers, each one with a two dimensional electron gas, are coupled by the Coulomb interaction. In this case, the many body state in the fractional quantum Hall regime is described by a generalization of the Laughlin wave function of the form (up to an exponential factor) [179]:

$$\Psi_{lmn} = \prod_{i<j} (z_i - z_j)^l (w_i - w_j)^m (z_i - w_j)^n \tag{5.11}$$

Where z_i, w_i are the positions of electrons in the upper and lower layer respectively. In the Chern-Simons language this would correspond to a K matrix [91]:

$$K = \begin{pmatrix} l & n \\ n & m \end{pmatrix}, \qquad Q = \begin{pmatrix} 1 \\ 1 \end{pmatrix}, \tag{5.12}$$

[2] The proof of such statements is out of the scope of the chapter. The Hall conductivity can be derived following Zee's book [2] chapter VI.2 for a single component gauge field and generalizing it to a several component field, that is explicitly shown in the original reference [206]. The value of the degeneracy is more intricate to prove and can be first derived for a single gauge field following Wen [207]. The generalization to the K matrix for an N component gauge field can be found in [205, 208].

with m and l odd and n a non negative integer. One may consider for example a $1/3$ state in each layer which would set $l = m = 3$ which have an ordinary coupling $n = 1$. The degeneracy of such a state is

$$\det K = \det \begin{pmatrix} 3 & 1 \\ 1 & 3 \end{pmatrix} = 8, \tag{5.13}$$

and a Hall conductivity $\sigma_{xy} = \frac{2}{3}\frac{e^2}{h}$.
To summarize this section, the effective Chern-Simons field theory will be useful as tool to relate the new fractional Chern insulator fractional states that could emerge from the exact diagonalization of Hamiltonian (5.8) with known fractional Hall states.

5.3.2. Laughlin's argument, flux insertion and Hall conductivity

As the understanding of both the integer and the fractional quantum Hall effect grew, it was argued that a fractional Hall conductivity could be explained as an interchange of degenerate ground states under an adiabatic flux insertion [51, 209, 210]. One may understand such a statement by following Tao and Wu [209] that generalized to the fractional case Laughlin's argument [211] for the integer quantum Hall effect. The argument, which we now describe, was introduced as a way to obtain the quantization of Hall conductance as a consequence of gauge invariance.
Laughlin considered a two dimensional electron gas constrained to move on a ribbon and inserted adiabatically a flux, from zero to $\phi_0 = hc/e$, the flux quantum. As electrons flow around the loop enclosing the flux, they will acquire an Aharanov-Bohm phase proportional to the flux ϕ. When the flux reaches ϕ_0, the phase reaches 2π and the system maps onto itself. The important fact is that this is only if the ground state is unique. During the process, the Landau orbits are pushed to the edges, since the effect of the vector potential from the flux can be shown to move their centres. At exactly ϕ_0, the system pushes exactly one Landau level out of one of the borders generating a Hall conductivity of $\sigma_{xy} = \frac{e^2}{h}$, the quantized value.
In the fractional case, there is a degenerate ground state manifold, and so, after inserting a flux ϕ_0, the system does not necessarily map into itself. If the ground state is p-fold degenerate, it is only after p fluxes that the system maps into itself [209]. When q electrons are transferred the Hall conductivity is quantized to q/p.
Consistently, Thouless [210] showed that the quasi-degenerate groundstates are expected to cross under flux insertion on the torus. It is easy to see that inserting a flux is equivalent to impose twisted boundary conditions, since the state needs to absorb the new Aharonov-Bohm phase in order to be periodic. Thus, for a many-body state $|\Psi\rangle$ with N particles inserting a flux $2\pi\gamma_i$ in the $\hat{e}_i$ direction is equivalent to imposing the twisted boundary conditions

$$\langle \boldsymbol{r}_1, \cdots, \boldsymbol{r}_j + L_i\hat{\boldsymbol{e}}_i, \cdots, \boldsymbol{r}_N|\Psi\rangle \quad = e^{\mathrm{i}\,2\pi\,\gamma_i}\langle \boldsymbol{r}_1, \cdots, \boldsymbol{r}_j, \cdots, \boldsymbol{r}_N|\Psi\rangle, \qquad j = 1, \cdots, N. \tag{5.14}$$

In practice, it is simple to impose such a boundary conditions in the exact diagonalization procedure. The observation of the spectral flow of the degenerate groundstates interchanging among flux insertion was first taken as an evidence of the fractional Chern insulator state. To be precise however, in small finite systems this is just a hint, not a proof. Regnault and Bernevig [188] pointed out that a commensurate charge density wave could also generate such a spectral flow and thus it did not exclude charge density wave ordering.
Therefore, it is important to elaborate tools to distinguish the fractional state from the charge density wave, two of which we now briefly describe.

5.3.3. Charge density wave order parameter

In this section we will put forward a construction that shall help us to distinguish between charge density wave order and a candidate fractional Chern state. As argued above, the fractional Chern insulator is expected to be a uniform incompressible liquid-like state [91, 201] while the charge density wave should have a non uniform density profile by definition. It is therefore appealing to construct density maps which shall distinguish between both phases. Consider to this extent the local density operator $\rho_{\boldsymbol{r}}$ defined by

$$\rho_{\boldsymbol{r}} = \frac{1}{L_1 L_2} \sum_{\boldsymbol{q},\boldsymbol{k}} \sum_{s} e^{\mathrm{i}\boldsymbol{q}\cdot\boldsymbol{r}}\, c^{\dagger}_{\boldsymbol{k}+\boldsymbol{q},s}\, c_{\boldsymbol{k},s}, \tag{5.15}$$

and construct the matrix with elements

$$\varrho_{\boldsymbol{r};ij} = \langle \Psi_i |\, \bar{\rho}_{\boldsymbol{r}}\, | \Psi_j \rangle. \tag{5.16}$$

where we assume that the ground state manifold of H is n-dimensional and spanned by the quasi-degenerate ground states $|\Psi_1\rangle, \cdots, |\Psi_n\rangle$.
For some finite lattice, it is possible to obtain a representative set of n maps of the local fermion density in the ground state manifold as follows. We first define $v^{(i)}_{\rho;\boldsymbol{r}_0}$, $i = 1, \cdots, n$ to be the set of orthonormal eigenvectors of $\varrho_{\boldsymbol{r}_0}$ at some arbitrarily chosen site $\boldsymbol{r}_0$ and evaluate the n real functions

$$n^{(i)}_{\boldsymbol{r}} = v^{(i)\dagger}_{\rho;\boldsymbol{r}_0}\, \varrho_{\boldsymbol{r}}\, v^{(i)}_{\rho;\boldsymbol{r}_0}, \qquad i = 1, \cdots, n. \tag{5.17}$$

The functions $n^{(i)}_{\boldsymbol{r}}$ are density maps of the n linearly independent combinations of the ground states $|\Psi_1\rangle, \cdots, |\Psi_n\rangle$ selected by the set of eigenvectors $v^{(i)}_{\rho;\boldsymbol{r}_0}$, $i = 1, \cdots, n$. These functions show the variation of the local fermion density in position space. The extrapolation of these density maps to the thermodynamic limit can be used to distinguish between a ground state manifold that supports a charge-density wave, a phase separation in position space, or is featureless as would be expected from a fractional Chern insulator.

5.3.4. Entanglement spectra

A different way to distinguish a charge density wave spectra from the fractional Chern insulator was put forward in Refs. [188, 193–195], by the use of the so called *entanglement spectra* [212]. We will now summarize how to implement it in practice and how it can distinguish the charge density wave state for the sake of completeness. We will not use it in this chapter and just cite the results where appropriate to complement the discussion of the fractional phases.

The idea of the entanglement spectra stems from a quantity known as the entanglement entropy, that measures the entanglement between two partitions of a system and is shown to contain topological properties. One first separates the system's Fock space $\mathcal{H}$ into two different parts A and B so that $\mathcal{H}_A \otimes \mathcal{H}_B$. Note that such a separation may not be spatial, but can be for instance in the number of particles. The wave function can be written as a Schmidt decomposition

$$|\Psi\rangle = \sum_i e^{-\frac{1}{2}\xi_i} \left|\Psi_A^i\right\rangle \otimes \left|\Psi_B^i\right\rangle, \tag{5.18}$$

where $\left|\Psi_{A,B}^i\right\rangle \in \mathcal{H}_{A,B}$. One can think of $\xi_i \in \mathbb{R}$ as eigenstates of a new Hamiltonian H [212] with thermodynamic entropy $S = -\sum_i \xi_i \log(\xi_i)$ which contains information on the topological properties of the many-body ground state [213]. Li and Haldane realized that further information about the many body ground state could be extracted from the complete spectrum ξ_i, defined as the entanglement spectra, and not only from S. If A and B are two spatial regions, by tracing out the B degree's of freedom we encode in the entanglement spectrum edge physics [212]. If instead we separate N_A particles from the rest (N_B) which we trace out, the entanglement spectrum probes the spectrum of quasihole excitations [214] of the system. For the fractional Chern insulator case this last form of partition was shown to give an entanglement spectrum with a gap when plotted as a function of total momentum $\mathbf{Q}$ [188]. The states below such a gap obey a counting principle which is distinct for a fractional Chern insulator and that of a charge density wave, providing, in principle [3], a distinguishing signature of both phases [193].

Having summarized the main tools to be used in this chapter, we now illustrate how to implement them in practice, which we shall use to extract information about the fractional insulator states that shall appear from the exact diagonalization of (5.8).

5.4. Characterization of $C = 1$ and $C = 2$ phases

As was discussed in section 5.2, the main advantage of the the model (5.1) is that it can realize band structures with Chern numbers $C = 0, \pm 1, \pm 2$ by tuning the four hopping parameters

[3] Exceptions to this counting rule have recently been found in $C > 1$ fractional Chern insulators [192].

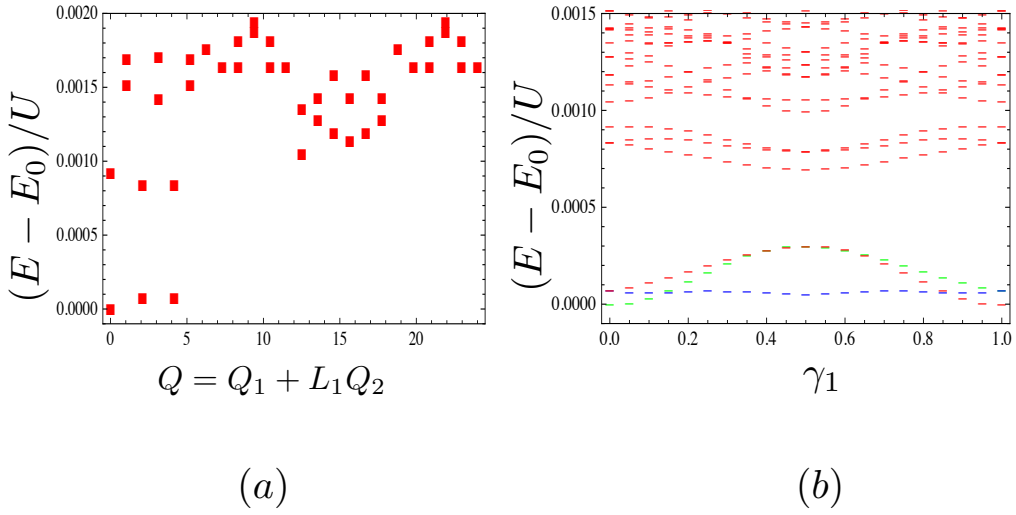

Figure 5.2.: (a) Energy eigenvalues of Hamiltonian (5.8) at $\lambda = 0$ measured relative to the ground state energy at the filling fraction $\nu = 1/3$ for $L = 6 \times 4$ and $N = 8$ particles. The noninteracting parameters of Hamiltonian (5.8) are $h_4 = 0$ and $h_1 = h_2 = -h_3 = -t$, corresponding to a noninteracting band with $C = 1$. The interacting parameters of Hamiltonian (5.8) are $U = 1$ and $V = 0$. A 3-fold quasi-degenerate ground state is observed in agreement with Ref [194]. (b) Spectral flow induced by a flux insertion in the γ_1 direction for $N = 8$ particles. The 3 lowest lying states do not mix with the excited states and return to the same configuration after three flux quanta have been inserted (only the insertion of one flux quantum is shown).

h_μ. Models that host bands with higher Chern number have been studied in the context of fractional Chern insulators obtaining both bosonic [196, 198] and fermionic [215] states consistent with fractional Chern insulators. We complement these findings by discussing and characterizing the information extracted from the exact diagonalization of model (5.8) by introducing interactions as specified in section 5.2.

5.4.1. $C = 1$

As anticipated, we first focus on the case $C = 1$. It can be realized by choosing $h_1 = h_2 = -h_3 = -t$ and $h_4 = 0$ in (5.1) and was previously studied in Ref. [194]. As a warm up for the novel $C = 2$ case, we will now apply some of the tools described in the previous section to argue that the model hosts a $1/3$ fractional Chern insulator state.

Figure 5.2 (a) shows the low-energy portion of the many-body spectrum plotted as a function of center of mass momentum $\boldsymbol{Q}$. The expected threefold quasi-degenerate fractional Chern ground state appears when $U = 1$ and $V = 0$ at the filling fraction $\nu = \frac{N}{L_1 L_1} = 1/3$ for a system size $L = 6 \times 4$ with $N = 8$ particles. Smaller sizes don't show a well defined ground

state manifold but such a state survives when $h_4 \neq 0$ as long as the Chern number remains $C = 1$.

The first thing to note is that the quasi-degenerate ground states fall in the sectors with center of mass momenta $(Q_1, Q_2)_{6\times4} = \{(0,0),(2,0),(4,0)\}$. They agree with a counting rule introduced in Ref. [188] which assumed that a so called generalized Pauli principle holds. In such a construction, only one particle is allowed in three consecutive orbitals to minimize the Coulomb repulsion. This constraint is enough to fix the total momentum sectors at which the degenerate ground states appear which are given by

$$\begin{pmatrix} Q_1 \\ Q_2 \end{pmatrix} = \begin{pmatrix} [N(L_1-3)/2 + mN] & \mod L_1 \\ N(L_2-1)/2 & \mod L_2 \end{pmatrix}, \tag{5.19}$$

with $m = 0, 1, 2$ and L_1 is assumed to be a multiple of three. Should L_2 be a multiple of three the same rule applies upon interchanging Q_1 for Q_2. At first, one could be fooled in thinking that such a counting rule could be taken as characteristic of each fractional quantum Hall state. However, a charge density wave will generate the same counting and therefore alternative tests are necessary. This counting is a necessary but not sufficient argument to prove the existence of the fractional state.

Similarly, the threefold quasi-degeneracy of the groundstate is consistent with a Chern-Simons theory (5.9) for a single species of gauge fields and $K = 3$, $Q = 1$ but still does not prove that this is a fractional quantum Hall state.

Consider now Figure 5.2 (b). It shows the evolution of the spectrum when flux is adiabatically inserted in the $\hat{e}_1$ direction for a 6×4 site lattice with $U = 1$, $V = 0$. The quasi-degenerate ground state manifold indeed evolves independently from the excited states consistent with a $\nu = 1/3$ fractional Chern state, but as argued above, this alone is not sufficient to ascertain that it is a fractional Chern insulator.

Finally, in Ref. [194] it was shown that the entanglement spectra counting for $N_B = 5$ particles traced out in a system with $N = 10$ and $L = 6 \times 5$ matched the expected counting for a fractional state confirming its fractional nature, since a charge density wave will have a different counting rule.

To complement such an approach, in the next section we will illustrate how two other tools, the direct calculation of the Hall conductivity and the construction of density maps can help to distinguish such a state from other competing instabilities.

5.4.2. $C = 2$

From eq. (5.2b) it is easy to see that for sufficiently large $h_4 > 0$ the Chern number becomes $C = 2$. Thus, the simplest set of parameters that hosts a Bloch band with $C = 2$ is $h_1 = h_2 = h_3 = 0$ and $h_4 \neq 0$. Note that for this set of the parameters, model (5.1) can be reinterpreted as a layered model where two square lattices are superimposed on each other without any

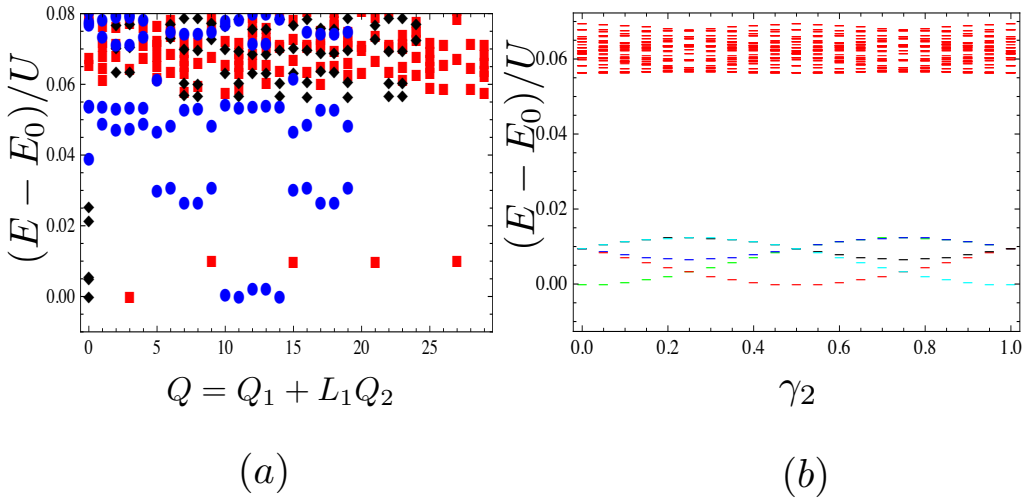

Figure 5.3.: (a) Energy eigenvalues of Hamiltonian (5.8) at $\lambda = 0$ measured relative to the ground state energy at the filling fraction $\nu = 1/5$ for three different system sizes corresponding to $N = 6, 5$, and 4 particles (green diamonds, red squares, and black circles, respectively). The noninteracting parameters of Hamiltonian (5.8) are $h_4 = 0.7$ and $h_i = 0$ for $i = 1, 2, 3$ corresponding to $C = 2$. The interacting parameters of Hamiltonian (5.8) are $U = V = 1$. All three systems show a 5-fold quasi-degenerate ground state (see text for details). (b) Spectral flow induced by a flux insertion in the γ_2 direction for $N = 6$ particles. The five lowest lying states do not mix with the excited states and return to the same configuration after five flux quanta have been inserted (only the insertion of one flux quantum is shown).

hopping term that connects them. By the use of the tools described above, we will now argue that when $h_1 = h_2 = h_3 = 0$, $h_4 = 0.7\,t$, and $U = V = t$, the many-body Hamiltonian $H(\lambda = 0)$ defined in Eq. (5.8) realizes a fractional Chern insulator at $\nu = 1/5$ filling [4].

As for the $C = 1$ case first, we show in Fig. 5.3 (a) that for system sizes 6×5, 5×5, and 5×4 with $N = L_1 L_2/5$ particles, the many-body eigenvalues possess a fivefold degenerate ground state.

The total momentum sectors $\boldsymbol{Q}$ at which these states should appear for a fractional Chern state can be calculated with a generalization of the counting rule of Ref. [188]. For a $L_1 \times L_2$ lattice with N particles where we choose L_1 to be a multiple of five, the momentum sectors are given by

$$\begin{pmatrix} Q_1 \\ Q_2 \end{pmatrix} = \begin{pmatrix} [N(L_1 - 5)/2 + mN] & \mathrm{mod}\, L_1 \\ N(L_2 - 1)/2 & \mathrm{mod}\, L_2 \end{pmatrix}, \tag{5.20}$$

[4] These parameters are not fine tuned. As long as $V > 0$ these state is realized for a range of values of h_4 and V in the $C = 2$ case.

with $m = 0, 1, 2, 3, 4$. As before, if L_2 is to be a multiple of five the same rule applies upon interchanging Q_1 for Q_2. For the square lattices made of 6×5, 5×5, and 5×4 sites, the momentum sectors should fall at

$$\begin{aligned}
\begin{pmatrix} Q_1 \\ Q_2 \end{pmatrix}_{6\times5} &= \begin{pmatrix} 3 \\ 0 \end{pmatrix}, \begin{pmatrix} 3 \\ 1 \end{pmatrix}, \begin{pmatrix} 3 \\ 2 \end{pmatrix}, \begin{pmatrix} 3 \\ 3 \end{pmatrix}, \begin{pmatrix} 3 \\ 4 \end{pmatrix}, \\
\begin{pmatrix} Q_1 \\ Q_2 \end{pmatrix}_{5\times5} &= \begin{pmatrix} 0 \\ 0 \end{pmatrix}, \begin{pmatrix} 0 \\ 0 \end{pmatrix}, \begin{pmatrix} 0 \\ 0 \end{pmatrix}, \begin{pmatrix} 0 \\ 0 \end{pmatrix}, \begin{pmatrix} 0 \\ 0 \end{pmatrix}, \\
\begin{pmatrix} Q_1 \\ Q_2 \end{pmatrix}_{5\times4} &= \begin{pmatrix} 0 \\ 2 \end{pmatrix}, \begin{pmatrix} 1 \\ 2 \end{pmatrix}, \begin{pmatrix} 2 \\ 2 \end{pmatrix}, \begin{pmatrix} 3 \\ 2 \end{pmatrix}, \begin{pmatrix} 4 \\ 2 \end{pmatrix},
\end{aligned} \tag{5.21a}$$

which is exactly what is found in Fig. 5.3 (a).

The flux insertion in the $\hat{e}_2$ direction for lattice size $L = 6 \times 5$ is shown in Fig. 5.3(b). Consistent with a fractional state the five low lying states corresponding to the ground-state manifold evolve independently from the continuum and they only recover their original position after five flux quanta have been inserted in the system. As before, this set of facts is not enough to ascertain that the state we observe corresponds to a fractional Chern insulator. We will thus calculate the Hall conductivity and characteristic density maps as an alternative to the entanglement spectra to show that the state is indeed a fractional Chern insulator with fractional Hall conductivity.

To do so, we will use a generalization of (4.18) that provided the Hall conductivity of a non-interacting system in terms of the non interacting occupation number $n(\mathbf{k})$. The many-body generalization was derived recently in Ref. [191] and can be written as[5]

$$\widetilde{\sigma}_{\mathrm{H}} = \frac{e^2}{h} \frac{2\pi}{L_1 L_2} \sum_{\boldsymbol{k}\in \mathrm{BZ}} \Omega_{\boldsymbol{k}}\, \bar{n}_{\boldsymbol{k}}, \tag{5.22a}$$

that gives the (many-body) quantum Hall conductivity σ_{H} in terms of the single-particle Berry curvature $\Omega_{\boldsymbol{k}}$ and the many-body occupation number $\bar{n}_{\boldsymbol{k}}$ averaged over the quasidegenerate ground states, five in our case, labelled by $|\Psi_i\rangle$, $i = 1, \cdots, 5$. The single-particle Berry curvature $\Omega_{\boldsymbol{k}}$ and the many-body occupation number $\bar{n}_{\boldsymbol{k}}$ are defined by

$$\Omega_{\boldsymbol{k}} = \mathrm{i} \sum_s \partial_{k_2} u^*_{\boldsymbol{k},s} \partial_{k_1} u_{\boldsymbol{k},s} - (1 \leftrightarrow 2) \tag{5.22b}$$

and

$$\bar{n}_{\boldsymbol{k}} = \frac{1}{5 L_1 L_2} \sum_{i=1}^{5} \left\langle \Psi_i \left| \chi^\dagger_{\boldsymbol{k}} \chi_{\boldsymbol{k}} \right| \Psi_i \right\rangle, \tag{5.22c}$$

respectively. In [191] it was proven that $\widetilde{\sigma}_{\mathrm{H}}$ converges to the Hall conductivity σ_{H} averaged over the degenerate ground states in the thermodynamic limit, provided no spontaneous symmetry-breaking of translation invariance occurs. Nonetheless, the accuracy of the quantization of $\widetilde{\sigma}_{\mathrm{H}}$ is limited by the finite size of the system, as the Berry curvature (5.22b) is only

[5] We use here the discretized version.

summed over $L_1 \times L_2$ points in the Brillouin zone to replace an integral in the thermodynamic limit.
For the values $h_1 = h_2 = h_3 = 0$, $h_4 = 0.7\,t$, and $U = V = t$ in the many-body Hamiltonian $H(\lambda = 0)$ defined by Eq. (5.8) the Hall conductivity (5.22a) in units of e^2/h is

	$L = 5 \times 5$	$L = 5 \times 6$	$L = 3 \times 10$
$\widetilde{\sigma}_{\mathrm{H}}$	0.391	0.401	0.400

Results with the same numerical accuracy are obtained for each ground state individually. These results realize the formula $\sigma_{\mathrm{H}} = \frac{e^2}{h} C\,\nu$, with $C = 2$ and $\nu = 1/5$ which is allowed but not guaranteed to be fulfilled [191]. Thus, it is manifest that this state carries a fractional Hall conductivity which seems to be quantized to $\frac{2e^2}{5h}$. This is consistent with a fractional Chern insulator described by the Chern-Simons theory (5.9) for two species of gauge fields and

$$K = \begin{pmatrix} 3 & 2 \\ 2 & 3 \end{pmatrix}, \qquad Q = \begin{pmatrix} 1 \\ 1 \end{pmatrix}. \tag{5.23}$$

since a single species of gauge fields with $K = 5$ would not explain the Hall conductivity $\sigma_{\mathrm{H}} = 2e^2/(5h)$.
To further confirm that the nature of the observed state is indeed of fractional nature, we now construct representative density maps as described in section 5.3.3 from which we expect that a uniform density emerges as expected from an incompressible state. It is known that fractional quantum Hall states on the torus turn smoothly into a charge density wave state, if the ratio $\min(L_1, L_2)/\ell \lesssim 1$. [201, 216]. Here, ℓ is the magnetic length. The counterpart to this so-called thin-torus limit also exists for fractional Chern insulators [193]. For concreteness, let us consider the $\nu = 1/5$ fractional Chern state at Chern number two. For the aspect ratio $L_1/L_2 = 1$, as is the case for a lattice of 5×5 sites with five particles, all five topological ground states have the same center-of-mass momentum $\boldsymbol{Q} = \boldsymbol{0}$. Therefore, $\varrho(\boldsymbol{r})$ is the unit matrix for all lattice sites $\boldsymbol{r}$ and all functions $n_{\boldsymbol{r}}^{(i)}$, $i = 1, \cdots, 5$, are independent of $\boldsymbol{r}$. As a consequence, the fractional Chern state is indeed featureless in this isotropic case. Upon choosing the slightly anisotropic lattice $L_1 = 5$, $L_2 = 6$ with $N = 6$ particles, the eigenvalues of $\varrho(\boldsymbol{r})$ lie between 0.994 and 1.007. This gives rise to a small density variation in position space of about 1% as shown in Fig. 5.4 (a). Increasing further the anisotropy to $L_1 = 2$, $L_2 = 15$ with $N = 6$ particles results in a spread of the eigenvalues of $\varrho(\boldsymbol{r})$ between 0.91 and 1.05 shown in see Fig. 5.4 (a). In this case, the functions $n_{\boldsymbol{r}}^{(i)}, i = 1, \cdots, 5$ form the expected charge density wave pattern with pronounced density minima and maxima along the $\hat{e}_1$ direction, shown in Fig. 5.4 (a).

To summarize, these facts taken together inevitably point to a fractional state. We will now study the effect of a finite band dispersion on the stability of such phases which is crucial to realize.

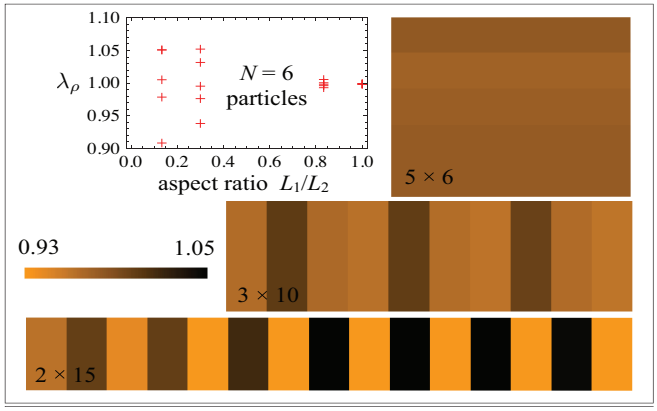

Figure 5.4.: Density profile $n_{\boldsymbol{r}}^{(i)}$ defined in Eq. (5.17) for one representative many-body ground state $|\Psi_i\rangle$ among the n linearly independent quasidegenerate many-body ground states. For the filling fraction $\nu = 1/5$ when the representative ground states for 5×6, 3×10, and 2×15 lattices would turn into a fractional Chern insulator in the thermodynamic limit, by which the two linear dimensions of the lattice are much larger than the correlation length. In a finite lattice, a charge density wave profile becomes more pronounced when the aspect ratio mimics the thin-torus limit, by which the thermodynamic limit is taken with one of the two linear dimensions of the lattice comparable to or smaller than the correlation length. The inset shows the evolution of the eigenvalues λ_ρ of the matrix $\varrho_{\boldsymbol{r};ij}$ defined in Eq. (5.16) as the aspect ratio of the lattice is changed.

5.5. The effect of band dispersion

The evidence presented above for the fractional Chern insulator state seems to rely crucially on the mathematical flatness of the band. However we expect that such a condition will be hardly achieved in realistic physical systems. Therefore, and despite the fact that the model (5.1) is still not associated to any known physical system, it is crucial to study how a departure of the flatness conditions affects the stability of the fractional phases discussed above.
In general terms, we can first trivially expect that as we increase the bandwidth of the flatband the hierarchy of scales (5.4) will break down at a critical value, and a transition to a new ground state may occur eventually leading perhaps to the usual Fermi-liquid paradigm. We must note however that lifting the degeneracy of a Landau level is not the same as lifting the degeneracy in a non trivial Chern band as the ones defined by (5.1). In a Chern band, even in a mathematically flatband, the electrons at each $\mathbf{k}$ are necessarily non equivalent in the sense that they feel a different Berry curvature Ω_k at each point in momentum space. Thus, the naive intuition that the fractional state should be less stable as we gradually increase the bandwidth may not be true. In general we should expect that there is an optimum band dispersion which stabilizes our fractional state by making the many-body gap as large

as possible. Therefore, a finite dispersion of the Bloch bands, that amounts to assigning a momentum-dependent energy penalty for occupying the single-particle states, may favour or not, the realization of a fractional Chern state with a large many-body gap.
We will now use two approaches to support this point. On the one hand, we give an analytical argument that applies to a generic lattice model of interacting fermions in the limit of a partially occupied flat band. We show that for every model that realizes a fractional Chern insulator state at ν, there exists a model with finite dispersion that realizes its particle hole conjugate with $\nu = 1 - \tilde{\nu}$. Second, we give supporting numerical evidences for a scenario by which switching on a finite bandwidth according to Eq. (5.7) can enhance the stability of a fractional Chern insulator state. We choose in particular the $\nu = 1/5$ in the $C = 2$ model discussed earlier.

For the analytical argument, consider an interacting Hamiltonian of the form

$$H = \sum_{\boldsymbol{k}_1,\boldsymbol{k}_2,\boldsymbol{k}_3,\boldsymbol{k}_4} V_{\boldsymbol{k}_1\boldsymbol{k}_2\boldsymbol{k}_3\boldsymbol{k}_4} \chi^\dagger_{\boldsymbol{k}_1} \chi^\dagger_{\boldsymbol{k}_2} \chi_{\boldsymbol{k}_3} \chi_{\boldsymbol{k}_4} \tag{5.24a}$$

that operates exclusively on the Fock space built out of the fermion creation operators $\chi^\dagger_{\boldsymbol{k}'}$, $\boldsymbol{k} \in \mathrm{BZ}$, of an isolated, mathematically flat band. This model is generic for translational invariant density-density interactions which have matrix elements of the form

$$V_{\boldsymbol{k}_1\boldsymbol{k}_2\boldsymbol{k}_3\boldsymbol{k}_4} = v_{\boldsymbol{k}_1-\boldsymbol{k}_3} \langle \chi_{\boldsymbol{k}_1} | \chi_{\boldsymbol{k}_3} \rangle \langle \chi_{\boldsymbol{k}_2} | \chi_{\boldsymbol{k}_4} \rangle \delta_{\boldsymbol{k}_1+\boldsymbol{k}_2,\boldsymbol{k}_3+\boldsymbol{k}_4} \tag{5.24b}$$

in the projected (flat) band, where $\langle \chi_{\boldsymbol{k}} | \chi_{\boldsymbol{k}'} \rangle$ denotes the overlap between a pair of normalized single-particle Bloch states at $\boldsymbol{k}, \boldsymbol{k}' \in \mathrm{BZ}$ and $v_{\boldsymbol{k}}$ is the Fourier component in the Brillouin zone of the unprojected and translational invariant two-body interaction.
Suppose that the ground state of H at filling ν is a fractional Chern state as is the case, for instance of the Hamiltonian (5.8) at $\nu = 1/5$.
Now apply a particle-hole transformation in this isolated band that amounts to the transformation $\chi^\dagger_{\boldsymbol{k}} \to \chi_{-\boldsymbol{k}}$, $\chi_{\boldsymbol{k}} \to \chi^\dagger_{-\boldsymbol{k}}$, $\boldsymbol{k} \in \mathrm{BZ}$. The transformed Hamiltonian reads

$$\widetilde{H} = \sum_{\boldsymbol{k}_1,\boldsymbol{k}_2,\boldsymbol{k}_3,\boldsymbol{k}_4} V_{-\boldsymbol{k}_1,-\boldsymbol{k}_2,-\boldsymbol{k}_3,-\boldsymbol{k}_4} \chi^\dagger_{\boldsymbol{k}_3} \chi^\dagger_{\boldsymbol{k}_4} \chi_{\boldsymbol{k}_1} \chi_{\boldsymbol{k}_2} - \sum_{\boldsymbol{k}} \varepsilon_{-\boldsymbol{k}} \chi^\dagger_{\boldsymbol{k}} \chi_{\boldsymbol{k}} + \text{constant} \tag{5.25a}$$

in a normal-ordered form, where

$$\varepsilon_{\boldsymbol{k}} = \sum_{\boldsymbol{k}'} (V_{\boldsymbol{k}\boldsymbol{k}'\boldsymbol{k}'\boldsymbol{k}} + V_{\boldsymbol{k}'\boldsymbol{k}\boldsymbol{k}\boldsymbol{k}'}) = \sum_{\boldsymbol{k}'} (v_{\boldsymbol{k}-\boldsymbol{k}'} + v_{\boldsymbol{k}'-\boldsymbol{k}}) \, |\langle \chi_{\boldsymbol{k}} | \chi_{\boldsymbol{k}'} \rangle|^2. \tag{5.25b}$$

We then conclude that, by construction, $\widetilde{H}$ supports a fractional Chern state (of holes) as its ground state at filling $\widetilde{\nu} = 1 - \nu$. For instance, $\widetilde{H}$ when derived from Hamiltonian (5.8) at $\nu = 1/5$ supports a fractional Chern state (of holes) as its ground state at the filling $\widetilde{\nu} = 4/5$. Note that this fractional Chern state of holes at $\widetilde{\nu} = 1 - \nu$ is stabilized in the presence of a one-body dispersion that is of the same order as the interaction itself and given by $\varepsilon_{\boldsymbol{k}}$.

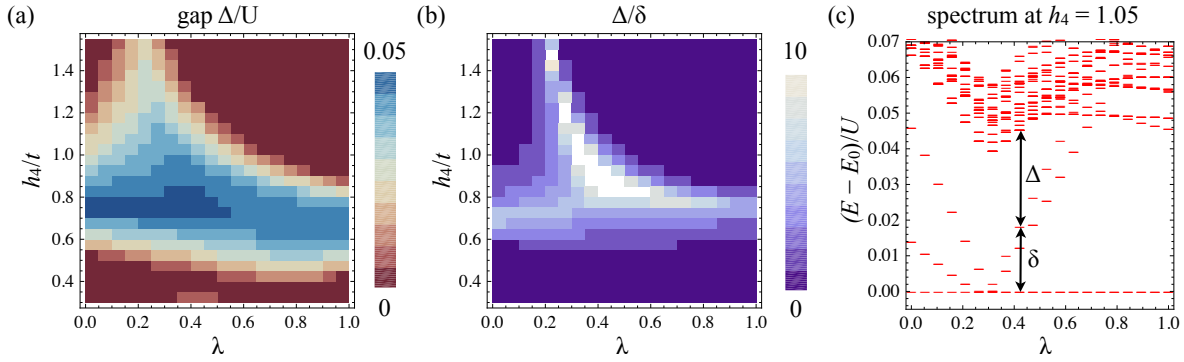

Figure 5.5.: Stability of the fractional Chern insulator phase at $\nu = 1/5$ for $C = 2$ as the bandwidth of the non-interacting Hamiltonian is changed via the parameter λ defined in Eq. (5.7). Panels (a) and (b) show the gap Δ between the fifth- and sixth-lowest energy eigenvalue of the many-body Hamiltonian and the quotient Δ/δ, where δ is the spread in energy of the five lowest eigenvalues, respectively. The region coloured blue in (a) and bright (b) is interpreted as a fractional Chern insulator with $\nu = 1/5$. In panel (c) the evolution of the lower portion of the many-body spectrum with increasing λ at constant $h_4 = 1.05\,t$ is plotted. For all figures the number of particles is $N = 6$ particles, while $L_1 = 6$, $L_2 = 5$, $h_i = 0$, $i = 1,2,3$, and $U = V = 1.5\,t$.

This one-body term can be interpreted as an optimal choice of the band dispersion that realizes a fractional Chern state at the filling fraction $\widetilde{\nu} = 1 - \nu$. It is a trivial constant if all overlaps between normalized Bloch states are functions of $(\boldsymbol{k} - \boldsymbol{k}')$ only. However, in general, the particle-hole transformed Hamiltonian $\widetilde{H}$ acquires a genuine one-body dispersion. Turning off adiabatically this dispersion can induce a phase transition to a ground state that does not display a fractional (hole) state at the filling fraction $\widetilde{\nu}$. For instance, at the filling fraction $\widetilde{\nu} = 4/5$,the Hamiltonians studied numerically in Refs. [190] and [189] can be interpreted as the Hamiltonian obtained from $\widetilde{H}$ upon subtracting the one-body term $\varepsilon_{\boldsymbol{k}}$. These Hamiltonians at this filling fraction do not support a fractional Chern ground state, although $\widetilde{H}$ does.

To conclude this section we now present a numerical study of the model defined in Eq. (5.7), in order to explore the effect of a band dispersion quantitatively. To quantify the stability of the fractional phase we shall use the ratio between the many-body gap Δ, that we define as the difference in energy between the highest of a manifold of quasidegenerate ground-state energies and the lowest-energy eigenvalue above it, and the splitting δ in energy between the highest and the lowest of the quasidegenerate ground states. An increase of the ratio Δ/δ should be interpreted as an increase in stability.

For concreteness, we focus on the fractional state described in section 5.4.2 at $\nu = 1/5$ with a fivefold quasidegenerate ground state. We will interpolate between the flat band and the original non-interacting Hamiltonian with the help of the family of non-interacting Hamiltonians (5.7) parametrized by $\lambda \in [0,1]$ and calculate how the stability of the candidate fractional Chern state phase changes, as measured by Δ and Δ/δ. Varying λ from 0 to 1

makes it possible to change the bandwidth W of the lower band relative to the energy scale of the interaction. The bandwidth of the Bloch band is thus given by $W = \lambda W_0$, where W_0 is the bandwidth of the non-interacting band, that depends on the parameters of the model, h_μ in our case. We still, however, project the Hilbert space to the one spanned by the single-particle states of the lower band for all values of λ.
The findings are summarized in Fig. 5.5 where both Δ and Δ/δ are plotted as a function of the bandwidth-parameter λ and the parameter h_4 of the non-interacting Hamiltonian (5.1), where the bandwidth is $W = \lambda \max\{\sqrt{2}, |\sqrt{2} - h_4|\}$. In summary, for a large range of values of h_4 both the gap Δ as well as the ratio Δ/δ can be substantially increased as λ becomes larger. This can be interpreted as an increase in the stability of the fractional Chern insulator phase with increasing bandwidth of the noninteracting band. (see Fig. 5.5 (c)). As a final remark, it is possible to check that the fractional Chern insulator is stable against a substantial bandwidth of the order of the interaction energy scale for $h_4 \approx 0.7\,t$.

5.6. Discussion and Conclusions

In this chapter we have showed that fractional Chern insulator states that carry a Hall conductivity quantized in fractions of e^2/h can emerge from Dirac quasiparticle systems. To generate such a state, the fractional Chern insulator state, we have defined as a starting point a model that hosts a topologically non trivial (finite Chern number) flat band with the hope to emulate a Landau level with a quantized Hall effect and high degeneracy. By introducing both the on-site interaction U and the nearest neighbour interaction V we have characterized such phases with several tools extracted from the exact diagonalization of the Schroedinger equation in small finite size systems.
For the case of a flat band with Chern number one we have presented evidence that at a filling $\nu = 1/3$ a state compatible with a fractional $1/3$ state is realized consistent with a previous work [194]. Extending these results for the flat-band with Chern number two, we have found that for finite $U, V > 0$ an isotropic phase at filling $\nu = 1/5$ with Hall conductivity $\sigma_{xy} = \frac{2e^2}{5h}$. This state is consistent with a two component fractional Hall state, similar to a bilayer fractional quantum Hall effect at filling $\nu = 2/5$. A priori, this correspondence was not guaranteed since a flat band with Chern number two has no straight forward analogue in the Landau level picture. The presented results are consistent with other works that study bands that host higher Chern numbers which also find fractional Chern insulator states [196, 198, 215]. However, [196] reported some anomalies in the counting rules of the entanglement spectra which are to be explained. In that sense, the density maps presented in this chapter might unambiguously rule out other competing states being a complementary tool to the entanglement spectra.
In addition to the characterization of fractional phases, we have relaxed the condition of the

flat-band adding a finite dispersion as a first step to get closer to physically realistic systems that host such fractional Chern insulator phases. We have seen that adding such a finite dispersion may help to stabilize the fractional state at an optimal band dispersion. This fact is to be expected since the electrons in a mathematically flat band, although degenerate, do not feel the same Berry curvature and thus are not equivalent. Thus in general there will be an optimal band dispersion, still with a characteristic band-width less than the single particle band gap, for which the fractional state is stabilized with the larger many body gap. These same lines of reasoning could be applied to any flat-band system, in particular those that have been obtained in more realistic models (see for example the perovskite model in [217]), although further work is needed to pin down the actual system that realizes such states.

Despite the theoretical understanding gained with the presented discussion together with other numerous efforts regarding the fractional Chern insulator states that have been presented in the literature in the past year [186–199], there are a vast amount of uncertainties regarding such fractional states. First of all, writing a wave function for such states is not an easy task and has led to some controversies [187, 196, 197, 218]. The first proposal motivated by a generalization of Laughlin's wave function [187] suffered from very low overlaps with the numerical wave functions, an issue fixed in [218]. The generalization to higher Chern number phases was given in [219]. In addition, there are still interesting open questions such as what is the nature of the counting anomalies in the entanglement spectra of higher Chern number phases revealed in Ref. [196] or whether all fractional Chern insulating phases have analogues in the fractional quantum Hall effect. Also it is to be understood the role, if any, of the underlying crystalline structure, i.e. the point group symmetry of each lattice, in determining the stability of such phases.

To conclude, with the findings in both the present and the previous chapter, we have learned that Dirac quasiparticle systems offer a natural playground to stabilize topological phases with quantized Hall conductivity out of many-body states that are generated from strong Coulomb interactions. Remarkably, both fractional and integer analogues of the quantum Hall state can be obtained and new physics regarding these remarkable quantum phenomena can be explored.

Part III.

Topology

6. Time reversal invariant topological phases from Dirac quasiparticles in $D = 2 + 1$

"Quantum field theory arose out of our need
to describe the ephemeral nature of life."
-Anthony Zee.

6.1. Introduction

So far in this thesis we have described interaction effects in Dirac quasiparticle systems. We have found that electron-electron interactions can lead to novel interesting phases characterized by topological properties such as the quantum Hall conductivity. This naturally leads to the question of how to characterize these topological phases, as well as what measurable physical effects might stem from them. Thus, this final part of the thesis will be concerned on the topological aspects of Dirac quasiparticle systems. We will try to describe precisely these phases, as well as to understand novel physical phenomena that stem from them. In the present chapter we will address partially the first question concerning the mathematical description of topological phases.

In more concrete terms, in past chapters we have understood how time reversal *breaking* topological phases, both integer and fractional can appear within two dimensional systems of Dirac quasiparticles out of interactions. The goal of this chapter is to introduce and describe how time reversal *invariant* topological phases in $D = 2 + 1$ dimensions arising from Dirac quasiparticles can be identified and analysed in a unifying way by means of the effective action formalism, a technique which has been widely used to understand and classify condensed matter systems [28].
The hallmark of time reversal invariant topological phases is the quantum spin Hall effect, characterized by a quantized spin Hall conductivity [1]. Research in this field had a crucial turning point with the proposal of Kane and Mele [60, 61] of realizing such a phase in graphene. This proposal was based on the realization of two copies of the spinless Haldane

[1] For an introduction to this phase we refer the reader to section 1.2.2 as well as the recent reviews [8, 9].

model [66] described in chapter 4, one for each spin so as to preserve time reversal symmetry. Bernevig Hughes and Zhang [67] proposed a different realization of the quantum spin Hall phase in Hg/Te heterostructures. The experimental confirmation of the latter proposal [69] together with the similarities to graphene through the Kane and Mele model, triggered the field of topological insulators and reinvigorated the use of tools borrowed from the mathematical field of topology [220] to understand physical phenomena.

In this context, the present chapter aims to deepen the understanding of the quantum spin Hall phases through a field theoretical approach that connects with the topological nature of the state. In the same way that the quantum Hall effect is characterized by a Hall conductivity related to a topological invariant [50], the quantum spin Hall effect will be characterized by a spin Hall conductivity which can be related to a different topological object [61]. We will therefore, try to unify and understand various Hall-like responses associated to different degrees of freedom. In particular we will identify valley [221–224] and spin [60, 61] Hall responses, to be defined precisely below, in mono and bilayer graphene. We will further extend these results analytically to a situation of finite chemical potential, generating time reversal invariant topological Fermi liquids in analogy with the time reversal broken topological phases we encountered in chapter 4.
The chapter is structured as follows. First we will present the graphene model as a realization of $D = 2 + 1$ Dirac quasiparticles, this time including the effects of spin-orbit coupling both in the intrinsic and Rashba forms, which shall generate topologically non trivial phases. We will also introduce a staggered potential to compete with the mentioned spin Hall phase. Next, we will generate the topological response by constructing the effective action that will define the topological invariant and give a concrete expression for it. Then, we will evaluate it for different physical situations and classify the phases focusing on the effect of chemical potential realizing in some cases time reversal invariant topological Fermi liquids. Finally we will apply the method to bilayer graphene focusing on both the spin and valley Hall responses.
As a whole, the present analysis tries to shed light, under a topological perspective, on the time reversal invariant topological phases that can arise from (non-interacting) Dirac quasiparticles realized in graphene and its bilayer.

6.2. Dirac quasiparticles in graphene with spin-orbit coupling

We begin by introducing the monolayer graphene model with different time reversal invariant perturbations. In order to connect the classification of topological phases that we will put forward in this chapter with real physical phenomena, we will use as a starting point the low energy theory for Dirac quasiparticles in graphene. As previously justified in this thesis,

one can construct a low energy Lagrangian in momentum space for Dirac quasiparticles in graphene at half-filling of the form [7]

$$\mathcal{H}_0(\mathbf{k}) = iv_F[\sigma_y\tau_z k_x - \sigma_x 1_\tau k_y]1_s \equiv \gamma^1 k_x + \gamma^2 k_y. \tag{6.1}$$

The Pauli matrices labelled σ, τ and s represent pseudospin, valley and spin degrees of freedom respectively. Therefore, the γ matrices are 8×8 matrices that form a representation of the Clifford algebra $\{\gamma^\mu, \gamma^\nu\} = 4\times 2g^{\mu\nu}$, with $g^{\mu\nu} = \text{diag}(1,-1,-1)$. With these conventions, the zeroth gamma matrix is defined as $\gamma^0 = 1_s 1_v \sigma_z$[2]. For convenience, we will use a set of units where the Fermi velocity $v_F = 1$ as well as $\hbar = 1$.

In many physical situations, most commonly concerning transport in graphene, it is enough to consider a spinless single valley Hamiltonian The effects of having two valleys and two spins can be taken into account simply by multiplying the result by 4 that accounts for the double degeneracy in valley and spin. It is important to note that, taken as an individual Hamiltonian, the 2×2 (sublattice) Hamiltonian constructed around a given Fermi point or valley $(K_{1,2})$ is not time reversal invariant ($\mathcal{T}$: $H(K_1) = H^*(K_2)$). Including the two valleys in a 4×4 matrix makes the full Hamiltonian $\mathcal{H}_0$ invariant under both inversion symmetry, realized as an interchange of sub-lattices A and B, and time reversal symmetry $\mathcal{T}$, realized by the interchange of the K_1 and K_2 valleys. These discrete symmetries, together with translation invariance, protect each of the Fermi points and prevent the opening of a gap in the spectrum [24].

In the following sections we will construct the various time reversal invariant topological phases that may arise from bilinear couplings in mono and bilayer graphene that can open topologically non trivial gaps. These can be included generically in the Lagrangian as

$$\mathcal{L}_0 = \bar{\psi}(\gamma^\mu k_\mu - \sum_i \lambda_i \Lambda_i)\psi, \tag{6.2}$$

where $\bar{\psi} = \psi^+\gamma_0$ and λ_i is the corresponding strength of the perturbation represented by the matrix Λ_i. These matrices model different physical phenomena in graphene that can generate time reversal invariant topological phases. With such a goal in mind we will consider the following time reversal invariant perturbations:

- **Staggered potential:** Physically this term is a charge asymmetry between the two sublattices A and B which breaks inversion and thus opens up a gap at zero energy. We have encountered such a phase when discussing topological Fermi liquids when including both nearest and next to nearest neighbour interaction in Chapter 4 and naturally occurs in hexagonal Boron Nitride monolayers. In the notation above it is represented by a matrix of the form

$$H_m = m\Lambda_m = m1_s 1_\tau 1_\sigma. \tag{6.3}$$

[2]Note that the matrices chosen differ from the convention used in [60] (γ_{KM}). The two are related by $\gamma^\mu = \sigma_z\gamma^\mu_{KM}$.

where the A and B have a certain on site energy $\pm m$. Since such an asymmetry does not break time reversal symmetry, the gap must have the same signs for both valleys.

- **Intrinsic spin orbit interaction:** In Ref. [60], Kane and Mele considered a spin orbit interaction in graphene that can arise from a spin dependent second nearest neighbour hopping term in the tight binding Hamiltonian (6.1). In the low energy sector it can be recast as a mass term with a structure given by

$$H_{so} = \Delta_{so}\Lambda_{so} \equiv \Delta_{so} s_z \tau_z 1_\sigma. \tag{6.4}$$

  This term preserves all the symmetries of the Hamiltonian (6.1) although it still opens a gap with different signs at the K and K' points. As a consequence, a Hamiltonian with Λ_m cannot be smoothly connected to a Hamiltonian with Λ_{so} since one has to pass through a gapless Hamiltonian. This fact turns out to be a distinguishing feature and will leave these Hamiltonians in different topological classes.
  The Kane and Mele model with Λ_{so} can be understood as two copies of the spinless Haldane model [66] discussed in the introduction of chapter 4, one for each spin. Separately the two copies violate time reversal symmetry and give a quantum Hall conductivity of $\sigma_{xy} = \pm e^2/h$ (one sign for each spin). If one considers both copies, the quantum Hall conductivity must be zero, since the system is time reversal invariant as we know from the table in section 4.3.2. However, the spin Hall conductivity ($\boldsymbol{J}_s = \boldsymbol{J}_\uparrow - \boldsymbol{J}_\downarrow$) need not be zero. In fact, as will be shown below, this last quantity is precisely what will be used to characterize the topological phases of the time reversal invariant insulator phases that can arise in graphene.
  It is worth pointing out that this type of term having an intrinsic origin is expected to be small, of the order of 1-15μeV [225] since it is proportional to the atomic number, which is small for graphene. Nevertheless, this value can be enhanced to the order of 0.1meV from the coupling of graphene electrons to phonons [73].

- **Rashba spin orbit coupling:** This type of spin orbit interaction has the same origin as the spin orbit interaction above but it is only present when mirror symmetry about the graphene plane is broken [60] for example from interaction with a substrate. It has the form

$$H_R = \lambda_R \Lambda_R \equiv \lambda_R i(s_y \tau_z \sigma_y + s_x 1_\tau \sigma_x). \tag{6.5}$$

  It is important to note that the Rashba coupling does not preserve s_z which will imply a non quantized spin Hall response.

- **Kekulé distortion:** This type of distortion also emerged from interactions in chapter 4 and can be interpreted as a spatial distortion of the hoppings with a larger (tripled) lattice periodicity [167, 226]. At low energies it can be described by a two atom unit cell and it takes the form $\lambda_K \Lambda_K = -i\lambda_K \tau_z 1_s \sigma_y$. We will omit any reference to this type of

term since the effect of the Kekulé distortion will be, as far as this chapter is concerned, equivalent to that of the staggered potential.

6.3. Constructing time reversal invariant topological phases using the effective action

As discussed in the introductory chapter, topological terms in the effective action can classify topological phases. In this chapter we are concerned with time reversal invariant topological phases in $D = 2+1$ dimensions, and thus we will discuss how to construct a response function which can distinguish between different phases. In particular, we will first summarize how the spin Chern-Simons term and its coefficient captures the essence of the Hall and spin Hall effect being thus a relevant term to characterize topological phases. Then we will introduce a way to generate such terms for generic topological phases on practical grounds when a generic mass like term Λ is considered in the Lagrangian (6.2) using graphene as an example (for a similar approach including other terms we refer the reader to Ref. [226]). A similar construction for topological insulators in three dimensions can be found in Ref. [227].

6.3.1. Hall and spin Hall conductivity from a Chern-Simons term

We start our discussion with the Chern-Simons action discussed in the introductory chapter which has, in $D = 2+1$ dimensions, the form

$$S_{CS} = \int d^3x \;\; \epsilon^{\mu\nu\rho} A_\mu \partial_\nu A_\rho, \tag{6.6}$$

where $\epsilon^{\mu\nu\rho}$ is the completely antisymmetric tensor and A_μ is the electromagnetic gauge field. In the presence of such term, the electromagnetic current defined as the variation of the action with respect to the gauge field A_μ through $j^\mu = \frac{\delta S}{\delta A_\mu}$ [75] is of the form

$$< j^\mu >= C\epsilon^{\mu\nu\rho}\partial_\nu A_\rho. \tag{6.7}$$

Choosing $\mu = x$ it is not difficult to see that the current is proportional to E_y and thus the coefficient is the Hall conductivity of such a system σ_{xy}. Therefore, the Chern-Simons theory encodes in this way all information about the Hall conductivity and its coefficient is related to a topological invariant [50].

Importantly, when two Dirac fermions related by time reversal symmetry are considered, each of them will contribute to C with an opposite value giving a null transverse current (6.7). Time reversal symmetry dictates that $C_\uparrow = -C_\downarrow$ and hence the total Chern number is $C = C_\uparrow + C_\downarrow = 0$. Therefore, in order to generate a Chern-Simons-like term in a time reversal invariant fashion we need to define the spin Hall current with $C_s = C_\uparrow - C_\downarrow$ that can be non zero in a time reversal invariant topological phase.

To show how this is achieved in practice consider the low energy model of graphene with

some mass-like term Λ. One can take for example the Kane and Mele model [60]. To describe the possible topological state originated by Λ, we need to couple the Dirac fermions to a proper background field V_μ which can describe the difference between a topological phase from a topologically trivial phase. To this extent, given a flavour, for example spin in the Kane and Mele model, we must couple the fermions to an external background V_μ field that couples to such a flavour:

$$S = \int \frac{d^3k}{(2\pi)^3}[\bar{\psi}(\gamma^\mu k_\mu - \Lambda)\psi - \bar{\psi}\gamma^\mu\psi A_\mu - \bar{\psi}\gamma^\nu\gamma_5\psi V_\nu]. \tag{6.8}$$

where we have included the coupling to an external electromagnetic field described by the gauge field A_μ.
The matrix γ_5 has to be chosen appropriately to ensure that the form of the current operator when we calculate the variation $\frac{\delta S}{\delta V_\mu}$ is such that the generalized Hall response is a sum in the flavour we are interested in. For instance, in the case of the spin current discussed by Kane and Mele [60] the matrix γ_5 is defined as

$$\gamma_5 = s_z 1_v 1_\sigma. \tag{6.9}$$

In this way after integrating out the fermions and calculating the lowest order terms in the effective action (explicit in the next section 6.3.2) , eq. (6.7) will be properly modified to give

$$< j^\mu_\uparrow - j^\mu_\downarrow > \equiv \frac{\delta S_{cs}}{\delta V_\mu} = C_s \epsilon^{\mu\nu\rho}\partial_\nu A_\rho. \tag{6.10}$$

The spin Chern-Simons coefficient C_s is given by $C_s = C_\uparrow - C_\downarrow$ [60] and can be non-zero for a time reversal invariant phase. Its value is related to a topological invariant [61], in a similar way as the coefficient C for the quantum Hall effect is also tied to a topological invariant [50]. It is possible to show [60, 63] that this phase is characterized by the presence of two spin polarized counter-propagating edge states at *each* edge.
This approach can be generalized to other degrees of freedom, in particular the valley degree of freedom. Similar to the Hall response (6.7) the valley Hall effect [221–224] has a quantized Hall response with valley polarized edge states. By properly modifying γ_5 to

$$\gamma_{5,v} = \tau_z 1_s 1_\sigma. \tag{6.11}$$

V_μ will couple to the valley index and a coefficient C_v can be defined in analogy with C and C_s which will also characterize the phase.

6.3.2. Emergence of Chern-Simons terms from Dirac quasiparticles

From the previous section the way to identify topological phases becomes clearer. If we are able to compute the coefficient C_s in the case of the spin Hall phase (or C_v in the case of the

valley Hall effect) for a given phase, we can classify it as trivial if it is zero or non trivial if it is different from zero. In this section we will write an explicit form for C_s (C_v can be obtained following analogous steps with $\gamma_{5,v}$ in (6.11)) in terms of the electronic Green's function.
To this extent, we will need the one-loop effective action $\Gamma_1[A,V]$ for the gauge field from which the linear response in A_μ and V_μ will be derived that shall contain the topological term. The effective action for A_μ is obtained by performing the functional Gaussian integration of the fermionic variables in the path integral as described in appendix C.2. Since (6.8) is quadratic in the fermions it is straightforward to evaluate the integral using the formulas in C.1 which is proportional to a functional determinant of the Kernel of (6.8). It reads

$$\Gamma[A,V] = \int \frac{d^3k}{(2\pi)^3} \mathrm{Tr} \ln \left(\gamma^\mu k_\mu - \Lambda - e\gamma^\mu A_\mu - \gamma^\nu \gamma_5 V_\nu\right). \tag{6.12}$$

The symbol Tr is to be understood as a trace over γ^μ matrices. We can now expand it in Taylor series of the potentials A_μ and V_ν to obtain the linear response that will generate the Chern-Simons terms that we are after. For that, we will formally define the free fermionic Green's function as

$$G(k,\Lambda) = \frac{i}{\gamma^\mu k_\mu - \Lambda}, \tag{6.13}$$

and we will write (6.12) as:

$$\Gamma[A,V] = \int \frac{dk^3}{(2\pi)^3} \sum_{n=1}^{\infty} -\frac{1}{n} \mathrm{Tr}\left[(G(k,\Lambda)(-ie\gamma^\mu A_\mu - ie\gamma^\nu\gamma_5 V_\nu))^n\right], \tag{6.14}$$

where we have dropped out an irrelevant (infinite) constant that does not depend on the fields A or V. In order to extract the spin Chern-Simons term we can concentrate in the $l=2$ term in this Taylor expansion since we are looking for a term of the form $V\partial A$. In momentum space, the $l=2$ term reads:

$$\Gamma^{l=2} = \frac{e^2}{2} \int \frac{d^3q}{(2\pi)^3} \frac{d^3k}{(2\pi)^3} \mathrm{Tr}\left[G(k)\gamma^\mu G(k+q)\gamma^\nu\gamma_5\right] V_\nu A_\mu. \tag{6.15}$$

Expanding $G(k+q)$ in series of q up to first order we can identify the corresponding Chern-Simons term which in real space reads:

$$S_{scs} = i \int d^3x C_s^{\mu\nu\rho} V_\mu \partial_\nu A_\rho, \tag{6.16}$$

where $C_s^{\mu\nu\rho}$ is defined as

$$C_s^{\mu\nu\rho} = -i\frac{e^2}{2} \int \frac{dk^3}{(2\pi)^3} \mathrm{Tr}\left[G(k,\Lambda)\gamma^\mu G(k,\Lambda)\gamma^\nu G(k,\Lambda)\gamma^\rho\gamma_5\right]. \tag{6.17}$$

Therefore, the coefficient of the spin Chern Simons term (6.10) is simply $C_s^{\mu\nu\rho} = C_s\epsilon^{\mu\nu\rho}$ and so we can use expression (6.17) to determine whether the system is in the quantum spin Hall

phase. For the case of the "valley" Hall insulator it is enough to substitute γ_5 defined in (6.9) for $\gamma_{5,v}$ (6.11) which will define C_v through (6.17).
Finally, it is interesting to note that (6.17) can be written in the form of a Pontryagin index [70, 220]

$$C_s^{\mu\nu\rho} = -i\frac{e^2}{2}\int \frac{d^3k}{(2\pi)^3} Tr[G\partial_{k^\mu}G^{-1}G\partial_{k^\nu}G^{-1}G\partial_{k^\rho}G^{-1}\gamma_5]. \tag{6.18}$$

which explicitly reveals the topological character of such a coefficient.

In what follows we will use these definitions to calculate the topological responses of the particular perturbations considered in section 6.2 that will serve to classify the topological phases. We will include the effect of the chemical potential to see how time reversal invariant topological Fermi liquids are realized in these systems as a generalization of the time reversal breaking topological Fermi liquid phases arising from electron-electron interaction studied in chapter 4.

6.4. Topological phases in monolayer graphene

6.4.1. An illustrative case: Intrinsic spin-orbit coupling

Although known in the literature for quite some time [60] it is illustrative to consider the case with only intrinsic spin orbit coupling (the Kane and Mele model) as a starting point to construct more elaborate situations. In the simple case of the spin orbit coupling with the chemical potential (μ) set to zero, it is trivial to check that Λ_{so} commutes with all the γ matrices and thus we can write $G(k, \Lambda_{so})$ as

$$G(k, \Lambda_{so}) = i\frac{\gamma^\rho k_\rho + \Delta_{so}\Lambda_{so}}{k^2 - \Delta_{so}^2}. \tag{6.19}$$

Written $G(k, \Lambda_{so})$ in this way, by the trace of the γ^μ matrices it is apparent that only the term proportional to Δ_{so}^3 will survive, being proportional to $8i\epsilon^{\mu\rho\nu}$ as well. Using (6.9), the integral (6.17) over momentum can be evaluated easily, as long as we note that the integral is insensitive to the sign of Δ_{so} (all the technical apparatus and details for the evaluation of this and the rest of the integrals in this chapter is included in appendix C.3). The result is [60]:

$$C_s^{\mu\nu\rho} = \epsilon^{\mu\nu\rho}\frac{e^2}{2}\int_0^\infty \frac{dk}{(2\pi)}\frac{2k\Delta_{so}}{(\mathbf{k}^2 + \Delta_{so}^2)^{3/2}} = e^2\epsilon^{\mu\nu\rho}\frac{\Delta_{so}}{2\pi|\Delta_{so}|} = e^2\frac{\epsilon^{\mu\nu\rho}}{2\pi}\text{sign}(\Delta_{so}). \tag{6.20}$$

This is a widely known result in field theory and can be related to the parity anomaly [65] among other phenomena. It can be proven that this number, $\text{sign}(\Delta_{so})$ is the same $\mathbb{Z}_2$ topological invariant defined by Kane and Mele in the case of two dimensional topological

insulators [61].

Consider now the case where a finite chemical potential is included. When $|\mu| > \Delta_{so}$, the chemical potential crosses one of the bands changing the position of the poles in (6.17). Thus, we obtain:

$$C_s^{\mu\nu\rho} = \epsilon^{\mu\nu\rho} \frac{\Delta_{so} e^2}{2\pi|\mu|}, \tag{6.21}$$

a result first obtained in [228]. When $|\mu| < \Delta_{so}$ the two poles in (6.17) are located always on different semi-planes (upper and lower) and so the integral gives the same result as in the case of zero chemical potential shown in (6.20).

These two results should be interpreted in analogy with the quantum Hall effect and the anomalous Hall effect along the lines of [55] and the discussion in chapter 4 (section 4.3.2) regarding the Hall conductivity of the emerging topological phases. Whenever the chemical potential lies inside the gap, the spin Hall response is quantized and given by the sign of the mass, in this case sign(Δ_{so}). As soon as we start filling the band, we enter a regime where there is a non quantized (or anomalous) contribution from electrons at the Fermi surface. The total spin Hall response in this case is non quantized and given by (6.21). Thus, as we increase the chemical potential from inside to outside of the gap there is a transition from a time reversal invariant topological insulator to a time reversal invariant topological Fermi liquid. We emphasize that this is the time reversal invariant version of the transition between the quantized Hall response in chapter 4 section 4.3.2 that lead to a non-quantized response as band five started to be filled.

It is also possible to calculate for this phase the valley Hall response by using (6.17) with the appropriate γ_5 as defined by (6.11) that couples to the valley degrees of freedom. In this case it is easy to show that $C_v = 0$ which can be understood in the following way. The valley Hall conductivity is a sum of the contributions of the two valleys $C_{K_{1,2}}$ so that $C_v = C_{K_1} + C_{K_2}$. As discussed above, the Kane and Mele model can be understood as two copies of the Haldane model, that has an opposite gap (mass) sign for each valley giving $C_v = C_{K_1} + C_{K_2} = 0$. Thus, this model is not a valley Hall insulator. Equivalently it is also possible to argue that the Kane and Mele model preserves inversion, which imposes that $C_{K_1} = -C_{K_2}$ and thus $C_v = 0$. With this simple calculation we learn how to proceed with more general cases and the effect that we should expect with the introduction of a chemical potential.

6.4.2. Competition between the intrinsic spin-orbit term and the staggered potential

We will follow the method sketched in the previous section to study analytically the competition of the spin-orbit term (6.4) with the staggered potential (6.3) in the presence of zero and finite chemical potential. The interest of this case resides on the fact that while both terms open a gap in the system, the nature of the insulating phase is different. Explicitly, the

relative magnitude of m and Δ_{so} will determine whether a valley, or a spin Hall insulator are realized. In fact, it will also introduce some technical complications whose resolution will be useful for the analysis of more complicated situations. The competition of the intrinsic spin-orbit term and the staggered potential was studied numerically in [60] for zero chemical potential. In what follows we will complete the discussion and give an analytical result valid for finite μ. A similar analysis for the Hall conductivity of a Haldane mass [66] and a staggered potential for zero chemical potential can be found in [226].

From section 6.2 the appropriate bilinear terms to be included in the Hamiltonian in this case is $M = m\Lambda_m + \Delta_{so}\Lambda_{so}$ where Λ_m and Λ_{so} are defined in (6.3) and (6.4) respectively. Consider first the case where the chemical potential is zero.

Zero chemical potential ($\mu = 0$)

The first difficulty that arises is that we can no longer write the Green's function in the simple form (6.19). In the previous case all the fermion flavours had the same dispersion relation, $E(\mathbf{k}) = \pm\sqrt{\mathbf{k}^2 + \Delta_{so}^2}$, and we were dealing with a multiflavour two band model. We only had two simple poles in the Green's function and the degeneracy of the system came from the matrix structure in the numerator of (6.19). When considering the two terms, this degeneracy is partially lifted and we have a non-degenerated multiband model. This can be easily seen by diagonalizing the Hamiltonian in the presence of the two terms. The four bands are given by the expressions $E_{1\pm}(\mathbf{k}) = \pm\sqrt{\mathbf{k}^2 + (m + \Delta_{so})^2}$ and $E_{2\pm}(\mathbf{k}) = \pm\sqrt{\mathbf{k}^2 + (m - \Delta_{so})^2}$. Effectively, our system is now made of two (doubly degenerated) two-band subsystems. However, although the denominator in (6.13) is not any more proportional to the identity matrix, it is still a diagonal matrix that can be easily inverted. Using expression (6.17) and following the recipe of the last section one can see that we have two copies of the spin orbit problem with two different masses given by $m \pm \Delta_{so}$. The result is accordingly:

$$C_s^{\mu\nu\rho} = e^2\frac{\epsilon^{\mu\nu\rho}}{4\pi}[\text{sign}(\Delta_{so} - m) + \text{sign}(\Delta_{so} + m)]. \tag{6.22}$$

It is clear that the interplay between a staggered potential and a spin orbit coupling is such that the Chern-Simons coefficient is still quantized. When $\Delta_{so} = 0$ we recover a topologically trivial insulator and when $m = 0$ we recover the result of the previous section, as expected. The new feature compared to previous results is that when both are non zero (and for $|\Delta| > |m|$) there is still a topological response of the system characterized by C_s.
In the opposite limit, $|\Delta| < |m|$, C_s is zero and it is possible to check that $C_v \neq 0$. The system is therefore a "valley" Hall insulator in this case. In general, the staggered potential m drives the system into a valley Hall insulator while Δ_s drives the system into a spin Hall insulator. When both are present, as in this case, the two perturbations compete and it is their relative magnitude that decides the type of topological phase that is realized.

Finite chemical potential $\mu \neq 0$

Let's turn now to the case of having a finite chemical potential, which shall complement the above result. Similarly to what happened in the intrinsic spin orbit case, depending on the relative value of μ against $\Delta_{so} \pm m$ we will have different results. Without doing any extra work we can read the result from the considerations made in the case of the intrinsic spin-orbit coupling by changing the masses appropriately. There are four different cases:

- $|\mu| < |\Delta_{so} - m|$ and $|\mu| < |\Delta_{so} + m|$: Under these conditions the chemical potential lies inside both gaps gap and the response is still quantized:

$$C_s^{\mu\nu\rho} = e^2 \frac{\epsilon^{\mu\nu\rho}}{4\pi} (\text{sign}(\Delta_{so} - m) + \text{sign}(\Delta_{so} + m)). \tag{6.23}$$

- $|\mu| > |\Delta_{so} - m|$ and $|\mu| > |\Delta_{so} + m|$:
  In this case, the chemical potential crosses the bands for both masses and hence both integrals give a non-quantized result analogous to (6.21):

$$C_s^{\mu\nu\rho} = e^2 \frac{\epsilon^{\mu\nu\rho}}{4\pi} \left(\frac{\Delta_{so} - m}{|\mu|} + \frac{\Delta_{so} + m}{|\mu|} \right) = e^2 \frac{\epsilon^{\mu\nu\rho}}{2\pi} \left(\frac{\Delta_{so}}{|\mu|} \right). \tag{6.24}$$

  It is interesting to note that this result does not depend on the value of m. Finally, the two cases left can be written in a compact way:

- $|\mu| > |\Delta_{so} \mp m|$ and $|\mu| < |\Delta_{so} \pm m|$:
  These are the cases where one integral gives a topological contribution, as the chemical potential lies inside one of the gaps, but the other subspace gives a non-quantized contribution as the chemical potential crosses one of its bands. Hence, the result is:

$$C_s^{\mu\nu\rho} = e^2 \frac{\epsilon^{\mu\nu\rho}}{4\pi} \left(\frac{\Delta_{so} \mp m}{|\mu|} + \text{sign}(\Delta_{so} \pm m) \right). \tag{6.25}$$

  The $\pm$ signs indicate whether it is the conduction or the valence band which is crossed by the chemical potential.

To summarize, from these simple analytic results one infers that there is a competition between the staggered potential and the intrinsic spin orbit, conditioned by the presence of the chemical potential.

6.4.3. Competition between a Rashba coupling and intrinsic spin-orbit coupling at finite chemical potential

The competition of the intrinsic spin orbit coupling and the Rashba contribution was already studied in the original reference [60] for zero chemical potential. As the Rashba term by itself does not open a gap in the spectrum it was found that the topological insulating phase only exists for absolute values of Δ_{so} bigger than $|\lambda_R|$. The inclusion of a finite chemical potential

makes the physical analysis more interesting. Unlike the previous cases, this is more complex and a general analytical treatment with arbitrary μ is cumbersome. A detailed calculation can be found in [228]; in what follows we will complete their analysis with analytical results together with an interpretation of the divergences that appear in this case.
The band structure when both Δ_{so} and λ_R couplings are included is shown in figure 6.1. As discussed earlier, in the presence of a Rashba term λ_R the s_z spin component is no longer a good quantum number and we do not expect the spin Hall conductivity to be quantized. After performing the trace in (6.17), the integral left is given by:

$$C_s^{\mu\nu\rho} = \frac{e^2}{2}\int \frac{dk^3}{(2\pi)^3}(-8i)\epsilon^{\mu\nu\rho}\frac{\left(4\lambda_R^2(k_0+\Delta_{so})\left(k_0(k_0+\Delta_{so})-k_x^2+k_y^2\right)+\Delta_{so}\left(-k_0^2+\mathbf{k}^2+\Delta_{so}^2\right)^2\right)}{\left(\left(-k_0^2+\mathbf{k}^2+\Delta_{so}^2\right)^2-4\lambda_R^2(k_0+\Delta_{so})^2\right)^2}, \tag{6.26}$$

In this particular case the poles are located at $k_0^{\pm A} = \pm\sqrt{\mathbf{k}^2+(\lambda_R-\Delta_{so})^2}-\lambda_R-\mu$ and $k_0^{\pm B} = \pm\sqrt{\mathbf{k}^2+(\lambda_R+\Delta_{so})^2}+\lambda_R-\mu$. We will now consider the cases where analytical results can be derived in order to complete the analysis of [228].

The case $\mu = -\Delta_{so}$

The simplest case (regarding its pole structure) is the case $\mu = -\Delta_{so}$ (see Fig. 6.1), since for all values of the parameters there are two bands below (and two above) the chemical potential, therefore defining the same pole structure for all values of $\mathbf{k}$. Since the chemical potential is placed at a special point of the band structure were the bands meet when the gap closes, we expect to have divergences which we interpret as the divergent contribution from the zero modes.
There are eight possible cases depending on the sign of λ_R, Δ_{so}, $\Delta_{so}+\lambda_R$ and $\Delta_{so}-\lambda_R$. Since the integral in (6.26) does not distinguish the sign of λ_R we can safely assume $\lambda_R > 0$. This reduces the problem to four cases:

- $\Delta_{so} > 0$, $\Delta_{so}+\lambda_R > 0$ and $\Delta_{so}-\lambda_R > 0$:
  In these conditions the gap remains open ($\Delta_{so} > \lambda_R$) we get a finite result:

$$C_s^{\mu\nu\rho} = e^2\frac{\epsilon^{\mu\nu\rho}}{4\pi}\frac{\Delta_{so}}{\lambda_R}\ln\left|\frac{\lambda_R+\Delta_{so}}{\lambda_R-\Delta_{so}}\right|. \tag{6.27}$$

  Note that when $\lambda_R/\Delta_{so} \to 0$ we can make use of the relation

$$\operatorname{arctanh}(x) = \frac{1}{2}\ln\left(\frac{1+x}{1-x}\right),$$

  to recover (6.20), the standard result with the sign function obtained for Δ_{so} only.

- $\Delta_{so} < 0$, $\Delta_{so} + \lambda_R < 0$ and $\Delta_{so} - \lambda_R < 0$:
  With an analogous analysis one arrives to the same expression but with a sign difference, which accounts for the change in sign of Δ_{so}.

- $\Delta_{so} > 0$, $\Delta_{so} + \lambda_R > 0$ and $\Delta_{so} - \lambda_R < 0$:
  In this case, one can see that the integral diverges. As explained above, we now have a semi metal with the chemical potential set at the touching point of the bands. The contribution of the $\mathbf{k} = 0$ particles turns the integral to be divergent.

- $\Delta_{so} < 0$, $\Delta_{so} + \lambda_R > 0$ and $\Delta_{so} - \lambda_R < 0$:
  Again, the integral is found to be divergent but with an opposite sign.

We can summarize the above result in two compact expressions. For the case when the gap is opened, i.e. $\Delta_{so} > \lambda_R > 0$ and $\Delta_{so} < -\lambda_R < 0$, one can write:

$$C_s^{\mu\nu\rho} = e^2 \text{sign}(\Delta_{so}) \frac{\epsilon^{\mu\nu\rho}}{4\pi} \frac{\Delta_{so}}{\lambda_R} \ln \left| \frac{\lambda_R + \Delta_{so}}{\lambda_R - \Delta_{so}} \right|. \tag{6.28}$$

For the other case ($\lambda_R > \Delta_{so} > -\lambda_R$) where the gap is closed the integral diverges as $C_5^{\mu\nu\rho} \to \text{sign}(\Delta_{so})\infty$ as a result of the particular position of the chemical potential, where it encounters an infinite contribution from degenerate zero modes.

The case $\mu = 0$

When $\mu = 0$ it is immediate to notice that two of the bands can cross the Fermi energy and so the chemical potential lies inside the gap or crosses one of the bands, depending on the value of the parameters (see figure 6.1). Again the integral (6.26) which we have to evaluate has poles at the dispersion relation. An important difference with respect to other cases is that the poles have a non-trivial dependence on $\mathbf{k}$. We consider some illustrative cases:

- $\Delta_{so} > 0$, $2\lambda_R > \Delta_{so} > \lambda_R$:
  This corresponds to a situation where the gap is open but the chemical potential is such that it intersects one of the bands, hence being the system metallic. The result is given by:

  $$C_s^{\mu\nu\rho} = e^2 \frac{\epsilon^{\mu\nu\rho} \Delta_{so}}{4\pi\lambda_R} \ln \left| \frac{\Delta_{so}}{2(\lambda_R + \Delta_{so})} \right|. \tag{6.29}$$

  Interestingly, the case where $\Delta_{so} > 0$, $\lambda_R > \Delta_{so}$ gives the same result. In this case the chemical potential intersects one of the bands but the gap is closed. These results suggest that when the chemical potential intersects one of the bands and hence the system becomes metallic, it does not matter whether a gap is open or not below the chemical potential as both situations give the result shown above.

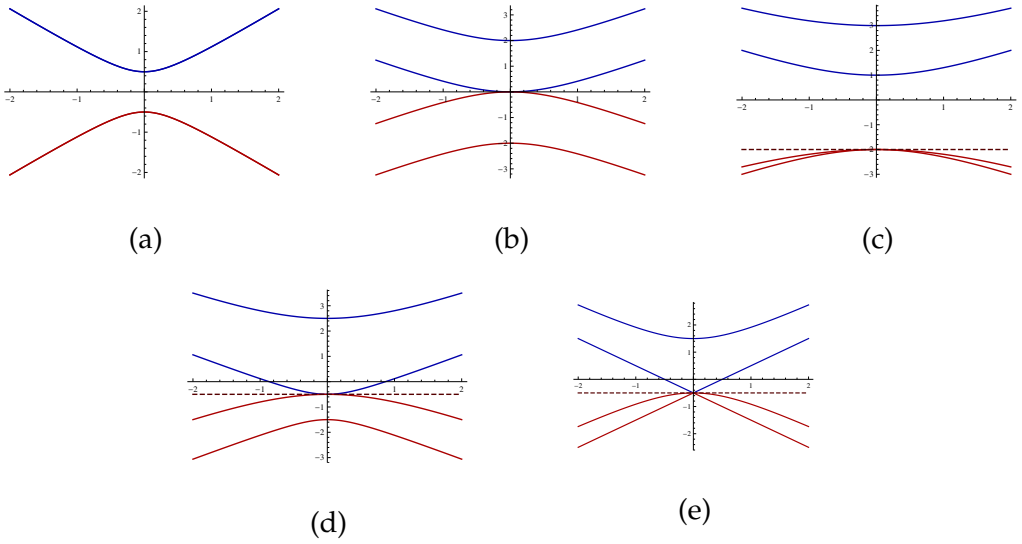

Figure 6.1.: Band structure for different values of λ_R and Δ_{so}. (a) With $\lambda_R = 0$ and $\Delta_{so} \neq 0$ a gap opens. The bands are degenerate in spin. (b) With $\lambda_R \neq 0$ and $\Delta_{so} = 0$ the gap is closed but the spin degeneracy is lifted. (c) With $\lambda_R < \Delta_{so}$ a gap opens in the spectrum.(d) With $\lambda_R > \Delta_{so}$ the gap closes. (e) When $\lambda_R = \Delta_{so}$ three of the bands touch which leads to a divergence in $C_5^{\mu\nu\rho}$ (see text). The horizontal solid line indicates where the chemical potential would lie if it was fixed at $\mu = -\Delta_{so}$. The band structure at this point generates a divergence when $\lambda_R > \Delta_{so}$.

- $\Delta_{so} > 0$, $\Delta_{so} > 2\lambda_R$:
  In this case, the chemical potential falls inside the bulk gap and so this situation is reminiscent of the situation with $\mu = -\Delta_{so}$ when the gap is open. The result is the one given in (6.27).

As expected, we recover the result for the previous section, but, since the chemical potential is not at a singular point we do not encounter divergences. The other cases left can be worked out in a similar fashion. Since the information they carry is redundant they will not be discussed further.

We have thus completed the analysis made in [228] by introducing several novel analytical results together with an interpretation on the origin of the divergences. The competition of Δ_{so}, λ_R and staggered potential at zero chemical potential was studied in [61] and we will not analyse it here.

6.5. Bilayer Graphene

6.5.1. The model

It is possible to extend the previous analysis to bilayer graphene where in addition to the valley ($\boldsymbol{\tau}$), spin ($\mathbf{s}$) and pseudospin ($\boldsymbol{\sigma}$) degrees of freedom we have the layer degree of freedom ($\boldsymbol{\mu}$). The new degree of freedom enables a richer playground for time reversal invariant topological phases. The effective action formalism allows to span these phases with little effort, as we shall discuss next.

To describe the Bernal stacked graphene bilayer we will use the simple model introduced in section 1.1.2 [7] which, in the notation of this chapter gives rise to the following Lagrangian

$$\mathcal{L}_0^{(b)} = \bar{\psi}(\gamma^\mu k_\mu - \sum_i \lambda_i \Lambda_i)\psi, \tag{6.30}$$

where the bilinear couplings will be described below and the γ matrices are now constructed in the space of valley, pseudospin, spin, and layer. Following the notation of the monolayer they are chosen to be $\gamma_0 = 1_\tau 1_s 1_\mu \sigma_z$, $\gamma_1 = i\tau_z 1_s 1_\mu \sigma_y$, $\gamma_2 = -i1_\tau 1_s 1_\mu \sigma_x$.

The first bilinear term included in this analysis is part of the bilayer model, the direct interlayer hopping term $t_\perp$, which in a consistent notation reads

$$\lambda_t \Lambda_t = \frac{1}{2} t_\perp 1_s 1_\tau i(\mu_y \sigma_x - \mu_x \sigma_y). \tag{6.31}$$

It is important to consider as well the effect of an external gate potential V which induces a charge asymmetry in both layers opening a gap [31]. This term has the form

$$\lambda_V \Lambda_V = V 1_s 1_\tau \mu_z \sigma_z. \tag{6.32}$$

In addition we shall consider two additional types of bilinear terms, the staggered potential and the various spin-orbit couplings given in [229]. The staggered potential is just the trivial extension of the monolayer inducing an asymmetry between A and B sublattices in each layer. It is given by

$$\lambda_m^{(b)} \Lambda_m^{(b)} = m 1_\tau 1_s 1_\mu 1_\sigma,$$

where the superscript (b) denotes bilayer graphene.

From symmetry considerations, it is possible following [229] (see also [230]), to construct the following spin orbit terms (in the notation of [60]):

$$\begin{aligned} \lambda_{so}^{(b)} \Lambda_{so}^{(b)} &= \lambda_1 \tau_z s_z 1_\mu \sigma_z + \lambda_2 \tau_z s_z \mu_z 1_\sigma + \lambda_3 \left(1_\tau s_x \mu_z \sigma_y - \tau_z s_y \mu_z \sigma_x\right) + \\ &+ \lambda_4 \left(1_\tau s_x \mu_y \sigma_z + \tau_z s_y \mu_x \sigma_z\right). \end{aligned}$$

The first term is the one corresponding to the (monolayer) intrinsic spin orbit coupling also known as the Kane and Mele spin orbit term. The last three terms, which involve μ are intrinsic to bilayer graphene where the ones proportional to λ_3 and λ_4 are Rashba-like terms. In

what follows we will see that the effect of λ_1 and λ_2 is to open a non-trivial gap in the spectrum and so turning the system into a topological insulator with unprotected edge states. As in the monolayer case, both Rashba-like terms will spoil the quantization of the topological phase having a similar effect as in the monolayer [231] and hence we will focus mainly on the effect of λ_1 and λ_2 as they compete with m and V.
The estimates from first principles set these parameters to be in the μeV range. In particular, $\lambda_1 \sim 12\mu$eV, $\lambda_2 \sim 10\mu$eV, $\lambda_3 \sim 5\mu$eV and $\lambda_4 \sim -12\mu$eV (see Table I in Ref. [232] and references therein). Although these are as small as in the monolayer case they could be enhanced in a similar manner by other effects such as electron-phonon coupling.
Having established the Lagrangian, it is possible to construct the spin Hall current in analogous way to the monolayer case. The spin Chern-Simons term will be associated to the matrix

$$\gamma_5 = 1_\tau s_z 1_\mu 1_\sigma.$$

As before, the presence of the topological phase is determined by the value of the coefficient C_s given by (6.17). Its computation follows the lines described in section 6.4. A non zero value indicates that the system is a spin topological Hall insulator [3] with edges that support spin currents. Also, as discussed in section 6.3.2, the present formalism allowed us to describe other types of insulators by appropriately redefining γ_5 to resolve other degrees of freedom. We will analogously compute the "valley" Chern number C_v to study the "valley" topological insulator character of the system. This insulator can be characterized by using a matrix

$$\gamma_{5,v} = \tau_z 1_s 1_\mu 1_\sigma,$$

in (6.17) tailored to resolve the valley degree of freedom, and thus generate a "valley" Hall conductivity. As before, a non zero value of this coefficient implies a topological insulator with valley polarized edges.

6.5.2. Summary of the results for bilayer graphene:

The calculation of C_s for bilayer graphene follows the same lines described previously for the case of the monolayer and the results are summarized in Table 6.1 where the non zero couplings are listed ($t_\perp$ is always non zero and positive). As discussed above, we have also calculated C_v, the "valley" Chern number calculated with γ_5 replaced by $\gamma_{5,v}$ in the trace (6.17). Technical details are omitted since in the derivation of the results the integrals appearing are similar to the monolayer case detailed earlier and no new technical issue appears for the case of the bilayer.
Nevertheless, the table also includes why the result vanishes in cases when it is zero, and the method of evaluation of the spatial part of the momentum integral if the result is finite.

[3] The chemical potential in all studied cases for bilayer graphene is set to zero, falling in all cases inside a gap, which justifies the word insulator.

The chemical potential in all cases is set to zero, which in all cases falls inside the gap. With this set up, no band crosses the Fermi energy and the integrals are easily evaluated since the poles do not switch complex semi-planes just as in the monolayer case at zero chemical potential (see appendix C.3)

$\neq 0$ couplings	C_s	C_v
$V \neq 0$	0 (trace vanishes)	$\frac{2e^2}{2\pi}\text{sgn(V)}$ (numerical)
$\lambda_1 \neq 0$	$\frac{2e^2}{2\pi}\text{sgn}(\lambda_1)$ (analytic)	0 (trace vanishes)
$\lambda_2 \neq 0$	$\frac{2e^2}{2\pi}\text{sgn}(\lambda_2)$ (numerical)	0 (trace vanishes)
$\lambda_3 \neq 0$	0 (vanishes by parity)	0 (trace vanishes)
$\lambda_4 \neq 0$	0 (trace vanishes)	0 (trace vanishes)
$\lambda_1 \neq 0\ \lambda_2 \neq 0$	$\frac{2e^2}{2\pi}\text{sgn}(\lambda_1+\lambda_2)$ (numerical)	0 (trace vanishes)
$\lambda_1 \neq 0\ V \neq 0$	$\frac{e^2}{2\pi}(\text{sgn}(\lambda_1+V)+\text{sgn}(\lambda_1-V))$ (numerical)	$\frac{e^2}{2\pi}(\text{sgn}(V+\lambda_1)+\text{sgn}(V-\lambda_1))$ (numerical)
$\lambda_2 \neq 0\ V \neq 0$	$\frac{e^2}{2\pi}(\text{sgn}(\lambda_2+V)+\text{sgn}(\lambda_2-V))$ (numerical)	$\frac{e^2}{2\pi}(\text{sgn}(V+\lambda_2)+\text{sgn}(V-\lambda_2))$ (numerical)
$m \neq 0$	0 (trace vanishes)	$\frac{2e^2}{2\pi}\text{sgn}(m)$ (analytic)

Table 6.1.: Classification of the two topological insulating phases of bilayer graphene considered in the text.

We will now comment shortly on the implications of the results presented in Table 6.1 regarding the topological nature of bilayer graphene.
The first thing to notice is that these results indicate that bilayer graphene can be a “valley" topological insulator, as it has been recently suggested [224] by only applying a gate voltage V and also a quantum spin Hall insulator when λ_1 and λ_2 are present. Both λ_1 and λ_2 open a gap in the spectrum and realize individually topologically non trivial phases characterized by a quantized C_s.
However, note that the Chern number for bilayer graphene is two times bigger than for the case of the monolayer in all cases. This even Chern number implies that we have two pairs of spin polarized channels in each edge which can hybridize with a time reversal invariant perturbation. This is in sharp contrast with the monolayer case with only one pair of spin polarized edge states at each edge, since only a time reversal breaking perturbation can hybridize these edge states. Thus, in the cases with $C_s \neq 0$ bilayer graphene behaves as a topological insulator with unprotected edge states [233]. The result that bilayer graphene is a topological insulator for λ_1 was already mentioned in [229]. Our new result is the addition of λ_2 that also seems to make the bilayer system a time reversal invariant topological insulator. The origin of a non-trivial gap given by λ_2 can be traced back to the matrix form of this coupling, together with the form of a $t_\perp$ coupling in bilayer graphene and the structure of γ_5. All these together provide the complete set of matrices in the layer index $(\mu_x, \mu_y, \mu_z, 1_\mu)$ so that the trace does not vanish and a non trivial spin Chern-Simons is generated, having however a “layer-like" origin. It is easy to check that when $t_\perp = 0$, λ_2 does not contribute to

the spin Chern-Simons term. In contrast, λ_1 in this situation still does contribute, indicating that the coupling between layers is of critical importance for this spin-orbit like coupling to have an effect.

From the table of results it is clear that the combined perturbation λ_1 and λ_2 can enhance the topological spin Hall response. That λ_2 has the same effect can be understood in terms of the effective low energy Hamiltonian since, if we only keep the two lowest energy bands in the model, and perform a symmetry analysis of the effective model, only the Kane-Mele term is allowed which will have a contribution from λ_1 and λ_2 [230].

The case with $\lambda_i \neq 0$ $(i = 1, 2)$ and $V \neq 0$ is analogous to the monolayer case where the staggered potential competes with the spin orbit coupling discussed in section 6.4.2. As expected, the trivial coupling is V when calculating C_s and λ_i when calculating C_v. This indicates that the (valley) topological nature of the bilayer dominates when the gate potential V wins over the spin-orbit coupling λ_i.

As expected from the monolayer case and discussed in detail in [231], the Rashba like terms λ_3 and λ_4 lead to a non quantized value of C_s since they do not conserve the spin component s_z.

Finally, putting together all the results of Table 6.1, it is evident that bilayer graphene is a rich playground to understand the competition between different topological phases, although this time edge states are not robust under generic time reversal invariant disorder (charged impurities for example), unlike for monolayer graphene. Note as well that the appearance of topological time reversal invariant Fermi liquids with a non quantized spin or valley Hall response will follow as in the discussion of the monolayer graphene case as soon as a finite chemical potential is considered.

6.6. Discussion and Conclusions

In this chapter we have developed a systematic method to classify time reversal invariant topological phases from an effective action formalism, arising from Dirac quasiparticle systems. This has enabled us to understand the topological invariants as arising from a Chern-Simons term in the effective action for a given fermionic flavour (spin, valley etc).

For monolayer graphene this approach has enabled us to calculate the spin Hall response whenever an intrinsic and/or Rashba type spin orbit coupling are included in the model. In the case of having zero chemical potential, a situation with intrinsic and Rashba spin-orbit term was studied in the original work of Kane and Mele [60]. Here, we have added chemical potential to the cases with and without the Rashba term to realize that the system manifests a non quantized spin Hall response. This response competes against a staggered potential, a charge imbalance between A and B sites whenever it is present which works to drive the system into a valley Hall insulator. The system realizes a topological time reversal invariant

Fermi liquid as soon as the chemical potential crosses one of the bands in the spin Hall phase. The spin Hall response, although still finite in this case, is not quantized.
For the bilayer case several spin-orbit couplings are allowed and not all of them drive the system to the spin Hall phase. We have shown that the system is a spin Hall insulator for $\lambda_{1,2}$ which are similar to the intrinsic spin-orbit in graphene of the Kane-Mele type. The staggered potential and an external gate voltage act against this phase, driving the system into a "valley" Hall insulator. Although encouraging, the topological phases in bilayer graphene are less robust since this time edge states can be hybridized under generic time reversal invariant disorder, charged impurities for example, unlike monolayer graphene spin Hall phase which can only open a gap in the edge states with a time reversal breaking perturbation such as with the presence of magnetic impurities [233].
In addition, to describe the bilayer, we have chosen the simplest Hamiltonian with only direct hopping between sites A and B in different layers. In general however, as discussed in section 6.5, other couplings could be taken into account which might act against the topological phases discussed here. An extension of the findings presented here that includes an intrinsic asymmetry between layers can be found in Ref. [234] (see also [235–237] for other couplings and AA stacking).

To summarize, the power of the effective action formalism is that it is generic. Any topological phase arising from Dirac quasiparticles systems in $D = 2 + 1$ can be classified using this approach, since, as we showed one can construct the appropriate topological response out of the effective action.
Having understood how the classification works for two dimensional topological Dirac quasiparticle systems, we will explore some physical effects of their three dimensional counterparts, the three dimensional time reversal invariant topological insulators, starting with the Casimir effect in the next chapter, that will motivate the study the finite frequency description of the response in these materials.

7. Repulsive Topological Casimir effect

"Une certaine force attractive"
-'Album of the Mariner' by P. C. Causseé

7.1. Introduction

The Casimir effect [238–240] is perhaps one of the most striking macroscopic quantum phenomena. In its simplest version it is the attraction between two uncharged metallic plates due to quantum fluctuations of the electromagnetic vacuum, which was discovered theoretically by H. B. G. Casimir when trying to model van der Waals forces between molecules. First and to understand intuitively what is meant by "quantum fluctuations of the electromagnetic vacuum" let us sketch a classical maritime analogy [92].
In the 19th century, P. C. Causse published in France the book "Album of the Mariner" containing drawings and advices to handle different marine situations. One of the situations he described was when two ships suffered from "une certaine force attractive" that was not originated in the wind, which he supposed to be calmed, but on the large swell which made the rolling of the boats undamped. In a beautiful paper, Boersma [92] showed that each of the two ships re-emitted the wave power as secondary waves which interfered with each other as resulting from imposing boundary conditions to the fluctuating vacuum, in this case the sea. If the swell had a bigger wavelength than the distance between the ships a smaller energy density is stored between the two ships than on the outside, creating an imbalance and thus attraction.
With this picture in mind, consider a toy model for the electromagnetic field considered as an infinite sum of oscillators with energy

$$E_n = \hbar\omega_n \left(n + \frac{1}{2}\right), \quad n \in \mathbb{Z}. \tag{7.1}$$

It's zero point energy is infinite and given by $E_0 = \sum_n \frac{1}{2}\hbar\omega_n$. For the proper electromagnetic vacuum, the modes are really labelled by the continuous three-dimensional wave vector $\mathbf{k}$. As we know, this vacuum energy is usually discarded since physical quantities depend only on energy differences. However, in the presence of two plates, perpendicular to the unit vector $\hat{z}$ for example, the fact that the fields must vanish at the plates imposes that the k_z

becomes discrete. The difference between the two energies (with and without plates) was first calculated by Casimir [238] building upon on a work published together with D. Polder [241]. He showed that, after regularizing the infinities (for instance introducing a physical frequency cut-off at the order of which the plates become transparent) the energy density per unit area stored between the plates is finite, only depends on the distance between these and it is given by

$$E(d) = -\frac{\pi^2}{720}\frac{\hbar c}{d^3} \tag{7.2}$$

From which an attractive pressure, the Casimir pressure is obtained through $P(d) = -\frac{\partial E(d)}{\partial d}$, predicting that two uncharged plates should attract in vacuum. Note that the Casimir force is both a relativistic and a quantum force, since it contains both $\hbar$ and c. For two atoms (or molecules) it is possible to show that its non-relativistic version is in fact the London-van der Waals force [239]. In this case, the fluctuating quantum vacuum induces electric dipoles at the two atoms or molecules resulting in an attraction between the dipoles. When distances are such that retardation effects become important, the London-van der Waals is known as the Casimir force, or sometimes, retarded van der Waals force. All of these phenomena are known collectively as *dissipation forces*.

The generalization of the theory to treat the Casimir force between dielectric bodies had to wait for the pioneering work of Dzyaloshinskii and E. M. Lifshitz and L. P. Pitaevskii [242] which is the basis of the modern formulation of the theory. The modern approach formulates the Casimir force in terms of the reflection coefficients of the involved bodies, which amounts to choose the boundary conditions on the electromagnetic vacuum [243]. The first experimental signature of the Casimir force came in 1997 with the pioneering experiments by Lamoreaux [244]. He placed an Au-coated spherical lens close to a flat plate from which the force is extracted with a torsion pendulum. This experiment triggered the field and paved the way to the understanding of other Casimir related phenomena.

Perhaps the most important of those, technologically speaking, are the efforts to revert the Casimir force. It is known for example that the Casimir force is responsible for the sticking of micro-mechanical parts in the so called micro-electro-mechanical systems (MEMS) an effect to be avoided if one is to use these systems technologically. Already from the Dzyaloshinskii-Lifshitz-Pitaevskii [242] formulation of the Casimir effect, it was known that introducing a dielectric medium with dielectric function ε_2 between the two bodies with dielectric functions ε_1 and ε_3 can revert the sign of the force if the dielectric functions of the three media satisfied the condition $\varepsilon_1 > \varepsilon_2 > \varepsilon_3$. This prediction was confirmed experimentally very recently, achieving repulsion between test bodies immersed in a dielectric fluid [245]. However, achieving repulsion in vacuum, which would have important consequences for device applications [239, 246], is still to be experimentally tested. Theoretically, there have been several proposals to achieve such situation. The first proposal considered magnetic versus

non-magnetic situations [247] and more recent proposals include the use of metamaterials [248–250] or engineered geometries to induce repulsive scenarios [251]. The difficulty in realizing such a repulsion is rooted on several theorems that show that for general dielectric-dielectric situations, there is no repulsive behaviour in vacuum [252–254].
In this chapter we will address this problem and show that repulsive behaviour could be achieved by using topological insulators [8, 255–257] by exploiting their topological features arising from Dirac quasiparticles. We will review the fact that the topological nature of these materials [77, 78] provides a magnetoelectric term that modifies their response to an external electromagnetic field, and then use it to show how it can cause the Casimir effect to reverse sign at short distances and remain attractive at large distances. Consequently, at an intermediate distance d_{eq}, the Casimir force vanishes and a stable configuration is possible. These materials, being magnetoelectric materials lie outside of the premises of the mentioned theorems and thus can host repulsive forces. To achieve a closer connection with experiments the effects of temperature and uniaxial anisotropy will be included.
Anisotropy can modify the Casimir force by changing the form of the reflection coefficients [239], an effect which has also been studied in the context of repulsive interactions [258] including the effect of temperature [259]. The question of whether uniaxial anisotropy and temperature can enhance or destroy the repulsive behaviour in the context of topological insulators will be addressed to pin down in what cases can this occur. To achieve this goal we will first introduce the modern formulation of the Casimir effect. Then derive the reflection coefficients for a generic topological insulator, first with and then without anisotropy. With the help of these coefficients, we will calculate the Casimir force between two topological insulating bodies and show that, under certain circumstances it can become repulsive at short distances and attractive at long distances with an intermediate distance d_{eq} where the force vanishes. We will then include the effect of temperature and anisotropy in these findings and show that low temperatures and enhancing uniaxial anisotropy in the direction parallel to the optical axis favours repulsion.

7.2. Casimir-Lifshitz force

The modern approach to Casimir forces for a collection of bodies of arbitrary shape was developed very recently by using a scattering approach [243]. The calculation amounts to determining the scattering amplitudes for the electromagnetic field from each object and then connecting them by an appropriate translation operation. For two semi-infinite parallel bodies however, the calculation is greatly simplified and the scattering is governed by the reflection coefficients of the objects. Here however we will not derive the general formula, which is outside the scope of the present chapter, but rather we will just state the result and then justify it *a posteriori* with two examples (see [239, 243] for details).

The Casimir energy density stored by two dielectric bodies (labelled 1 and 2) of cross-sectional area A, separated by a distance d, at zero temperature ($T = 0$) can be written as [239, 242, 243, 260]:

$$\frac{E_c(d)}{A\hbar} = \int_0^\infty \frac{d\xi}{2\pi} \int \frac{d^2\mathbf{k}_\parallel}{(2\pi)^2} \log\det\left[1 - \mathbf{R}_1 \cdot \mathbf{R}_2 e^{-2k_3 d}\right], \tag{7.3}$$

where $k_3 = \sqrt{\boldsymbol{k}_\parallel^2 + \xi^2/c^2}$ is the wave vector perpendicular to the plates, $\boldsymbol{k}_\parallel$ is the vector parallel to the plates and ξ is the imaginary frequency defined as $\omega = i\xi$. The matrices $\mathbf{R}_{1,2}$ are 2×2 reflection matrices of the two bodies. The entries of these matrices, the Fresnel coefficients, can be labelled as:

$$\mathbf{R} = \begin{bmatrix} R_{s,s}(i\xi, \mathbf{k}_\parallel) & R_{s,p}(i\xi, \mathbf{k}_\parallel) \\ R_{p,s}(i\xi, \mathbf{k}_\parallel) & R_{p,p}(i\xi, \mathbf{k}_\parallel) \end{bmatrix}, \tag{7.4}$$

where $R_{i,j}$ describes the reflection amplitude of an incident wave with polarization i which is reflected with polarization j. The label s (p), equivalent to TE (TM) modes, describes parallel (perpendicular) polarization of the electric field with respect to the plane of incidence. The Casimir force per unit area on the plates is obtained by differentiating expression (7.3) through $F = -\partial_d E_c(d)$. A negative (positive) force, or equivalently a positive (negative) slope of $E_c(d)$, corresponds to attraction (repulsion) of the plates.
From (7.3) it is clear that in order to calculate the Casimir energy one needs to compute the reflection coefficients of the bodies composing the Casimir system. These coefficients relate the amplitude of the incident and reflected electric fields for different polarizations. Since the normal components of $\boldsymbol{D}$ and $\boldsymbol{B}$ and tangential components of $\boldsymbol{E}$ and $\boldsymbol{H}$ must be continuous along the interface, one can obtain the reflection amplitudes by solving Maxwell's equations at each side and then imposing the mentioned matching conditions for the fields.
Although we have not derived (7.3), its structure is similar to that of the zero point energy of a quantum field theory because of the typical functional form $\sim \log[\det[A]]$ [243]. In fact, recall that for perfectly metallic plates the reflection coefficients are $\mathbf{R}_{ij} = \mathrm{diag}(-1, 1)$. Introducing this for each $\mathbf{R}$ in (7.3) it is not difficult to show that one recovers the original Casimir result for parallel metallic plates (7.2). To generalize this argument to dielectric bodies and recover the Dzyaloshinskii-Lifshitz-Pitaevskii expression [242] it suffices to read out $\mathbf{R}_{ij}$ from any textbook on classical electromagnetic fields or optics ([261, 262] for example) and substitute it in (7.3). In fact, expression (7.3) is very general, and one can recover even the correct London forces experienced by two atoms from their fluctuating dipole moments, by calculating the scattering for each atom [243].

In what follows we will use the fact that for topological insulators, the reflection coefficients are not diagonal which is true in general for magnetoelectric materials. These extra terms introduce new degrees of freedom which can be used to favour repulsion. This ap-

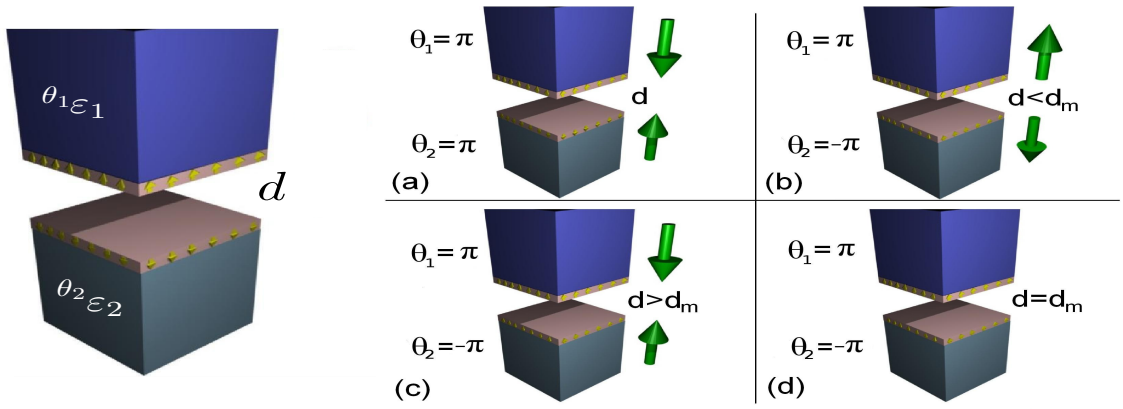

Figure 7.1.: Topological insulating plates separated by a distance d covered with a thin ferromagnetic layer of thickness $l << d$ (not to scale). Changing the sign of the magnetization of one of the plates (parallel or antiparallel to the surface normal) is equivalent to changing the sign of (either) $\theta_{1,2}$. (a) The magnetization is of the same sign on each surface resulting in a case where $\theta_1 = \theta_2$ giving Casimir attraction. In (b), (c) and (d) the magnetizations have opposite signs on the surface ($\theta_1 = -\theta_2$) leading to attraction when $d > d_m$, repulsion when $d < d_m$ and to a quantum levitation configuration at d_m where the net force is zero (see text).

proach was also used for the case of chiral metamaterials, which introduce as well off diagonal elements [248–250]. The crucial difference will be the presence of the topological term, which will act as an independent controllable parameter, giving even more tunnability to the system.

7.3. Casimir-Lifshitz force between topological insulators at $T = 0$

7.3.1. Topological insulators: The model

Our starting point will be a Casimir system composed by two topological insulator semi-infinite plates separated by a distance d, shown in Fig. 7.1. The electromagnetic response of three dimensional topological insulators, which determines the reflection coefficients, is as discussed in section 1.2.2, governed by the Lagrangian:

$$\mathcal{L} = \mathcal{L}_0 + \mathcal{L}_\theta = (\boldsymbol{E} \cdot \boldsymbol{D} + \boldsymbol{B} \cdot \boldsymbol{H}) \tag{7.5}$$

where the constitutive relations for the electric displacement field **D** and the magnetic field **H** are given by:

$$D_i = \epsilon_{ij} E_j + \frac{\alpha\theta}{\pi} B_i, \tag{7.6}$$

$$H_i = (\mu)^{-1}_{ij} B_j - \frac{\alpha\theta}{\pi} E_i, \tag{7.7}$$

that recover the properly modified Maxwell's equations (1.22)-(1.25). The first term of each constitutive equation is the usual one defined in terms of the dielectric function $\epsilon(\omega)$ and magnetic susceptibility $\mu(\omega)$, giving rise to the ordinary electromagnetic term in the Lagrangian (7.5) which we label $\mathcal{L}_0$. We will restrict the discussion to non-magnetic topological insulators and so $\mu(\omega) = 1$. The second term in each constitutive equation is the axionic [263] or topological magnetoelectric term [77, 78] written in terms of the fine structure constant ($\alpha = \frac{e^2}{\hbar c}$) which gives rise to a topological $\mathcal{L}_\theta$ term in the Lagrangian introduced in (1.21). As argued in the introduction, time reversal symmetry in the bulk imposes that $\theta = 0, \pi$ (mod 2π) being $\theta = \pi$ the case for topological insulators and $\theta = 0$ the case for trivial insulators. Note that, as discussed in section 1.2.2, θ only enters the equations of motion through its space and time derivatives (see (1.22)-(1.25)). For a topological insulator, θ is constant in the bulk and only varies spatially at the surface.

When the boundary is included, the action corresponding to the Lagrangian (7.5), $S_0 + S_\theta$, is a fair description of the topological insulator *only* when a time reversal breaking perturbation is induced on the surface to gap the surface states [77] (see also section 1.2.2). Several perturbations of that kind have been proposed and experimentally realized in the literature, which include for example doping the material with magnetic nano-particles [88–90]. Along the lines of similar situations [77, 264], in this work we will assume that the time reversal perturbation is a magnetic coating of small thickness $l << d$ (in a typical situation, d will be of the order of μm) which gaps the surface states. In the described situation, θ is quantized in odd integer values of π such that

$$\theta = (2n+1)\pi, \tag{7.8}$$

where $n \in \mathbb{Z}$ is determined by the nature of the coating, but independent of the absolute value of the magnetization of the coating. As described in the introduction, positive or negative values of θ are related to different signs of the magnetization on the surface [264], which we consider to be perpendicular to the plane of the plates .

Each topological insulator plate is characterized by the frequency dependent dielectric function $\epsilon(\omega)$ and the quantized magnetoelectric term θ. Being a topological contribution, θ is defined in the bulk as a constant whenever the bulk Brillouin zone is defined [78]. Nevertheless, at the surface, the effective action must be valid as long as the condition $l << d$ is fulfilled, where magnetic effects from the covering magnetic layer could renormalize its

value, and the system should be treated as a layered system [1]. We henceforth assume that this is not the case and consider only the region where $l << d$ (nm $<<$ μm in practical terms).

The parasitic magnetic forces between the magnetic layers can be estimated following Ref. [265]. The dipole-dipole interaction is of the order of attoN at distances of 50 nm and the magnetic Casimir force is $\sim 1fN$ [265]. Since we will be dealing with distances of the order of μm the magnetic forces will be even smaller compared to the Casimir force that is of the order of pN. Note also that for wavelengths of the order of $d \sim \mu$m it is reasonable to assume that $\mu(\omega) \sim 1$ [266]). Thus, justified by the preceding arguments we will completely neglect these parasitic magnetic interactions, and focus only on the Casimir force experienced by the plates.

7.3.2. Casimir force for isotropic topological insulator plates at $T = 0$

Consider first, for simplicity, the case of two isotropic topological insulator plates. The topological part S_θ in the action does not modify Maxwell's equations as long as the constituent relations are changed according to (7.6) and (7.7), taken at this stage to be isotropic. Equivalently, we might choose the $\theta = 0$ constituent relations but change the boundary conditions which will be modified because of the presence of the boundary term S_θ.

In any of the two equivalent approaches, we can obtain the reflection matrices (7.4) by imposing the continuity of the tangential component of $\mathbf{H}$ and the normal component of $\mathbf{D}$ following any standard textbook on electrodynamics [261]. For a plate described by the optical responses θ_i and $\varepsilon_i(\omega)$ immersed in vacuum the reflection matrices are given by [267, 268]

$$\mathbf{R}_i = \frac{1}{\Delta}\begin{pmatrix} 1 - n_i^2 - \bar{\alpha}_i^2 + n_i\chi_- & 2\bar{\alpha}_i \\ 2\bar{\alpha}_i & -1 + n_i^2 + \bar{\alpha}_i^2 + n_i\chi_- \end{pmatrix}, \tag{7.9}$$

where $i = 1, 2$ labels each plate, $\bar{\alpha}_i = \frac{\alpha\theta_i}{\pi}$, α is the fine structure constant ($\alpha = \frac{e^2}{\hbar c}$), $n_i = \sqrt{\varepsilon_i(\omega)}$ is the refractive index of each plate, $\Delta = 1 + n_i^2 + \bar{\alpha}_i^2 + n_i\chi_+$ and

$$\chi_\pm = \frac{\xi^2 + \mathbf{k}_\parallel^2 \pm \left(\xi^2 + \frac{\mathbf{k}_\parallel^2}{n_i^2}\right)}{\sqrt{\left(\xi^2 + \mathbf{k}_\parallel^2\right)\left(\xi^2 + \frac{\mathbf{k}_\parallel^2}{n_i^2}\right)}}. \tag{7.10}$$

It is possible to show that when $\bar{\alpha} = 0$ and after a little algebra, these coefficients reduce to the ordinary Fresnel coefficients for a dielectric-dielectric interface [261]. By its definition, Δ is always positive and the off-diagonal terms have a an overall sign governed by the sign of θ_i.

[1] In this chapter we will assume that $\theta(\omega)$ is independent of the frequency since the exact function $\theta(\omega)$ is still not known for topological insulators. Some properties of this function can be accessed analytically, as will be discussed in the next chapter.

At this point it is necessary to propose a model for $\varepsilon(i\xi)$. Due to the low concentration of free carriers in insulators the most general phenomenological model to describe the optical response of a dielectric is a sum of oscillators to account for particular absorption resonances [246]:

$$\varepsilon(i\xi) = 1 + \sum_i \frac{\omega_{e,i}^2}{\xi^2 + \omega_{R,i}^2 + \gamma_{R,i}\xi}, \tag{7.11}$$

In this model, $\omega_{R,i}$ are the resonant frequencies of the oscillators while $\omega_{,ie}$ accounts for the oscillators strengths. The damping parameter $\gamma_{R,i}$ satisfies $\gamma_{R,i} << \omega_{R,i}$ playing therefore a secondary role. In what follows, it has been assumed for simplicity a single oscillator model and thus we have rescaled all quantities in units of ω_R leaving the quantity $\varepsilon(0) \equiv 1 + (\omega_e/\omega_R)^2$ as the dielectric parameter of the model. A good candidate to be described by this model is the topological insulator $TlBiSe_2$ [88]. Experimentally [269] it is found that this material shows a value $\varepsilon(0) \sim 4$ [2] and has a single resonant frequency near $56cm^{-1}$. Other topological insulators could need more oscillators to be added in (7.11).

Introducing these matrices in (7.3) and assuming that both topological insulators are described by a single oscillator model of the form (7.11) It is possible to numerically evaluate the integrals as a function of $\varepsilon(0)$ and $\theta_{1,2}$. The results from the numerical integration of (7.3) are shown in Figs. 7.2 and 7.3 (a) where the Casimir energy density is plotted against the dimensionless distance $\bar{d} \equiv \frac{\omega_R}{c} d$.

From the numerical results in Fig. 7.2 it is possible to distinguish two situations: 1) when the topological terms have the same signs, i.e. $\text{sgn}(\theta_1) = \text{sgn}(\theta_2)$ the Casimir force is attractive for all distances, and 2) when the signs are opposite $\text{sgn}(\theta_1) = -\text{sgn}(\theta_2)$, a repulsive region at small distances appears, while, at large distances, attraction is recovered, having therefore two regions separated by a minimum in the Casimir energy; an equilibrium point. As shown in Fig 7.3, the repulsive behaviour is favoured by reducing the ratio $\frac{\omega_e}{\omega_R}$.

Remarkably, all these results can be understood analytically. It is possible to show that for the assumptions made above, there must exist a minimum when $\text{sgn}(\theta_1) = -\text{sgn}(\theta_2)$. A detailed version of the proof of the existence of a minimum, together with the analytic analysis of the large and short distances limits of the Casimir energy is given in appendix D.1.

To end this section we complete the analysis by studying the explicit dependence of the position of the equilibrium point (d_{eq}) with θ_1 and θ_2. Whenever the condition $\text{sgn}(\theta_1) = -\text{sgn}(\theta_2)$ is satisfied, it is easy to study numerically the dependence of $\bar{d}_{\text{eq}}$, the equilibrium position as a function of both $\theta_{1,2}$. In Fig. 7.3 (b) we plot $\bar{d}_{\text{eq}}$ against θ_1 for different values of θ_2 ranging from π to 5π. A numerical fit indicates that for small magnetoelectric couplings

[2] Neglecting free carrier contributions and assuming high frequency transparency.

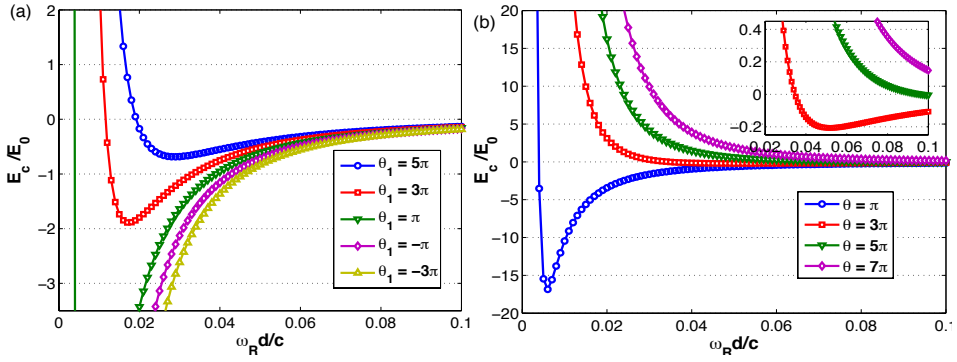

Figure 7.2.: Casimir energy density (in units of $E_0 = A\hbar c/(2\pi)^2(\omega_R/c)^3$) as a function of the dimensionless distance $\bar{d}$ for $\omega_e/\omega_R = 0.45$. In (a) $\theta_2 = -\pi$ is fixed. Whenever $\mathrm{sgn}(\theta_1) = -\mathrm{sgn}(\theta_2)$ a minimum $\bar{d}_m$ appears leading to a vanishing net force on the plates. Increasing θ_1 within positive values suppresses the minimum shifting $\bar{d}_m$ towards lower values (if both signs are equal then only attractive behaviour occurs). Complete repulsion is achieved when one of the topological magnetoelectric term is much bigger than the other. (b) The optimal situation $\theta_1 = -\theta_2 = \theta$. Different values of θ show that the minimum is enhanced when the difference between the two values is as small as possible ($\theta = \pi$).

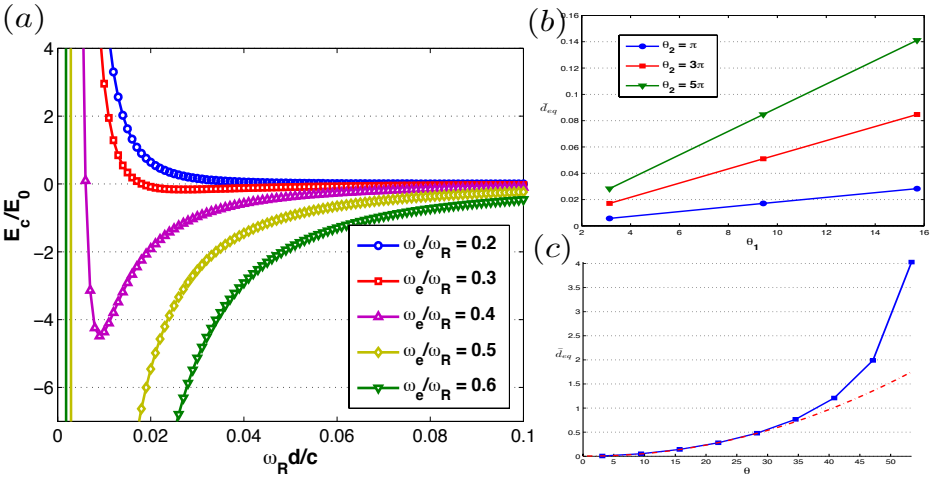

Figure 7.3.: Effect of parameter $\varepsilon(0)$ with fixed $\theta_1 = -\theta_2 = \pi$. The effect of increasing $\varepsilon(0)$ is to develop a minimum, which shifts to smaller $\bar{d}_m$ as $\varepsilon(0)$ is increased. (b) $\bar{d}_{eq}$ as a function of θ_1 for different values of θ_2 ranging from π to 5π. The solid blue line represents $\bar{d}_{eq} \propto |\theta_1\theta_2|$. (c) $\bar{d}_{eq}$ as a function of $\theta \equiv \theta_1 = -\theta_2$ (blue solid line). The behaviour deviates from θ^2 (dashed red line) for small θ. For both figures $\frac{\omega_e}{\omega_R} = 0.45$.

the dependence is given by

$$\bar{d}_{eq} \propto |\theta_1 \theta_2|. \tag{7.12}$$

For higher magnetoelectric couplings, the behaviour deviates from the simple θ^2 law. This is shown in Fig. 7.3 (c) where we plot $\theta \equiv \theta_1 = -\theta_2$. For high values of θ the equilibrium position grows faster to larger distances. Beyond a critical value, the magnetoelectric part of the reflection coefficients overwhelms the ordinary dielectric part giving rise to purely repulsive behaviour and the equilibrium position disappears (in the same way as for the $\varepsilon(0) \to 1$ limit discussed in appendix D.1). The inclusion of temperature will modify further (7.12), as shown in the next section.

As a final comment we note that the obtained dependence of the minimum with θ suggests that an analytic way of deriving this result might be possible, especially in the case where $\theta_1 = -\theta_2$. Nevertheless, the derivation of this result is not transparent from this formalism and no analytical progress has been made for this issue.

7.4. Casimir-Lifshitz force between isotropic topological insulators at $T \neq 0$

In this section we include the effect of temperature for isotropic plates and we discuss how the repulsive behaviour can be affected by changes in temperature.

7.4.1. Inclusion of finite temperature effects

To take into account finite temperature effects within the Lifshitz theory one must assume that the system is in thermal equilibrium. As a first step, the formal replacement [239, 243]

$$\frac{\hbar}{2\pi} \int_0^\infty d\xi \longleftrightarrow k_B T \sum_{l=0}^{\infty\,\prime}, \tag{7.13}$$

in (7.3) together with the replacement of ξ with $\xi_l = 2\pi \frac{k_B T}{\hbar} l$, the discrete Matsubara frequencies, takes into account the effect of temperature. We have defined k_B to be Boltzmann's constant and the prime denotes that the term $l = 0$ contains a prefactor $\frac{1}{2}$ compared to the other terms in the sum. This set of substitutions imply some assumptions which we now briefly discuss.

First of all we note that formally the dielectric function can also have temperature dependence through the parameters ω_{R_i},ω_{e_i} and γ_i defined in (7.11). Although at the time of writing there is no experimental data for topological insulators, these parameters are almost temperature independent for most dielectrics and so we exclude this effect in our analysis. In addition, it is known that all dielectrics have non zero conductivity $\sigma(T)$ at $T \neq 0$ which

modifies the dielectric function through $\varepsilon(\omega, T) = \epsilon(\omega) + i4\pi\frac{\sigma(T)}{\omega}$. For dielectrics $\sigma(T)$ depends on the band gap Δ as $\sigma(T) \sim \exp(-\frac{\Delta}{2k_BT})$.
Note however that since topological insulators such as Bi_2Se_3 have $\Delta \sim 0.3$eV [270] we can neglect this contribution as a first approximation for temperatures below $T \sim 3 \cdot 10^3$ K which is enough for practical purposes. Nevertheless, it is possible to show [239] that the inclusion of the finite conductivity term within the Lifshitz formalism leads to a violation of Nernst theorem which states that the entropy should tend to zero when $T \to 0$. Physically this is related to the appearance of a drift current, which leads to Joule heating and violates the condition of thermal equilibrium, necessary to apply the Lifshitz theory. Hence, the inclusion $\sigma(T)$ is therefore not justified within the Lifshitz theory and leads to large, unphysical thermal corrections which do not account for experimental data [239]. Either way, we are forced to neglect this contribution. Other effects of temperature on the coating are discussed in the concluding section 7.7.
Having considered these points, we will assume that the formal substitution (7.13) is enough to take into account the effect of temperature on the Casimir effect in anisotropic topological insulators.

7.4.2. Results at $T \neq 0$ isotropic plates

Once established the method to include temperature effects we analyse the case of two isotropic topological insulating plates described by (7.11) at $T \neq 0$. The Lifshitz equation (7.3) transforms for finite temperatures to

$$\frac{E_c(d)}{A} = k_B T {\sum_{l=0}^{\infty}}' \int \frac{d^2\mathbf{k}_\parallel}{(2\pi)^2} \log\det\left[1 - \mathbf{R}_1 \cdot \mathbf{R}_2 e^{-2k_3 d}\right]. \tag{7.14}$$

Where the transverse momentum k_3 is now evaluated at discrete frequencies ξ_l such that $k_3 = \sqrt{\boldsymbol{k}_\parallel^2 + \xi_l^2/c^2}$. It is convenient to define the dimensionless temperature $\bar{T}$

$$\bar{T} \equiv \frac{2\pi k_B T}{\hbar\omega_R}. \tag{7.15}$$

For frequencies in the optical region, $\bar{T} = 1$ correspond to temperatures $T \sim 2 \cdot 10^3$ K, while frequencies in the microwave region $\bar{T} = 3.7$ correspond to temperatures $T \sim 300$K. Since we will be interested in the latter (the topological insulator $TlBiSe_2$ has a resonance frequency [88] at $\omega_R = 56\text{cm}^{-1}$) our plots will range from $\bar{T} = 0$ to $\bar{T} = 10$. We note that the behaviour is dominated by low frequency resonances as long as higher resonance frequencies have similar oscillator strengths in (7.11) (see appendix D.1.2). Because of this, and the absence, to our knowledge, of broad frequency experimental data regarding the optical response of topological insulators (due mainly to their interest as thermoelectrics) we assume that this is the case and restrict to a one oscillator model throughout the chapter. Nevertheless, as optical data becomes available, it is simple to implement these techniques and substitute the

relevant parameters in the model since the overall assumptions will still hold (namely, the insulating behaviour and the existence of a topological magnetoelectric polarizability).
We end here the discussion regarding the model and the theoretical tools and we now proceed to analyse both numerically and analytically the results obtained from integrating (7.14).

Classical ($T \to \infty$) and quantum ($T \to 0$) limits

To get some insight into the finite temperature behaviour of the system one can ask what happens to the Casimir force in the (formal) limits when $T \to \infty$ and $T \to 0$. Trivially, if one first sets $T \to 0$ the expression (7.3) is recovered and the analysis $T = 0$ developed above still holds. Hence a region of repulsion is expected to exist if the topological magnetoelectric polarizabilities of the plates have different signs.
For high temperature, $T \to \infty$ also referred to as the classical limit, all the terms in the l sum above are exponentially suppressed except for the $l = 0$ term [239]. Thus, for isotropic plates, the dielectric function can be replaced by the zero frequency dielectric function. Let us derive the reflection coefficients in this case.
Directly from (7.9), and taking into account that $n_i^2 = \epsilon_i$ the reflection coefficients at zero frequency take the form

$$r_s = \frac{1}{\Delta_{l=0}}(1 - \varepsilon(0) - \bar{\alpha}^2 + \sqrt{\varepsilon(0)}\chi_-(0, \boldsymbol{k}_\parallel)) \tag{7.16}$$

$$r_s = \frac{1}{\Delta_{l=0}}(-1 + \varepsilon(0) + \bar{\alpha}^2 + \sqrt{\varepsilon(0)}\chi_-(0, \boldsymbol{k}_\parallel)) \tag{7.17}$$

$$r_{sp} = \frac{2\bar{\alpha}}{\Delta_{l=0}} = r_{ps}, \tag{7.18}$$

where $\Delta_{l=0} = 1 + \varepsilon(0) + \bar{\alpha}^2 + \sqrt{\varepsilon(0)}\chi_+(0, \boldsymbol{k}_\parallel)$. From their definition (7.10), the functions $\chi_\pm$ at zero frequency can be expressed in terms of $\varepsilon(0)$ only ($\boldsymbol{k}_\parallel$ dependence cancels in this limit):

$$\chi_\pm = \sqrt{\varepsilon(0)}\left[1 \pm \frac{1}{\varepsilon(0)}\right] \tag{7.19}$$

Bringing together all simplifications the reflection coefficients (7.9) take the form:

$$\mathbf{R}_i = \frac{1}{2(\varepsilon(0)+1) + \bar{\alpha}^2}\begin{pmatrix} -\bar{\alpha}^2 & 2\bar{\alpha} \\ 2\bar{\alpha} & 2(\varepsilon(0)-1) + \bar{\alpha}^2 \end{pmatrix}, \tag{7.20}$$

It is worth to emphasize that although similar in structure, these reflection coefficients are different to the ones obtained at zero temperature and $d \to \infty$ in appendix D.1 by rescaling the Casimir energy density with d.
As before, one can introduce this expression in (7.14) and study the behaviour of the Casimir energy as a function of the two parameters of the model: $\varepsilon(0) = 1 + \frac{\omega_e^2}{\omega_R^2}$ and $\theta_{1,2}$. In this case one can rescale the integration variables with d and focus on the force defined as $F = -\partial_d E_c(d)$ which takes the form:

$$F_{cl}(d) = \frac{k_B T}{d^3 \pi} f(\epsilon(0), \theta_1, \theta_2), \tag{7.21}$$

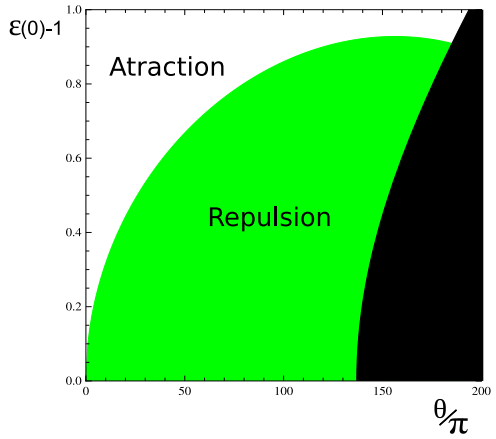

Figure 7.4.: Attraction versus repulsion in the classical limit ($T \to \infty$) as a function of $\frac{\omega_e}{\omega_R}$ and $\frac{\theta}{\pi}$ where $\theta_1 = -\theta_2 \equiv \theta$. The white upper region shows attraction while the lower green region shows repulsion. The black region is a forbidden region for the parameters due to the positive energy condition $\frac{\alpha|\theta|}{\pi} < \sqrt{\varepsilon(0)}$ (see text).

where f is a complicated integral expression of the parameters (see appendix D.2 for details). It is evident from the functional form of (7.21) with d that in the classical limit the Casimir force is either attractive or repulsive for all distances, depending only on the sign of f. Thus, in contrast to the zero temperature case, no equilibrium point is expected.
When $\text{sgn}(\theta_1) = \text{sgn}(\theta_2)$ no repulsion is obtained for any values of the parameters, similar to the $T = 0$ limit. Whenever $\text{sgn}(\theta_1) \neq \text{sgn}(\theta_2)$, Fig. 7.4 shows where the attractive and repulsive behaviours occur, plotted as a function of $\epsilon(0)$ and $\theta_1 = -\theta_2 \equiv \theta$.
The black region in Fig. 7.4 is excluded from the positive energy condition for magnetoelectric materials [271] which in this context implies that $\frac{\alpha|\theta|}{\pi} < \sqrt{\varepsilon(0)}$. The two other regions indicate attractive (white top) or repulsive (green low) behaviour. Therefore, even in the limit of very high temperature there exists a region of parameters where complete repulsion is obtained. Low dielectric response and high topological magnetoelectric polarizability favour in this case the repulsive behaviour.
As before it is possible to understand the origin of repulsion in the classical limit analytically. For small $\theta_{1,2}$ and $1 - \varepsilon(0)$, it is possible to write a closed analytical form for the Casimir force of the parameters although for the sake of clarity we leave this to appendix D.2. From this analysis it is straightforward to conclude that repulsion is possible in the classical limit for a certain range of parameters which are summarized in Fig. 7.4. Having studied these limiting cases we know proceed to the general case where $T \neq 0$.

$T \neq 0$: the general case

The effect of increasing temperature for a situation where $\text{sgn}(\theta_1) = -\text{sgn}(\theta_2)$ is presented in Fig. 7.5. In general, temperature acts against repulsive behaviour, driving it towards shorter

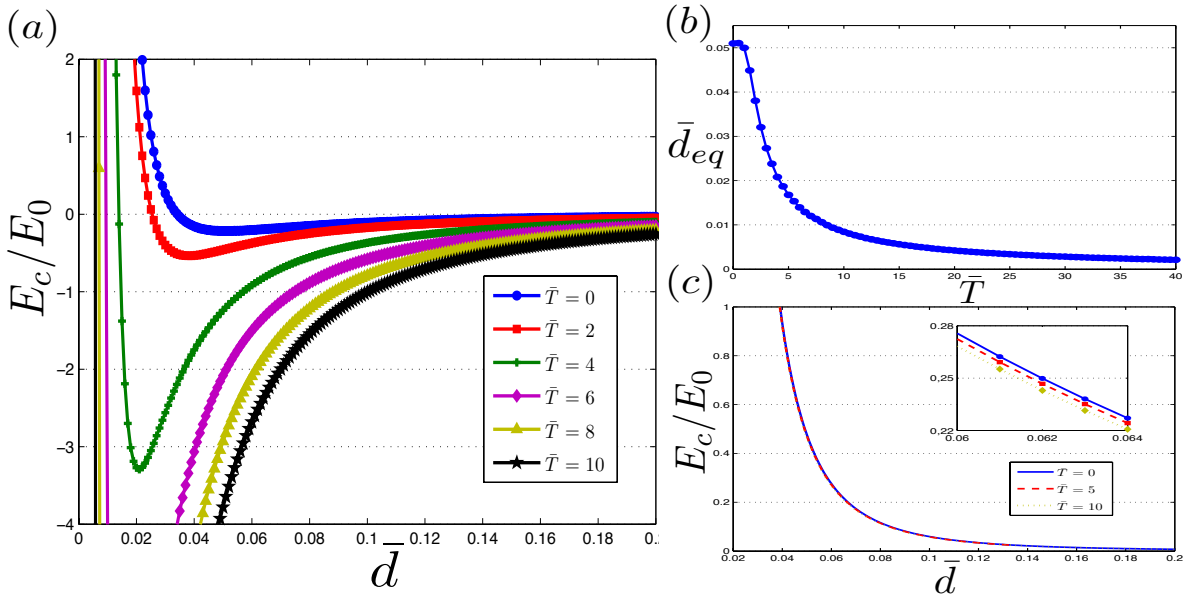

Figure 7.5.: (a) Casimir energy density (in units of $E_0 = A\hbar c/(2\pi)^2(\omega_R/c)^3$) as a function of the dimensionless distance $\bar{d}$ for $\frac{\omega_e}{\omega_R} = 0.45$ for temperatures ranging from $\bar{T} = 0 - 10$ and $\theta_1 = -\theta_2 = 3\pi$. Temperature pushes the repulsive behaviour to shorter distances. (b) Equilibrium distance as a function of temperature. (c) Casimir energy density (in units of $E_0 = A\hbar c/(2\pi)^2(\omega_R/c)^3$) as a function of $\bar{d}$ for $\frac{\omega_e}{\omega_R} = 0.16$ for temperatures ranging from $\bar{T} = 0 - 10$. For values where there is repulsion, decreasing the temperature shifts the curve towards smaller distances as shown inside the inset figure.

distances as temperature increases. The evolution of the equilibrium position with respect to the dimensionless temperature $\bar{T}$ is shown in Fig. 7.5 (b). For high values of $\bar{T}$ ($\bar{T} > 5$) it is possible to complete equation (7.12) (valid for small values of $\theta_{1,2}$) to write:

$$\bar{d}_{eq} \propto \frac{|\theta_1\theta_2|}{\bar{T}}. \tag{7.22}$$

This simple relation, extracted from numerical data, shows that for small topological magnetoelectric charge and high temperature both effects compete as regards to the equilibrium position.

One can summarize the results for this section as follows. In the classical limit, one can have either attraction or repulsion, regardless of the distance. Starting with attraction at the classical limit, i.e $\bar{T} \to \infty$, decreasing temperature will develop a minimum which will shift to longer distances as shown in Fig. 7.5 (a) and (b). Consistent with the discussion presented the end of section 7.3, in some special cases where the magnetoelectric is bigger than a critical value one can end with repulsion at $T = 0$ without a minimum.
Starting from repulsion in the classical limit will not develop a minimum when decreasing $\bar{T}$ but it will shift the curve of repulsive behaviour towards larger distances to end with

repulsion in the quantum limit. This is shown in Fig. 7.5 (c). It must be noted that for this to happen, a very low $\varepsilon(0)$ is needed when $\theta \sim \pi$ and as θ is increased, higher $\varepsilon(0)$ are capable of giving rise to the complete repulsive behaviour. Therefore we expect this not to be the relevant situation for real topological insulators, which have low θ, but rather the one presented in Fig. 7.5 (a). An extension of this analysis could be relevant for other magnetoelectric materials such as Cr_2O_3 that can present higher axion coupling as well as more general magnetoelectric couplings [272].
We note for completeness that when both topological magnetoelectric couplings have equal signs, temperature acts to increase attraction as expected from ordinary dielectrics.

7.5. Casimir force between topological insulators with uniaxial anisotropy at $T = 0$

In this section we again set the temperature to zero and focus on the effect that uniaxial anisotropy has on the repulsive behaviour.

7.5.1. Anisotropy in topological insulators

For a given material its linear response to an electromagnetic wave, or in turn, its reflection coefficients defined in (7.4) depend strongly on the dielectric tensor ε_{ij}, the magnetic susceptibility tensor μ_{ij} and the magnetoelectric tensor θ_{ij}. Since we are dealing with non magnetic topological insulators we will assume that $\mu_{ij} = \delta_{ij}$, although we shall derive the reflection coefficients for the general case in which the susceptibility is considered.

Crystal symmetry defines the other two tensors. Due to time reversal symmetry in the bulk, for topological insulators the magnetoelectric tensor can only have the form $\theta_{ij} = \theta\delta_{ij}$ with $\theta = \pi \ (\mathrm{mod}(2\pi))$ for topological insulators and $\theta = 0$ for ordinary insulators [273]. It is interesting to note that for general magnetoelectric crystals, other magnetoelectric couplings can be present in the action (7.5), and θ_{ij} could have a more elaborate form [266, 273] which could in principle affect the sign of the Casimir force. We will restrict ourselves to the case of a constant isotropic magnetoelectric tensor $\theta_{ij} = \theta\delta_{ij}$, relevant for crystalline topological insulators [273].
The form of ε_{ij} is also determined by crystal symmetry and one can distinguish the cubic, uniaxial and biaxial crystals [266]. The simplest case, the cubic structure, has $\epsilon_{ij} = \varepsilon(\omega)\delta_{ij}$, which is just the isotropic case considered in previous sections. Although interesting as a first approximation, this model is incomplete for topological insulators. The prototypical examples of topological insulating crystals Bi_2Se_3, Bi_2Te_3, Sb_2Te_3 [82, 83, 88] or the novel Thallium based III-V-VI_2 compounds [88, 274–276] all have rhombohedral symmetry, which fall into the category of uniaxial crystals and hence we will focus on this case, leaving biaxial crystals aside. Uniaxial crystals have a definite optical axis which coincides with the principal

crystal axis. The dielectric tensor can thus be written in the form: $\varepsilon_{ij} = \mathrm{diag}(\varepsilon_\perp, \varepsilon_\perp, \varepsilon_z)$, where the optical axis is aligned with the z axis. In all the following calculations, the optical axis of the two Casimir plates are supposed to be aligned so that no torque is induced in the system [239] which can alter the presented findings.

7.5.2. Fresnel coefficients for topological insulators with uniaxial anisotropy at $T = 0$

Fresnel coefficients are derived from Maxwell's equations by imposing continuity relations for the normal components of **D** and tangential components of **H** as discussed above for the isotropic case (see appendix D.3). After some tedious but straightforward work one obtains the reflection matrices for an anisotropic topological insulator-vacuum interface

$$\mathbf{R}_i = \frac{1}{\Delta_{an}} \begin{pmatrix} (\mu_\perp k_z - q')(\varepsilon_\perp k_z + q'') - q'' k_z \mu_\perp \bar{\alpha}^2 & 2\bar{\alpha} q'' \mu_\perp k_z \\ 2\bar{\alpha} q'' \mu_\perp k_z & (\varepsilon_\perp k_z - q'')(\mu_\perp k_z + q') + q'' k_z \mu_\perp \bar{\alpha}^2 \end{pmatrix} \tag{7.23}$$

where $\Delta_{an} = (\mu_\perp k_z + q')(\varepsilon_\perp k_z + q'') + q'' k_z \mu_\perp \bar{\alpha}^2$, $k_z^2 = \frac{\omega^2}{c^2} - k_\parallel^2$, $q'^2 = \frac{\omega^2}{c^2}\varepsilon_\perp \mu_\perp - k_\parallel^2 \frac{\mu_\perp}{\mu_z}$, $q''^2 = \frac{\omega^2}{c^2}\varepsilon_\perp \mu_\perp - k_\parallel^2 \frac{\varepsilon_\perp}{\varepsilon_z}$ and $\bar{\alpha} = \alpha\theta/\pi$. To compute the Casimir energy, one should define these in the imaginary frequency axis and perform the substitution $\omega = i\xi$. We stress that these reduce to the ordinary anisotropic coefficients presented in appendix D.3 when $\bar{\alpha} = 0$ and to the isotropic reflection coefficients (7.9) when μ and ε are isotropic.
To investigate the effect of anisotropy it is necessary to model the dielectric response of the material. Following the considerations made above we model $\varepsilon_\perp$ and ε_z with a sum of oscillators

$$\varepsilon_z(i\xi) = 1 + \sum_i \frac{\omega_{e_z,i}^2}{\xi^2 + \omega_{R_{z,i}}^2 + \gamma_{z,i}\xi}, \tag{7.24}$$

$$\varepsilon_\perp(i\xi) = 1 + \sum_i \frac{\omega_{e_\perp,i}^2}{\xi^2 + \omega_{R_{\perp,i}}^2 + \gamma_{\perp,i}\xi}, \tag{7.25}$$

that we will further restrict as above to a one oscillator model. In this scheme we will investigate two aspects: (i) the effect of modifying the relative strength of the parallel component against the perpendicular i.e. ω_{e_z} over $\omega_{e_\perp}$ and (ii) the effect of the relative movement of the position of the resonance frequencies $\omega_{R_\perp}$ and ω_{R_z}.

7.5.3. Effect of the relative strength of the parallel component against the perpendicular component

To study this effect we simplify equations (7.24) and (7.25) to unmask the effect under study (i.e. point (i) above). Redefining the parameters in units of $\omega_{R_\perp}$

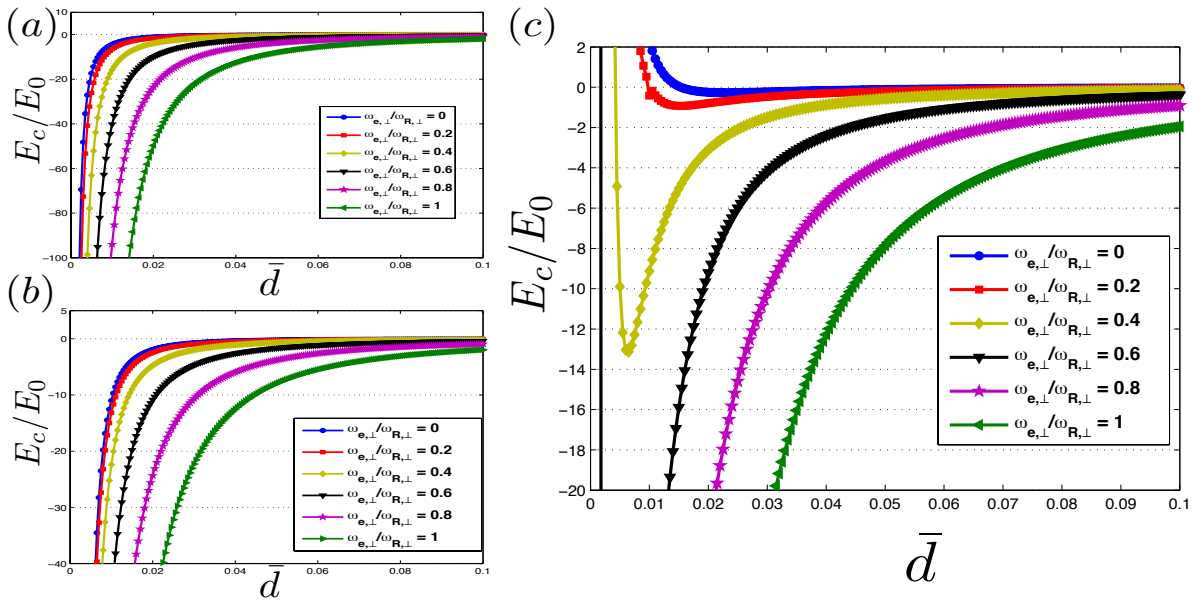

Figure 7.6.: Effect of changing the relative oscillator strengths between parallel and perpendicular components of the dielectric function on the Casimir energy density (in units of $E_0 = A\hbar c/(2\pi)^2(\omega_{R_z}/c)^3$) as a function of the dimensionless distance $\bar{d}$ with (a) $\theta_{1,2} = 0$ and (b) $\theta_1 = \theta_2 = \pi$ (c) $\theta_1 = -\theta_2 = \pi$. (a) Attraction is obtained as no magnetoelectric term is included. (b) Both magnetoelectric couplings have the same sign and so no repulsion occurs. (c) Repulsion appears at short distances. Increasing $\omega_{e_\perp}$ makes the minimum shift to lower distances while increasing its depth. Therefore, repulsion is favoured by the condition $\omega_{e_z} > \omega_{e_\perp}$.

$$\varepsilon_z(i\xi) = 1 + \frac{\omega_{e_z}^2}{\xi^2 + 1 + \gamma\xi}, \quad \varepsilon_\perp(i\xi) = 1 + \frac{\omega_{e_\perp}^2}{\xi^2 + 1 + \gamma\xi}. \tag{7.26}$$

In this case we have chosen $\omega_{R_\perp} = \omega_{R_z}$ and $\gamma \equiv \gamma_{R_\perp} = \gamma_{R_z} = 0.01$ in units of $\omega_{R_\perp}$. To study the effect of changing the relative strength of the dielectric components we may fix $\omega_{e_z} = 0.45$ (in units of $\omega_{R_\perp}$) and change $\omega_{e_\perp}$ in the interval $[0, 1]$.

The results are shown in Fig. 7.6. Fig. 7.6 (a) is a reference figure where only anisotropy is studied with $\theta_i = 0$. In this case, attraction occurs because there is no mixing of polarizations since the diagonal component in (7.23) is zero (see appendix D.3). As $\omega_{e_\perp}$ grows the tendency is to favour attraction and to increase the absolute value of the Casimir energy at a given distance. In Fig. 7.6 (b) the magnetoelectric terms have equal sign and so no repulsion is obtained just as it is expected from the isotropic case studied in section 7.3.2. When θ_1 and θ_2 have opposite sing, $\theta_1 = -\theta_2 = \pi$, the Casimir energy develops a minimum, shown in Fig. 7.6 (c). The actual distance at which the minimum appears is shifted to shorter distances as $\omega_{e_\perp}$ is increased. This enables to draw the conclusion that for the minimum to shift to

larger distances, or in other words, for the repulsive behaviour to be enhanced, the material in question has to favour the strength of oscillators in the direction parallel to the optical axis.
Physically, repulsion in this system is due to the mixing of polarizations. Thus, suppression of repulsion can be traced back to the relative suppression of the off-diagonal terms in (7.23) versus the diagonal terms just as in the isotropic case. Analytically, increasing $\varepsilon_\perp$ while fixing ε_z to a constant makes the off-diagonal terms vanish in the end, confirming the numerical analysis.

7.5.4. Effect of the relative position of the oscillator frequencies

To study this case, the dielectric functions of both components can be written in units of $\omega_{R_\perp}$:

$$\varepsilon_z(i\xi) = 1 + \frac{\omega_e^2}{\xi^2 + 1 + \gamma\xi}, \quad \varepsilon_\perp(i\xi) = 1 + \frac{\omega_e^2}{\xi^2 + \beta + \gamma\xi}. \tag{7.27}$$

In this case we have chosen $\omega_{e_\perp} = \omega_{e_z} \equiv \omega_e = 0.45$ and as before $\gamma = 0.01$ (in units of $\omega_{R_\perp}$). The parameter $\beta \equiv \frac{\omega_{R_\perp}^2}{\omega_{R_z}^2}$ determines the relative position between both oscillators. For $\beta > 1$, $\epsilon_\perp$ has a higher resonance frequency than ϵ_z and for $\beta < 1$ the opposite situation occurs. The results are shown in Fig. 7.7. As in the previous case, Fig. 7.7 (a) is a reference figure where only parameter β is modified. We have chosen the values of β ranging from $\beta = 10^{-3}$ to $\beta = 10^3$, so a broad range of situations are represented. In this situation, attraction occurs since $\theta_i = 0$ and there is no mixing of polarizations. As β grows the tendency is to favour attraction and to increase the absolute value of the Casimir energy at a given distance. In Fig. 7.7 (b) the magnetoelectric terms have equal sign and so no repulsion is obtained. Fig. 7.7 (c) shows how the minimum is shifted to lower distances as $\omega_{R_\perp}$ is increased, i.e. β is increased. Hence, for the repulsive behaviour to be favoured, the material in question has to favour low resonance frequencies in the parallel direction, while high frequencies in the perpendicular direction. This is consistent with the behaviour discussed above where suppression of $\varepsilon_\perp$ enhances repulsion. In this case, increasing β suppresses $\varepsilon_\perp$ and favours repulsion [3].

We now summarize the results of this section. From the numerical results one can readily infer what conditions are necessary for repulsion to be observed, given that the topological magnetoelectric terms of the two materials have opposing signs. For the repulsive behaviour to appear at the largest distances possible, one should search for a material where the direction parallel to the optical axis has a bigger oscillator strength than the corresponding strength of the oscillator in the parallel direction $\omega_{e_z} \gg \omega_{e_\perp}$. Further enhancement of the repulsive behaviour can be achieved if the oscillator resonances in the direction perpendicular to the optical axis are at higher frequency than resonances for the perpendicular direction,

[3] This effect is analogous to the effect of a higher oscillator frequency in the isotropic case, which enhances repulsion.

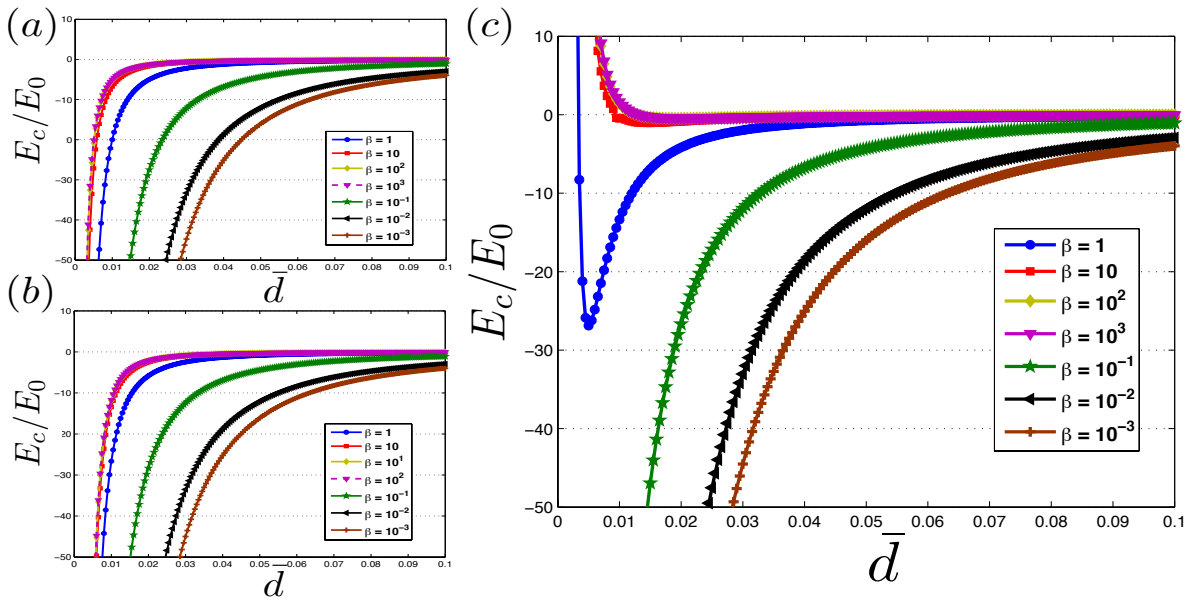

Figure 7.7.: Effect of changing the relative positions of the oscillator resonances between parallel and perpendicular components of the dielectric function on the Casimir energy density (in units of $E_0 = A\hbar c/(2\pi)^2(\omega_{R_z}/c)^3$) as a function of the dimensionless distance $\bar{d}$ with (a) $\theta_{1,2} = 0$ and (b) $\theta_1 = \theta_2 = \pi$ (c) $\theta_1 = -\theta_2 = \pi$. (a) Attraction is obtained as no magnetoelectric term is included. (b) Both magnetoelectric couplings have the same sign and so no repulsion occurs. (c) Increasing $\omega_{R_\perp}$ makes the minimum shift to higher distances while decreasing its depth. Therefore, repulsion is favoured by increasing β.(see text)

i.e $\omega_{R_z} \ll \omega_{R_\perp}$. In both situations, $\varepsilon_\perp$ is suppressed relative to ε_z and the mixing of polarizations is maximized.

With these numerical calculations we have established the main directions to enhance repulsive behaviour with topological insulators at low temperature. We now discuss the effect of temperature on these findings.

7.6. Casimir force between topological insulators with uniaxial anisotropy at $T \neq 0$

The result of including both temperature and anisotropy together is shown in Fig 7.8. To illustrate that the repulsive behaviour is still present we study two different cases. In the first of them, corresponding to Fig. 7.8 (a) we vary the dimensionless temperature from $\bar{T} = 0$ to $\bar{T} = 7$ while fixing the uniaxial anisotropy parameters and $\theta_1 = -\theta_2 = \pi$. In particular we fix the oscillators strengths to $\omega_{e_z} = 0.45$, $\omega_{e_\perp} = 0.3$ and the relative position of the resonances to $\beta = 5$, i.e. the perpendicular oscillator is shifted by a factor of five with respect

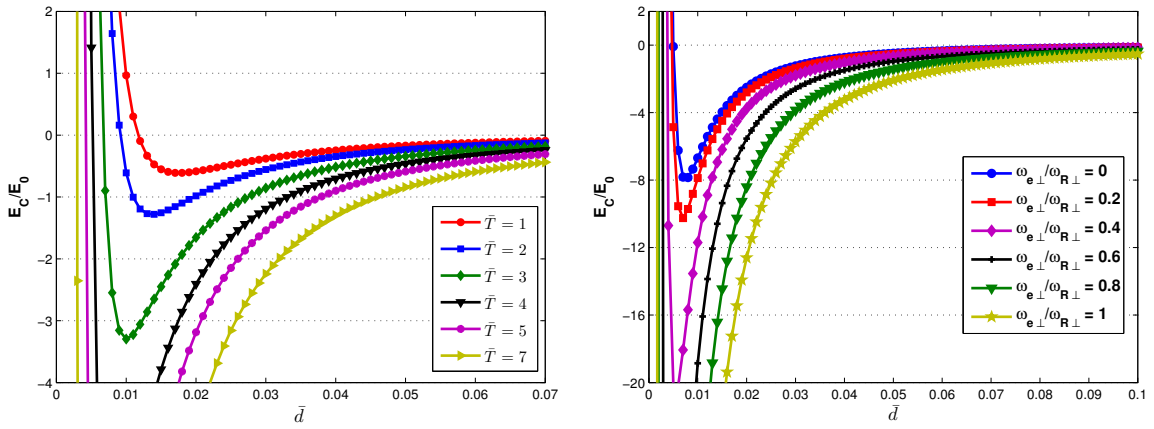

(a) (b)

Figure 7.8.: Casimir energy density (in units of $E_0 = A\hbar c/(2\pi)^2(\omega_{R,z}/c)^3$) and $\theta_1 = -\theta_2 = \pi$ including anisotropy and temperature effects: (a) Effect of changing the temperature from $\bar{T} = 0 - 7$ with $\omega_{e,z} = 0.45$, $\omega_{e,\perp} = 0.3$ and $\beta = 5$. (b) Effect of varying $\omega_{e,\perp} = 0 - 1$ with $\bar{T} = 5$, $\omega_{e,z} = 0.45$ and $\beta = 5$.

to ω_{R_z}. As expected by previous sections, the figure proves that temperature works against the repulsive behaviour, shifting repulsion to shorter distances as temperature is increased. In a second situation we illustrate the effect of varying anisotropy at a given temperature. In this case, we fix the temperature to $\bar{T} = 5$, the oscillator strength in the parallel direction to $\omega_{e_z} = 0.45$ and $\beta = 5$ while varying $\omega_{e_\perp}$ from $\omega_{e_\perp} = 0$ to $\omega_{e_\perp} = 1$. The results show that enhancing perpendicular response, even at finite temperature, favours repulsive behaviour. Consistently with previous sections, equal signs of $\theta_{1,2}$ the system returns to attraction at all distances.

7.7. Discussion and Conclusions

In the first part of the chapter it was shown that a repulsive Casimir effect can arise from the presence of a topological term in the electromagnetic response of topological insulators. Being magnetoelectric materials, a Casimir system formed by topological insulators with gapped surface states is outside the theorems that prevent repulsion in vacuum [252–254]. Physically, the mixing of the s and p polarizations governed by the topological magnetoelectric coefficient θ, rooted on the surface Dirac-quasiparticles, that enables the appearance of a repulsive (attractive) behaviour at short (long) distances whenever the signs of the topological terms of the two involved bodies are distinct. In principle, the sign of θ can be governed experimentally through the sign of the magnetization on the surface although this is still far from being achievable in practice. Whenever both topological terms have the same sign,

attraction is recovered at all distances.
In the second part of the chapter, the effect of anisotropy and temperature on the repulsive Casimir effect with three dimensional topological insulators was studied. It was found that the repulsive behaviour is still present even when including these effects. In particular, increasing temperature tends to reduce repulsion, similar to what is expected from different situations such as metamaterials [277]. On the other hand, enhancing the optical response in the direction parallel to the optical axis of the topological insulator works in favour of repulsion. This can be achieved either by increasing the relative strength of the oscillator in the parallel direction or by searching for resonance frequencies which suppress the perpendicular response. We have also determined that both effects together still allow for repulsion. All these effects can be understood as an enhancement of the off-diagonal terms in the reflection coefficients, which favours polarization mixing and thus repulsion, whenever the signs of the topological magnetoelectric terms are opposite in both plates.
In this chapter we have aimed also to establish the theoretical framework for handling anisotropy in topological insulators in the context of their optical properties. The reflection coefficients for anisotropic materials can also be helpful in achieving the optical characterization of these materials and could be relevant for metrology purposes, as suggested in previous works [278, 279].
Although these promising conclusions are reached, it is difficult to draw conclusions for real materials since the optical response of topological insulators still needs further experimental characterization. We now discuss some future directions to further characterize this effect to get closer to real experimental situations regarding topological insulators. Firstly, values for $\varepsilon(\omega)$ for wide ranges of frequencies are still lacking for the vast majority of topological insulators, in sharp contrast with other materials which are traditionally useful for measuring the Casimir force [239, 280]. The interest of these materials as thermoelectrics possibly has prevented systematic studies of the optical properties. If one is to achieve repulsion out of topological insulators it is also necessary to address the effect of temperature on the magnetic coating, left out of the present analysis. Even though magnetic interactions where shown to be irrelevant as discussed in section 7.3.1, temperature will have an effect on the magnetization. In particular, the magnetic moments will fluctuate with increasing temperature and destroy ferromagnetism when the system is over the Curie temperature (T_c) of the coating. This temperature depends on the specific coating material which should be an insulating or semiconducting ferromagnet with as high as possible Curie temperature. Although ferromagnets are usually metallic, examples of insulating ferromagnets exist, for example oxides such as the rare earth oxide $Eu0$ with Curie temperature close to 70K [281], and have been synthesized and used in the past, such as the ferromagnetic insulator GdN. The latter has been shown to have a Curie temperature close to 60K [281], it can be grown as a thin film of thickness $\sim$ 6nm [282] and could be a suitable candidate for the ferromagnetic covering. It is also possible that other antiferromagnetic and ferrimagnetic materials might be useful as

well, along the lines suggested in Ref. [90].
A second important issue left out of this analysis is the possibility that the topological magnetoelectric term can be frequency dependent $\theta = \theta(\omega)$ which is in general expected for any realistic system. The exact dependency is in fact an interesting question on its own that will motivate the calculations presented in the next chapter. Physically, only the surface electrons can contribute to this frequency dependent function. Since time reversal symmetry must be broken at the surface, this dependency will be very similar the optical Hall response of a single Dirac-cone.
Finally we suggest a different but equally promising route towards achieving repulsion in Casimir systems which is the study of other magnetoelectric materials such as Cr_2O_3 [272]. However, although these materials posses a naturally occurring θ-term other magnetoelectric couplings are in general necessary to fully describe the optical response of such materials. Nevertheless, it will be interesting to see whether these new terms, which will certainly modify the Casimir force, will compete or favour Casimir repulsion.

In conclusion, this chapter has shown that topological insulators, rooted on the topological properties of Dirac quasiparticles, offer promising new possibilities to achieve the extremely elusive Casimir repulsion in vacuum, although further investigation is needed to asses its experimental feasibility. Furthermore, this chapter has pointed out a new route to achieve repulsion through the study and characterization of Casimir systems composed by magnetoelectric materials. Motivated by these results, in the next chapter we will try to model the dependence of the topological magnetoelectric term on frequency $\theta(\omega)$ and envision how it may arise from a generic three dimensional topological insulator model.

8. Finite frequency magnetoelectric response of a three dimensional topological insulator

"I have nothing to offer anybody but my own confusion."
-Jack Kerouac.

8.1. Introduction

In the introduction and the previous chapter, it was argued that topological insulators with gapped surface states are characterized by a dielectric response function $\varepsilon(\omega)$ and a quantized topological magnetoelectric response θ [8, 9, 77, 78], of the form (1.21)

$$S_\theta = \int dt d^3x (\alpha/4\pi^2)\theta \mathbf{E}\cdot\mathbf{B},$$

where $\alpha = e^2/\hbar c$ and $\theta = \pi$. In fact, it is natural to suspect that even θ should be a *response function* and depend on frequency, which in general will alter the optical response of the topological insulator.
In this chapter we will try to obtain, from a generic model of a topological insulator, such a dependence and try to clarify its origin. It will be shown that a constant and quantized θ term is only a reasonable approximation when the frequencies of the relevant fields are much smaller than the surface gap m. In general however, the magnetoelectric response will depend on the frequency, and permeate into physical observables, just as the dielectric function or the magnetic permeability do in conventional dielectrics, thus modifying all the described phenomena related to this topological term.
Despite the fact that this term still remains experimentally elusive, there has been much ongoing work on its consequences. It has has been predicted to give rise to a plethora of phenomena including the Kerr and Faraday rotation of light determined by the fine structure constant [278, 279] together with the Casimir effect described in the preceding chapter, all of which would be substantially modified if $\theta = \theta(\omega)$.

In this chapter, we derive the finite frequency magnetoelectric response of a model Hamiltonian which captures the basic features of a three dimensional topological insulator. To do

so, and before treating a $D = 3+1$ topological insulator model, we will first study a toy version model of a topological insulator in $D = 1+1$. The insight gained by such a model will serve as a benchmark for the more complicated $D = 3+1$ case. In both cases we will generalize the method introduced in Ref. [77] to finite frequency which relates the response of topological insulators to that of an effective model with an extra dimension, that behaves as a higher dimensional analogue of the quantum Hall effect [283]. This approach has been shown to be helpful to understand the topological origin of this response, and it is also an efficient computational tool in practice. It has proven useful to predict the magnetoelectric response in a related physical situation [284–286] where the bulk of the topological insulator is assumed to be doped. In this particular case, the magnetoelectric response is not quantized if the chemical potential is outside the band gap, a behaviour that may be interpreted as arising from the corresponding anomalous quantum Hall effect analogue in five dimensions. Therefore in this chapter we will extend these analysis to a more general and potentially relevant experimental situation where both the frequency and the chemical potential are kept finite, a case that can also be understood as descending from a five dimensional finite frequency quantum Hall effect at finite chemical potential. As a consistency check we will show how known results are recovered in the appropriate limits, giving further physical insight into them.

Hopefully, by the end of this chapter we will have gained some further understanding on the topological response of Dirac quasiparticles under finite frequency electromagnetic fields, in line with the second guiding principle of this thesis which is the understanding of the interplay between topological effects and Dirac quasiparticles.

8.2. Finite frequency topological response of a $D = 1+1$ topological insulator

Topological properties of $D = 1+1$ models have been extensively studied as toy models for higher dimensional theories [287–290]. They have also found their own celebrated applications, being the case of Polyacetylene the paradigmatic example [291–294]. Analogous to the $D = 3+1$ case discussed in chapter 1, a domain wall in the mass generates a zero mode at the boundary. The charge carried by such a defect was shown to be quantized to $e/2$ by Jackiw and Rebbi [79]. Equivalently, it can be understood as arising from a theta like term in $D = 1+1$, where the charge is given by the Goldstone-Wilzeck formula [295]. Building up on these ideas, in this section we will analyse the finite frequency topological response of a $D = 1+1$ topological insulator model which will serve as a starting point to understand the conceptually equal, but technically more intricate, case of a $D = 3+1$ topological insulator.

8.2.1. (Toy) Model

To begin our discussion we will first define the $D = 1 + 1$ model that will serve to illustrate the procedure in the more complete $D = 3 + 1$ model. Our starting point will be the model introduced in [77] for which we now summarize its main properties. As discussed in chapter 1, a time reversal invariant topological insulator is a bulk insulator with protected surface states. Analogously, in $D = 1 + 1$ dimensions, the time reversal symmetry is replaced by the charge conjugation matrix C which will now protect the surface states [77]. Keeping in mind these points, consider the following tight binding model on a square lattice (we set the hopping parameter to $t = 1$)

$$H_0^{1D} + H_M = \sum_x \left[c_x^\dagger \frac{(\sigma_z - i\sigma_x)}{2} c_{x+\hat{s}} + h.c. \right] + (M-1) c_x^\dagger \sigma_z c_x, \tag{8.1}$$

where $\hat{s}$ runs to nearest neighbours at each site of the chain and the operators $c_x^\dagger (c_x)$ create (annihilate) an electron at site x. To gain some intuition we can transform it into Fourier space

$$H_0^{1D}(k) + H_M(k) = \sum_k c_k^\dagger (\sin(k)\sigma_x + (\cos(k) + M)\sigma_z) c_k. \tag{8.2}$$

It is now evident that with the chemical potential chosen to be $\mu = 0$ this Hamiltonian describes a $D = 1 + 1$ insulator which has a massive Dirac spectrum at $k = 0$ with a gap of magnitude $2M$ which we will henceforth refer to as the bulk gap. As in section 1.2.2, the presence of a boundary in the Hamiltonian can be modelled by making the gap position dependent, promoting the mass term of (8.1) to [1]

$$H_M = \sum_x M \cos\theta(x) c_x^\dagger \sigma_z c_x. \tag{8.3}$$

This will account for the band inversion by setting $\theta(-\infty) = \pi$ in the bulk of the topological insulator and $\theta(\infty) = 0$, which defines the anticipated domain wall in the mass, parametrized by $\theta(x)$. Following the discussion in section 1.2.2 a quantized topological response is possible when the boundary states are gapped. This is taken into account by introducing a C-breaking term with strength m

$$\begin{aligned} H^{1D} &= H_0^{1D} + H_M + H_m \\ H_m^{1D} &= m \sum_x \sin\theta(x) c_x^\dagger \sigma_y c_x. \end{aligned} \tag{8.4}$$

Note that, in contrast with the simplified model of section 1.2.2 we here allow the size of the surface gap m, described by the surface term $m \sin\theta(x)$, to be different than the bulk gap M. The domain wall imposed for $\theta(x)$ recovers Hamiltonian (8.1) with $\pm M$ when $x \to \pm\infty$ describing the interface between a trivial insulator and a topological insulator. Therefore, the

[1] Together with a trivial redefinition of parameter M.

Hamiltonian (8.4) models the boundary between a $D = 1+1$ topological insulator and a trivial insulator with a gapped boundary state. We will now elaborate on the topological response of such a model.

8.2.2. Topological response

In this section we will define the response of the toy model presented above that will serve as an analogue to the topological magnetoelectric response in $D = 3+1$. The response of Hamiltonian (8.4) is encoded in the expectation value of the current operator $\langle j^\mu(x_0)\rangle$ at a point x_0 as we now show.

For a profile $\theta(x)$ that is sufficiently smooth over length scales $l_m \equiv 1/(v_F m)$ (this is, $|\partial_x\theta| << 1/l_m$), the current at x_0 is mainly determined by θ around $\theta(x_0) \equiv \theta_0$, because correlation functions decay exponentially with l_m.

We may therefore include its effects in perturbation theory in $\partial_x\theta$, which is by assumption small. Thus, for the calculation of $j^\mu(x_0)$, we approximate [284]

$$\theta(x) \approx \theta_0 + \partial_x\theta|_{x=x_0}(x-x_0) + \cdots, \tag{8.5}$$

in the Hamiltonian (8.1), where $\theta_0 \equiv \theta(x_0)$. To first order in $\partial_x\theta$ the Hamiltonian (8.1) reads

$$\begin{aligned} H_{1D} &= H_0^{1D} + \sum_x c_x^\dagger(M\cos\theta_0\sigma_z + m\sin\theta_0\sigma_y)c_x \\ &+ \partial_x\theta|_{x_0}\sum_x (x-x_0)c_x^\dagger(-M\sin\theta_0\sigma_y + m\cos\theta_0\sigma_z)c_x. \end{aligned} \tag{8.6}$$

Note that in this Hamiltonian θ_0 is just a constant parameter that we will deal with later.

As mentioned in the introduction one should recall that in $D = 3+1$ dimensions, the functional form in the effective action is $\theta\mathbf{E}\cdot\mathbf{B} \sim \theta\partial A\partial A$, which can be rewritten as $A\partial\theta\partial A$ by integrating by parts [75, 77]. On the other hand, in $D = 1+1$ dimensions, the topological term is of the form [93] $A\partial\theta$. Since the current is defined as a functional derivative of the action with respect to the gauge field, it is nothing but $j^\mu = \delta S/\delta A_\mu \sim \partial\theta$, which is the essence of the celebrated Goldstone-Wilzeck formula [295].

Therefore, the topological contribution is computed through a calculation of the expectation value of j^μ to first order in $\partial_x\theta$. It is not difficult to show, using standard quantum field theory methods [75] that to this order, the current is given by

$$\langle j^\mu(x_0)\rangle = \partial_x\theta|_{x_0}\sum_x \left\langle \hat{J}^\mu(x_0)\hat{J}^\theta(x)\right\rangle, \tag{8.7}$$

where $J^\mu(x)$, to be defined below, is the current operator and $J^\theta(x)$ is the operator attached to $\partial_x\theta$ in (8.4). In momentum space, the latter is represented by a vertex in momentum space of the form

$$\hat{J}^\theta(k) = (M\sin\theta_0\sigma_z - m\cos\theta_0\sigma_y)\partial_k \equiv J^\theta\partial_k. \tag{8.8}$$

Gathering these ingredients, the Fourier transform of (8.7) reads [2]:

$$\langle j^{\mu}(x_0)\rangle \;=\; -i\,\partial_x\theta|_{x_0}\sum_{k,p} e^{ix_0 p} J^{\mu}_k G_{k,\theta_0} J^{\theta}\partial_{p_1} G_{k+p,\theta_0}, \tag{8.9}$$

where the integral spans the entire Brillouin zone. Note that all variables are to be taken as two component space-time vectors, while the derivative only acts on the spatial component, which we denote with p_1 to emphasise its spatial nature. The electronic Green's function depends on the two-momentum vector (k_0, k) which can be written as $G(k_0, k, \theta_0) = (k_0 - H^{(1D)}(k, \theta_0))^{-1}$. It is defined through the Fourier transformed version of Hamiltonian (8.4)

$$H^{1D}(\mathbf{k}, \theta_0) = \sum_k c^{\dagger}_k(\sin(k)\sigma_x + (\cos(k) + M)\sigma_z)c_k + (M\cos\theta_0\sigma_z + m\sin\theta_0\sigma_y), \tag{8.10}$$

that depends parametrically on θ_0, the bulk mass M and the surface mass m. The current vertex is defined as $J^1(k) = \frac{\partial H^{1D}(k,\theta_0)}{\partial k}$, $J^0 = \mathrm{I}_{2\times 2}$ [3].

Note that (8.9) determines the topological response completely, given a particular profile of $\theta(x)$, which would end our computation. However, one can use this expression to calculate a quantized quantity which is independent on the exact form of $\theta(x)$, and will only depend on its asymptotic values at $\pm\infty$.

To this extent, consider the total charge accumulated at the domain wall

$$\begin{aligned} Q &= \int_{-\infty}^{\infty}\frac{dx_0}{2\pi}\,\langle j^0(x_0)\rangle && (8.11)\\ &= -i\int_{-\infty}^{\infty}\frac{dx_0}{2\pi}\partial_{x_0}\theta(x_0)\sum_k J^0_k G_{k,\theta_0} J^{\theta}\,\left[\partial_{p_1} G_{k+p,\theta_0}\right]\big|_{p=0} && (8.12)\\ &= \int_{-\pi}^{0}\frac{d\theta_0}{2\pi}\sum_k J^0_k G_{k,\theta_0} J^{\theta}\,\left[\partial_{p_1} G_{k+p,\theta_0}\right]\big|_{p_1=0}. && (8.13)\end{aligned}$$

In the last step we have performed a change of variables from x_0 to the equivalent integral in terms of θ_0. This in fact turns out to be a neat trick since now, θ_0 acts like a momentum coordinate in a higher dimension. Therefore, mathematically, we can rewrite this last expression in terms of the response function of a $D = 2 + 1$ dimensional insulator. The integral is exactly the finite frequency optical (Hall) response of a $D = 2 + 1$ insulator described by (8.10) with θ_0 acting as an extra momentum coordinate, with the only important difference that $\theta_0 \in [-\pi, 0]$. Explicitly

$$\begin{aligned} Q(p_0) &= \int_{-\pi}^{0} d\theta_0\partial_{p_1}\sum_k \left[J^0_k G_{k,\theta_0} J^{\theta} G_{k+p,\theta_0}\right]\Big|_{p_1=0} && (8.14)\\ &= \partial_{p_1}\Pi^{0\theta}(p_0, p_1), && (8.15)\end{aligned}$$

[2] The Hamiltonian of the system coupled to an external electromagnetic field can be written as $H^{1D} = \sum_k c^{\dagger}_k h(k,\theta_0)c_k + \sum_{k,q} c^{\dagger}_{k+q/2}\frac{\partial h(k,\theta_0)}{\partial k}c_{k-q/2}A_1 - i\,\partial_x\theta|_{x_0}\sum_k c^{\dagger}_k\partial_q c_{k-q}$ where $h(k) = (\sin(k)\sigma_x + (\cos(k) + M\cos\theta_0)\sigma_z) + m\sin\theta_0\sigma_y$ and A^{μ} is the gauge field. The current response in momentum space can be determined from its definition $j^{\mu} = \delta S/\delta A_{\mu}$

[3] In the derivation we have omitted terms arising from vertices with higher derivatives of $H^{1D}(k, \theta_0)$ with respect to k [296], that will not contribute to the topological response

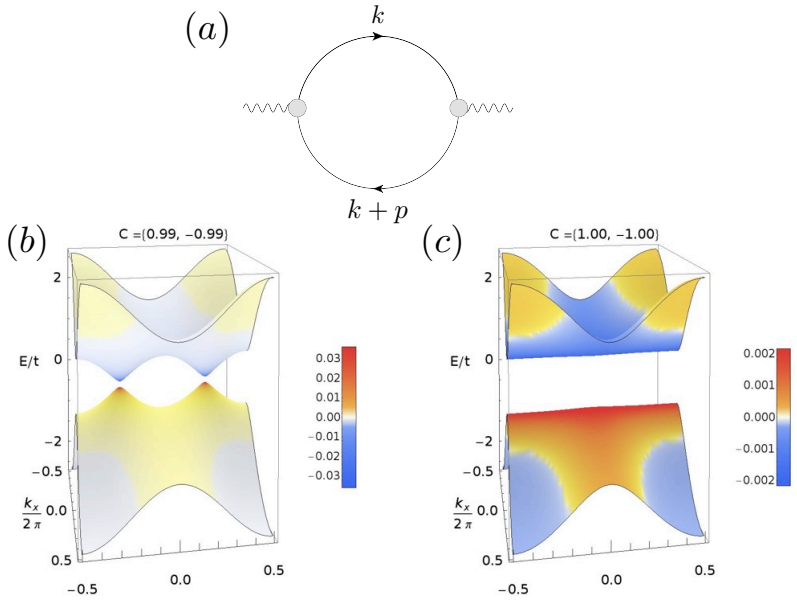

Figure 8.1.: (a) Bubble diagram. (b), (c) Berry curvature for $m \neq M$ and $m = M$ respectively.

where the last line is nothing but the antisymmetric part of the $D = 2+1$ bubble diagram shown schematically in Fig. 8.1 (a) and given by

$$\Pi^{\mu\nu}(p) = \int d^3k G(k) J_k^{\mu} G(k+p) J_k^{\nu}$$

with the spatial momenta set to zero, i.e. $\Pi^{0\theta}_{odd}(p_0)$.
As a consistency check it is easy to see that for the zero frequency limit this formula reduces to the Goldstone-Wilzeck formula [295] for the charge

$$Q = e\int_{-\infty}^{\infty}\frac{dx}{2\pi} j_{\theta}^{\mu=0}(x) = e\int_{-\infty}^{\infty}\frac{dx}{2\pi}\partial_x\theta(x) = \frac{e}{2\pi}[\theta(\infty)-\theta(-\infty)] = \frac{e}{2}, \tag{8.16}$$

that shows that a domain wall carries a $e/2$ charge [79]. Away from small frequencies compared to M and m, the quantization breaks down, as will be shown immediately below.
To summarize, in this section we have calculated the charge bound to the domain wall at a finite frequency for a $D = 1+1$ topological insulator model. This topological response function is only sensitive to the asymptotic values of the domain wall, and not to its precise functional form, and it is quantized at low frequencies. Importantly, we have also shown that this topological response of the $D = 1+1$ system can be written in terms of a the Hall response of a topological insulator in an extra dimension. We will see that this is possible also in the $D = 3+1$ case but, before doing so, it is instructive to consider some particular limits of the $D = 1+1$ model.
The way we will proceed is the following. The Hamiltonian (8.10) will be treated as a $D = 2+1$ Hamiltonian with a topological optical response governed by the antisymmetric part of $\Pi^{\mu\nu}(p_0)$. To give some analytical insight on this function it is useful to study how

the band structure and Berry curvature in (k, θ_0) space behave as one considers different cases in the mass parameter space (m, M). This will tell us how the integrand behaves and therefore how to approximate it. We will see that some of this limits will turn to be useful also for the $D = 3+1$ topological response.

The case where $m \ll M$

In this case, the surface gap is much smaller than the bulk gap which, translated to $D = 3+1$ insulator, will represent a physically realistic limit since in real materials the bulk gap must be larger than the surface gap.
The first thing to notice is the presence of a massive Dirac fermion at $(k, \theta_0) = (0, \pi/2)$, where all the Berry curvature is accumulated (see Fig. 8.1 (b)). It is therefore reasonable to approximate the model by a *single* effective Dirac model around that point. The reason it is just one Dirac cone stems directly from the fact that the θ integral is to be evaluated in the interval $[-\pi, 0]$. Thus, expanding the Hamiltonian (8.10) around $(0+k, \pi/2+\tilde{\theta})$ to first order reads

$$H(k, \theta) \approx \sigma_x k + M\tilde{\theta}\sigma_z + m\sigma_y. \tag{8.17}$$

Considering this model as a massive $D = 2+1$ Dirac Hamiltonian amounts to identify $k_y = M\tilde{\theta}$, and the gap as the surface gap m. With this Hamiltonian, the antisymmetric part of $\Pi^{\mu\nu}(p_0)$ that determines the topological frequency response of the $D = 1+1$ insulator amounts to compute the Hall conductivity of a Dirac fermion in $D = 2+1$, given by the antisymmetric part of

$$\Pi^{\mu\nu}(p) = \int \frac{d^3k}{(2\pi)^3} G(k)\gamma^\mu G(k+p)\gamma^\nu, \tag{8.18}$$

at zero spatial momenta, with the particular representation of the Clifford algebra $\gamma_0 = \sigma_y$, $\gamma_1 = \sigma_y\sigma_x$ and $\gamma_2 = \sigma_y\sigma_z$. The integral can be computed analytically [297] and so one can write the finite frequency response of the system as

$$Q(p_0) \quad = \quad \frac{e}{2}\frac{m}{p_0}\log\left|\frac{2m+p_0}{2m-p_0}\right|, \tag{8.19}$$

which reduces to $Q = \frac{e}{2}$ when $p_0 \to 0$. Note also, that there is a logarithmic divergence when the frequency of the external field is equal to two times the surface gap, a feature that will be encountered again in the $D = 3+1$ case.
In essence, the main result of this section is that we have described a way to calculate physical responses using Dirac Hamiltonians greatly simplifying the task of analytically resolving the integral. The agreement between the numerical integration of (8.14) compared to equation (8.19) with $m = 0.5$ is shown in Fig. 8.2 (a). The mild deviation can be attributed to the finite imaginary part introduced in the Green function to perform the numerical integral.

The case where $m = M$

In this case, as it might be expected the response is quite different. The band structure with its Berry curvature is plotted in Fig. 8.1 (c). It is apparent that the Berry curvature is constant in the θ direction, and so the expansion around $(0, \pi/2)$ is not justified. However, we can still expand Hamiltonian (8.10) in the k direction to obtain the Hamiltonian:

$$H(k,\theta) \approx \sigma_x k_x + M\cos\theta\sigma_z + M\sin\theta\sigma_y. \tag{8.20}$$

The action corresponding to this Hamiltonian can be recast in the following, equivalent form:

$$S = \int d^2x\bar{\psi}(\gamma^\mu\partial_\mu - Me^{i\gamma_5\theta})\psi, \tag{8.21}$$

with $\gamma_5 = i\sigma_z\sigma_y = \sigma_x$. In this case, when we compute the response diagram in Fig. the phase factor $e^{i\gamma_5\theta}$ cancels out [4]. Technically this suppresses the θ_0 dependency in (8.14). The θ integral is thus trivially evaluated to give a prefactor of π. The k integral can also be evaluated analytically to obtain:

$$Q(p_0) = \frac{e}{2}\frac{4m|m|}{p_0\sqrt{(2m)^2 - p_0^2}}\arctan\left[\frac{p_0}{\sqrt{(2m)^2 - p_0^2}}\right]. \tag{8.22}$$

We show numerical integration of (8.14) for $M = m = 1$ in Fig. 8.2 (b) as compared to (8.22). The pole is located at $2m$ which is smeared in the numerical integration by choosing a finite imaginary part introduced in the Green function.

The general case $m \neq M$

The general case can be treated numerically by integrating $\Pi^{\mu\nu}(p_0)$ directly at a given (m, M). The interpolation between the limits $m \ll M$ and $m = M$ is shown in Fig. 8.2. It is apparent that in general two poles appear, one at $2M$ and another at $2m$ although analytically however, it is only easy to obtain the two extreme cases. Nevertheless, this is already premonitory of what we can expect in $D = 3 + 1$ although in this chapter we will only analyse the $m \ll M$ limit for this case, physically relevant for the present experimental situation. It is tentative to speculate that the general picture will also hold in higher dimensions, although the proof, which is necessarily numeric, will not be addressed and is left for a future work.

In summary, in this first part of the chapter, the topological optical response, i.e. the charge accumulated at the boundary of a $D = 1 + 1$ topological insulator has been related to the topological response of a higher dimensional insulator which is nothing but the quantum Hall effect arising from considering θ as the extra coordinate in momentum space. Furthermore, we have gained analytic and numeric insight on the structure of such a response

[4] The $e^{i\gamma^5\theta}$ from the vertex cancels with a $e^{-i\gamma^5\theta}$ of the Green's function

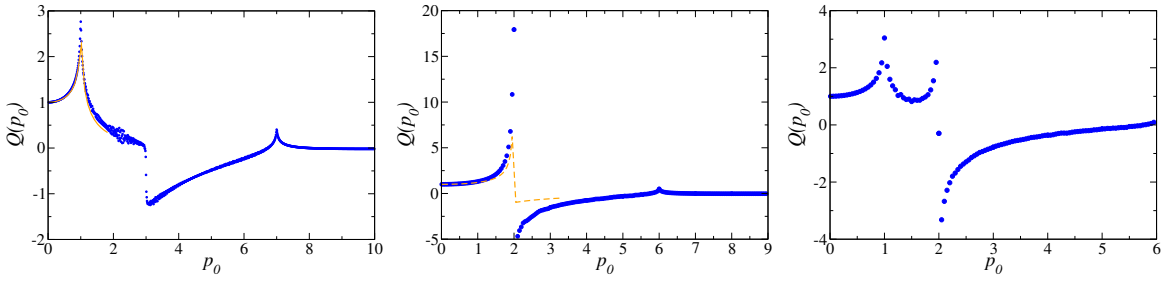

Figure 8.2.: Charged (in units of $e/2$) bound to a mass domain wall in a $D = 1 + 1$ dimensional Insulator as a function of external frequency for (a) $m << M$ where the solid line is plotted from (8.19) (not a fit) (b) $M = m = 1$ where the dashed line is plotted from (8.22) (not a fit)(c) $M = 1$ and $m = 0.5$.

showing that i) it is not quantized for frequencies of the order or bigger than the relevant gap scale and ii) under certain limits, the response can be computed analytically using a Dirac type Hamiltonian, justified by a concentrated Berry curvature close to the massive Dirac points.

The purpose of the following sections is to extend this construction to a generic $D = 3 + 1$ topological insulator model that captures the basic features of real materials, which we now address.

8.3. Finite frequency topological response of a $D = 3 + 1$ topological insulator

Having established the general procedure in the $D = 1 + 1$ toy model it is now conceptually simple, although mathematically more tedious to establish the analogous result for the topological magnetoelectric term. We will first motivate the model and then apply the knowledge gained in previous sections to this higher dimensional case, trying to emphasize the similarities and differences between both cases.

8.3.1. The model

Let us start by choosing a model which captures the essence of a generic $D = 3 + 1$ topological insulator. To this extent consider the lattice Hamiltonian introduced in Ref. [77], which captures the low energy description of a generic topological insulator, for instance Bi_2Se_3

[285, 298]. This Hamiltonian can be written as $H = H_0 + H_M$ with

$$H_0 = t\sum_{\mathbf{x},\mathbf{s}} c^\dagger_{\mathbf{x}} \frac{\Gamma_0 - i\Gamma_s}{2} c_{\mathbf{x}+\hat{\mathbf{s}}} + h.c. - 3tc^\dagger_{\mathbf{x}}\Gamma^0 c_{\mathbf{x}}, \tag{8.23}$$

$$H_M = M\sum_{\mathbf{x}} c^\dagger_{\mathbf{x}}\Gamma^0 c_{\mathbf{x}}, \tag{8.24}$$

with $\mathbf{x}$ running through all unit cells of a cubic lattice, $s = 1,2,3$, and $\hat{\mathbf{s}}$ is the lattice vector in the s direction. Γ_μ are defined as the set of 4×4 matrices that satisfy $\{\Gamma_\mu, \Gamma_\nu\} = 2\delta_{\mu\nu}$, with $\mu,\nu = 0,1,2,3,4$ including an extra Γ_4 that will be used shortly. In momentum space the Hamiltonian reads

$$H(\mathbf{k}) = \left(t\sum_{s=1}^{3}\cos(k_s) + M - 3t\right)\Gamma_0 + t\sum_{s=1}^{3}\sin(k_s)\Gamma_s \tag{8.25}$$

These models, parametrized by t and M, can be thought of as lattice models that host an odd number of low energy massive Dirac fermions [5]. For example, for $|M| < t$ there is a single Dirac fermion at $\mathbf{k} = 0$ of gap M.

As in the $D = 1+1$ case, the presence of a boundary in the Hamiltonian can be modelled by making the gap position dependent by promoting (8.24) to

$$H_M = \sum_{\mathbf{x}} M\cos\theta(\mathbf{x}) c^\dagger_{\mathbf{x}}\Gamma_0 c_{\mathbf{x}}. \tag{8.26}$$

which again accounts for the band inversion by setting $\theta(-\infty) = \pi$ in the bulk of the topological insulator and $\theta(\infty) = 0$. Both experimentally [82] and from *ab initio* calculations [298] the bulk band gap is known to be of the order of $M \simeq 0.3$ eV for Bi_2Se_3. Note that, also in analogy with the $D = 1+1$ case, the specific dependence of θ on x will not be needed for our purposes, only its asymptotic values.

Consider now a time reversal symmetry breaking perturbation at the surface, the effect of which gaps the surface states. Mathematically it can be generically be included as [284]

$$H_m = \sum_{\mathbf{x}} m\sin\theta(\mathbf{x}) c^\dagger_{\mathbf{x}}\Gamma_4 c_{\mathbf{x}}, \tag{8.27}$$

which is localized at the boundary and opens a surface gap m. This surface gap can arise from doping the topological insulator with magnetic impurities for example, and has been measured to be $m \sim 50$ meV [299, 300]. As mentioned above, these experimental observations will justify the limit $m \ll M$ where analytical results may be computed.

8.3.2. Finite frequency electromagnetic response of a topological insulator

To obtain the finite frequency response of the topological insulator system to electromagnetic fields in the presence of $\theta(x)$, we will first generalize the procedure used above for the

[5] A term of the type $\epsilon(\mathbf{k})\mathrm{I}_{4\times 4}$ can also be included but it does not affect the topological properties so we neglect it for simplicity

$D = 1+1$ case to the $D = 3+1$ dimensional case. It is worth to emphasize here that the current response of the system is computed in a way that the effect of $\theta(x)$ is included in a manifestly perturbative fashion along the derivation.
As before, our starting point is to consider the current density at some particular point in space-time x_0:

$$j^\mu(x_0) = \frac{\delta S}{\delta A_\mu(x_0)}, \tag{8.28}$$

where S is the action functional of the system. For a profile $\theta(x)$ that is smooth enough (see discussion in section 8.2.2) we may include its effects in perturbation theory in $\partial_i\theta$, which is by assumption small. For the calculation of $j^\mu(x_0)$, we again use the approximation [284]:

$$\theta(x) \approx \theta(x_0) + \partial_i\theta|_{x=x_0}(x^i - x_0^i) + \cdots, \tag{8.29}$$

in the Hamiltonian $H = H_0 + H_M + H_m$ defined by (8.23),(8.26) and (8.27) respectively. It is time to expand up to first order in $\partial_i\theta$ which affects the mass terms, that now reads

$$\begin{aligned} H_M + H_m &= \sum_{\mathbf{x}} c^\dagger_{\mathbf{x}}(M\cos\theta_0\Gamma_0 + m\sin\theta_0\Gamma_4)c_{\mathbf{x}} \\ &+ \partial_i\theta|_{\mathbf{x}_0}\sum_{\mathbf{x}}(x^i - x_0^i)c^\dagger_{\mathbf{x}}(-M\sin\theta_0\Gamma_0 + m\cos\theta_0\Gamma_4)c_{\mathbf{x}}. \end{aligned} \tag{8.30}$$

As before, in this Hamiltonian θ_0 is just a constant parameter.
We can now compute the current response at x_0 when a time dependent but spatially uniform electric field is applied to the system. This is done by computing the expectation value of j^μ to first order in both $\partial_i\theta$ and the electromagnetic field A_μ, with a generalized Kubo formula, equivalent to (8.7)

$$j^i(x_0) = \partial_s\theta|_{\mathbf{x}_0}\sum_{x,x'}\left\langle \hat{J}^i(x_0)\hat{J}^j(x)\hat{f}^s_\theta(x')\right\rangle A_j(x) \tag{8.31}$$

where $i,j,s = 1,2,3$, repeated indices summation is implied and x_0, x, x' are full space-time variables. In this expression $\hat{J}^i(x)$ are the current operators, and $\hat{f}^s_\theta(x)$ is the operator attached to $\partial_s\theta$ in (8.30) which defines the following vertex in momentum space

$$J^s_\theta(k) = (-M\sin\theta_0\Gamma_0 + m\cos\theta_0\Gamma_4)\partial_{k_s} \equiv J_\theta\partial_{k_s}. \tag{8.32}$$

With this, the Fourier transform of the current reads

$$\begin{aligned} j^i(x_0) &= \partial_s\theta|_{\mathbf{x}_0}\int_{BZ}\frac{d^4p}{(2\pi)^4}e^{-ipx_0}A^j_p\int_{BZ}\frac{d^4k}{(2\pi)^4} \\ &\times\left[\mathrm{Tr}J^i_{k-p/2}G_{k-p}J^j_{k-p/2}G_kJ_\theta\partial_{k_s}G_k + \left\{\begin{array}{c} p \longleftrightarrow -p \\ i \longleftrightarrow j \end{array}\right\}\right]. \end{aligned} \tag{8.33}$$

where the integral spans the entire Brillouin zone. The electronic Green's function, which depends now on a four-momentum vector $k = (k_0, \mathbf{k})$ is given by $G(k, \theta_0) = (k_0 - H(\mathbf{k}, \theta_0))^{-1}$ defined through the Fourier transformed Hamiltonian

$$H(\mathbf{k}, \theta_0) = H(\mathbf{k}) + (M \cos\theta_0 \Gamma_0 + m \sin\theta_0 \Gamma_4), \tag{8.34}$$

that depends parametrically on θ_0, the bulk mass M and the surface mass m. The current vertices are defined as $J^i(k) = \frac{\partial H(\mathbf{k},\theta_0)}{\partial k_i}$, $J^0 = \mathrm{I}_{4\times 4}$ with $i = 1, 2, 3$. As in the $D = 1+1$ case, in the derivation we have omitted terms arising from vertices with higher derivatives of $H(\mathbf{k}, \theta_0)$ with respect to k [296], that will not contribute to the magnetoelectric response. It is now evident that being $D = 3+1$ introduces some extra complications regarding the analytic form of $j^\mu(x_0)$, although every step is conceptually equivalent to the $D = 1+1$ case. Before we proceed further, it is worth noting that this equation may also be written as

$$j^i(x_0) = \partial_s \theta|_{\mathbf{x}_0} \int_{BZ} \frac{d^4p}{(2\pi)^4} e^{-ipx_0} \partial_{q_s} \left[\Pi_4^{ij}(p, q, \theta_0) \right]_{q=0} A^j_p, \tag{8.35}$$

where

$$\Pi_4^{\mu\nu}(p, q, \theta_0) = -ie^2 \int_{BZ} \frac{d^4k}{(2\pi)^4} \tag{8.36}$$
$$\times \left[\mathrm{Tr} J^i_{k-(p+q)/2} G_{k-p} J^j_{k-p/2} G_k J_\theta G_{k-q} + \left\{ \begin{array}{c} p \longleftrightarrow -p+q \\ i \longleftrightarrow j \end{array} \right\} \right].$$

and again the identity holds disregarding higher derivatives of $H(\mathbf{k}, \theta_0)$. The function $\Pi_4^{ij}(p, q)$ can be considered the response function to $\delta\theta = \theta_0 - \theta(x)$

$$j^i(x_0) = \int_{BZ} \frac{d^4p}{(2\pi)^4} \frac{d^4q}{(2\pi)^4} e^{-i(p+q)x_0} \Pi_4^{ij}(p, q, \theta_0) A^j_p \delta\theta_q, \tag{8.37}$$

which is the generalization to finite frequency and momenta of Ref. [77]. Equation (8.33) represents an equivalent statement that features an explicit small parameter throughout the derivation.

Consider now the case where the boundary of the topological insulator is in the z direction, so that $\theta(\mathbf{x}) = \theta(z)$. A uniform but time dependent electric field E_j in momentum space can be written in terms of an external vector potential A_i that is constant in space, so that $A_i(p_0, \mathbf{p}) = \delta(\mathbf{p}) A_i(p_0)$.

The total current density in the xy plane, shown to be quantized in the DC limit [77, 284] is defined as $\mathcal{J}^i_{2D} = \int dz j^i(z)$ with $i = x, y$ which is the analogous quantity to the charge stored by the domain wall used in the previous section for the $D = 1+1$ model. The finite frequency generalization of this quantity, i.e. the integrated current density, thus reads

$$\mathcal{J}^i_{2D}(p_0) = \int dz_0 \partial_{z_0} \theta(z_0) \partial_{q_z} \left[\Pi_4^{ij}(p, q, \theta_0) \right]_{q=0, \mathbf{p}=0} A^j_{p_0}. \tag{8.38}$$

With the change of variables $\int_{-\infty}^{\infty} dz_0 \partial_{z_0}\theta = \int_{-\pi}^{0} d\theta$ the current is finally

$$\mathcal{J}^i_{2D}(p_0) \;=\; 2\pi \int_{-\pi}^{0} \frac{d\theta}{2\pi} \partial_{q_z} \left[\Pi_4^{ij}(p,q,\theta)\right]_{q=0,\mathbf{p}=0} A^j_{p_0}. \tag{8.39}$$

As argued in the $D = 1+1$ case, the parameter θ can be thought of as the fifth coordinate of a higher dimensional model in $D = 4+1$ space-time dimensions described by $H(\mathbf{k},\theta)$, whose response functions are integrated only over half of the Brillouin zone, because $-\pi \leq \theta_0 \leq 0$. The topological finite frequency response of a $D = 3+1$ topological insulator is thus intimately related to the finite frequency response of a $D = 4+1$ quantum Hall insulator in the same sense as the response of a $D = 1+1$ topological insulator is related to the finite frequency Hall response of a $D = 2+1$ quantum Hall insulator.

8.3.3. The $m \ll M$ limit

Consider now the experimentally relevant limit where $m \ll M$. In this limit the response in (8.39) can be obtained analytically, which is by now not surprising considering the analogous case of the $D = 1+1$ topological insulator. This is again due to the fact that the low energy physics of Hamiltonian (8.34), considered now as $D = 4+1$ Hamiltonian in half of the Brillouin zone, is dominated by an effective 4+1 Dirac fermion of gap m located at $(\mathbf{k},\theta) = (0,\pi/2)$, where the $D = 4+1$ analogue of the Berry curvature is largest. Integrals in the five dimensional Brillouin zone are thus well approximated by a region of momenta around $(0,\pi/2)$ within some cut-off Λ. The effective Hamiltonian in the vicinity of that point is given by

$$\begin{aligned} H(\mathbf{k},\theta) \approx & H(0,\pi/2) + \partial_{k_i} H\big|_{(0,\pi/2)} k_i + \partial_\theta H\big|_{(0,\pi/2)} \tilde{\theta} \\ = & \Gamma^i k_i + M\tilde{\theta}\Gamma^0 + m\Gamma^5 \end{aligned} \tag{8.40}$$

with $\theta = \pi/2 + \tilde{\theta}$. In analogy with the $D = 1+1$ case and Hamiltonian (8.17) we can identify Hamiltonian (8.40) as that of a $D = 4+1$ Dirac fermion where $k_4 = M\tilde{\theta}$. The cut-off for this model is of order $\Lambda \approx M$, and for frequencies that satisfy $p_0 << M$ may be taken to infinity. Within this approximation, the integral in (8.39) is

$$\begin{aligned} \Pi_5^{ij0}(p,q) \equiv & \int_{-\pi}^{0} \frac{d\theta}{2\pi} \Pi_4^{ij}(p,q,\theta) \\ \approx & \frac{-ie^2}{M} \int^{\infty} \frac{d^5k}{(2\pi)^5} \mathrm{Tr}\Big[\Gamma^i G_{k-p} \Gamma^j G_k M\Gamma^0 G_{k-q} + \Gamma^j G_{k+p-q} \Gamma^i G_k M\Gamma^0 G_{k-q}\Big], \end{aligned} \tag{8.41}$$

where we have used $d\tilde{\theta} = dk_4/M$, and eq. (8.36) with the current vertices approximated around $(0,\pi/2)$: $J^i = \Gamma^i$, $J^\theta = M\Gamma^0$. The Green functions in these expressions are those of a $D = 4+1$ Dirac fermion, obtained as $G(k) = (k_0 - H(\mathbf{k}))^{-1}$ from eq. (8.40), where now $\mathbf{k}$ has four components. Consequently, the function Π_5^{ij0} corresponds to the Dirac fermion triangle diagrams shown in Fig. 8.3 (a) that can be computed analytically with standard methods

that are detailed in appendix E.1 (see also Ref. [301]), and can be considered as the optical response of the five dimensional analogue of the quantum Hall effect. The magnetoelectric response is given by the antisymmetric part of the diagram and thus the total current finally reads

$$\begin{aligned} \mathcal{J}^i_{2D}(p_0) &= 2\pi\Pi_5(p_0,\mu)\epsilon^{ij}E_j(p_0) \\ &\equiv \sigma(p_0,\mu)\epsilon^{ij}E_j(p_0), \end{aligned} \tag{8.42}$$

where the function

$$\Pi_5(p,q) = \frac{\epsilon_{ij}}{2}\frac{1}{p_0}\partial_{q_z}\left[\Pi_5^{ij0}(p,q)\right]_{q=0,\mathbf{p}=0}, \tag{8.43}$$

and we have used that $E^j_p = ip_0A^j_p$.
Equations (8.42) and (8.43) define the finite frequency response of our topological insulator and are the analogue of (8.14). As mentioned earlier, the total current is here analogous to the total charge carried by the domain wall in the $D = 1+1$ model.
It is now interesting to interrogate this equation to understand different experimentally relevant scenarios. In the next section we will investigate the case of a finite frequency response in the presence and absence of a finite chemical potential. Regarding this last possibility note that it is possible to restore the dependence on the chemical potential in the Green's function as explained in appendix E.2 since nothing in the above argument depends on whether or not the chemical potential is finite as long as $\mu << M$.

8.4. Results

8.4.1. Finite frequency response with zero chemical potential

In this section we compute the function $\sigma(p_0, \mu = 0)$ defined above which determines the response of the topological insulator to an external electromagnetic field of finite frequency. For a massive Dirac fermion at zero chemical potential, our precise case when $m \ll M$, the function $\Pi_5(p_0, \mu = 0)$ can be analytically computed following [301] for example (we refer the reader to appendix E.1 for details) resulting in

$$\sigma(p_0,\mu=0) = \frac{1}{2}\frac{e^2}{h}\frac{m}{p_0}\log\left|\frac{2m+p_0}{2m-p_0}\right|. \tag{8.44}$$

This function, plotted in Fig. 8.3 (b), governs the finite frequency response of a topological insulator for frequencies much smaller than the bulk gap M but of the order of the surface gap m. The first thing to note is that the quantization of the real part at low frequencies is broken down at finite frequency giving rise to a logarithmic divergence at $p_0 = 2m$. Therefore, close to this range of frequencies, the θ term will dominate the electromagnetic response of the topological insulator. This is particularly important for Casimir type experiments discussed in the last chapter, where the interplay between the optical properties of ordinary

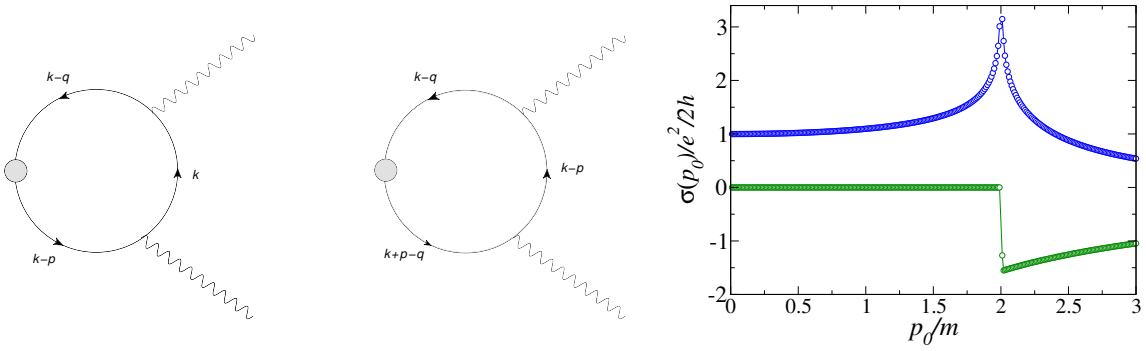

(a) (b)

Figure 8.3.: (a) Feynman diagrams corresponding to eq. (8.41). The second diagram is obtained from the first by by $i \leftrightarrow j$ and $p \leftrightarrow -p+q$. The grey dot represents the $\partial_s\theta$ vertex. (b) Real (top) and imaginary (bottom) parts of $\sigma(p_0, \mu = 0)$ given by (8.44) as a function of p_0 in units of the surface gap m. The quantization is lost at higher frequency and a logarithmic singularity appears at $p_0 = 2m$

and topological response determines not only the sign of the force, but also at what distance does the crossover between attractive and repulsive behaviour happens. The precise way this response alters the Casimir force is an interesting and intricate issue on its own, and it is left for a future study.

This being said, it is important to note as well that the analytic result (8.44) coincides exactly with the optical Hall conductivity of a massive $D = 2+1$ dimensional Dirac fermion (8.19), although with important conceptual differences that we now comment on.

Note first that the DC (zero frequency) response of a single Dirac fermion is quantized to $e^2/2h$, which is consistent with the fact that in the lattice model the integrals span only half of the Brillouin zone. We thus recover the well known result that the boundary of a topological insulator with broken time reversal symmetry hosts a half-integer quantum Hall effect [77].

Being precise, this result should not be interpreted as if there is a massive $D = 2+1$ Dirac fermion somewhere in the system. Instead, these results imply that the three-dimensional optical response of a topological insulator is characterized by spatial average in the z direction of all the $\sigma_{xy}(z)$ Hall conductivities that occur wherever there is a non zero gradient of $\partial_z\theta(z)$. This situation is relevant for the recent experiments described in [299, 300] where the topological insulator is doped with magnetic impurities that break time reversal symmetry. It is remarkable nevertheless that a full $D = 3+1$ calculation reduces to a $D = 2+1$ result. As will be shown immediately below, this statement does not hold for the case of finite chemical potential.

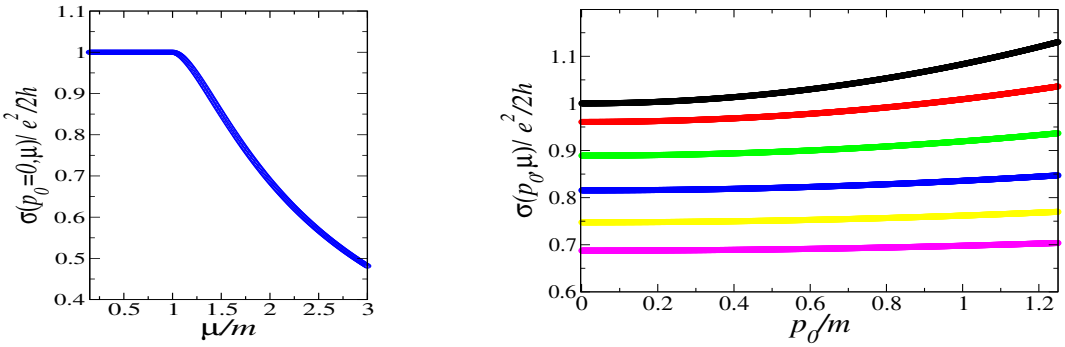

(a) (b)

Figure 8.4.: $\sigma(p_0, \mu)$ as a function of (a) the chemical potential μ for zero frequency in units of the surface gap m and (b) as a function of the external frequency p_0 for $\mu/m = 1.0 - 2.0$ in steps of 0.2 (top to bottom). There is a quantization plateau whenever $|\mu| \leq m$ and a decay for $\mu \geq m$ given by (8.45). For finite frequencies and whenever $|\mu| \geq m$ is satisfied the DC value is not quantized and given by (8.46).

8.4.2. Finite frequency response with finite chemical potential

In order to include the effect of a finite chemical potential, one should compute $\Pi_5(p_0, \mu)$. This can be exactly evaluated for some cases which we proceed to describe (again technical details are left for appendix E.2).

The first case is the DC response at finite μ. This limit was discussed earlier in Ref. [284–286] having obvious interest on its own since topological insulators appear naturally doped in experiments. The numerical evaluation for $\Pi_5(p_0 \to 0, \mu)$ in the DC limit is exactly given for our model by the expression

$$\sigma(p_0 \to 0, \mu) = \frac{e^2}{h} \begin{cases} \frac{1}{2}\text{sgn}(m) & \text{if } |\mu| \leq m \\ \frac{1}{4}\left[\frac{3m}{|\mu|} - \frac{m^3}{|\mu|^3}\right] & \text{if } |\mu| \geq m \end{cases} \tag{8.45}$$

The result is shown in Fig. 8.4 (a). The analytical expression reveals that although there is a quantized value at values of $|\mu| \leq m$ which also occurs for $D = 2+1$ fermions [60], already one can notice very important differences with respect to the $D = 2+1$ case.

In $D = 2+1$ it can be shown (see chapter 6 and [60]) that only a term $m/|\mu|$ arises at fillings larger than the gap. In the present case however, there is a second term which has a different behaviour and scales like $m^3/|\mu|^3$. This term is therefore intrinsically related to the $D = 3+1$ nature of the carriers which is only fully transparent in the analytic result. The extra term turns the kink between the two regimes $|\mu| \leq m$ and $|\mu| \geq m$ smoother, making the curve in Fig. 8.4 (a) differentiable at all μ, in contrast with the $D = 2+1$ result.

Finally it is possible to gain analytic insight into the regime where both the frequency p_0

and μ are kept finite, a situation that can be clearly relevant for experimentally realistic situations (again we refer the reader to appendix E.2 for details). It is easy to see that whenever $|\mu| \leq m$ and $p_0 < 2m$ the result is the same as in (8.44). However there is an experimentally more relevant situation when $|\mu| \geq m$ but still $p_0 < 2m$. This is the case of a doped topological insulator at finite frequency. Evaluating $\Pi_5(p_0 << 2m, |\mu| > m)$ one obtains the first non trivial order in p_0:

$$\sigma(p_0, |\mu| > m) = \frac{1}{4}\frac{e^2}{h}\left[\frac{3m}{|\mu|} - \frac{m^3}{|\mu|^3} + \frac{mp_0^2}{6|\mu|^3}\right], \tag{8.46}$$

which is plotted as a function of the external frequency p_0 for different values of the chemical potential μ in Fig. 8.4 (b). In the limit where $\mu = m$ this coincides with the expansion of (8.44) when $p_0 << 2m$. In this general case, the quantization of the zero frequency value is also absent for finite values of μ and p_0.
These results imply in particular that the Kerr and Faraday rotation proposed in [278, 279] will turn not to be quantized in units of the fine structure constant if the samples are doped and/or if the frequency of the probe is of the order of the surface gap, a common situation in actual experiments [8, 275].

8.5. Discussion and Conclusions

In this chapter, and motivated by the preceding results regarding the Casimir effect on topological insulators, the quantized finite frequency topological response of a generic three dimensional topological insulator model was studied. The cumbersome computation of such a response has made it instructive to address first a discussion of a $D = 1+1$ topological insulator model which prepared the ground for the more intricate $D = 3+1$ case. In the former case, the quantized topological response is given by a generalization to finite frequency of the Goldstone-Wilczek formula for the charge carried by a domain wall. It was found that the quantization is lost for frequencies of the order of the surface m and/or the bulk gap M. Interestingly, the response was related to the optical response of a $D = 2+1$ quantum Hall insulator. In some particular cases, the response could be computed analytically. Remarkably, a $D = 2+1$ Dirac type model emerged for the case $m \ll M$ which gave a first insight into the finite frequency topological response of $D = 1+1$ Dirac quasiparticles. Furthermore, the general case for other (m, M) values was addressed numerically where it was shown that the response presents singularities at $p_0 = 2m$ and $p_0 = 2M$ for the general case when these are different.
After establishing the basic features of this toy model, the generalization of this ideas to the $D = 3+1$ case was discussed. It was found analogously that for the case where the surface gap was much smaller than the bulk gap, a higher dimensional model, in this case in $D = 4+1$ space time dimensions emerged. It was shown that it was possible to rewrite the

response of the $D = 3 + 1$ topological insulator in terms of a $D = 4 + 1$ analogue of the quantum Hall effect. Once established this correspondence, analytical results where obtained for the case of finite frequency and finite chemical potential results which are closely related to the present experimental situation.
In fact, it is reasonable to expect that the presented findings will permeate into physically observable quantities whenever optical probes have a frequency comparable or larger than the surface gap. Given the sizes of the gaps, which are as large as 0.3 eV for the bulk gap and 50 meV for the surface gap [299, 300], it should be possible to observe these effects with infra-red probes, which are fully controllable within current state of the art technology [302]. More elaborate scenarios, such as the proposed repulsive Casimir effect described in chapter 7, the Topological Kerr and Faraday effect [278, 279] or even the optical-modulator device proposed in [303] should be revisited. Finally, these findings can be generalized to other classes of topological materials such as certain classes of Weyl semi-metals that host a Carroll-Field-Jackiw term [304–306]. The description of these novel materials will be the subject of the next chapter where we will try to construct a consistent theory that describes non interacting electrons in Weyl semi-metals. It is possible to generalize these ideas to higher dimensional analogues of topological insulators in the spirit of [77] to construct a hierarchy of finite frequency topological responses.

In conclusion the electrodynamic response of topological insulators at finite frequencies and finite chemical potential has been calculated, relating it to the response of a higher dimensional analogue of a quantum Hall effect. These findings will permeate and strongly affect physical observables, just as any other finite frequency response function and should be taken into account when describing realistic experimental probes.
Hopefully these results at finite frequency will further complement our understanding of the topological response of Dirac quasiparticles, one of the goals that was sought in this thesis.

9. Emergent Lorentz violating QED from Dirac quasiparticles in topological insulator heterostructures

"Kapitza: *A frying pan is tied to the tail of a dog. At what speed does the dog have to run to stop hearing the frying pan hitting the floor*
Landau thought deeply for a long time.
Kapitza: *Do you give up?*
Landau nodded unwillingly.
Kapitza: *The speed is equal to zero*"

- *Landau* by M. Bessarav

9.1. Introduction

In previous chapters, we have encountered and understood different aspects of Dirac quasiparticles, from interaction driven effects to topological states that can arise in these systems. In this chapter however, we will try to build up on the knowledge gained from these situations to engineer a system out of Dirac quasiparticles that can shed light onto theories describing different physical systems, in particular to some extensions of the standard model of particle physics.
The standard model of particle physics has been proven experimentally to be the most complete attempt of humanity to understand the interactions between what to our knowledge are point-like, indivisible or fundamental particles [43]. The fundamental particles are classified into two types, quark and leptons, which, up to the smallest measurable scales have shown no evidence of further internal structure. They interact through the interchange of bosonic particles that describe three of the four fundamental forces found in nature namely the electromagnetic, weak and strong forces. Unifying the fourth force (gravity) with the other three, drives today the efforts of high energy physics and has lead to the development of string theory, potentially the single framework for the fundamental interactions in nature

[307, 308]. Work on these ideas has also motivated possible extensions of the standard model in an attempt to explore different physical phenomena which can lead to progress in this field.

In this context, there has been recent interest on exploring the consequences of breaking Lorentz invariance [309], that establishes the invariance of physics under a change of inertial reference frame, introduced by the pioneering works of Einstein and Lorentz [262, 310, 311]. For instance, some candidate theories to explain quantum gravity suggest that Lorentz invariance can be broken in some regimes [309].

Today, the subject of Lorentz violating extensions of the standard model is a well established discipline in particle physics, although experimentally it seems that the present universe is to a very high accuracy Lorentz invariant [304, 312]. The possibility of a violation of Lorentz symmetry in quantum electrodynamics has been subject of intense theoretical research and its modern approach can be traced down to the studies by Carroll, Field, Jackiw, Colladay and Kostelecky in the 1990s [304, 313, 314]. Despite these efforts it seems that finding a coherent formulation of Lorentz violating QED is challenging, and has generated a very active theoretical debate [314–324].

In this chapter I will address how some of the puzzling issues arising in the simplest extension of Lorentz violating quantum electrodynamics can be resolved in an emergent theory designed out of Dirac quasiparticles. It will be discussed how, with the appropriate choice of parameters, an heterostructure made up of topological insulator stacked with ordinary insulators can host low energy quasiparticles which are described by the Weyl equations. For a general choice of parameters however, the low energy quasiparticles are well described by the $D = 3 + 1$ massive Dirac equation. Concretely, as will be shown below, the effective low energy theory resembles a relativistic field theory which can be then modified with appropriate perturbations, so as to take the form of a Lorentz violating version of QED, described by the following action:

$$S = \int dx^4 \bar{\psi} \left(i\partial\!\!\!/ - m - b\!\!\!/\gamma_5 - eA\!\!\!/ \right) \psi, \tag{9.1}$$

which will serve as a starting point for the discussion. The presence of the constant four vector b_μ implies that the theory breaks Lorentz invariance since it chooses a preferred spacetime direction, given precisely by b_μ. In condensed matter, this is not the first example of such a theory, being ^{3}He a particularly fruitful example [70, 318, 325].

In the context of high energy physics it was realized from the beginning [314] that an action of the form (9.1) generated a Chern-Simons term in the effective action for the electromagnetic gauge field with Lagrangian $\mathcal{L} = \frac{1}{2} k_\mu \tilde{F}^{\mu\nu} A_\nu$ where $\tilde{F}^{\mu\nu} = \epsilon^{\mu\nu\rho\sigma} F_{\rho\sigma}$. Intriguingly, the coefficient of this term turns out to be finite but undetermined [326]. Ever since, there has been considerable theoretical work in order to clarify this issue under several perspectives which we will briefly review at the beginning of the chapter [315–317, 324, 327–329]. A representative list of possible realizations of the coefficient k_μ can be found in [319].

In this chapter, making use of the condensed matter realization of such a theory in the context of Weyl semi-metals, it is shown that a finite and determined value of the radiatively induced Chern-Simons term can be fixed unambiguously. In this case, this is possible due to the fact that a high energy theory exists for this particular system [318], originated in the microscopic model of the Weyl semi-metal, that enables to determine an unambiguous value of the Chern-Simons coefficient k_μ.
The chapter is structured as follows. Firstly, we will give a brief introduction to Lorentz symmetry violation when considering extensions of the standard model. Then, we will review different models of Weyl semi-metals to motivate, in section 9.2 the exact connection between a low energy description of a particular model of a Weyl semi-metal phase and the Lorentz violating quantum electrodynamics (9.1). Then, in section 9.2.1 the radiatively induced Chern Simons term will be derived making emphasis on the peculiarities of this particular condensed matter system. In section 9.2.2, the microscopic theory will be reviewed to fix the uncertainty in the low energy theory. Since the Chern Simons term modifies Maxwell's equations inside this material in section 9.2.3 some physical implications of this term such as birefringence will be discussed. Finally the main conclusions are presented in section 9.3.

9.1.1. Lorentz violating extensions of the standard model

A fundamental principle in physics is the invariance of the speed of light as measured in an arbitrary inertial frame of reference. This property, postulated first by Einstein [310, 311] as part of his special theory of relativity is the basis of our modern understanding of relativistic mechanics and relativistic quantum mechanics which reduce to classical and quantum mechanics when the speed of light is much greater than the characteristic speeds at which the inertial frames, or objects inside them move.
More precisely, the relation between two inertial coordinate systems x' and x is given by a set of transformations, the Lorentz transformations

$$x'^{\mu} = \Lambda^{\mu}_{\nu} x^{\nu}. \tag{9.2}$$

These transformations are defined such that they leave the elementary line element $ds^2 = cdt^2 - dx^2$ invariant [126] which thus defines their precise mathematical form. In particular it is not difficult to show that one recovers the ordinary Galilean transformations when the velocity of light is much bigger than the velocity of the inertial frames.
Any theory we construct should be invariant under this transformation, since imposing this symmetry amounts to impose that the theory is consistent with the postulates of special relativity. This symmetry is known as Lorentz invariance, and has survived as a fundamental theory of nature after numerous experimental tests [1]. In fact, even before this guiding prin-

[1] This condition is to be modified whenever the curvature of space time has to be taken into account, for which we need the theory of general relativity. Then Lorentz invariance becomes a local symmetry which must be satisfied at each point in space, as opposed to a global symmetry

ciple was postulated, the first Lorentz invariant theory already existed: Maxwell's theory of electromagnetism.
This theory describes the effect of electric and magnetic fields on charges and magnets and can be formulated by means of a gauge and Lorentz invariant electromagnetic Lagrangian [262, 311]

$$\mathcal{L}_{EM} = \frac{1}{4} F^{\mu\nu} F_{\mu\nu}. \tag{9.3}$$

It is defined in terms of $F^{\mu\nu} = \partial_\mu A_\nu - \partial_\nu A_\mu$ and by using classical field theory it is not difficult to show that by applying the Euler-Lagrange equations with respect to the electromagnetic gauge field A_μ it is possible to obtain the equations of motion, which are nothing but the conventional Maxwell equations. One can show that Maxwell's equations are Lorentz invariant by direct computation [262, 311] or by noticing that the gauge field A_μ transforms as a vector under a Lorentz transformation [75]. The Lorentz transformations form the Lorentz group which can be decomposed into rotations under three elementary axes and the so called boosts, which relate the two moving frames.
The simplest way to relax Lorentz invariance in Maxwell's theory while preserving gauge invariance, defined as $A_\mu \to A_\mu + \partial_\mu \phi$ where ϕ is a scalar quantity, is to add a term to the Lagrangian [304]

$$\mathcal{L}_{CS} = -\frac{1}{2} s_\mu A_\nu \tilde{F}^{\mu\nu}, \tag{9.4}$$

with $\tilde{F}^{\mu\nu} = \epsilon^{\mu\nu\rho\sigma} F_{\rho\sigma}$ [2]. The vector s_μ chooses a preferred direction in space time and thus breaks Lorentz invariance. For the Lagrangian $\mathcal{L} = \mathcal{L}_{EM} + \mathcal{L}_{CS}$, the Maxwell equations in this case are modified to be

$$\nabla \cdot \mathbf{E} = 4\pi\rho - \mathbf{s} \cdot \mathbf{B}, \tag{9.5}$$

$$\nabla \cdot \mathbf{B} = 0, \tag{9.6}$$

$$\nabla \times \mathbf{E} = -\frac{1}{c}\frac{\partial \mathbf{B}}{\partial t}, \tag{9.7}$$

$$\nabla \times \mathbf{B} = \frac{4\pi}{c}\mathbf{j} + \frac{1}{c}\frac{\partial \mathbf{D}}{\partial t} - \mathbf{s} \times \mathbf{E} + s^0 \mathbf{B}, \tag{9.8}$$

Note in particular that if s^μ is the divergence of a scalar field θ such that $s^\mu = \partial_\mu \theta$ one obtains the Maxwell equations for the case of the so called axion electrodynamics [331] discussed in section 1.2.2, relevant for topological insulators.
At this point it is possible to ask, given this form of Lorentz violation, how can it be obtained from a fermionic Dirac theory. Consider a single fermionic species, which will serve as a test particle to which we will try to add Lorentz violating terms. As we know from chapter 3,

[2] A delicate technical point here is that only the action, and not the Lagrangian constructed out of 9.4 is gauge invariant since there is a surface term which has to be discarded. This surface term is responsible of Fermi arcs in Weyl semi-metals [330].

the theory that describes the interaction of this particle with the electromagnetic field is the usual version of quantum electrodynamics given by the Lagrangian first introduced in (3.4)

$$\mathcal{L}_{QED} = \bar{\psi}(i\Gamma^\mu \partial_\mu - M - e\not{A})\psi - \frac{1}{4}F^{\mu\nu}F_{\mu\nu}. \tag{9.9}$$

If $\Gamma^\mu = \gamma^\mu$ and $M = m$ (γ_μ being the ordinary Dirac matrices that satisfy $\{\gamma^\mu, \gamma^\nu\} = 2g^{\mu\nu}$ and m the fermionic mass) we recover conventional quantum electrodynamics discussed in chapter 3. The reason to use these different symbols is to motivate the generalization to

$$M = m + \not{a} - \not{b}\gamma_5 + \frac{1}{2}H^{\mu\nu}\sigma_{\mu\nu} + im_5\gamma_5, \tag{9.10}$$

$$\Gamma^\mu = \gamma^\mu + c^{\mu\nu}\gamma_\nu - d^{\mu\nu}\gamma_\nu\gamma_5 + e^\mu + if^\mu\gamma_5 + \frac{1}{2}g^{\mu\nu\lambda}\sigma_{\nu\lambda}, \tag{9.11}$$

where we used Feynman's slashed notation $\not{a} = \gamma^\mu a_\mu$ with $\gamma_5 = i\prod\gamma_i$ and $\sigma_{\mu\nu} = \frac{i}{2}[\gamma_\mu, \gamma_\nu]$. The quantities M and Γ^μ contain all possible Lorentz contractions which generate local, gauge invariant and renormalizable couplings in $D = 3+1$. Introducing more flavours increases the number of possibilities, which could explain unusual features such as neutrino oscillations [309]. We will restrict however the analysis to a single species in order to make contact with a particular model of Weyl semi-metals later in the section.

Firstly, notice that not all of the possible terms in (9.10) and (9.11) induce Lorentz violation. This is the case of the m_5 which can be reabsorbed in a redefinition of the fields and the rest of the couplings. Furthermore, the terms e, f and g are usually discarded because of their incompatibility with the electroweak structure [309, 313]. A further redefinition of $\psi \to e^{-ia\cdot x}\psi$ can be also argued to get rid of the term proportional to a^μ [313].

The question is now how the leftover terms affect the photon sector of the theory. In other words, we can couple (9.9) to an external gauge field A_μ (the $\not{A}$ term in (9.9)) representing the electromagnetic field and calculate the effective action for the photons living in a medium described by the fermionic part of (9.9). Calculating the effective action for the photon in this theory amounts to calculate the photon self energy $\Pi^{\mu\nu}$ which was introduced in chapter 3. The effective action will have the general form

$$S = \int dx^4 A_\mu \Pi^{\mu\nu} A_\nu = \int dx^4 \frac{1}{4}F^{\mu\nu}F_{\mu\nu} + \frac{1}{2}k_o^\mu A^\nu \tilde{F}_{\mu\nu} - \frac{1}{4}k_e^{\mu\nu\rho\sigma}F_{\mu\nu}F_{\rho\sigma}, \tag{9.12}$$

The labels e and o indicate whether these terms arise from CPT even or odd terms in (9.9), where C, P and T denote charge conjugation, parity ($\vec{x} \to -\vec{x}$) and time reversal inversion ($x_0 \to -x_0$) operations. Note in particular that the second term in (9.12) is exactly of the form (9.4). The effective action (9.12) is a Lorentz symmetry breaking theory for the photon generated out of Dirac fermions.

In this chapter however, we will try to make contact with a particular Weyl semi-metal model and therefore we will keep only a minimal form of the above introduced by Colladay and Kostelecky [313, 332] which only retains the CPT breaking term proportional to $\not{b}\gamma_5$:

$$S = \int dx^4 \bar{\psi}\left(i\not{\partial} - m - \not{b}\gamma_5 - e\not{A}\right)\psi, \tag{9.13}$$

where the constant four vector b_μ chooses a preferred space-time direction thus explicitly breaking Lorentz invariance. This is a CPT breaking term and thus, from the argument above it will generate an effective action term for the gauge field of the form (9.4).
As explained above, the effective action for the photon in this theory is given directly by the photon self energy $\Pi^{\mu\nu}$. Starting with (9.13) and calculating the one loop vacuum polarization just as in chapter 3 given by the first order bubble diagram in Fig. 3.2 (c) various authors [313, 314, 314–324] were able to show that indeed a term of the form (9.4) emerged from the antisymmetric part of such a diagram [3]

$$\Pi^{\mu\nu}_{\text{odd}} \sim C\epsilon^{\mu\nu\rho\sigma} b_\rho p_\sigma. \tag{9.14}$$

Interestingly, the value of the constant C has been a matter of deep controversy among the cited authors for over a decade now. There is a consensus that the coefficient is finite (in the sense discussed in chapter 3) but undetermined [326] in that they depended on the implementation of the calculation despite the considerable theoretical work in order to clarify this issue under several perspectives. To further understand the origin of such an ambiguity, a few comments are in order. First of all, there are other examples such as the chiral Schwinger model [326] where radiative corrections turn out to be finite but undetermined. In our particular case it is possible to show that different regulators realize different values of C (very similar to what was discussed in chapter 3 for graphene, see (3.41) and [141, 146–151]). The value of C can be shown to be completely arbitrary from a Fujikawa type analysis [316], independent of any regulator and analogous to the one used originally by Fujikawa to derive the axial anomaly [85] discussed in the introductory chapter, a result which was further verified by other non-perturbative (in b) considerations [317], whenever the theory was massive [327]. A different way to understand the origin of the discrepancy is related to gauge invariance. It is only the integral of the term (9.4) which is gauge invariant at the classical level and thus, imposing gauge invariance at all momenta at the quantum level yields $C = 0$ [315]. On the other hand, if one imposes that the quantum action is invariant only at zero momentum, which is equivalent to impose that only the integral of the (9.4) term is gauge invariant, then a finite value is obtained [314]. Finally, several works have suggested under different symmetry and causality considerations that there is no room for such a correction and that it should vanish [315, 324, 328, 329]. A representative list of possible realizations of C can be found in [319].

It is now convenient to anticipate our aim in this chapter. First we will show how the low energy effective theory in the so called Weyl-semi metals realizes the theory (9.1). Secondly, it will be discussed how this theory will provide a finite and unambiguous value for C which we will denote as $C|_{WSM}$ that will turn out to be *zero*, a result which has motivated the quote

[3] This result is in fact perturbative in b. However it can be shown that the ambiguity holds for a non perturbative (in b) calculation [316, 317] which will be discussed in section 9.2.1.

at the beginning of the chapter. The reason for this particular value will be traced back to the originating high energy theory which in this case is the microscopic theory describing these materials, as opposed to the effective low energy description. Finally we will discuss some experimental consequences for Weyl semi-metals emerging from such a theory.
Before describing these in detail we will review some of the proposed realizations of Weyl-semimetals in order to motivate our model.

9.1.2. Weyl semi-metals

Since the advent of graphene [7], systems that host low energy Dirac quasiparticles have been one of the cornerstones of recent condensed matter physics. In the search for novel materials that realize Dirac-like quasiparticles in different dimensions it was recently realized that a generalization of the massless Dirac equation to $D = 3+1$ dimensions

$$H_{\mathbf{k}} = \boldsymbol{\sigma} \cdot \mathbf{k}, \tag{9.15}$$

could be realized in novel materials known as Weyl semi-metals [333–340]. Note here that in contrast with the $D = 2+1$ case the vectors involved are three dimensional such that $\boldsymbol{\sigma} = (\sigma_x, \sigma_y, \sigma_z)$ where σ_i are the Pauli matrices and $\mathbf{k}$ is the three-component momentum vector.
In particle or high energy physics, the corresponding massless fermions that are described by this Hamiltonian are known as Weyl fermions thus giving name to these materials. These spinors transform as irreducible representation of the Lorentz group in $D = 3+1$ dimensions obtained by decomposing the reducible representation that describes Dirac fermions in $D = 3+1$ dimensions when the mass is set to zero in the usual Dirac equation

$$(i\gamma^\mu \partial_\mu - m)\psi = 0. \tag{9.16}$$

When $m = 0$, the four component spinor ψ reduces to two component spinors that satisfy two Weyl equations stemming from the Hamiltonian (9.15) [75]. The question is now to find a microscopic model that realizes such a Hamiltonian for the low energy excitations near the Fermi surface, which, as in graphene, will consist of two points in momentum space.
Emergence of such accidental degeneracy was known to exist from the early days of solid state physics [341]. However, their topological properties and spinorial structure were understood much later in the context of the low energy excitations of ^{3}He-A [70, 318, 325]. More recently, and based on the development of topological insulators, novel systems where these Dirac nodes appear have been proposed. Before going to the particulars of a specific model let us list some general features that a material should posses in order to host topologically *stable* Weyl nodes.
Firstly note the very important fact that, due to the Nielsen Ninomiya theorem [342, 343], only an even number of Weyl species can emerge from a lattice model at low energies. In general, any model with time reversal and inversion symmetry will contain a collection of pairs

of Weyl nodes, located at different points in the Brillouin zone. Each pair is composed of two Weyl fermions of different chirality, analogous to the valley degree of freedom of graphene. Since the two species appear at the same point in the Brillouin zone they are connected by a lattice vector ($\mathbf{G} = 0$) and are topologically unstable and subject to the opening of a gap.
However, the situation is different whenever time reversal or inversion symmetry is broken. In this case the pairs of Weyl nodes separate in momentum space and they will be topologically stable. The topological structure of each node is dictated by chiral symmetry; each Weyl node has a topological number defined by its chirality [318].
Having established these general considerations, we now review briefly some of the proposed models.

- **Strongly correlated electronic phases in Pyrochlore iridates** These materials have a composition of the form $A_2Ir_2O_7$ with $A = Eu, Sm, Nd, Y$ for example. Considering both electron correlations and a spin orbit coupling it was shown through LDA calculations [336, 340] that these materials may host 24 fermionic nodes all related by lattice cubic symmetry for a Hubbard U interaction in the interval $U \in [1, 2]$. Although it is a proof of principle that Weyl semi-metals can be generated from interactions, this proposal has the drawbacks of having a numerous number of fermionic species as well as the fact that it is realized as a competition of interacting phases, making its experimental feasibility somewhat restricted. It might be desirable to have other models which arise from crystalline structures rather than interacting systems.

- **Magnetic doping of topological insulators** It has also been suggested that the topological insulator Bi_2Se_3 could be turned into a Weyl semi-metal by doping the sample with magnetic impurities that order ferromagnetically, which acts as a time reversal symmetry perturbation that separates the Weyl nodes [344]. This is the crystalline version of the heterostructure of alternating topological insulators and ordinary insulators model proposed previously by Burkov and Balents [333] that will be described an used in detail in the next section. The advantage of both of these proposals is that they host the minimal number of species (two) of Weyl fermions which simplifies their theoretical description in contrast with the model based on Pyrochlore iridates described above.

- **Flux insertion in cubic lattices** Alternatively, it is also possible to obtain Weyl semi-metal phases by inserting a number of magnetic fluxes per plaquette in cubical lattices [339, 345] that could be realized experimentally by the use of optical lattices. The number of Weyl nodes depends on the number of fluxes per unit cell which might offer some degree of tunability over the other described approaches.

- **Systems without inversion symmetry** As argued above, breaking inversion can also lead to Weyl semi-metal phases. It was shown by means of *ab initio* calculations that $TlBiSe_2$ can be turned into a Weyl semi-metal by tuning sulphur dopants, which break

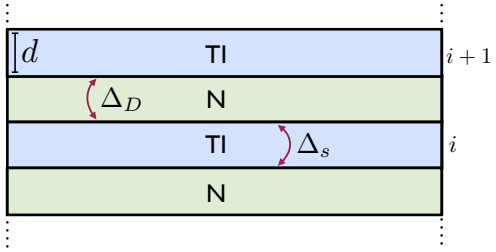

Figure 9.1.: Illustrative picture of a system that realizes the Weyl semi-metal phase at low energies: a periodic array of alternating normal (N) and topological insulators (TI) [333]. The various parameters of the model are shown schematically: Δ_s is the hopping of an electron to a different surface within the same layer, Δ_D controls the hopping of an electron to a different layer, d is the spacing between topological insulator layers and the symbol i labels the layers.

inversion in a layer-by-layer growth, and thus can realize the Weyl semi-metal phase although in this case six Weyl nodes would be realized.

In what follows, we will choose to work with the model proposed by Burkov and Balents in [333] not only because it realizes the minimal number of Weyl nodes but also because it is a model that lies very close to the current experimental state of the art since heterostructures of alternating topological and trivial insulators have been already designed experimentally [346] and it does not require external fluxes or the presence of strong electron-electron interactions. Conclusions which are general to any Weyl semi-metal phase will be emphasized as we proceed through the derivation of the results in the following sections.

9.2. Emergence of Lorentz violating QED in a Weyl semi-metal

In order to understand how the ambiguity affecting radiative correction is resolved in the context of Weyl semi-metals, it is necessary to understand precisely how the action (9.1) is realized from a microscopic model. This section is thus devoted to provide a pedagogical and self contained introduction to a particular model of Weyl semi-metals [333] which will realize the mentioned action with the minimum number of fermionic species.
The model, originally proposed by Burkov and Balents [333], considers the periodic array of alternating topological insulators and ordinary insulators as shown schematically in Fig. 9.1. As discussed earlier in this thesis, topological insulators are 3+1 bulk insulators that posses 2+1 dimensional Dirac fermions at each surface [8, 9] described by the effective low energy Hamiltonian

$$H = \sum_{\mathbf{k}_\perp, i} \left[v_F \tau_z \otimes (\hat{z} \times \boldsymbol{\sigma}) \cdot \mathbf{k}_\perp \right] c^\dagger_{\mathbf{k}_\perp} c_{\mathbf{k}_\perp}, \tag{9.17}$$

where $\boldsymbol{\sigma} = (\sigma_x, \sigma_y)$ represents the spin subspace, v_F is the Fermi velocity and $\mathbf{k}_\perp = (k_x, k_y)$ and $\hat{z}$ is a unitary vector along the growth direction chosen arbitrarily to be in the z direction. The τ subspace selects at which surface the two species of Dirac fermions live. The operators $c^\dagger_{\mathbf{k}_\perp}$ ($c_{\mathbf{k}_\perp}$) create (annihilate) quasiparticles at momenta $\mathbf{k}_\perp$. Note that two species of 2+1 Dirac fermions are realized in concordance to the Nielsen Ninomiya theorem, one at each surface. They can be thought of as the two species or "valleys" of graphene, with the pseudospin being here the real spin.

When the topological insulators are sufficiently thin, the two surfaces can couple through a hopping amplitude Δ_s which enters the Hamiltonian as

$$H_{\Delta_s} = \sum_{\mathbf{k}_\perp, i} \left[\Delta_s \tau_x \otimes 1_\sigma\right] c^\dagger_{\mathbf{k}_\perp} c_{\mathbf{k}_\perp}, \tag{9.18}$$

where 1_σ is the identity matrix in spin subspace. In order to couple different surfaces it is necessary to introduce a label i that indicates to which layer the electron is hopping to. If the hopping amplitude is governed by a parameter Δ_D then the coupling between different layers takes the form

$$H_{\Delta_D} = \sum_{\mathbf{k}_\perp, i, j} \left[\Delta_D \tau^+ \delta_{i,j+1} + \Delta_D \tau^- \delta_{i,j-1}\right] \otimes 1_\sigma c^\dagger_{\mathbf{k}_\perp, i} c_{\mathbf{k}_\perp, j}, \tag{9.19}$$

where $\tau^\pm \equiv \frac{1}{2}\left(\tau_x \pm i\tau_y\right)$. The full Hamiltonian then reads

$$\begin{aligned} H &= \sum_{\mathbf{k}_\perp, i} [v_F \tau_z \otimes (\hat{z} \times \boldsymbol{\sigma}) \cdot \mathbf{k}_\perp \delta_{i,j} + \Delta_s \tau_x \otimes 1_\sigma \delta_{i,j} \\ &+ \Delta_D \left(\tau^+ \delta_{i,j+1} + \Delta_D \tau^- \delta_{i,j-1}\right) \otimes 1_\sigma] c^\dagger_{\mathbf{k}_\perp, i} c_{\mathbf{k}_\perp, j}. \end{aligned} \tag{9.20}$$

Fourier transforming $c^\dagger_{\mathbf{k}_\perp, i} = \sum c^\dagger_{\mathbf{k}_\perp, k_z} e^{i k_z R_i}$, where $R_m = dm$ with m an integer and d being the spacing between the layers, the Hamiltonian is diagonalized in momentum space

$$H = \sum_{\mathbf{k}_\perp, k_z} \left[v_F \tau_z \otimes (\hat{z} \times \boldsymbol{\sigma}) \cdot \mathbf{k}_\perp + \hat{\Delta}(k_z)\right] c^\dagger_{\mathbf{k}_\perp, k_z} c_{\mathbf{k}_\perp, k_z}, \tag{9.21}$$

where $\hat{\Delta}(k_z) \equiv \Delta_s \tau_x \otimes 1_\sigma + \Delta_D \left(\tau^+ e^{i k_z d} + \tau^- e^{-i k_z d}\right) \otimes 1_\sigma$. To make the connection with Weyl fermions consider a low energy theory of such a system. The Hamiltonian (9.21) has two doubly degenerate eigenvalues given by

$$\epsilon^2_{\mathbf{k}} = v_F^2 (k_x^2 + k_y^2) + \Delta_s^2 + \Delta_D^2 + 2\Delta_s \Delta_D \cos(k_z d). \tag{9.22}$$

Expanding near $k_z = \pi/d$ one obtains

$$\epsilon^2_{\mathbf{k}} = v_F^2 (k_x^2 + k_y^2) + (\Delta_s - \Delta_D)^2 + d^2 \Delta_s \Delta_D k_z^2, \tag{9.23}$$

where the third momentum is redefined to be $k_z - \pi/d \to k_z$. This Hamiltonian corresponds to a massive 3+1 Dirac fermion at point $\mathbf{k} = (0, 0, \pi/d)$ of the Brillouin zone

$$\begin{aligned} H &= \sum_{\mathbf{k}_\perp, k_z} [v_F \tau_z (\hat{z} \times \boldsymbol{\sigma}) \cdot \mathbf{k}_\perp + (\Delta_s - \Delta_D) \tau_x \otimes 1_\sigma \\ &+ d\sqrt{\Delta_s \Delta_D} k_z \tau_y \otimes 1_\sigma] c^\dagger_{\mathbf{k}_\perp, k_z} c_{\mathbf{k}_\perp, k_z}, \end{aligned} \tag{9.24}$$

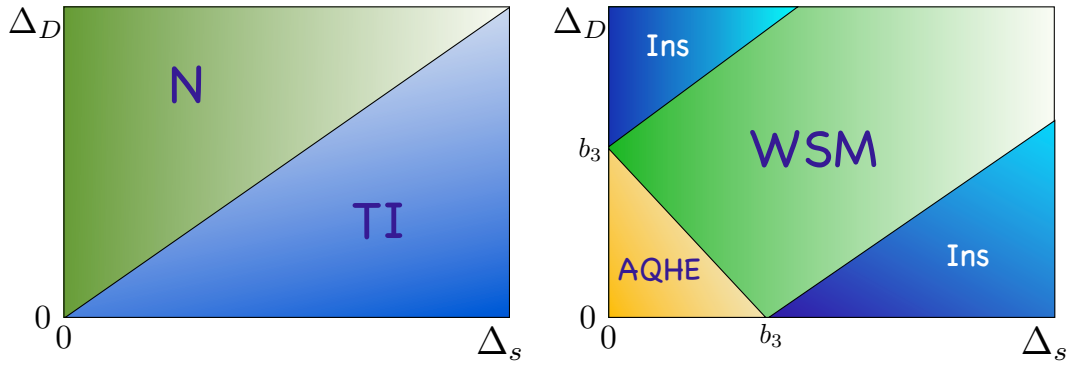

(a) (b)

Figure 9.2.: Phase diagram for the Burkov-Balents model of a Weyl Semi-metal (a) $b_3 = 0$ The critical Weyl line $\Delta_s = \Delta_D$ separates a trivial insulator from a topological insulator (b) $b_3 \neq 0$ For the region where $(\Delta_s - \Delta_D)^2 \leq b_3^2 \leq (\Delta_s + \Delta_D)^2$ there exists a topologically stable Weyl semi-metal phase.

with dispersion relation

$$\epsilon_{\pm}(\mathbf{k}) = \pm\sqrt{v_F^2(k_x^2 + k_y^2) + \tilde{v}_F^2 k_z^2 + m^2}, \tag{9.25}$$

where $\tilde{v}_F^2 = d^2\Delta_s\Delta_D$ and $m^2 = (\Delta_s - \Delta_D)^2$. The Hamiltonian (9.24) can be recast in a more familiar form

$$H = \sum_{\mathbf{k}} \psi_{\mathbf{k}}^{\dagger} \left(\alpha^i k_i + \beta m\right) \psi_{\mathbf{k}}, \tag{9.26}$$

where $i = 1, 2, 3$, $\psi_k = c_{\mathbf{k}_\perp, k_z}$ and the matrices α (following the traditional notation for a Dirac Hamiltonian) are defined as $\alpha_1 = v_F\tau_z \otimes \sigma_y$, $\alpha_2 = -v_F\tau_z \otimes \sigma_x$ and $\alpha_3 = \tilde{v}_F\tau_y \otimes 1_\sigma$ where the Fermi velocities v_F are provisionally included inside the definition. A small deviation from $\Delta_s/\Delta_D = \pm 1$ defines the fourth matrix to be $\beta = \tau_x \otimes 1_\sigma$. Note in particular that at the critical line $\Delta_s/\Delta_D = \pm 1$ the quasiparticles are governed by the Weyl equations, where the four component spinor decouples into a pair of two-component Weyl spinors, giving name to the Weyl semi-metal. Away from this critical line, the system is a gapped insulator defined by the Hamiltonian (9.26) as shown in Fig. 9.2 (a).

With this Hamiltonian in mind, it is possible to write the effective action for the system, which resembles a QED action, but this time for effective quasiparticles inside the material

$$S = \int \frac{d^4k}{(2\pi)^4} \bar{\psi}_k \left(\gamma_\mu M^\mu{}_\nu k^\nu - m\right) \psi_k, \tag{9.27}$$

where it is convenient to introduce the diagonal matrix $M^\mu{}_\nu = diag(1, v_F, v_F, \tilde{v}_F)$ to adequately manage the anisotropic Fermi velocities. The exact relation between γ and α and β

can be obtained with the usual procedure, and it is detailed in appendix F.1. Let us also point out the fact that an analogous Dirac Hamiltonian can be obtained near $\mathbf{k} = 0$ but this time with a mass $m = \Delta_s + \Delta_D$, to which the following sections would also apply with some modifications. Although we will ignore this fact for the moment, we will refer to this possibility to make a comment regarding the results we obtain in further sections.

In view of the action (9.27), and postponing to the end of this section the discussion concerning Lorentz invariance, a natural question arises: is it possible to introduce a term of the form $\bar{\psi}\not{b}\gamma_5\psi$ to reproduce an action that resembles (9.1)? The answer, is indeed affirmative. Doping these materials with magnetic impurities breaks time reversal symmetry and produces a splitting the Weyl nodes in momentum space [333]. In a consistent notation this magnetization introduces a term of the form

$$H_{m_{1c}} = \sum_{\mathbf{k}} m_{1c}\psi^{\dagger}_{\mathbf{k}} 1_{\tau} \otimes \sigma_z \psi_{\mathbf{k}}, \tag{9.28}$$

which in the γ matrix representation is nothing but $\bar{\psi}\gamma^3 b_3\gamma_5\psi$ (see appendix F.1 for details). The presence of this term opens a gap of size m_{1c} at the surface of each topological insulator layer. Physically, this term can be understood as arising from a magnetization determined by the density of magnetic impurities. For sufficiently weak magnetizations, the magnetic field only couples to the surface states as a Zeeman field, which for the massless 2+1 Dirac fermions at the surface is exactly a mass term that opens a gap at the surface, with the magnitude of m_{1c} proportional to the magnetization. Experimentally, it was confirmed in Ref. [88] that for the topological insulator Bi_2Se_3, the magnitude of the gap increases with the impurity density and can be as large as 60meV for a concentration of 0.12 Fe impurities per Bi atom. The phase diagram for the complete theory in this case is somewhat more interesting since their interplay between m and b_3 gives rise to a Weyl semi-metal phase whenever $(\Delta_s - \Delta_D)^2 \leq b_3^2 \leq (\Delta_s + \Delta_D)^2$. This phase neighbours a quantum anomalous Hall insulator and an insulator with broken time reversal symmetry.

Similarly, in [337] it was shown that if an inversion breaking spin orbit coupling term is allowed, it has the form

$$H_{\lambda} = \sum_{\mathbf{k}} \lambda\psi^{\dagger}_{\mathbf{k}}\tau_y \otimes \sigma_z \psi_{\mathbf{k}}. \tag{9.29}$$

In this case, this corresponds exactly to a term of the form $\bar{\psi}\gamma^0 b_0\gamma_5\psi$. Unfortunately, the precise value of $b_0 = \lambda$ in this system is still unknown. However, it can still be expected to be large since all topological insulators have intrinsically a large spin orbit coupling which is a necessary ingredient for their topological nature. Note as well that λ in this model is assumed to be an independent parameter and therefore can be either larger or smaller than m.

With these two terms we finally arrive to the action

$$S = \int \frac{dk^4}{(2\pi)^4}\bar{\psi}\left(\gamma_\mu M^\mu{}_\nu k^\nu - m - \not{b}\gamma_5\right)\psi. \tag{9.30}$$

When coupled to an electromagnetic gauge field, this action is the condensed matter analogue of a Lorentz violating QED with a CPT violating term given by (9.1), and constitutes both the starting point of and the first new result presented in this chapter.
It is evident that this action, arising from a condensed matter system, breaks Lorentz invariance even without the term proportional to b, due to the appearance of the matrix $M^{\mu}{}_{\nu}$ in the action which does not transform as a Lorentz tensor. However, this is, in a way, a trivial violation of the symmetry. As it will be shown below, the consequences of the CPT violating term $\bar{\psi}\not{b}\gamma_5\psi$ are much more profound, and so they will be the focus of the following sections.

9.2.1. Radiatively induced Chern-Simons term

As in ordinary QED, the coupling to the external gauge field is determined through a term of the form $j^{\mu}A_{\mu}$, where j_{μ} is the current operator, defined by the free fermionic action. In this case the current operator is defined in terms of $M^{\mu}{}_{\nu}$ containing the Fermi velocities

$$j^{\mu} = M^{\mu}{}_{\alpha}\bar{\psi}_{\mathbf{k}}\gamma^{\alpha}\psi_{\mathbf{k}}. \tag{9.31}$$

Consider now the quantum expectation value for such a current operator. To one loop, it is defined by the polarization of the photon $\Pi^{\mu\nu}$ and it is given by

$$\begin{aligned}\langle j^{\mu}\rangle &= \left\langle M^{\mu}{}_{\alpha}M^{\nu}{}_{\beta}\bar{\psi}_{\mathbf{k}}\gamma^{\alpha}\psi_{\mathbf{k}}\bar{\psi}_{\mathbf{k}}\gamma^{\beta}\psi_{\mathbf{k}}\right\rangle A_{\nu} \\ &= M^{\mu}{}_{\alpha}M^{\nu}{}_{\beta}\Pi^{\alpha\beta}A_{\nu}.\end{aligned} \tag{9.32}$$

In terms of Feynman diagrams, $\Pi^{\alpha\beta}$ is the analogous to the QED photon bubble with the fermionic propagator $G(k,b)$ given by

$$G(k,b) = \frac{i}{\not{k} - m - \not{b}\gamma_5}. \tag{9.33}$$

The integral determining $\Pi^{\mu\nu}$ is the appropriate generalization of the one loop vacuum polarization diagram

$$\Pi^{\mu\nu} = \frac{e^2}{v_F^2\tilde{v}_F}\int\frac{dk^4}{(2\pi)^4}\mathrm{Tr}\left\{\gamma^{\mu}G(k,b)\gamma^{\nu}G(k+p',b)\right\}. \tag{9.34}$$

As before, the prefactor $\frac{1}{v_F^2\tilde{v}_F}$ stems from a rescaling of the momenta with the corresponding Fermi velocities and $p'^{\mu} = M^{\mu}{}_{\nu}p^{\nu}$ is the rescaled external four-momentum vector. Once established this connection between Lorentz violating QED and Weyl semi-metals it is straightforward to calculate the odd part of (9.34) non perturbatively in b following for instance Ref. [317]

$$\Pi^{\mu\nu}_{\mathrm{odd}} = \frac{e^2}{v_F^2\tilde{v}_F}\epsilon^{\mu\nu\rho\sigma}p'_{\rho}b_{\sigma}\begin{cases} C & \text{if } -b^2 \leq m^2 \\ C - \dfrac{1}{2\pi^2}\sqrt{1-\dfrac{m^2}{b^2}} & \text{if } -b^2 \geq m^2 \end{cases}, \tag{9.35}$$

where C is a finite but undetermined constant [314, 316, 317]. Introducing (9.35) into (9.32) one obtains the response of the Weyl semi-metal to an external electromagnetic field in the presence of both spin orbit coupling, given by b_0 and magnetic impurities governed by b_3

$$j^{\mu}_{\text{odd}} = M^{\mu}{}_{\alpha} M^{\nu}{}_{\beta} \frac{e^2}{v_F^2 \tilde{v}_F} A_{\nu} \epsilon^{\alpha\beta\rho\sigma} p'_{\rho} b_{\sigma} \begin{cases} C & \text{if } -b^2 \leq m^2 \\ C - \dfrac{1}{2\pi^2}\sqrt{1-\dfrac{m^2}{b^2}} & \text{if } -b^2 \geq m^2 \end{cases}, \tag{9.36}$$

This is itself a novel result in the context of Weyl semi-metals being a non perturbative calculation in both the spin orbit coupling and the magnetic impurity strength. However, it is necessary to fix the constant C in order to argue that this is the physical response of the system. This issue is addressed in detail in the next section.

9.2.2. Fixing the ambiguity

As introduced in the first section and argued by many preceding works [314–320, 323, 324] under very different approaches, the constant C is finite and undetermined. It depends strongly on the regularization method used. It is only in the massless case, that this constant is fixed unambiguously [317, 327]. This ambiguity in the context of Weyl semi-metals seems at least paradoxical, since this constant defines physically measurable observables such as the conductivity, which I proceed to discuss.

Consider for example a constant electric field in the y direction. The Hall conductivity, is defined as the off diagonal part of the proportionality tensor between the current and the electric field

$$j^x = \sigma^{xy} E_y, \tag{9.37}$$

and can be measured in transport experiments. If $b = (0, 0, 0, b_3)$ setting $\mu = x$ in (9.36) gives

$$\begin{aligned} j^x_{\text{odd}} &= \frac{e^2}{\tilde{v}_F} E_y b_3 \begin{cases} C & \text{if } b_3^2 \leq m^2 \\ C - \dfrac{1}{2\pi^2}\sqrt{1-\dfrac{m^2}{b_3^2}} & \text{if } b_3^2 \geq m^2 \end{cases} \\ &\equiv \sigma^{xy} E_y, \end{aligned} \tag{9.38}$$

Does this result imply that the Hall conductivity is ambiguous in these materials? The answer turns out to be negative owing to the fact that there is a microscopic model, or in other words, a high energy theory, from which this conductivity can also be calculated. As it will now be shown, a consistent matching of these two theories will imply that $C = 0$.

As a starting point consider the limit of decoupled layers where $\Delta_s \gg \Delta_D$ in the complete theory. In this case, the Hall conductivity is determined by the Hall conductivity of the two massive 2+1 Dirac fermions at each surface of the topological insulator and it is proportional to the sum of the signs of the masses of each fermionic species [65]

$$\sigma^{xy}_{2D} = \frac{e^2}{2h} \sum_i \text{sign}(m_i), \tag{9.39}$$

where the sum i runs over all fermionic species, in this case two. In this limit, the Hamiltonian (9.21) together with the b_3 perturbation is independent of k_z and it is that of two 2+1 massive Dirac fermions with masses $m_{2D} = b_3 \pm \Delta_s$. Whenever $b_3 < \Delta_s$ is satisfied σ^{xy}_{2D} vanishes and so does σ_{xy}. Comparing this result with the corresponding case $b_3^2 < m^2$ in (9.38) one is forced to set

$$C\Big|_{\text{WSM}} = 0. \tag{9.40}$$

This is the central result of this chapter since this constant is precisely the one that enters the odd part of the polarization tensor (9.35) that determines the response of Weyl semi-metals to an external electromagnetic field.

A second argument, perhaps physically more transparent, comes by introducing a finite Δ_D. In this case, there is a set of $2+1$ massive Dirac Hamiltonians with masses that depend parametrically on k_z. Thus, only at certain values of the vector k_z the Hall conductivity vanishes. The 2D Hall conductivity is now a step function [333, 334]

$$\sigma^{xy}_{2D} = \frac{e^2}{h}\Theta(k_0 - |\pi/d - k_z|), \tag{9.41}$$

where k_0 is the separation in k space between the two Dirac fermions given by

$$k_0 = \frac{1}{d}\arccos\left[1 - \frac{b_3^2 - m^2}{2\Delta_s\Delta_D}\right]. \tag{9.42}$$

The integral over the whole Brillouin zone defines de conductivity through

$$\sigma^{xy} = \int_{-\pi/d}^{\pi/d}\frac{dk_z}{2\pi}\sigma^{xy}_{2D}(k_z) = \frac{e^2 k_0}{\pi h}. \tag{9.43}$$

The conductivity is proportional to the separation of the Dirac Fermions in the reciprocal space, a result first proven in [333]. To compare with (9.38) it is necessary to expand (9.42) near $b_3^2 \sim m^2$ which is the case of the low energy theory. This gives a Hall conductivity of

$$\sigma^{xy} = \frac{e^2 k_0}{\pi h} \simeq \frac{e^2}{\pi h}\frac{b_3}{d\sqrt{\Delta_D\Delta_s}}\sqrt{1 - \frac{m^2}{b_3^2}}. \tag{9.44}$$

Restoring $\hbar$ and using that $\tilde{v_F} = d\sqrt{\Delta_D\Delta_s}$ it is straightforward to see that (9.38) reproduces this result only if $C = 0$ in agreement with (9.40). The microscopic theory, which considered the whole Brillouin zone in the k_z direction has fixed the value of the arbitrary but finite constant generated in the low energy theory to be zero. As it turns out, having a *lattice* model from which the low energy theory is derived regularizes the theory to fix the ambiguity.

A final comment is in order. With this analysis it has been proven that a zero Hall conductivity for the lattice model would always imply a zero Hall conductivity calculated within the low energy effective field theory and fixes $C = 0$. However, the inverse statement is not always true. This means that, if one calculates a non zero Hall conductivity in the lattice model, it might be proportional to a lattice vector $\mathbf{G}_j$ [347], a result which the effective low energy field theory approach will never obtain. One can check with a similar analysis to the one described above that this is indeed the case for Hamiltonian (9.21) when $b_3 \gtrsim \Delta_s + \Delta_D$.

9.2.3. Physical consequences

I now turn to discuss measurable physical consequences derived from this theory. As discussed in section 9.1.1, the complete polarizability $\Pi^{\mu\nu}$ modifies Maxwell's equations inside the material and will govern the electrodynamic response of this system. Its even part $\Pi_e^{\mu\nu}$ will define the dielectric function and the magnetic permeability of the material while its odd part will add novel terms which will drastically modify the response of the material to an external perturbation. Integrating out fermions the effective action for the gauge field inside the material is

$$S = \int \frac{d^4k}{(2\pi)^4} A_\mu \Pi_e^{\mu\nu} A_\nu - \frac{1}{2} s_\mu \tilde{F}^{\mu\nu} A_\nu, \tag{9.45}$$

where $s^\mu = \dfrac{e^2}{v_F^2 \tilde{v}_F} \sqrt{1 - \dfrac{m^2}{b^2}}\, b^\mu$ is defined by (9.35) whenever $-b^2 \geq m^2$ and zero otherwise and $\tilde{F}^{\mu\nu} = \epsilon^{\mu\nu\rho\sigma} k'_\rho A_\nu$. This action is known to generate a modified version of Maxwell's equation [304], although in this case it is necessary to keep track of the anisotropic Fermi velocity. For the case where only b_3 is non zero it is possible to write the set of Maxwell equations given by

$$\nabla \cdot \mathbf{D} = 4\pi\rho + v_F^2 \mathbf{s} \cdot \mathbf{B}, \tag{9.46}$$

$$\nabla \cdot \mathbf{B} = 0, \tag{9.47}$$

$$\nabla \times \mathbf{E} = -\frac{1}{c}\frac{\partial \mathbf{B}}{\partial t}, \tag{9.48}$$

$$\nabla \times \mathbf{H} = \frac{4\pi}{c}\mathbf{j} + \frac{1}{c}\frac{\partial \mathbf{D}}{\partial t} - v_F^2 \mathbf{s} \times \mathbf{E}, \tag{9.49}$$

where now $s_\mu = (0, 0, 0, s_3)$ and the v_F^2 coefficient is fixed by (9.38). Note the similarity between these equations and the ones corresponding to axion electrodynamics [86] which could be realized in topological insulators [77]. As in topological insulators, the novel terms in the equations of motions give rise to new physical phenomena.

Consider as an example, light propagation in a Weyl semi-metal system described by (9.46)-(9.49). From the source free ($\rho = 0, \mathbf{j} = 0$) equations it is easy to derive the following wave equation inside the Weyl semi-metal

$$\nabla^2 E - \frac{1}{c_w^2}\frac{\partial^2 E}{\partial t^2} + \nabla\left(\nabla \cdot E\right) = v_F^2 \mathbf{s} \times \frac{\partial E}{\partial t}, \tag{9.50}$$

where $\mu \sim 1$ is assumed being satisfied in a wide range of frequencies [348] and $c_w = 1/\sqrt{\epsilon}$ is the velocity of light inside Weyl semi-metals. Following [304], it is possible to derive the dispersion relation that photons entering the Weyl semi-metal should satisfy

$$\left(\frac{\omega^2}{c_w^2} - k^2\right)^2 - v_F^2(\omega^2 - k^2)s_3^2 = (v_F^2 k_3 s_3)^2, \tag{9.51}$$

which characterize a birefringent media that in this approximation is due entirely to the induced Chern-Simons term. Birefringence of this kind will be generic to all Weyl semi-metals phases that have a term of the form $\bar{\psi}\not{b}\gamma_5\psi$, i.e. whenever the Weyl nodes are separated in momentum space. This result is therefore independent of the particular microscopic model that realizes such a phase, and in particular, on the extrinsic details of the lattice model. An observation of birefringence with light of sufficiently long wavelength would provide an experimental measurement of the constant C. For example, linearly polarized light entering such a medium will leave it in the form of elliptically polarized light.
The action (9.45) can potentially host other interesting physical phenomena. One very appealing possibility is that these materials, in analogy with topological insulators, could posses a repulsive Casimir effect which might be suppressed but still exist in anisotropic materials like the ones described here, as discussed in chapter 7.
Finally, the coupling between magnetic and electric degrees of freedom can enable routes towards exploring exotic phenomena similar to the effective magnetic monopoles possible in axion electrodynamics [87] and chiral gauge fields [338].

9.3. Discussion and Conclusions

In this chapter the emergence of a Lorentz violating QED in the novel class of materials known as Weyl semi-metals was explored in detail. It was found that Weyl semi-metals in the presence of magnetic impurities and spin orbit coupling realize a Lorentz violating version of QED with a term of the form $\bar{\psi}\not{b}\gamma_5\psi$. The electromagnetic response of such a system includes a radiatively induced Chern Simons term in the effective action for the electromagnetic gauge field of the form $\frac{1}{2}k_\mu\tilde{F}^{\mu\nu}A_\nu$ defined by the odd part of the photon self energy $\Pi^{\mu\nu}_{\text{odd}}$. This correction to the photon self energy is finite but undetermined, also in the low energy theory of Weyl semi-metals. However, it has been shown that in this system it is possible to fix the ambiguity due to the existence of a microscopic model from which this result can be derived. The comparison between these two approaches fixes the value for the constant that parametrizes the uncertainty (C) to zero for this system.
Although in this case, the finite value of C turns to be zero, it is in principle possible that other Weyl semi-metals might realize other values. In particular, the most favourable situation would be that where a Weyl semi-metal phase is realized on the border of an anomalous Hall phase so that there is a finite Hall conductivity on both sides of such a transition described by an equation of the form of (9.35). This situation is realized in this model whenever $b_3 \gtrsim \Delta_s + \Delta_D$ although here, the anomalous Hall conductivity is proportional to a lattice vector [333] and will never appear in a low energy description such as the one presented in this work. The analysis presented in this chapter can be applied to other more sophisticated examples of Weyl semi-metal systems [336, 339, 340, 349–351] to determine whether $C = 0$ is

a generic feature in condensed matter systems as suggested by topological arguments [325]. In addition to the finite and unambiguous result determined by (9.35) with $C = 0$, the formulation in terms of a Lorentz violating QED of the low energy theory of Weyl semi-metals enables to perform calculations non perturbatively both in the spin orbit coupling and in the magnetic impurity strength.
Finally, it has been shown that when $-b^2 \geq m$ the coefficient k^μ enters the effective Maxwell equations inside the material, substantially modifying the electrodynamics of the system. In particular the new terms proportional to b_μ will give rise to birefringence when light enters the material. Being a condensed matter system, an observation of such a birefringence is a feasible experiment, in contrast to conventional astrophysical observations which strongly constrain the observability of Lorentz violating QED phenomena. More exotic scenarios derived from the modified Maxwell equations, such as the stationary magnetic order proposed in [304], could be realized in these types of systems, although they will only occur in the situation where $C \neq 0$ which will produce the right form of electromagnetic solutions.

10. Conclusions

"It is important to do everything with enthusiasm, it embellishes life enormously"
-L. D. Landau.

Dirac quasiparticle systems, both interacting and non interacting, together with topological phases of matter have become central to the development of condensed matter physics. Not only they provide the basis of novel fundamental phenomena but they might also provide answers to incipient technological problems. In addition, the strong connection of such systems with other fields of physics is just as remarkable and makes them perhaps even more worth studying. Under this framework, the findings in this thesis provide ways to understand and efficiently describe the physical consequences of introducing the elements of electron-electron interactions and topology in Dirac quasiparticle systems.
To this extent we have studied graphene and topological insulators as examples of systems that realize such elements in various situations, each of which revealed important information about how Dirac quasiparticles behave under different circumstances. Since in each chapter we already included a conclusion section we will here only review the main findings and comment on a personal perception of their importance. We will end with a final digression on the general, overall conclusions of this thesis.

In chapters 2 and 3, we have learned how to construct a consistent theory of interactions between Dirac quasiparticles in graphene as well as understanding how different physical observables can be affected by such corrections. This has been done by providing first a phenomenological model for the self energy of graphene which could account for features observed in early experiments regarding the optical conductivity. Then, a microscopic model that included long range interaction was described, which we used to show explicitly how to construct observables as cut-off independent quantities, a non trivial statement that follows from the renormalizability of the theory.
In an attempt to understand and clarify the interplay of interactions and topology in Dirac quasiparticle systems in chapters 4 and 5 we looked for realizations of integer and fractional topological phases in interacting Dirac quasiparticle systems. To this extent it was shown first that allowing phases with enlarged unit cells helps to stabilize novel topological phases. Within mean field, we found that such phases exist in the honeycomb lattice near the filling

with four electrons per six atom unit cell. These were characterized by the Chern number of the effective bands, a topological invariant related to the Hall conductivity. The phases survived when charge density wave order and next to nearest neighbour interactions were allowed. In chapter 5 we went a step further and showed that it is possible to realize stable fractional Chern insulator phases in fractionally filled bands of Dirac quasiparticle systems. We departed from the traditional Landau level intuition that motivates the study of bands that are as flat as possible to mimic the high degeneracy and with Chern number one. We showed that, contrary to naive expectation, the stability is enhanced by considering higher Chern numbers and deviating from mathematical flatness, since electrons in a band feel a different Berry curvature at each point in $\mathbf{k}$ space. Both findings are important since both the integral and fractional cases are permitted but not guaranteed to arise in Dirac quasiparticle systems out of interaction. The fact that they do appear is truly remarkable and is one central result of this thesis.

We then considered, in chapter 6 an effective action approach to time reversal invariant topological insulators realizable in graphene and its bilayer. This provided a unified view to several extensions to the quantum spin Hall effect of the Kane and Mele model, the valley Hall effect and its bilayer counterparts.

We focused, in chapter 7 on the physical consequences of having three dimensional time reversal invariant topological phases can have. In particular, we provided the prediction that two topological insulators, under the right circumstances might achieve Casimir repulsion in vacuum. This departure for conventional dielectric behaviour, which always attract in vacuum is solely due to the presence of topological terms in the response of these systems to an external electromagnetic field. Repulsion in vacuum could prevent stiction of different components in nano-mechanical systems and only a handful of proposal of this type exist for simple parallel plates since the late 1940's. Therefore such an achievement is also remarkable within the results of this thesis and may provide novel routes to study repulsion, for instance by considering other types of magnetoelectric materials.

Next, in chapter 8, we investigated, motivated by the previous study of the Casimir effect, the way that the θ-term behaved for finite frequency and finite chemical potential, a usual situation in present experimental systems. We found that for finite frequency and chemical potential the theta term is not quantized. This is a novel result that could have been expected from the intuition of the optical Hall conductivity which behaves in an analogous way. The importance of this finding relies on the fact that any optical measurement of the topological magnetoelectric response will be affected by such behaviour, and thus it is important to characterize it.

Finally, in chapter 9 we put forward the idea that systems that realize Weyl semi-metals, i.e. low energy three dimensional massless Dirac quasiparticles, can also be a platform to study models beyond the standard model of particle physics that break Lorentz invariance. Of course, in any condensed matter system Lorentz invariance is always broken. In this

case, what is meant is that the theory has the same mathematical form as its high-energy counterpart, something which is not at all guaranteed to happen. Such high energy theory possesses some ambiguities when calculating observables. Importantly, we showed that their condensed matter analogues are not ambiguous and provide a natural realization to resolve the puzzle, which enabled us to predict the response of these materials to external electromagnetic fields.

This last chapter opens the old question of how much can we learn about fundamental theories of nature by finding analogues in condensed matter. However, I believe that one can learn a perhaps even more valuable lesson. In the case of Weyl semi-metals it was the occurrence of a higher energy theory (the lattice condensed matter realization) which we used to fix the ambiguous response. We therefore could extend such idea to the context of Lorentz violating extensions of the standard model, where one could cure the ambiguities by introducing also a high energy theory. This is knowledge that flows from condensed matter to high-energy theory and not viceversa. Generalizing such an approach, we can then motivate the search for high energy theory analogues (instead of condensed matter analogues) which can complement our imagination to propose novel fundamental physical theories.
As in the modest case of Weyl semi-metals, I am keen and excited to think that realization of theories beyond the standard model of particle physics in condensed matter can serve to gain perspective on the fundamental theories of nature. There is an infinite set of possibilities in this area which might open new fields of research both in high and low energy sectors of physical phenomena, since the emergent realization will most probably introduce novel elements perhaps overlooked in other more traditional approaches.

To conclude, in this thesis we have studied, under a global perspective and leaving aside particular conclusions for each chapter, a unified framework of how from a single equation, the Dirac equation, it is possible to build robust bridges between different areas of physics, from condensed matter systems to the mathematical field of topology and high energy physics of elementary particles.
The fact that different fundamental phenomena can be described with similar language is remarkable, to say the least. The mere emergence of such a connection seems profound to me. Nevertheless, it could also be the manifestation of our own limitations to understand our world. Whichever is the case, it brings us a feel of perspective and such a feeling is, I believe, fundamental in providing new insights to our physical reality. Therefore, and overall, perhaps the most important finding in this thesis is the lesson on perspective and why not, unification. Under such paradigms, different fields feed each other driving faster and robust progress in science. Such an important concept, in my opinion, must always be present in any kind of research.

11. Conclusiones

El estudio de sistemas de cuasipartículas de Dirac, tanto interactuantes como no interactuantes, así como el estudio de fases topológicas de la materia se ha convertido en una piezas fundamental en el campo de la física de la materia condensada. No sólo son la base de nuevos fenómenos fundamentales, sino que también pueden proporcionar respuestas a problemas tecnológicos incipientes. Además, la fuerte conexión de dichos sistemas con otros campos de la física los hace incluso más dignos de estudio. En este contexto, con esta tesis se pretende proporcionar nuevas maneras de entender y describir eficientemente las consecuencias físicas que tienen en estos sistemas la topología y las interacciones electrón-electrón.
En este sentido se han estudiado tanto aislantes topológicos como grafeno, siendo ambos ejemplos de sistemas descritos mediante cuasiparticulas de Dirac, explorando distintas situaciones. En cada una de estas, se extrajo información importante acerca de cómo las cuasipartículas de Dirac se comportan bajo diferentes circunstancias. Dado que en cada capítulo ya se discutieron las conclusiones más importantes, en este capítulo sólo se resumirán los principales hallazgos incluyendo un análisis subjetivo sobre la importancia de estos. Finalmente, se terminará con una digresión final sobre el sentido general de esta tesis.

En los capítulos 2 y 3, se ha estudiado y descrito una teoría de cuasiparticulas de Dirac en grafeno, teniendo en cuenta las interacciones entre dichas cuasipartículas, así como la descripción de cómo diferentes observables físicos pueden verse afectados por dichas correcciones. En primer lugar se presentó un modelo fenomenológico para la autoenergía de los electrones en grafeno con el fin de explicar parcialmente las características observadas en experimentos de conductividad óptica. A continuación, se describió un modelo microscópico que incluye la interacción de largo alcance entre electrones, y que se usó para mostrar explícitamente cómo construir observables independientes del "cut-off", un hecho no trivial que se desprende de la renormalizabilidad de la teoría.
En un intento por entender y aclarar la conexión entre las interacciones electrón-electrón y la topología en los sistemas de cuasipartículas de Dirac, se encontraron en los capítulos 4 y 5 realizaciones de fases topológicas, tanto enteras como fraccionarias, en sistemas interactuantes. En el primero, se demostró que al permitir fases electrónicas con celdas unidad más grandes, es posible estabilizar nuevas fases topológicas. Dentro de la aproximación de campo medio, se encontró que tales fases existen en la red hexagonal cerca del llenado correspondiente a cuatro electrones por celda unidad de seis átomos. Dichas fases se caracterizaron mediante el número de Chern correspondiente a las bandas efectivas, un invariante topológico rela-

cionado con la conductividad Hall. Se demostró que las fases existen incluso si se permiten ondas de densidad de carga siempre y cuando existan interacciones a segundos vecinos finitas. En el capítulo 5 se demostró que es posible estabilizar fases Hall fraccionarias en aislantes topologicos de Chern en bandas de cuasiparticulas de Dirac con llenados fraccionarios. En este contexto, se demostró que, contrariamente a lo esperado desde un razonamiento basado en niveles de Landau, las fases fraccionarias son más estables si se escogen bandas con un número de Chern mayor de uno y no perfectamente planas, ya que los electrones de una banda sienten una curvatura Berry diferente en cada punto del espacio $\vec{k}$. Ambos hallazgos son importantes dado que, a pesar de que las fases topológicas enteras y fraccionarias están permitidas, nada garantiza que surjan en sistemas de cuasipartículas Dirac en interacción. El hecho de que efectivamente emergen es verdaderamente notable y es uno de los resultados centrales de esta tesis.
A continuación, en el capítulo 6, se consideraron, bajo el punto de vista de la acción efectiva, aislantes topológicos invariantes bajo inversión temporal en grafeno y su bicapa. Este estudio proporciona un enfoque unificado de varias extensiones del efecto Hall cuántico de spin en modelos Kane y Mele, el efecto Hall de valle en grafeno y sus realizaciones en la bicapa de grafeno.
En el capítulo 7, el enfoque recayó sobre las consecuencias físicas a las que dan lugar sistemas de aislantes topológicos invariantes bajo inversión temporal en tres dimensiones. En particular, se presentó la predicción de que dos aislantes topológicos, bajo las circunstancias adecuadas, puede lograr repulsión de Casimir en el vacío. Este comportamiento, que contrasta con el de un sistema de materiales dieléctricos convencionales en los que la fuerza de Casimir es siempre atractiva en vacío, se debe únicamente a la presencia de términos topológicos en la respuesta de estos sistemas a un campo electromagnético externo. Es importante destacar que existen pocas propuestas de este tipo para un sistema de placas paralelas desde finales de los años cuarenta. La repulsión en el vacío podría resolver problemas de fricción entre diferentes componentes de sistemas nanomecánicos. Por lo tanto, este hallazgo también se puede destacar como uno de los más importantes de esta tesis dado que puede proporcionar nuevas vías para estudiar la repulsión en sistemas de Casimir, por ejemplo, considerando otros tipos de materiales magnetoeléctricos.
A continuación y motivados por lo anterior, en el capítulo 8, se investigó la forma en que el término topológico conocido como θ-term depende de la frecuencia y del potencial químico. Se encontó que para el caso general dicho término no está cuantizado. Este es un resultado novedoso, consistente con lo que cabría esperar del comportamiento de la conductividad Hall óptica de un fermión de Dirac. La importancia de este hallazgo se basa por tanto en el hecho de que cualquier medición óptica de la respuesta magnetoeléctrica topológica se verá afectada por tal comportamiento, y por lo tantol su caracterización precisa es fundamental.
Por último, en el capítulo 9 se discutió la idea de que los sistemas conocidos como semimetales de Weyl, es decir, sistemas de tres dimensiones de cuasipartículas de Dirac sin masa,

también puede ser una plataforma para estudiar modelos más allá del modelo estándar de la física de partículas que rompen invariancia Lorentz. Por supuesto, en cualquier sistema de materia condensada la invariancia Lorentz siempre esta rota. En este caso nos referimos a que la teoría tiene la misma forma matemática que su análogo de alta energía, algo que no está en absoluto garantizado que ocurra. Tal teoría de alta energía posee algunas ambigüedades en el cálculo de observables. En este capítulo se puso de manifiesto que sus análogos en materia condensada no son ambiguos y proporcionan un sistema natural para resolver dicho rompecabezas. Finalmente esto permitió formular la respuesta de estos materiales a campos electromagnéticos externos, en particular, la manera en la que la luz viaja a través de estos materiales.

Con este último capítulo se abre la vieja pregunta de cuánto se puede aprender acerca de las teorías fundamentales de la naturaleza mediante la búsqueda de análogos en materia condensada. Sin embargo, es posible que se pueda aprender una lección tal vez más valiosa. En el caso de los semimetales de Weyl fue la aparición de una teoría a energía más alta (la teoría en la red) la que permitió fijar la respuesta ambigua. Por tanto, sería en principio posible extrapolar estas ideas al contexto de las extensiones del modelo estándar, donde se podían curar las ambigüedades introduciendo también una teoría de alta energía. Este es un conocimiento que se origina en materia condensada y se aplica entonces a teorías de alta energía, y no viceversa. Generalizando este enfoque, se podría motivar la búsqueda de análogos de alta energía en lugar de análogos en materia condensada, que pueden complementar nuestra imaginación para proponer nuevas teorías físicas fundamentales.
Al igual que en el modesto caso de los semimetales de Weyl, es interesante pensar que la realización de teorías más allá del modelo estándar de la física de partículas en materia condensada puede servir para promover una perspectiva más amplia sobre teorías fundamentales de la naturaleza. Existe un conjunto infinito de posibilidades desde este punto de vista, que podrían abrir nuevos campos de investigación, tanto en los sectores de alta como los de baja energía de la física. La realización emergente de dichas teorías podría introducir elementos novedosos quizás pasados por alto en otros enfoques más tradicionales.

Bajo una perspectiva quizá más global, en esta tesis se ha estudiado un marco unificado de cómo a partir de una sola ecuación, la ecuación de Dirac, es posible construir puentes sólidos entre distintas áreas de la física, desde sistemas de materia condensada, hasta el campo matemático de la topología o la física que gobierna el comportamiento de las partículas elementales. El simple hecho de que fenómenos aparentemente tan diferentes se puedan describir con un lenguaje similar es, cuanto menos, fascinante. La aparición de esta simple conexión parece realmente profunda. Sin embargo, también podría ser la manifestación de nuestras propias limitaciones para comprender nuestro mundo. Sea cual sea el caso, esto nos da una sensación de perspectiva y tal sentimiento es, en mi opinión, fundamental en la

búsqueda de nuevos conocimientos. Por lo tanto, y en general, tal vez el resultado más importante de esta tesis es la lección sobre la necesidad de perspectiva y, por qué no, también de unificación. Gracias a estos dos paradigmas es posible que diferentes campos se beneficien mutuamente, dando lugar a un progreso científico rápido pero sobre todo robusto. Estos importantes conceptos siempre deberían estar, en mi opinión, presentes en cualquier tipo de investigación.

Part IV.

Appendices

A. Kramers-Kronig transformations

The Kramers-Kronig transformations relate the real and imaginary parts of a complex analytic function $f(\omega) = f_1(\omega) + if_2(\omega)$. It is possible to show [352] that these transformations take the form:

$$f_1(\omega) = \frac{1}{\pi}\mathcal{P}\int_{-\infty}^{\infty}\frac{f_2(\omega')}{\omega' - \omega}d\omega' \tag{A.1}$$

$$f_2(\omega) = -\frac{1}{\pi}\mathcal{P}\int_{-\infty}^{\infty}\frac{f_1(\omega')}{\omega' - \omega}d\omega', \tag{A.2}$$

where $\mathcal{P}$ denotes Cauchy principal value. When the function $f_2(\omega)$ is odd, these relations simplify to:

$$f_1(\omega) = \frac{2}{\pi}\mathcal{P}\int_{-\infty}^{\infty}\frac{\omega' f_2(\omega')}{\omega'^2 - \omega^2}d\omega' \tag{A.3}$$

$$f_2(\omega) = -\frac{2}{\pi}\mathcal{P}\int_{-\infty}^{\infty}\frac{\omega f_1(\omega')}{\omega'^2 - \omega^2}d\omega'. \tag{A.4}$$

These relations usually specify the real and imaginary parts up to a cut-off frequency. To illustrate this fact, some examples will be worked through in what follows.

A.0.1. Example 1: 3D Fermi Liquid self-energy

The self-energy is supposed to follow the relations defined by (A.1) and (A.2). In the case of a three-dimensional Fermi Liquid, the energy dependent self-energy takes the form:

$$\mathrm{Im}\Sigma(\omega) = a\omega^2, \tag{A.5}$$

where a is some constant with inverse energy units. The method to apply the Kramers-Kronig transformation is to define a cut-off frequency ω_c and a small parameter δ, that will be set to zero at de end, in order to calculate the integral's principal value. Introducing both of these, the integral (A.1) is:

$$\mathrm{Re}\Sigma(\omega) = \frac{a}{\pi}\lim_{\delta\to 0}\left[\int_{-\omega_c}^{\omega-\delta}\frac{\omega'^2}{\omega' - \omega}d\omega' + \int_{\omega+\delta}^{\omega_c}\frac{\omega'^2}{\omega' - \omega}d\omega'\right].$$

The integrals are easily worked out to give:

$$\mathrm{Re}\Sigma(\omega) = \frac{2a\omega\omega_c}{\pi}\left[1 + \frac{\omega}{2\omega_c}\ln\left(\frac{\omega - \omega_c}{\omega + \omega_c}\right)\right].$$

The last logarithm vanishes in the limit $\omega \ll \omega_C$ leaving a linear energy dependence. It is evident here that there is a severe cut-off dependence but, since the behaviour of the self-energy (A.5) is only valid at small ω we can consider the linear dependence correct in this limit.

A.0.2. Example 2: Marginal Fermi Liquid self-energy

The Marginal Fermi Liquid was born as a hypothesis [99] where a polarizability function was given and a self-energy was deduced from it. The imaginary part of this self energy is given by:

$$\mathrm{Im}\Sigma(\omega) = a|\omega|. \tag{A.6}$$

Applying the Kramers-Kronig transformation in the same way as in the previous example gives a cut-off dependent real part of the form:

$$\mathrm{Re}\Sigma(\omega) = \frac{2a}{\pi}\omega \ln\left(\frac{\omega_c}{\omega}\right). \tag{A.7}$$

It is worth to notice that since (A.6) is not an analytic function, the Kramers-Kronig transformations are not valid. However, relaxing the condition of analyticity of the function has given good results and so, these transformations are commonly applied to non-analytic functions.
Another example of this is the phenomenological self-energy that centred this work, which was defined as:

$$\mathrm{Im}\Sigma(\omega) = \begin{cases} a|\omega| + b & ,|\omega| < \Lambda \\ a\Lambda + b & ,|\omega| > \Lambda \end{cases}. \tag{A.8}$$

In this case, the real part turns to be:

$$\mathrm{Re}\Sigma(\omega) = \frac{a}{\pi}\left[\Lambda \ln\left(\frac{\Lambda+\omega}{\Lambda-\omega}\right) + \omega \ln\left(\frac{\omega^2-\Lambda^2}{\omega^2}\right)\right] \tag{A.9}$$

which was used inside the spectral function (2.9) to obtain the results of Chapter 1.

B. Variational mean field: Derivation of the mean field equations and order of the phase transitions

B.1. Derivation of the mean field equations

B.1.1. Unfolded case

In this appendix we will give details of the derivation of the mean field equations for the unfolded case. As in the main text, the free energy of the system $\mathcal{F} \leq \mathcal{F}_{MF} + \langle H - H_{MF} \rangle_{MF} \equiv F$, where $\mathcal{F}_{MF} = \Omega_{MF} + \mu \langle \mathcal{N} \rangle_{MF}$ and μ is fixed by imposing $\langle \mathcal{N} \rangle_{MF} = N_e$ with N_e being the number of fermions i.e. Luttinger's theorem [164]. The best approximation to the actual free energy of the system with a particular mean field ansatz $\mathcal{H}_{MF}$ is obtained by minimizing the functional F with respect to some order parameters $\{\xi_i\}$ such that $\mathcal{F} = \min_{\{\xi_i\}} F[\xi_i]$, which is performed by imposing a variation on the parameters $\{\xi_i\} + \{\delta\xi_i\}$ such that $\delta F = 0$. In our case $\mathcal{H}_{MF}$ is by construction (4.7)

$$\mathcal{H}_{MF} = \mathcal{H}_{TB} + V \sum_{\mathbf{k}} \psi^\dagger_{\mathbf{k}} \boldsymbol{\sigma} \cdot \boldsymbol{\Delta}_{\mathbf{k}} \psi_{\mathbf{k}} \tag{B.1}$$

with $\mathcal{H}_{TB}$ given by (4.4). As described above the mean field equations are derived from the condition $\delta F = 0$. The functional F itself consists of two parts $\mathcal{F}_{MF}$ and $\langle H - H_{MF} \rangle_{MF}$.
Consider first the second part. We will be interested in the expectation value of the interaction term in (4.6). Using Wick's theorem:

$$\begin{aligned}
\left\langle a^\dagger_{\mathbf{k}} a_{\mathbf{k}-\mathbf{q}} b^\dagger_{\mathbf{k}'} b_{\mathbf{k}'+\mathbf{q}} \right\rangle_{MF} &= \left\langle a^\dagger_{\mathbf{k}} a_{\mathbf{k}-\mathbf{q}} \right\rangle_{MF} \left\langle b^\dagger_{\mathbf{k}'} b_{\mathbf{k}'+\mathbf{q}} \right\rangle_{MF} - \left\langle a^\dagger_{\mathbf{k}} b_{\mathbf{k}'+\mathbf{q}} \right\rangle_{MF} \left\langle b^\dagger_{\mathbf{k}'} a_{\mathbf{k}-\mathbf{q}} \right\rangle_{MF} \\
&+ \left\langle a^\dagger_{\mathbf{k}} b^\dagger_{\mathbf{k}'} \right\rangle_{MF} \left\langle a_{\mathbf{k}-\mathbf{q}} b_{\mathbf{k}'+\mathbf{q}} \right\rangle_{MF} \qquad \text{(B.2)} \\
\left\langle a^\dagger_{\mathbf{k}} a_{\mathbf{k}-\mathbf{q}} a^\dagger_{\mathbf{k}'} a_{\mathbf{k}'+\mathbf{q}} \right\rangle_{MF} &= \left\langle a^\dagger_{\mathbf{k}} a_{\mathbf{k}-\mathbf{q}} \right\rangle_{MF} \left\langle a^\dagger_{\mathbf{k}'} a_{\mathbf{k}'+\mathbf{q}} \right\rangle_{MF} - \left\langle a^\dagger_{\mathbf{k}} a_{\mathbf{k}'+\mathbf{q}} \right\rangle_{MF} \left\langle a^\dagger_{\mathbf{k}'} a_{\mathbf{k}-\mathbf{q}} \right\rangle_{MF} \qquad \text{(B.3)} \\
&+ \left\langle a^\dagger_{\mathbf{k}} a^\dagger_{\mathbf{k}'} \right\rangle_{MF} \left\langle a_{\mathbf{k}-\mathbf{q}} a_{\mathbf{k}'+\mathbf{q}} \right\rangle_{MF} \\
\left\langle b^\dagger_{\mathbf{k}} b_{\mathbf{k}-\mathbf{q}} b^\dagger_{\mathbf{k}'} b_{\mathbf{k}'+\mathbf{q}} \right\rangle_{MF} &= \left\langle b^\dagger_{\mathbf{k}} b_{\mathbf{k}-\mathbf{q}} \right\rangle_{MF} \left\langle b^\dagger_{\mathbf{k}'} b_{\mathbf{k}'+\mathbf{q}} \right\rangle_{MF} - \left\langle b^\dagger_{\mathbf{k}} b_{\mathbf{k}'+\mathbf{q}} \right\rangle_{MF} \left\langle b^\dagger_{\mathbf{k}'} b_{\mathbf{k}-\mathbf{q}} \right\rangle_{MF} \qquad \text{(B.4)} \\
&+ \left\langle b^\dagger_{\mathbf{k}} b^\dagger_{\mathbf{k}'} \right\rangle_{MF} \left\langle b_{\mathbf{k}-\mathbf{q}} b_{\mathbf{k}'+\mathbf{q}} \right\rangle_{MF}
\end{aligned}$$

Each one generates a Hartree term, a Fock or exchange term and a superconducting term. The mean field ansatz (B.1) is diagonal in $\mathbf{k}$ and therefore, since the above expectation val-

ues are calculated with the mean field Hamiltonian, all those that don't preserve $\mathbf{k}$ will be identically zero. The Hartree channel has $\mathbf{k} = \mathbf{k} + \mathbf{q} \rightarrow \mathbf{q} = 0, \gamma_{\mathbf{q}=0}$, the bond or hopping like ordering has $\mathbf{k} = \mathbf{k}' + \mathbf{q} \rightarrow \mathbf{q} = \mathbf{k} - \mathbf{k}', \gamma_{\mathbf{k}-\mathbf{k}'}$ and the superconducting order is $\mathbf{k} = -\mathbf{k}'$ to relabel $\mathbf{k} - \mathbf{q} \equiv -\mathbf{k}', \gamma_{\mathbf{k}+\mathbf{k}'}$. However, since we have not included superconducting order or charge density wave decoupling in the ansatz (B.1) the only expectation values which are finite with this choice are of the form $\left\langle b^\dagger_{\mathbf{k}} a_{\mathbf{k}} \right\rangle_{MF}$.

$$\langle H_{int} \rangle_{MF} = -\frac{V}{N} \sum_{\mathbf{k},\mathbf{k}'} \gamma_{\mathbf{k}-\mathbf{k}'} \left\langle a^\dagger_{\mathbf{k}} b_{\mathbf{k}} \right\rangle_{MF} \left\langle b^\dagger_{\mathbf{k}'} a_{\mathbf{k}'} \right\rangle_{MF}$$

To calculate $\delta F = 0$ we need $\langle H - H_{MF} \rangle_{MF}$ which turns to be:

$$\langle H - H_{MF} \rangle_{MF} = \langle H_{int} \rangle_{MF} - \sum_{\mathbf{k}} (\xi_{20} + f_2(\mathbf{k})) \left\langle a^\dagger_{\mathbf{k}} b_{\mathbf{k}} \right\rangle_{MF} + h.c.$$

Introducing the variation $\{\xi_i\} + \{\delta\xi_i\}$ one obtains:

$$\delta \langle H - H_{MF} \rangle_{MF} = \delta \langle H_{int} \rangle_{MF} - \sum_{\mathbf{k}} \{ (\delta\xi) \left\langle c^\dagger_{\mathbf{k}} c_{\mathbf{k}} \right\rangle_{MF} + \xi\delta \left\langle c^\dagger_{\mathbf{k}} c_{\mathbf{k}} \right\rangle_{MF} + h.c. \} \tag{B.5}$$

where we are using a shorthand notation inside the sum.
Now that we have the second part of $\delta F = 0$ consider the first part $\delta \mathcal{F}_{MF}$. I will now show that:

$$\delta\Omega_{MF} = \langle \delta H_{MF} \rangle_{MF} = (\delta\xi) \sum_{\mathbf{k}} \left\langle c^\dagger_{\mathbf{k}} c_{\mathbf{k}} \right\rangle_{MF}. \tag{B.6}$$

The proof goes as follows. Introducing $H + \delta H$ we have:

$$\begin{aligned}
\mathrm{Tr} e^{-\beta(H+\delta H)} &= \mathrm{Tr} \sum_n \frac{(-\beta)^n}{n!} (H + \delta H)^n \\
&= 1 + \mathrm{Tr} \sum_{n=1} \frac{(-\beta)^n}{n!} (H)^n \\
&+ \mathrm{Tr} \sum_{n=1} \frac{(-\beta)^n}{(n-1)!} (\delta H H^{n-1} + H \delta H H^{n-2} + \cdots + H^{n-1} \delta H) + \mathcal{O}(\delta H^2) \\
&= \mathrm{Tr} e^{-\beta H} + \mathrm{Tr}[\delta H \sum_{n=1} \frac{(-\beta)^n}{(n-1)!} H^{n-1}] + \mathcal{O}(\delta H^2) \\
&= \mathrm{Tr} e^{-\beta H} - \beta \delta H \mathrm{Tr}[e^{-\beta H}] + \mathcal{O}(\delta H^2),
\end{aligned}$$

So that:

$$\delta \mathrm{Tr} e^{-\beta H} = -\beta \delta H \mathrm{Tr}[e^{-\beta H}]. \tag{B.7}$$

Now we can calculate:

$$\begin{aligned}
\delta\Omega_{MF} &= -k_B T \delta \ln \mathrm{Tr} e^{-\beta H_{MF} - \mu N} \\
&= -k_B T \frac{\delta \mathrm{Tr} e^{-\beta H_{MF} - \mu N}}{\mathrm{Tr} e^{-\beta H_{MF} - \mu N}} \\
&= \langle \delta H_{MF} \rangle_{MF}
\end{aligned} \tag{B.8}$$

where in the last step (B.7) was used to arrive to the final result. Putting together (B.6) and (B.5) and assuming that μ is independent of the mean field parameters together with the condition $\delta F = 0$, we arrive to the mean field equation written in (4.9)

$$\Delta_{\mathbf{k}} = -\frac{2}{N}\sum_{\mathbf{k}'}\gamma_{\mathbf{k}-\mathbf{k}'}\left\langle b^{\dagger}_{\mathbf{k}'}a_{\mathbf{k}'}\right\rangle_{MF}. \tag{B.9}$$

B.1.2. Folded case

The derivation in this case is analogous to the unfolded case except for the fact that the mean field $\mathcal{H}_{MF}$ is now a 6×6 matrix, thus introducing more parameters in the derivation. The derivation goes exactly as shown above except this time the mean field ansatz $\mathcal{H}_{MF}$ is explicitly given by:

$$\mathcal{H}_{MF} = \mathcal{H}^{(6)}_{TB} + V\sum_{\mathbf{k}}\psi^{\dagger}_{\mathbf{k}}\begin{pmatrix} 0 & \xi_1 & 0 & e^{i\mathbf{a}_2\cdot\mathbf{k}}\xi_1' & 0 & \xi_1'' \\ \xi_1^* & 0 & \xi_2'^* & 0 & e^{-i\mathbf{a}_1\cdot\mathbf{k}}\xi_3'^* & 0 \\ 0 & \xi_2' & 0 & \xi_2 & 0 & e^{-i(\mathbf{a}_1+\mathbf{a}_2)\cdot\mathbf{k}}\xi_2'' \\ e^{-i\mathbf{a}_2\cdot\mathbf{k}}\xi_1'^* & 0 & \xi_2^* & 0 & \xi_3''^* & 0 \\ 0 & e^{i\mathbf{a}_1\cdot\mathbf{k}}\xi_3' & 0 & \xi_3'' & 0 & \xi_3 \\ \xi_1'' & 0 & e^{i(\mathbf{a}_1+\mathbf{a}_2)\cdot\mathbf{k}}\xi_2''^* & 0 & \xi_3^* & 0 \end{pmatrix}\psi_{\mathbf{k}} \tag{B.10}$$

where $\mathcal{H}^{(6)}_{TB}$ is the free graphene Hamiltonian for a six atom unit cell:

$$\mathcal{H}^{(6)}_{TB} = -t\sum_{\mathbf{k}}\psi^{\dagger}_{\mathbf{k}}\begin{pmatrix} 0 & 1 & 0 & e^{i\mathbf{a}_2\cdot\mathbf{k}} & 0 & 1 \\ 1 & 0 & 1 & 0 & e^{-i\mathbf{a}_1\cdot\mathbf{k}} & 0 \\ 0 & 1 & 0 & 1 & 0 & e^{-i(\mathbf{a}_1+\mathbf{a}_2)\cdot\mathbf{k}} \\ e^{-i\mathbf{a}_2\cdot\mathbf{k}} & 0 & 1 & 0 & 1 & 0 \\ 0 & e^{i\mathbf{a}_1\cdot\mathbf{k}} & 0 & 1 & 0 & 1 \\ 1 & 0 & e^{i(\mathbf{a}_1+\mathbf{a}_2)\cdot\mathbf{k}} & 0 & 1 & 0 \end{pmatrix}\psi_{\mathbf{k}} \tag{B.11}$$

Following the procedure described above it is straightforward to arrive to equation (4.17) where ξ_{ij} is defined as:

$$\xi_{ij} = \begin{bmatrix} \xi_1 & \xi_1' & \xi_1'' \\ \xi_2' & \xi_2 & \xi_2'' \\ \xi_3' & \xi_3'' & \xi_3 \end{bmatrix} \tag{B.12}$$

Note that these order parameters are to be interpreted as corrections to the nine independent hoppings of the six-atom unit cell.

B.1.3. Folded case with V' and charge density wave order

The procedure to derive the mean field equations in this case is analogous to the above although one now has $\mathcal{H}_{int}$ with a second nearest neighbour term. Other than that detail the

derivation proceeds identically with the ansatz Hamiltonian.

$$\mathcal{H}_{MF} = \mathcal{H}_{TB}^{(6)} + \sum_{\mathbf{k}} \psi_{\mathbf{k}}^{\dagger} \begin{pmatrix} \rho_1^A & \xi_1 & \chi_{12}^A(\mathbf{k}) & e^{i\mathbf{a_2}\cdot\mathbf{k}}\xi_1' & (\chi_{31}^A(\mathbf{k}))^* & \xi_1'' \\ \xi_1^* & \rho_1^B & \xi_2'^* & \chi_{12}^B(\mathbf{k}) & e^{-i\mathbf{a_1}\cdot\mathbf{k}}\xi_3'^* & (\chi_{31}^B(\mathbf{k}))^* \\ (\chi_{12}^A(\mathbf{k}))^* & \xi_2' & \rho_2^A & \xi_2 & \chi_{23}^A(\mathbf{k}) & e^{-i(\mathbf{a_1}+\mathbf{a_2})\cdot\mathbf{k}}\xi_2'' \\ e^{-i\mathbf{a_2}\cdot\mathbf{k}}\xi_1'^* & (\chi_{12}^B(\mathbf{k}))^* & \xi_2^* & \rho_2^B & \xi_3''^* & \chi_{23}^B(\mathbf{k}) \\ \chi_{31}^A(\mathbf{k}) & e^{i\mathbf{a_1}\cdot\mathbf{k}}\xi_3' & (\chi_{23}^A(\mathbf{k}))^* & \xi_3'' & \rho_3^A & \xi_3 \\ \xi_1''^* & (\chi_{31}^B(\mathbf{k}))^* & e^{i(\mathbf{a_1}+\mathbf{a_2})\cdot\mathbf{k}}\xi_2''^* & (\chi_{23}^B(\mathbf{k}))^* & \xi_3^* & \rho_3^B \end{pmatrix} \psi_{\mathbf{k}} \tag{B.13}$$

where $\mathcal{H}_{TB}^{(6)}$ is the free graphene Hamiltonian for a six atom unit cell defined in the previous section and

$$\chi_{12}^A(\mathbf{k}) = \chi_{12}^{A,u} + e^{i(\mathbf{a_1}+\mathbf{a_2})\cdot\mathbf{k}}\chi_{12}^{A,d} + e^{i\mathbf{a_2}\cdot\mathbf{k}}\chi_{12}^{A,h} \tag{B.14}$$

$$\chi_{23}^A(\mathbf{k}) = e^{-i(\mathbf{a_1}+\mathbf{a_2})\cdot\mathbf{k}}\chi_{23}^{A,u} + \chi_{23}^{A,d} + e^{-i\mathbf{a_1}\cdot\mathbf{k}}\chi_{23}^{A,h} \tag{B.15}$$

$$\chi_{31}^A(\mathbf{k}) = e^{-i\mathbf{a_2}\cdot\mathbf{k}}\chi_{31}^{A,u} + e^{i\mathbf{a_1}\cdot\mathbf{k}}\chi_{31}^{A,d} + \chi_{31}^{A,h} \tag{B.16}$$

$$\chi_{12}^B(\mathbf{k}) = \chi_{12}^{B,h} + e^{i\mathbf{a_2}\cdot\mathbf{k}}\chi_{12}^{B,d} + e^{-i\mathbf{a_1}\cdot\mathbf{k}}\chi_{12}^{B,u} \tag{B.17}$$

$$\chi_{23}^B(\mathbf{k}) = e^{-i\mathbf{a_2}\cdot\mathbf{k}}\chi_{23}^{B,h} + \chi_{23}^{B,d} + e^{-i(\mathbf{a_1}+\mathbf{a_2})\cdot\mathbf{k}}\chi_{23}^{B,u} \tag{B.18}$$

$$\chi_{31}^B(\mathbf{k}) = e^{i\mathbf{a_1}\cdot\mathbf{k}}\chi_{31}^{B,h} + e^{i(\mathbf{a_1}+\mathbf{a_2})\cdot\mathbf{k}}\chi_{31}^{B,d} + \chi_{31}^{B,u} \tag{B.19}$$

After a tedious calculation one arrives to the set of mean field equations (4.25). The phase factors that define these equations are:

$$\gamma_{\mathbf{k}} = \begin{bmatrix} 1 & e^{-i\mathbf{a_2}\cdot\mathbf{k}} & 1 \\ 1 & 1 & e^{i(\mathbf{a_1}+\mathbf{a_2})\cdot\mathbf{k}} \\ e^{-i\mathbf{a_1}\cdot\mathbf{k}} & 1 & 1 \end{bmatrix},$$

together with

$$\begin{array}{ccc} \Gamma_{12,\mathbf{k}}^{A,u} = 1 & \Gamma_{12,\mathbf{k}}^{A,d} = e^{-i(\mathbf{a_1}+\mathbf{a_2})\cdot\mathbf{k}} & \Gamma_{12,\mathbf{k}}^{A,h} = e^{-i\mathbf{a_2}\cdot\mathbf{k}} \\ \Gamma_{23,\mathbf{k}}^{A,u} = e^{i(\mathbf{a_1}+\mathbf{a_2})\cdot\mathbf{k}} & \Gamma_{23,\mathbf{k}}^{A,d} = 1 & \Gamma_{23,\mathbf{k}}^{A,h} = e^{i\mathbf{a_1}\cdot\mathbf{k}} \\ \Gamma_{31,\mathbf{k}}^{A,u} = e^{i\mathbf{a_2}\cdot\mathbf{k}} & \Gamma_{31,\mathbf{k}}^{A,d} = e^{-i\mathbf{a_1}\cdot\mathbf{k}} & \Gamma_{31,\mathbf{k}}^{A,h} = 1 \end{array} \tag{B.20}$$

for the next to nearest neighbours in the A sublattice and

$$\begin{array}{ccc} \Gamma_{12,\mathbf{k}}^{B,h} = 1 & \Gamma_{12,\mathbf{k}}^{B,d} = e^{-i\mathbf{a_2}\cdot\mathbf{k}} & \Gamma_{12,\mathbf{k}}^{B,u} = e^{-i\mathbf{a_1}\cdot\mathbf{k}} \\ \Gamma_{23,\mathbf{k}}^{B,h} = e^{i\mathbf{a_2}\cdot\mathbf{k}} & \Gamma_{23,\mathbf{k}}^{B,d} = 1 & \Gamma_{23,\mathbf{k}}^{B,u} = e^{i(\mathbf{a_1}+\mathbf{a_2})\cdot\mathbf{k}} \\ \Gamma_{31,\mathbf{k}}^{B,h} = e^{-i\mathbf{a_1}\cdot\mathbf{k}} & \Gamma_{31,\mathbf{k}}^{B,d} = e^{-i(\mathbf{a_1}+\mathbf{a_2})\cdot\mathbf{k}} & \Gamma_{31,\mathbf{k}}^{B,u} = 1 \end{array} \tag{B.21}$$

for the next to nearest neighbours in the B sublattice.

B.2. Order of the phase transitions

To distinguish between different classes of phase transitions we study the way the free energy behaves as the electron density changes. A crossing between two phases will be an indication

of a first order phase transition, while a continuous evolution of one phase into the other will be reminiscent of second order phase transition. As will be shown below for the studied phase transitions, only the first type is found.
For these, we employ here a common method in statistical physics known as Maxwell's construction which gives a prescription to describe physically the first order phase transitions as a coexistence state where the system breaks into domains each hosting one of the two phases relevant to the transition.

B.2.1. Maxwell's construction

Maxwell's construction is a geometrical tool to study first order phase transitions [41, 171, 172] based on constraints regarding the stability of the different phases that manifest themselves through jumps or crossings in the different thermodynamical potentials.
A prototypical example is the first order Liquid-Vapour phase transition. The pressure (P) - volume diagram (V), which in our case will translate into a chemical potential μ versus density n diagram, has a region of instability which the system avoids by separating into two coexisting phases. The concept of thermodynamic stability can be elaborated from basic thermodynamic principles [171]. In particular recall that the entropy of a system is always maximal, thus $d^2S < 0$. The entropy is thus a concave function as a function of internal energy or volume, or any extensive variable, in particular particle number N. Analogously, the internal energy should be a minimum and thus convex with these variables. This defines stability. Any region where this is not fulfilled is declared unstable and signals a phase transition. Mathematically, the internal energy satisfies:

$$\frac{\partial^2 E}{\partial N^2} \equiv \frac{\partial \mu}{\partial N} \geq 0 \tag{B.22}$$

This extends to the free energy defined as $F = E - TS$, provided that we are considering an extensive variable such as N (note in particular that F is a concave function of the intensive variable T). In turn, any of the Legendre transforms that one can think of involving F are concave with respect to the corresponding intensive variable which defines the transformation. This applies in particular the grand potential $\Omega = F - \mu N$ with respect to μ.
Following the above statements, an instability region for a particular phase changing into another can look as in the upper sketch in Fig. B.1 where the free energy per particle in the unstable region is concave, instead of convex (curve labelled I). This is can be translated into a $\mu(n)$ diagram, being n the electron density, where the central region indicates instability, according to (B.22) (strictly speaking the central region also contains a metastable region where $\frac{\partial \mu}{\partial N} \geq 0$ is satisfied). Note also that the always $f \equiv F/N$ against n is plotted which is equivalent to F versus N, which is in a strict sense what it should be studied, since n is an intensive variable. Maxwell's construction is a way to constrain this instability between densities n_1 and n_2. The method goes as follows.

Consider an inhomogeneous sample with two phases coexisting together with densities $n_1 = N_1/V_1$ and $n_2 = N_2/V_2$. The sample has fixed number of particles $N = N_1 + N_2$ and volume $V = V_1 + V_2$. The free energy of this state is in general a linear combination of the two free energies:

$$F(N,V,T) = V_1 f(T, \frac{N_1}{V_1}) + V_2 f(T, \frac{N_2}{V_2}) \tag{B.23}$$

Minimizing the free energy with respect to N_1 and V_1 one obtains two conditions for phase equilibrium:

$$\mu(T,n_1) = \mu(T,n_2) \equiv \mu_0 \tag{B.24}$$

$$f(T,n_2) - f(T,n_1) = n_2\mu(T,n_2) - n_1\mu(T,n_1) \tag{B.25}$$

The first condition is simply stating the fact that for phase equilibrium we need equal chemical potential [41]. The second condition is easily interpreted if we restate it in the following way:

$$\frac{f(T,n_2) - f(T,n_1)}{n_2 - n_1} = \mu_0 \tag{B.26}$$

where (B.24) has been used. In this form, the equation implies that the two phases lie on the same line in an f versus n plot with its slope being the chemical potential μ_0. This is precisely the curve labelled II in the upper diagram in Fig B.1. We see that, at the phase transition, a phase separation is energetically more favourable than path represented by curve I.
Now we calculate n_1 and n_2. Recalling that $f = \int \mu dn$ (which follows from $d\Omega = 0 = dF - \mu dN$) and using (B.26) it easy to see that:

$$f(T,n_2) - f(T,n_1) = \int_{n_1}^{n_2} \mu(n) dn = \mu_0(n_2 - n_1) \tag{B.27}$$

which implies immediately that the areas A and B in Fig B.1 have to be equal. This defines $n_{1,2}$ unambiguously and completes Maxwell's construction.
A final technical remark is in order. To find μ_0, one should compute the slope of curve II in Fig B.1, but this is not numerically efficient. Thus, in practice, it is better to look at Ω against μ, which is, as mentioned above concave. Numerically, the two phases will not describe a smooth curve but rather a crossing and the crossing point defines μ_0.
In the following sections the technique summarized here will be applied for three representative points in diagram Fig. 4.4 that generate, among similar constructions at different interactions V the coexistence region of Fig. 4.8.

B.2.2. $V = 3$: Pomeranchuk to T-I transition

Consider a line of points with $V = 3$ in the phase diagram in Fig. 4.4 close to the P to T-I transition. It is possible to trace the evolution of the free energy for the Pomeranchuk and

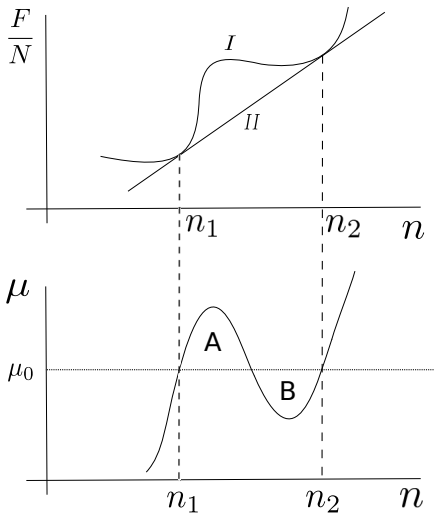

Figure B.1.: Maxwell's construction for a first order phase transition. The upper digram shows the free energy for a typical first order phase transition (I) and the coexistence free energy (II). The lower diagram shows a Maxwell's construction to identify the phase separation parameters, in this case n_1 and n_2 and μ_0.

the T-II phases as the electron density n is increased. This is shown in Fig. B.2(a). Although hardly visible, when starting from the lowest densities the Pomeranchuk phase (black) has the lowest energy until at $n \sim 3.97$ the T-I overtakes and turns to be the phase with lowest energy. This is an indication of a first order phase transition.

To treat this phase transition we will make use of the Maxwell's construction discussed above. The first thing to notice is that the crossing in Fig. B.2(a) is thermodynamically unstable. Following Maxwell's construction we consider a state which consists in a mixture of the two phases in equilibrium (i.e. same chemical potential μ) but with different densities n_P and n_{T-I}. In Fig. B.2(a) this corresponds to tracing a straight line between points with the same chemical potential. This line is a linear combination of the free energies of the two phases with the same chemical potential and hence it is the free energy of the an inhomogeneous coexistence phase. If one plotted this line in Fig. B.2(a), it will fall just below the crossing. However, the scale of the plot itself makes it difficult to draw such a line. Equivalently we will focus on the grand potential (discussed below) versus μ and the curve $\mu(n)$ where the coexistence region is explicitly seen. Nevertheless, the mixed phase has less free energy in that region than either of the individual phases and so it is more stable in the region between n_P and n_{T-I}.

To find the chemical potential at which these phases coexist, μ_0, we study the behaviour of the grand potential Ω against the renormalized chemical potential μ_r, which avoids calculating the derivative of the free energy numerically. The point at which both phases have the same chemical potential will define μ_0. This is shown in Fig. B.2 (b) with a vertical blue-dashed line.

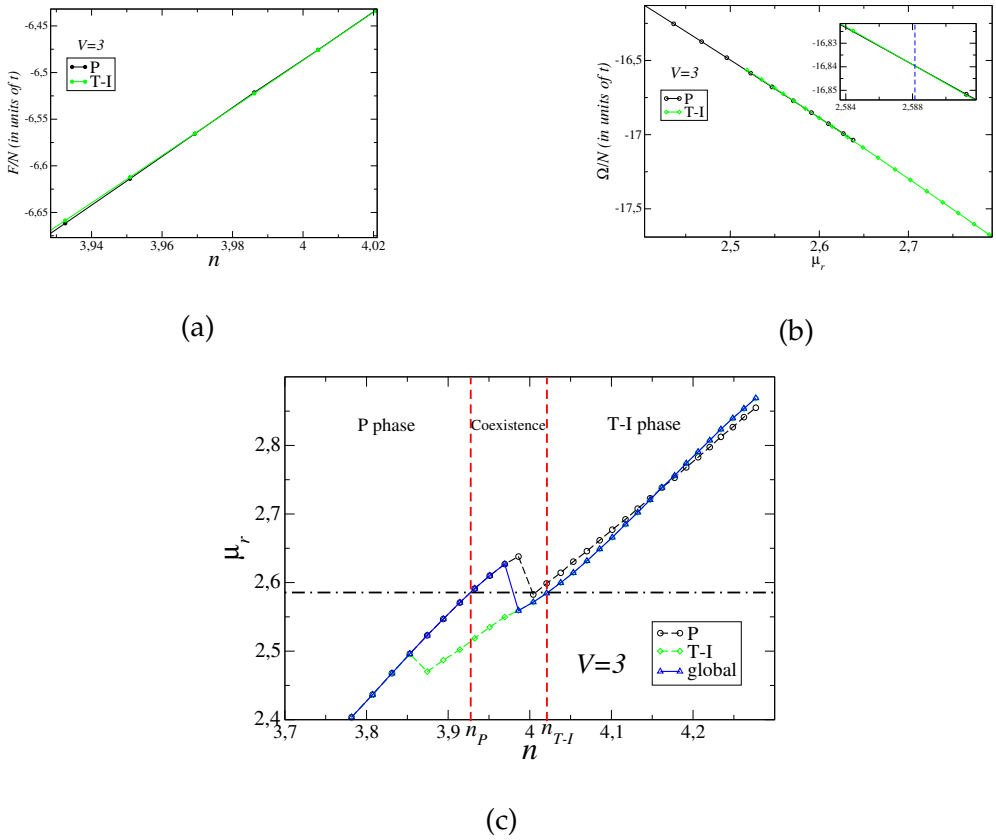

Figure B.2.: Maxwell's construction for the Pomeranchuk to T-I phase transition at $V = 3$: (a) Free energy versus n for the two involved phases. The intersection of the two phases (P in black and T-I in green) indicates a first order phase transition. Near the crossing, the coexistence energy is lower and so the sample will separate into an homogeneous mixture of both phases with chemical potential μ_0. (b) Grand potential versus μ_r. The crossing gives the mixture's chemical potential (vertical blue-dashed line) situated at $\mu_0 = 2.588$. (c) Chemical potential versus n for the two different phases and for the lowest energy phase at each point, in solid-blue labelled global. The vertical black-dash-dotted line indicates the coexistence chemical potential μ_0 found in (b). The region between red-dashed vertical lines is the region with phase coexistence at that chemical potential, with different densities, namely $n_P = 3.92$ for the P phase and $n_{T-I} = 4.02$ for the T-I phase.

The phases cross at chemical potential $\mu_0 = 2.59$. This information serves to finally identify the two densities at which the two phases coexist by depicting μ_r against n, shown in Fig. B.2(c). The central region of this plot, delimited by the vertical red-dashed lines corresponds to the coexistence region mentioned above. Thus, when this region is reached from either side, the sample will separate in regions hosting a Pomeranchuk phase at density $n_P = 3.92$ and regions hosting a T-I phase at density $n_{T-I} = 4.02$.

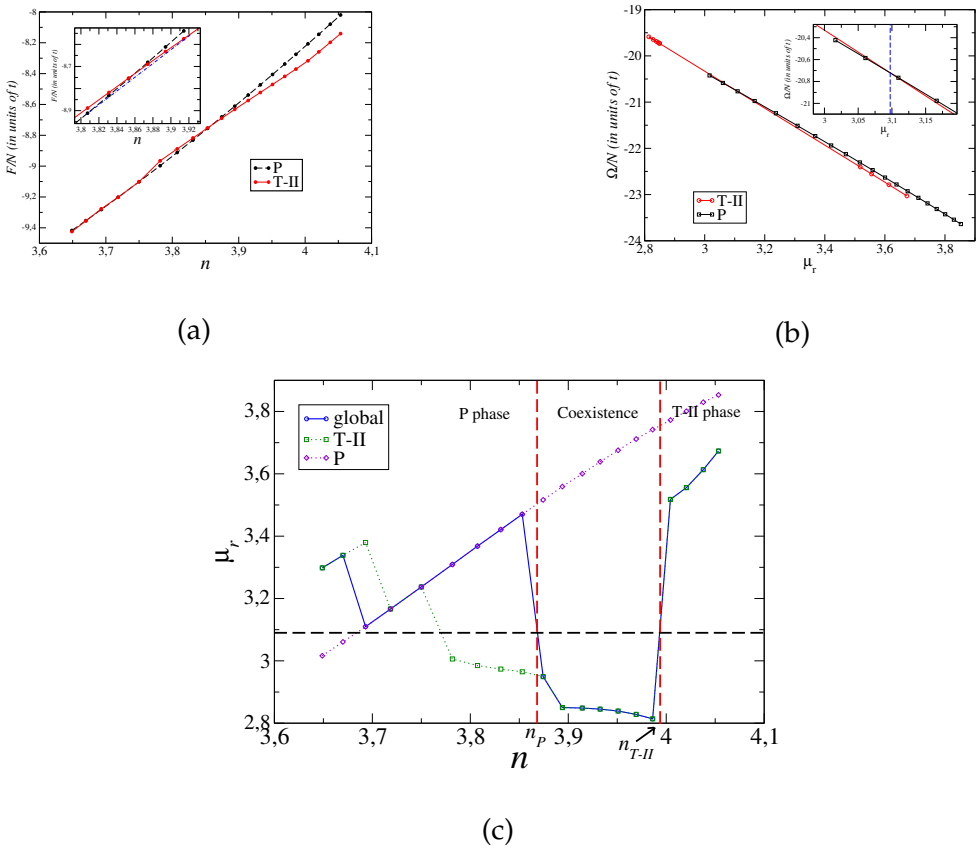

Figure B.3.: Maxwell's construction for the Pomeranchuk to T-I phase transition at $V = 5$: (a) Free energy versus n for the two involved phases. The intersection of the two phases (P in black and T-II in red) indicates a first order phase transition. Near the crossing, the coexistence energy is lower and so the sample will separate into an homogeneous mixture of both phases with chemical potential μ_0 (see blue dashed line in inset). (b) Grand potential versus μ_r. The crossing gives the mixture's chemical potential (vertical blue-dashed line) situated at $\mu_0 = 3.09$. (c) Chemical potential versus n for the two different phases and for the lowest energy phase at each point, in solid-blue labelled global. The vertical black-dash-dotted line indicates the coexistence chemical potential μ_0 found in (b). The region between red-dashed vertical lines is the region with phase coexistence at that chemical potential, with different densities, namely $n_P = 3.86$ for the P phase and $n_{T-II} = 3.99$ for the T-II phase.

B.2.3. $V = 5$: Pomeranchuk to T-II transition

Consider now a line of points with $V = 5$ in the phase diagram in Fig. 4.4 close to the P to T-II transition. We study the free energy for the Pomeranchuk and the T-II phases as the electron density is increased. This is shown in Fig. B.3(a). For small V two different starting order parameters converge to the same solution, a Pomeranchuk solution until the T-II phase kicks in with a greater free energy. In this situation the Pomeranchuk phase is favourable until, at $n \sim 3.85$ ($n \sim 0.85$ in the notation of Fig. 4.4), the T-II phase takes over in a discontinuous

fashion signalling the first order phase transition.
As before, we use Maxwell's construction to study the first order phase transition. In Fig. B.3(a) one can observe that the free energy for an inhomogeneous phase (a linear combination between two points with equal chemical potential (tangent) shown in the inset) where the two phases coexist, is smaller than the free energy of either phase. Thus, the system will prefer to be in this inhomogeneous phase.
Fig. B.3(b) represents the grand potential through the phase transition against the renormalized chemical potential μ_r. Proceeding as above the coexistence chemical potential for this phase transition lies at $\mu_0 = 3.09$ and it is represented inside the inset of Fig. B.3(b). In Fig. B.3(c) the function $\mu_r(n)$ for the two relevant phases are plotted together with the minimum energy $\mu_r(n)$ shown in solid blue. For low n the chemical potential follows the Pomeranchuk phase. At $n \sim 3.7$ the chemical potential jumps to a different solution, in this case the T-II solution. The horizontal line indicates the mixture's chemical potential μ_0 and the vertical lines the coexistence region where both phases are mixed with densities $n_P = 3.86$ for the Pomeranchuk phase and $n_{T-II} = 3.99$ for the T-II phase.
Finally note that $n_{T-II} \sim 4$, the commensurate filling. One can ask if this is still true as V is increased. One can numerically check by using the same construction that this is indeed the case and that the T-II phase really appears for fillings $n \geq 4$ which is reasonable from the commensurably argument: Before $n \sim 4$ the intracell currents cannot form and it is only when n exceeds that value when currents form. When the number of spare electrons is too large, the reduced symmetry phase pops in and destroys the T-II phase.

B.2.4. $V = 4$: Pomeranchuk to T-I transition and T-I to T-II transition

At $V = 4$ the analysis is slightly more involved. In this case, the system crosses two phase transitions, Pomeranchuk to T-I and T-I to T-II. Both transitions are first order phase transitions as shown in Fig. B.4(a) and (b).
One has to find now the coexistence chemical potential μ_0 for the phases, just as done above. In this case however there are two values of μ_0 corresponding to each phase transition: $\mu_0^{(P-TI)}$ and $\mu_0^{(TI-TII)}$ and the relative magnitude of these will determine which phases coexist. Interestingly, there is another possibility, that is to have a Pomeranchuk to T-II without passing through T-I. The chemical potential that describes this possibility is labelled $\mu_0^{(P-TII)}$.
In order to find these, and following Maxwell's construction, we plot the grand potential Ω against the renormalized chemical potential μ_r for each phase, shown in Fig. B.4 (c) (d). The former shows the two crossing points, one between the Pomeranchuk and the T-I phase and the other corresponding to the Pomeranchuk with the T-II. From it we can read out the chemical potentials: $\mu_0^{(P-TII)} = 2,909$ and $\mu_0^{(P-TI)} = 2,913$. On the other hand Fig. B.4(d) shows the other relevant crossing point involving the TI and the T-II phase. From these plot it is apparent that $\mu_0^{(TI-TII)} = 2,886$.

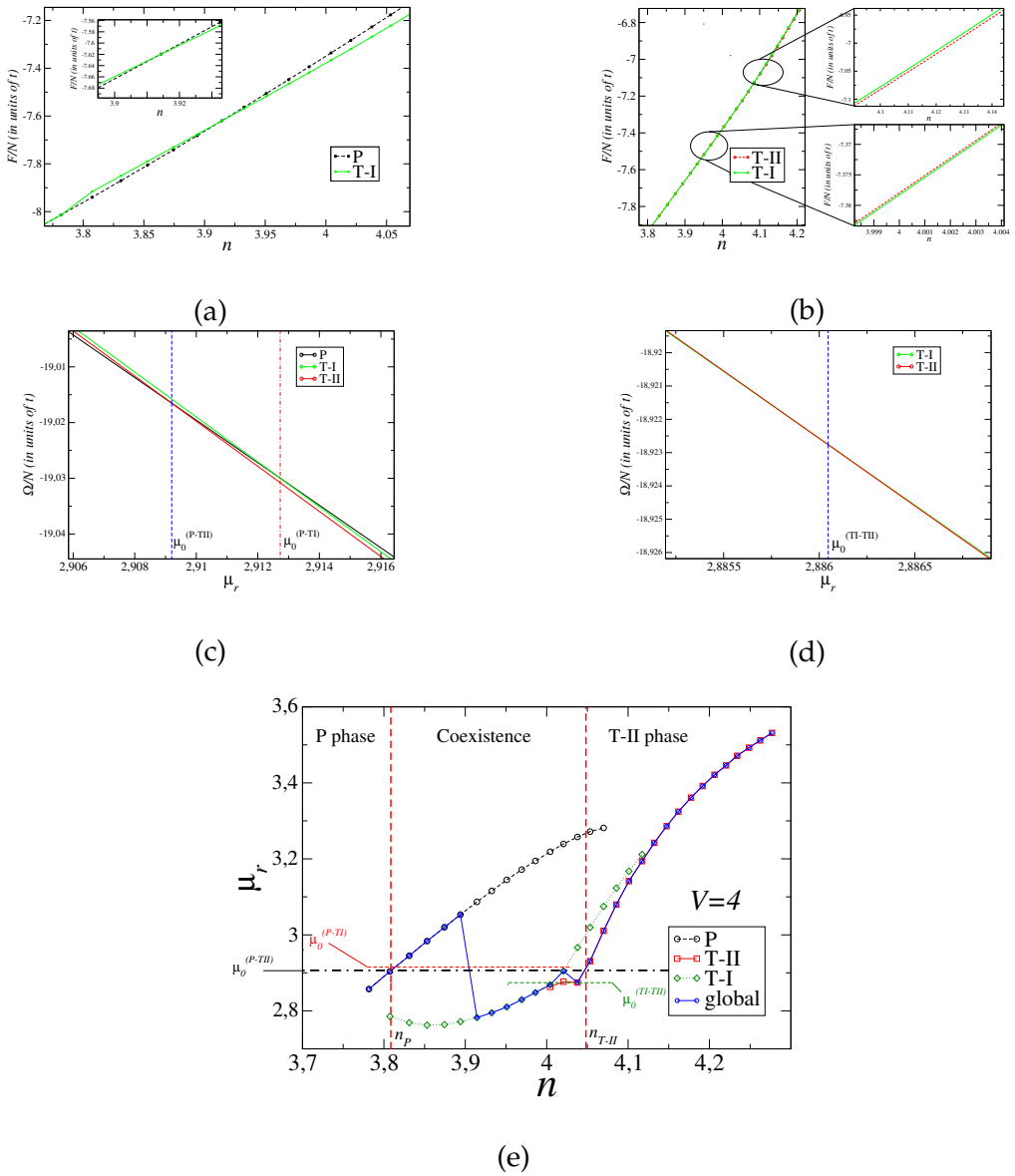

Figure B.4.: (a) Pomeranchuk phase (black dashed) and T-I phase (green-solid) free energy as a function of electron density for $V = 4$. As in the P-TII transition, crossing phases indicates a first order phase transition. (b) T-I phase (green-solid) and T-II phase (red-dashed) free energy as a function of electron density for $V = 4$. The zoomed in regions indicate a first order phase transition. (c) and (d) show the grand potential Ω per particle against the renormalized chemical potential μ_r. The crossing points (vertical dashed lines) indicate the chemical potential of the coexistence phase for each phase transition. (d) Renormalized chemical potential against the electronic density n. The three horizontal lines indicate the chemical potentials obtained in (c) and (d). The vertical lines show the coexistence region for the two stable phases: P and T-II with $n_P = 3,808$ and $n_{T-II} = 4.05$ (see text).

These values are traduced to the horizontal lines in Fig B.4(e) showing also $\mu(n)$. Invoking Maxwell's construction we see that as we increase the electron density n starting from the Pomeranchuk phase, the system reaches the P-TII instability, the black dashed-dotted $\mu_0^{(P-TII)}$ line, in B.4(d) before reaching the μ_0^{P-TI} line (red-dashed), making the TI phase unstable. Starting from higher densities, i.e. from the T-II phase, and reducing n, the system reaches the P-TII instability (represented by the black $\mu_0^{(P-TII)}$ line) before reaching the TI-TII instability (the green-dashed line labelled $\mu_0^{(P-TII)}$). Thus, in the intermediate region there is a phase coexistence region of phases P and T-II with densities $n_P = 3,808$ and $n_{T-II} = 4.05$ and the T-I phase is unstable and does not appear.

Putting all these results together, the phase diagram is now modified with the region of coexistence shown in Fig. 4.8. It should be noted that the boundaries of the coexisting region are determined by an interpolation of the above results together with more points that can be found with the same construction.

C. Spin Chern Simons terms and effective actions

C.1. Gaussian integration

This appendix is a short review of the Gaussian integration formulas for Grassmann variables used in the text. A Gaussian integral for Grassmannian variables can be shown to give [126]

$$\int \mathcal{D}\bar{\theta}\mathcal{D}\theta e^{\sum_i \theta_i b_{ij}\theta_j} = \Pi_i b_i = \mathrm{det}B = e^{\mathrm{Tr}Ln(B)} \tag{C.1}$$

If we have a more general integral

$$\int \mathcal{D}\bar{x}\mathcal{D}x\mathcal{D}\bar{y}\mathcal{D}y e^{\bar{x}Ax+\bar{y}x+\bar{x}y} = \mathrm{det}A\; e^{-\bar{y}A^{-1}y} \tag{C.2}$$

where in the second equality we have completed squares in the exponent to obtain: $(\bar{x} + \bar{y}A^{-1})A(A^{-1}y + x) - \bar{y}A^{-1}y$. Then with a change such as $x' = x + yA$ and using (C.1) we arrive to the result in (C.2).

C.2. Chern-Simons term from the path integral formalism

In order to calculate the Chern-Simons term for our model we should couple the fermions to an external vector potential A_μ and an extra field V_μ that couples adequately to the relevant degree of freedom (spin or valley in our case). Explicitly the action reads

$$S = \int \frac{dk^3}{(2\pi)^3}\bar{\psi}(\gamma^\mu k_\mu - \Lambda)\psi - e\bar{\psi}\gamma^\mu\psi A_\mu - e\bar{\psi}\gamma^\nu\gamma_5 V_\nu \tag{C.3}$$

for an arbitrary bilinear mass term characterized by the matrix Λ. From which we obtain the spin Chern Simons part of the current by a functional derivative of the action

$$< j_5^\mu > \equiv \frac{\partial S}{\partial V_\mu} = C_5\epsilon^{\mu\nu\rho}\partial_\nu A_\rho \tag{C.4}$$

We define γ_5 in this case to be $\gamma_5 = 1_\tau s_z 1_\sigma$. It is now possible to calculate explicitly the topological term by using the effective action formalism and integrating out fermions. The partition function is given by an integral to all paths of the exponential of the action (C.3)

($\hbar = 1$)

$$\begin{aligned} Z &= \int \mathcal{D}A\mathcal{D}\bar{\psi}\mathcal{D}\psi e^{iS} = \int \mathcal{D}A \det(\not{k} - \Lambda - e\not{A} - e\gamma_5 \not{V}) \\ &= \int \mathcal{D}A \det(\not{k} - \Lambda)\, \det(1 - \frac{i}{\not{k} - \Lambda}(-ie\not{A} - ie\gamma_5 \not{V})) \\ &= \int \mathcal{D}A \det(\not{k} - \Lambda)\, \exp\mathrm{Tr}\left[\ln(1 - G_0(k,\Lambda)(-ie\not{A} - ie\gamma_5 \not{V}))\right] \end{aligned}$$

where we have used (C.1) and have defined $G_0^{-1}(k,\Lambda) = -i(\not{k} - \Lambda)$. Since the first term is an irrelevant (infinite) constant independent of the fields it can be safely dropped out. Now we can expand the logarithm and end up with the effective action

$$S_{eff} = \int \frac{dk^3}{(2\pi)^3} \sum_{n=1}^{\infty} -\frac{1}{n} \mathrm{tr}\left[(G_0(k,\Lambda)(-ie\not{A} - ie\gamma_5 \not{V}))^n\right] \tag{C.5}$$

where now tr is over gamma matrices. Now we can compute the second term ($n = 2$) in the effective action, and in particular the part depending on the product VA which is the one that will give the spin-Chern Simons term through (C.4). This reads

$$S_{eff}^{n=2} = \int \frac{dk^3}{(2\pi)^3} \frac{dp^3}{(2\pi)^3} - \frac{1}{2} \mathrm{tr}\left[(G_0(k,\Lambda)(-ie\not{A} - ie\gamma_5 \not{V}))^2\right] \tag{C.6}$$

In terms of Feynman diagrams this is the photon bubble with a $\gamma_\mu\gamma_5$ vertex. Since we are interested in the $V\partial A$ term we can expand one of the Green's functions for small external momenta as

$$G(k+p) \simeq G(k) + p_\mu \partial_k^\mu G(k+p)\big|_{p_\mu = 0} = -ip_\rho G(k,\Lambda)\gamma_\rho G(k,\Lambda)$$

Inserting this into the effective action we can write it in real space as

$$S_{eff}^{n=2} = -i \int dx^3 C_5^{\mu\nu\rho} V_\mu \partial_\nu A_\rho$$

where we have to determine, for each Λ

$$C_5^{\mu\nu\rho} = i\frac{1}{2} \int \frac{dk^3}{(2\pi)^3} \mathrm{tr} G(k,\Lambda)\gamma^\mu G(k,\Lambda)\gamma^\nu G(k,\Lambda)\gamma^\rho\gamma_5 \tag{C.7}$$

As was suggested before, a non zero $C_5^{\mu\nu\rho}$ term in the action implies that a topologically non trivial time reversal invariant phase is present in the system.

C.3. Technical details for the evaluation of the integrals

C.3.1. Pole prescription

To evaluate the integrals at finite chemical potential we need to define our pole prescription. Consider an free electron gas. We know that by the definition of Fermi surface and considering $T = 0$ we have that $< \Omega | c_{\mathbf{k}}^\dagger c_{\mathbf{k}} | \Omega >= \theta(\mathbf{k}_F - \mathbf{k}) \equiv \theta(\xi_{\mathbf{k}})$ and $< \Omega | c_{\mathbf{k}} c_{\mathbf{k}}^\dagger | \Omega >=$

$\theta(\mathbf{k}-\mathbf{k}_F) \equiv \theta(-\xi_{\mathbf{k}})$ which is just stating the fact that we have a filled Fermi surface defined by $\mathbf{k}_F$, the Fermi wave vector (just for completeness we note that a different notation can be $\xi_{\mathbf{k}} = E(\mathbf{k}) - \mu$ where $E(\mathbf{k})$ is the dispersion relation of the system and μ is the chemical potential). In this context the Green's function is properly defined as a time ordered product of creation operators

$$\begin{aligned} G(\mathbf{k}, t-t') &= -i < \Omega | \mathrm{T} c_{\mathbf{k}}(t) c^{\dagger}_{\mathbf{k}}(t') | \Omega > \\ &= -i(\theta(t-t')\theta(\xi_{\mathbf{k}}) - \theta(t'-t)\theta(-\xi_{\mathbf{k}}))e^{-i\xi_{\mathbf{k}}(t-t')} \end{aligned}$$

Fourier transforming the last expression one obtains

$$\begin{aligned} G(\mathbf{k}, E) &= -i\left(\theta(\xi_{\mathbf{k}})\int_0^{\infty} dt e^{it(E-\xi_{\mathbf{k}}+i\delta)} - \theta(-\xi_{\mathbf{k}})\int_{-\infty}^{0} dt e^{it(E-\xi_{\mathbf{k}}-i\delta)}\right) \\ &= \frac{\theta(\xi_{\mathbf{k}})}{E-\xi_{\mathbf{k}}+i\delta} + \frac{\theta(-\xi_{\mathbf{k}})}{E-\xi_{\mathbf{k}}-i\delta} \qquad \text{(C.8)} \\ &= \frac{1}{E-\xi_{\mathbf{k}}+i\delta(\mathrm{sign}(\xi_{\mathbf{k}}))} \qquad \text{(C.9)} \end{aligned}$$

Notice that the last line (C.9) defines the Feynman propagator, composed of both particles and hole propagator in (C.8). The convergence parameter δ and, in particular its sign, is only important near the pole and so $\mathrm{sign}(\xi_{\mathbf{k}})$ can be replaced by $\mathrm{sign}(E)$ which is the standard notation in condensed matter physics. This is equivalent to the prescription used in high energy physics which is defined as $p_0 \to p_0(1+i\epsilon)$. The chemical potential is introduced with the matrix that is associated with p_0, i.e. γ_0. Again, the sign which matters is $\mathrm{sign}(\xi_{\mathbf{k}})$. With these prescriptions, causality is respected as seen explicitly above, with the $\theta(t-t')$ functions.

C.3.2. Intrinsic spin orbit interaction

Zero chemical potential (μ=0):

With only the spin orbit coupling, the propagator takes the form $G(k, \Delta_{so}) = -i(\not{k} - \Delta_{so}\Lambda_{so})$. Note that in general, the mass matrix Λ_i does not commute with the γ^{μ} matrices one has to be careful. In particular, one cannot use the usual form of the propagator $G(k,\Lambda) = i\frac{\not{k}+\Lambda}{k^2-\Lambda^2}$ used to calculate integrals with Dirac propagators. Instead, one should evaluate the matrix in the denominator of $G(k,\Lambda)$, then invert it and finally compute the trace as indicated in (6.17). Although this is the general case, note that Λ_{so} commutes with all of the matrices and one can still use this form. Anyhow, we will stick to the procedure described above. By performing the inversion and evaluating the trace $C^{\mu\nu\rho}$ takes the simple form:

$$C_5^{\mu\nu\rho} = \frac{1}{2}\int \frac{dk^3}{(2\pi)^3}\epsilon^{\mu\nu\rho}\frac{-8\Delta_{so}i}{(-k_0^2+\mathbf{k}^2+\Delta_{so}^2)^2} \qquad \text{(C.10)}$$

Some comments are in order at this point. First, note that the poles after doing the trace are still at the dispersion relation. This is a consistency check to ensure that the inverse and

traces have been calculated correctly. Second, we need to introduce a pole prescription. The correct way to do it (see section C.3.1 above) is to redefine de time part of the momentum as $p_0 \to p_0(1+i\epsilon)$. This prescription ensures that particles with positive (negative) energies travel forwards (backwards) in time and hence are casual. When a finite chemical potential is fixed, the zero of energies is switched so that positive energies defined to be above the Fermi surface and negative energies are defined to live below the Fermi surface. Finite chemical potential will be dealt with in the next subsection. Introducing this prescription, the integral reads

$$C_5^{\mu\nu\rho} = \frac{1}{2}\int \frac{dk^3}{(2\pi)^3}\epsilon^{\mu\nu\rho}\frac{-8i\Delta_{so}}{(-k_0^2 - i\epsilon + \mathbf{k}^2 + \Delta_{so}^2)^2} = \int \frac{dk^3}{(2\pi)^3}\epsilon^{\mu\nu\rho}\frac{-8i\Delta_{so}}{(k_0 - k_0^+)^2(k_0 - k_0^-)^2} \tag{C.11}$$

Where the poles are now $k_0^{\pm} = \pm\sqrt{\mathbf{k}^2 + \Delta_{so}^2} \mp i\epsilon$ and so we can close the contour either above or below to perform the p_0 integral. Since they are double poles the residue is calculated with a derivative $\text{Res}[p_0^{\pm}] = \lim_{p\to p_0^{\pm}}(p - p_0^{\pm})^2\frac{df(p)}{dp}$. This integral gives

$$C_5^{\mu\nu\rho} = \epsilon^{\mu\nu\rho}\frac{1}{2}\int_0^{\infty}\frac{dk}{(2\pi)}k\frac{2\Delta_{so}}{(\mathbf{k}^2 + \Delta_{so}^2)^{3/2}} = \epsilon^{\mu\nu\rho}\frac{\Delta_{so}}{2\pi|\Delta_{so}|} = \frac{\epsilon^{\mu\nu\rho}}{2\pi}\text{sign}(\Delta_{so}) \tag{C.12}$$

The sign function appears because the integral does not know about the sign of Δ_{so} but the prefactor does. With this result it has been checked that the spin Hall conductivity is quantized in units of e^2/h as was first shown by [60].

Finite chemical potential ($\mu \neq 0$):

We will now add a finite chemical potential to the above calculation. One has to notice that the position of the poles will change for different chemical potentials. In particular depending of the value of $\mathbf{k}$ one can trace the sign of k_0 which determines the position of the poles. With an arbitrary chemical potential the integral reads:

$$C_5^{\mu\nu\rho} = \frac{1}{2}\epsilon^{\mu\nu\rho}\int \frac{dk^3}{(2\pi)^3}\frac{-8\Delta_{so}i}{(k_0 - k_0^+)^2(k_0 - k_0^-)^2} \tag{C.13}$$

where now $k_0^{\pm} = \pm\sqrt{\mathbf{k}^2 + \Delta_{so}^2} - \mu - i\epsilon(\text{sgn}(\pm\sqrt{\mathbf{k}^2 + \Delta_{so}^2} - \mu))$. It is simple to see that k_0^- is always negative and so it has always the pole in $\pm\sqrt{\mathbf{k}^2 + \Delta_{so}^2} - \mu - i\epsilon$. The sign of the other pole depends on the value of μ.

Lets consider for instance the case $|\mu| > \Delta_{so}$. Notice that k_0^+ is positive if $k^2 > \mu^2 - \Delta_{so}^2$ and negative if $k^2 < \mu^2 - \Delta_{so}^2$. It is necessary therefore to split the integral over $|\mathbf{k}|$ into a sum of two integrals, the first from zero to $|\mathbf{k}| = \sqrt{\mu^2 - \Delta_{so}^2}$ and the second one from $|\mathbf{k}| = \sqrt{\mu^2 - \Delta_{so}^2}$ up to infinity. It is simple to see that the first integral has both poles in the same complex semi-plane (upper) and the integral is zero. However, we are still left with the integral:

$$C_5^{\mu\nu\rho} = \frac{1}{2}\int_{\sqrt{\mu^2-\Delta_{so}^2}}^{\infty}\frac{dk}{(2\pi)}k\epsilon^{\mu\nu\rho}\frac{2\Delta_{so}}{(\mathbf{k}^2 + \Delta_{so}^2)^{3/2}} = \epsilon^{\mu\nu\rho}\frac{\Delta_{so}}{2\pi|\mu|} \tag{C.14}$$

Note that when $|\mu| < \Delta_{so}$ both poles are always on different semi-planes (upper and lower) and so the integral gives the same result as in the case of zero chemical potential. These results were first obtained analytically in ref [228].

C.3.3. Staggered potential

Graphene with a staggered potential generates the following band dispersion $k_0^{\pm} = \pm\sqrt{\mathbf{k}^2 + m^2} \mp i\epsilon$ and as discussed above it opens a gap in the spectrum. However, it is straight forward to see that the staggered potential alone gives a zero contribution to the spin Chern-Simons term. Technically, this is due to the vanishing of the trace. As discussed above, the physical reason is that the staggered potential generates an insulator with equal masses in both valleys and so the Hamiltonian is adiabatically connected to the one of a trivial insulator.

C.3.4. Rashba coupling

The band spectrum given by considering graphene with Rashba coupling is given by: $k_0^{\pm,A} = \pm\sqrt{\mathbf{k}^2 + \lambda^2} - \lambda$ and $k_0^{\pm,B} = \pm\sqrt{\mathbf{k}^2 + \lambda^2} + \lambda$, and so breaks the spin degeneracy of the system, although preserving the valley degeneracy. The bands are plotted in figure 6.1 where it is evident that Rashba coupling on its own does not generate a gap, hence the definition of a topological insulator is out of context. Technically, if one calculates the trace, the spin Chern Simon term gives a contribution which vanishes by parity of the integral (specifically, the integral is odd in k_0 and so it vanishes).

C.3.5. Staggered potential and intrinsic spin-orbit coupling

Zero chemical potential ($\mu = 0$):

This case is interesting since the interplay of both couplings m and Δ_{so} will generate different topological phases. The eigenvalues of the Hamiltonian are given by: $k_0 = \pm\sqrt{\mathbf{p}^2 + (\Delta_{so} + m)^2}$ and $k_0 = \pm\sqrt{\mathbf{p}^2 + (\Delta_{so} - m)^2}$ which open a gap in the spectrum. Performing the trace one obtains the integral for $C_5^{\mu\nu\rho}$:

$$C_5^{\mu\nu\rho} = \frac{1}{2}\int \frac{dk^3}{(2\pi)^3} - 4i\epsilon^{\mu\nu\rho}\left(\frac{(\Delta_{so} - m)}{(-k_0^2 + \mathbf{k}^2 + (\Delta_{so} - m)^2)^2} + \frac{(\Delta_{so} + m)}{(-k_0^2 + \mathbf{k}^2 + (\Delta_{so} + m)^2)^2}\right) \quad \text{(C.15)}$$

Technically these are two copies for the integral that was obtained for the spin-orbit coupling alone but for different masses and so the result is simply:

$$C_5^{\mu\nu\rho} = \frac{\epsilon^{\mu\nu\rho}}{4\pi}(\text{sign}(\Delta_{so} - m) + \text{sign}(\Delta_{so} + m)) \quad \text{(C.16)}$$

It is clear that the interplay between a staggered potential and a spin orbit coupling is still quantized. When either $\Delta_{so} = 0$ or $m = 0$ we recover the result of the previous sections. The new feature compared to previous results is that when both are non zero there is still a topological response of the system.

Finite chemical potential ($\mu \neq 0$):

We again have two copies of the intrinsic spin-orbit case and so, depending on the relative value of μ against $\Delta_{so} \pm m$ we will have different results. Without doing any extra work we can read the result from the considerations made in the case of the intrinsic spin-orbit coupling from where the four cases in the main text follow.

C.3.6. Rashba coupling and intrinsic spin-orbit coupling

When both Rashba and intrinsic orbit-coupling are considered, several new features arise. In the first place, Rashba does not preserve s_z and so we do not expect the spin Hall conductivity to be quantized. Secondly, when $\lambda_R > \Delta_{so}$ the system develops an asymmetric gap (See figure 6.1). After performing the trace, the integral left is given by:

$$C_5^{\mu\nu\rho} = \frac{1}{2}\int \frac{dk^3}{(2\pi)^3}(-8i)\epsilon^{\mu\nu\rho}\frac{\left(4\lambda_R^2(k_0+\Delta_{so})\left(k_0(k_0+\Delta_{so})-k_x^2+k_y^2\right)+\Delta_{so}\left(-k_0^2+\mathbf{k}^2+\Delta_{so}^2\right)^2\right)}{\left(\left(-k_0^2+\mathbf{k}^2+\Delta_{so}^2\right)^2-4\lambda_R^2(k_0+\Delta_{so})^2\right)^2} \tag{C.17}$$

As usual the integral has poles at the dispersion relation. However, one needs to be careful since, again poles will switch sides depending on the value of the chemical potential μ. A general analytical treatment with arbitrary μ is messy and thus we will focus in two different chemical potentials $\mu = 0$ and $\mu = \Delta_{so}$.

An important difference with respect to other cases is that at zero chemical potential the poles change semi-plane depending on the value of $\mathbf{k}$. However, technically, the integral is not different to the other cases except for the fact that now we have four poles instead of two. In some region of $\mathbf{k}$ there will be three poles above the real axes (or one below the real axis) to consider and in the other region there will be two (above or below the real axis). The bands, or equivalently the pole structure is the following $k_0^{\pm A} = \pm\sqrt{\mathbf{k}^2+(\lambda_R-\Delta_{so})^2}-\lambda_R-\mu$ and $k_0^{\pm B} = \pm\sqrt{\mathbf{k}^2+(\lambda_R+\Delta_{so})^2}+\lambda_R-\mu$. The band structure for $\Delta_{so} > \lambda_R$ is shown in Fig. 6.1. This case can be treated in an analogous way as before for the cases discussed in the main text, always being careful of considering each pole contribution.

D. Casimir effect with topological insulators

D.1. Proof of the existence of the minimum at $T = 0$

In this appendix a proof is provided of the existence of the minimum at $T = 0$ by discussing the high and low frequency limits of the Casimir energy density. The Casimir energy stored between the plates is given by

$$\frac{E_c(d)}{A\hbar} = \int_0^\infty \frac{d\xi}{2\pi} \int \frac{d^2\mathbf{k}_\parallel}{(2\pi)^2} \log\det\left[1 - \mathbf{R}_1 \cdot \mathbf{R}_2 e^{-2k_3 d}\right], \tag{D.1}$$

To prove the existence of the minimum we assume that the $\mathbf{R}_i$ is the 2x2 matrix defined in (7.9) and that the dielectric function satisfies the following two analytical properties: 1) finite dielectric permittivity at zero frequency ($\epsilon(0) < \infty$) and 2) high frequency transparency: $\epsilon(\omega) \to 1$ when $\omega \to \infty$. For an insulator one can assume the dielectric function a sum of oscillators (7.11) although for simplicity let's assume that

$$\epsilon(i\xi) = 1 + \frac{\omega_e^2}{\xi^2 + \omega_R^2 + \gamma_R \xi}. \tag{D.2}$$

The derivation does not depend on the analytical form of the dielectric function as long as it fulfils the mentioned conditions and in particular the proof holds for more than one oscillator. We further assume the particular situation where $\theta_1 = -\theta_2$, where labels 1 and 2 identify the Casimir plates to present analytic results.

The first step is to rescale $E_c(d)$ with d. If in the expression for $E_c(d)$, ξ and $\mathbf{k}_\parallel$ are rescaled to contain d, tan overall factor $1/d^3$ appears in front of the integral. The reflection matrices are to be evaluated now at the rescaled frequency and momenta ξ/d and $\mathbf{k}_\parallel/d$. Thus, all of the d dependence can be transferred to the reflection matrices and the overall $1/d^3$ prefactor. The expression for the energy is

$$\frac{E_c(d)}{E_0} = \frac{1}{d^3} \int_0^\infty d\xi \int d^2\mathbf{k}_\parallel \log\det\left[1 - \mathbf{R}_1\left[\frac{\xi}{d}, \frac{\mathbf{k}_\parallel}{d}\right] \cdot \mathbf{R}_2\left[\frac{\xi}{d}, \frac{\mathbf{k}_\parallel}{d}\right] e^{-2k_3}\right], \tag{D.3}$$

where $k_3^{2(r)} = \xi^2 + k_\parallel^2$ is defined through the rescaled variables (which include c the speed of light in vacuum and ω_R) and $E_0 = A\hbar c/(2\pi)^2 (w_R/c)^3$ where A is the area of the plates. The key point is that reflection matrices are evaluated at these rescaled variables, with a rescaled

dielectric function

$$\epsilon(i\xi/d) = 1 + \frac{\left(\frac{\omega_e}{\omega_R}\right)^2}{\left(\frac{\xi}{d}\right)^2 + 1 + \frac{\gamma_R}{\omega_R}\frac{\xi}{d}}. \tag{D.4}$$

The two conditions imposed to $\epsilon(i\xi)$ ensure that the reflection matrices are not singular in the limits $\xi/d \to 0$ and $\xi/d \to \infty$. Hence, $E_c(d \to 0) \to \pm\infty$ and $E_c(d \to \infty) \to 0$.
The way the integrand approaches these limits determines the sign of $E_c(d)$. For instance, if the integrand is positive at small distances and negative at large distances, necessarily a minimum exists at an intermediate distance. When $\theta_1 = -\theta_2$, this is exactly what happens (unless $\epsilon(0) = 1$, where both limits are positive and hence long range repulsion is obtained), as it will be shown in what follows.
We now evaluate the integrand in (D.1). When $\theta_1 = -\theta_2 = \theta$ the reflection matrices describing both topological insulators can be written as:

$$\mathbf{R}_{\pm} = \begin{bmatrix} r_s(i\xi, \mathbf{k}_\parallel) & \pm r_{sp}(i\xi, \mathbf{k}_\parallel) \\ \pm r_{sp}(i\xi, \mathbf{k}_\parallel) & r_p(i\xi, \mathbf{k}_\parallel) \end{bmatrix}. \tag{D.5}$$

Introducing this inside (D.1) the integrand follows:

$$I = \log\det\left[1 - \mathbf{R}_+ \cdot \mathbf{R}_- e^{-2k_3^{(r)}}\right] = \log\left[1 + e^{-2k_3^{(r)}}\left(2r_{sp}^2 - r_p^2 - r_s^2\right) + e^{-4k_3^{(r)}}\left(r_{sp}^2 - r_p r_s\right)^2\right],$$

Notice that the last term although always positive, will play no role in what follows since it is always suppressed over the first term (note that $r_s, r_p, r_{sp} < 1$).

The limit of short distances

For $d \to 0$ and using the high frequency transparency of the dielectric function we now show that $|r_i| << |r_{sp}|$ $(i = s, p)$. Notice first that the denominator Δ defined in (7.9) is common to all terms so it cannot play a role on the relative magnitude of the coefficients. We hence study the behaviour of χ_- at small distances, given by:

$$\chi_-\left(\frac{\xi}{d}, \frac{\mathbf{k}_\parallel}{d}\right) = \frac{\xi^2 + \mathbf{k}_\parallel^2 - \left(\xi^2 + \frac{\mathbf{k}_\parallel^2}{n_2^2}\right)}{\sqrt{\left(\xi^2 + \mathbf{k}_\parallel^2\right)\left(\xi^2 + \frac{\mathbf{k}_\parallel^2}{n_2^2}\right)}}. \tag{D.6}$$

Remembering that at small distances (large frequencies) we have transparency, $n_2^2(\xi/d) = \epsilon(\xi/d) \to 1$ then we see that $\chi_- \to 0$ and:

$$r_s = \frac{-\bar{\alpha}^2}{2 + \bar{\alpha}^2 + \chi_+} = -r_p,$$

and

$$r_{sp} = \frac{2\bar{\alpha}}{2 + \bar{\alpha}^2 + \chi_+},$$

since the first are of order $\mathcal{O}(\alpha^2)$ and the second are of order $\mathcal{O}(\alpha)$ (remember that $\bar{\alpha}$ is proportional to the fine structure constant α) we have that $|r_i| << |r_{sp}|$ $(i = s, p)$. Hence the integrand is positive (since the integrand has the form $I = \ln(1 + A)$ where $A > 0$) and so $E_c(d \to 0) \to +\infty$.

The limit of large distances

When $d \to \infty$ the reflection coefficients take the form

$$r_s = \frac{1 - \epsilon(0) - \bar{\alpha}^2 + \sqrt{\epsilon(0)}\chi_-}{1 + \epsilon(0) + \bar{\alpha}^2 + \sqrt{\epsilon(0)}\chi_+},$$

for the diagonal part (with a similar expression for r_p) and

$$r_{sp} = \frac{2\bar{\alpha}}{1 + \epsilon(0) + \bar{\alpha}^2 + \sqrt{\epsilon(0)}\chi_+},$$

for the off diagonal. We have defined the quantity $\epsilon(0) \equiv 1 + \left(\frac{w_e}{w_R}\right)^2$. In this case, depending on the values of $\epsilon(0)$ different behaviours emerge. Since $\epsilon(0) \geq 1$ we can distinguish to extreme limits, one where $\epsilon(0) = 1$ and the other with $\epsilon(0) >> 1$.

When $\epsilon(0) = 1$ one can see that we return to the previous case since the quantity χ_- in this limit also goes to zero. Hence $|r_{sp}| >> |r_i|$ $(i = s, p)$ is satisfied for all distances and $E_c(d)$ is always positive .Therefore, using the fact that that $E_c(d) \to 0$ when $d \to \infty$ and that $E_c(d) \to +\infty$ when $d \to 0$ we deduce that there is no minimum and that the force is always repulsive. This was confirmed by the numerical calculations presented in the main text.

When $\epsilon(0) >> 1$, we see that the opposite condition, $|r_{s,p}| >> |r_{sp}|$, is satisfied. Even in the worst case when χ_- is smallest, $\epsilon(\xi)$ in r_s is always larger than 2α in r_{sp}. The integrand at large distances is a negative quantity (since the integrand now has the form $I = \ln(1 - B)$ with $B > 0$) and so $E_c(d)$ approaches to zero from negative values ($E_c(d) \to -\infty$ for $d \to \infty$). Since at small distances $E_c(d) \to +\infty$ we conclude that there must be a minimum at an intermediate distance $0 < d_m < \infty$, since the function must cross the d axis.

Notice that when $\epsilon(0)$ is strictly infinity we recover the case of an ideal metal where $r_{s,p} = \mp 1$ and $r_{sp} = 0$, with attraction at all distances.

To sum up, as we increase $\epsilon(0)$ from one, a minimum develops at an intermediate distance d_m. This distance shifts to lower values as we increase $\epsilon(0)$ until, at $\epsilon = \infty$ we recover the ideal metal case where complete attraction occurs.

In the case where $\theta_1 = \theta_2$ the signs inside I change to give:

$$I = \log\left[1 - e^{-2k_3^{(r)}}\left(2r_{sp}^2 + r_p^2 + r_s^2\right) + e^{-4k_3^{(r)}}\left(r_{sp}^2 - r_p r_s\right)^2\right].$$

The predominant term inside the logarithm is always negative and hence the integrand is always negative. Therefore at small distances $E_c(d) \to -\infty$ and at large distances $E_c(d) \to 0$ approaching this limit from negative values, recovering attraction at all intermediate distances.
Finally, it can be checked by analogous methods, that the case where one θ is zero and the other one is not (dielectric - topological insulator case) results in Casimir attraction for all distances.

D.1.1. Comparison with chiral metamaterials

It is instructive to compare our results with the results obtained by Zhao *et al.* in [353]. In their work, the relevant parameter to obtain repulsion is the chirality which mixes transverse electric and transverse magnetic polarizations giving in turn the off-diagonal r_{sp} components. When calculating the Casimir force, by differentiation of the Lifshitz formula they obtain the following integrand (in our notation):

$$J = \frac{(r_s^2 + r_p^2 - 2r_{sp}^2)e^{-2kd} - (r_{sp}^2 + r_s r_p)^2 e^{-4kd}}{1 - (r_s^2 + r_p^2 - 2r_{sp}^2)e^{-2kd} + (r_{sp}^2 + r_s r_p)^2 e^{-4kd}}. \tag{D.7}$$

Note that when r_{sp} becomes dominant, J turns negative as discussed in [353], enabling thus the possibility of repulsion when r_{sp} is sufficiently large. In chiral metamaterials this occurs for large chirality at high frequencies (short distances) hence giving repulsion at short distances. The comparison with the topological insulator case is straightforward. Analytical derivation shows that the integrand for opposing signs of the topological magnetoelectric response ($\theta_1 = -\theta_2$) has the exact same form as the integrand given by (D.7) (with properly modified reflection coefficients). In the last section we showed that, for high frequencies (short distances) r_{sp} becomes dominant and hence, the topological part becomes dominant analogous to the case of large chirality in chiral metamaterials. When both topological magnetoelectric terms have equal signs ($\theta_1 = \theta_2$) one obtains the same integrand with the important difference of the signs in front of the off-diagonal terms:

$$J = \frac{(r_s^2 + r_p^2 + 2r_{sp}^2)e^{-2kd} - (r_{sp}^2 - r_s r_p)^2 e^{-4kd}}{1 - (r_s^2 + r_p^2 + 2r_{sp}^2)e^{-2kd} + (r_{sp}^2 - r_s r_p)^2 e^{-4kd}}. \tag{D.8}$$

As shown in the last section, even with dominant r_{sp} repulsion is not possible at any frequency. Therefore the case with opposing $\theta_{1,2}$ signs is analogous to a high chirality metamaterial.
Related to the previously discussed works there are other studies where repulsion is realised in the context of dielectric and magnetic anisotropy [354–356] in metamaterials (leaving chirality aside). Anisotropy can mix polarizations and thus, under the right circumstances induce repulsion as shown by [354–356]. The effect of anisotropic corrections to the Casimir force in topological insulators is presented in the main text.

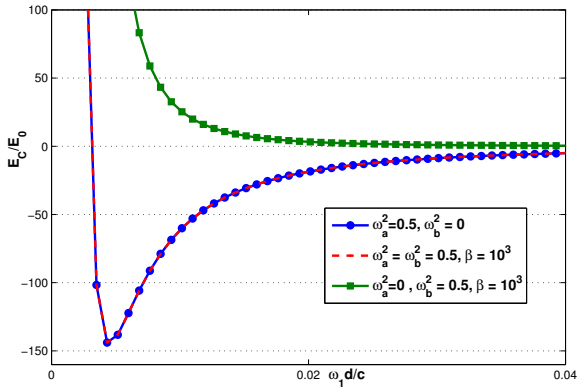

Figure D.1.: Effect of a high frequency oscillator on the dielectric permittivity. The units are the same as in the figures of the main text. Green squares represent the high frequency oscillator (eq (D.9) with $\omega_a = 0$), blue circles the low frequency oscillator (eq (D.9) with $\omega_b = 0$) and the dashed red line represents the model in (D.9)

D.1.2. Effect of including two oscillators

In the main text we have modelled $TlBiSe_2$ with a single oscillator given experimentally by [269]. However in general other oscillators at different frequencies can be present when considering other topological insulators. Nevertheless, as stated above, the proof for the existence of the minimum still holds even when more oscillators are considered in the dielectric function model, as long as high frequency transparency and finite zero frequency dielectric response is respected, which is in general true for insulators at low temperatures. The presence of other resonance frequencies can modify the position of the minimum just as discussed in the main text. To explore this issue a little further we have studied the case when the dielectric function is given by

$$\epsilon(i\xi) = 1 + \frac{\omega_a^2}{\xi^2 + 1 + \gamma_R \xi} + \frac{\omega_b^2}{\xi^2 + \beta^2 + \gamma_R \xi}, \tag{D.9}$$

in units of ω_1 the frequency of the first oscillator. The parameter $\beta \equiv \frac{\omega_2}{\omega_1}$ measures the position of the resonance of the second oscillator with respect to the first. To illustrate the effect of adding a high frequency oscillator we study the particular case where $\beta \sim 10^3$ and $\omega_a^2 = \omega_b^2 = 0.5$ shown in Figure D.1. We have plotted the cases where both oscillators are included red dashed curve) together with the two isolated oscillators (green squares for $\omega_a = 0$ $\omega_b \neq 0$ and blue circles for $\omega_a \neq 0$ $\omega_b = 0$). Figure D.1 shows that the effect of a high frequency oscillator is suppressed whenever $\omega_a \neq 0$ and it is only when $\omega_a = 0$ that it plays a role shifting the repulsive zone to higher distances, as expected from the analysis in the main text. Although the minimum still exists in this last case, the dielectric function is so close to one that nearly complete repulsion is obtained, as discussed in the first

section. These analysis can be summarized up as follows: 1) The minimum still exists when more oscillators are considered, in agreement with the analytical proof and 2) The lower frequency will dominate the position of the minimum since its contribution to the dielectric function will be less suppressed.

D.2. Classical limit: analytical expressions

The Casimir force at non zero temperature is defined as $F = -\partial_d E_c(d)$ with $E_c(d)$ given by (7.14):

$$\frac{F(T,d)}{A} = -\frac{\hbar\omega_R^4}{4\pi^2c^3}\bar{T}{\sum_{l=0}^{\infty}}' \int_0^\infty dk_\parallel k_\parallel k_3 \mathrm{Tr}\left[\left(1-\mathbf{R}_1\cdot\mathbf{R}_2 e^{-2k_3\bar{d}}\right)^{-1}\mathbf{R}_1\cdot\mathbf{R}_2 e^{-2k_3\bar{d}}\right], \tag{D.10}$$

where $k_3 = \sqrt{k_\parallel^2 + \bar{T}^2 l^2}$ and R_i are the reflection coefficients of each plate. In this expression the momentum variable is rescaled in units of ω_R and the integral depends only on $\bar{d}$ and $\bar{T}$. As discussed in the main text, at high temperature, only the $l = 0$ term contributes since the rest are exponentially suppressed. Keeping only this term in the integral one can recast this expression as

$$F_{cl}(d) = \frac{k_B T}{d^3\pi} f(\epsilon(0),\theta_1,\theta_2). \tag{D.11}$$

Integrating this expression for different values of $\theta_{1,2}$ and $\epsilon(0)$ one obtains the diagram in Fig. 7.4 (whenever $\theta_{1,2}$ have opposite signs but equal magnitude θ).
In order to derive analytical results further approximations must be considered. In the rest of this appendix we will assume that we are always in the region of small magnetoelectric coupling $\bar{\alpha} << 1$, which is justified as long this coefficient is of the order of the fine structure constant, assumption to be expected in real topological insulators. Hence, for small topological magnetoelectric couplings we can evaluate the integral to give

$$\begin{aligned} F_{cl}(d) &= -\frac{k_B T}{8d^3\pi}\Big[Li_3\left(\frac{(\epsilon(0)-1)^2}{(\epsilon(0)+1)^2}\right) + \\ &+ \left(\bar{\alpha}_1^2+\bar{\alpha}_2^2+2\bar{\alpha}_1\bar{\alpha}_2\frac{\epsilon(0)+1}{\epsilon(0)-1}\right)\frac{1}{(\epsilon(0)-1)(\epsilon(0)+1)}Li_2\left(\frac{(\epsilon(0)-1)^2}{(\epsilon(0)+1)^2}\right)\Big], \end{aligned} \tag{D.12}$$

where $\bar{\alpha} = \frac{\theta\alpha}{\pi}$ and Li_n is the polylogarithm of order n. When $\epsilon(0) \to 1$, the force takes the simple form

$$F_{cl}(d) = -\frac{k_B T}{16d^3\pi}\bar{\alpha}_1\bar{\alpha}_2. \tag{D.13}$$

From this last expression it is transparent that one can still get repulsion in the classical limit when the signs of θ_1 and θ_2 are opposite.
As anticipated in the main text one can analyse the Casimir energy density in the classical

limit, that is, exploring the relative magnitudes of the diagonal and off-diagonal parts of the reflection coefficients. In this case, we assume for simplicity that both topological magnetoelectric polarizabilities have the same magnitude but can have equal or opposite signs, i.e. $\mathrm{sgn}(\theta_1) = \pm\mathrm{sgn}(\theta_2)$. If we introduce these reflexion matrices in expression (7.14) and take the high temperature limit ($l = 0$), after some algebra one arrives to:

$$\frac{E_c^{\pm}(d)}{A} = \frac{k_B T}{4\pi d^2}\int_0^{\infty} k_{\parallel} dk_{\parallel} \log\left[1 - A_{\pm}e^{-2k_{\parallel}} + Be^{-4k_{\parallel}}\right], \tag{D.14}$$

where the $\pm$ corresponds to each of the two cases $\mathrm{sgn}(\theta_1) = \pm\mathrm{sgn}(\theta_2)$ and we have rescaled the integral variables with the distance. The functions $A_{\pm}$ and B are defined as

$$A_{\pm} = \frac{1}{D}(4(\epsilon(0)-1)^2 + (4(\epsilon(0)-1) \pm 8)\bar{\alpha}^2 + 2\bar{\alpha}^4),$$

and $B = \frac{\bar{\alpha}^4}{D}$ where $D \equiv \left(2(\epsilon(0)+1) + \bar{\alpha}^2\right)^2$. Note that these two coefficients depend on the zero frequency dielectric function $\epsilon(0)$ and the absolute value of the topological magnetoelectric polarizability $|\theta|$ as well as its sign in the case of $A_{\pm}$. These functions govern the sign of the integral. Function B plays a secondary role since it is exponentially suppressed. It is clear, that when $\epsilon(0) \to 1$ the integrand takes the form $I = \ln(1-x)$ where x is positive or negative depending on $A_{\pm}$. For A_{-}, i.e. $\mathrm{sgn}(\theta_1) = -\mathrm{sgn}(\theta_2)$ and $\epsilon(0) \to 1$, $x < 0$ so $I > 0$ which makes $E \propto \frac{k_B T}{4\pi d^2}$ and the force is repulsive since a negative (positive) force, or equivalently a positive (negative) slope of $E_c(d)$, corresponds to attraction (repulsion) of the plates.

Indeed, when one neglects the second term inside the logarithm in (D.14) the integral can be expressed in terms of a Polylogarithm

$$\frac{E_c^{\pm}(d)}{A} = -\frac{k_B T}{16\pi d^2}\mathrm{Li}_3(A_{\pm}) \tag{D.15}$$

The function $\mathrm{Li}_3(A_{\pm})$ has the sign of $A_{\pm}$. Therefore, when $A_{\pm} > 0 (< 0)$ we have attraction (repulsion). Using the fact that $\mathrm{Li}_3(x) \sim x + \mathcal{O}(x^2)$ when $x \to 0$ and that $A_{-} \sim -\frac{\bar{\alpha}^2}{2}$ when $\epsilon(0) \to 1$ and to leading order in $\bar{\alpha}^2$ we can readily obtain the Casimir force from (D.15) which gives

$$F_{cl}(d) = \frac{k_B T}{16 d^3 \pi}\bar{\alpha}^2. \tag{D.16}$$

This equation is exactly equation (D.13) when $\bar{\alpha}_1 = -\bar{\alpha}_2 = \bar{\alpha}$. Consistently, both approaches are equivalent and confirm our numerical results, where we found that even at high temperature repulsion can occur. Nevertheless, for more realistic situations where higher values of $\epsilon(0)$ are expected, there is a competition between parameters, which is represented in Fig.7.4. Only high values of θ can compete with large enough $\epsilon(0)$ and thus we expect attraction to occur at high temperatures.

D.3. Fresnel coefficients for topological insulators with uniaxial anisotropy

In this appendix, the Fresnel coefficients for topological insulators with uniaxial anisotropy will be discussed. First, we will briefly review the derivation of the reflection coefficients for an ordinary dielectric - vacuum interface so that the extension to the topological insulator - vacuum interface is more transparent.

Fresnel coefficients for uniaxial material plates

As an illustrative case, before adding the axionic term, we proceed to solve Maxwell's equations for an uniaxial material which will demonstrate the procedure to follow in the next section. We start with an uniaxial material with its optical axis parallel to the plate's normal. The corresponding dielectric permittivity tensor is given by $\epsilon_{ij} = \text{diag}(\epsilon_\perp, \epsilon_\perp, \epsilon_z)$ and, for completeness, the magnetic susceptibility tensor will be included as $\mu_{ij} = \text{diag}(\mu_\perp, \mu_\perp, \mu_z)$. The subindex z indicates that the optical axis is aligned with the z axis, chosen also to be the surface normal. The procedure is to solve Maxwell's equation in vacuum, then inside the uniaxial media, and finally impose boundary conditions to determine the reflection amplitudes. The first step is therefore to solve Maxwell's equations in vacuum by proposing a plane wave solution of the form (see for instance Ref.[259])

$$\begin{aligned} \mathbf{E}_{in} &= \left(A_\perp \mathbf{y} + A_\parallel \frac{c}{\omega}(k_z \mathbf{x} - k_x \mathbf{z})\right) e^{i(k_x x + k_z z - \omega t)}, \\ \mathbf{H}_{in} &= \left(A_\parallel \mathbf{y} - A_\perp \frac{c}{\omega}(k_z \mathbf{x} - k_x \mathbf{z})\right) e^{i(k_x x + k_z z - \omega t)}, \end{aligned}$$

For the incoming wave, and

$$\begin{aligned} \mathbf{E}_{r} &= \left(R_\perp \mathbf{y} - R_\parallel \frac{c}{\omega}(k_z \mathbf{x} + k_x \mathbf{z})\right) e^{i(k_x x - k_z z - \omega t)}, \\ \mathbf{H}_{r} &= \left(R_\parallel \mathbf{y} + R_\perp \frac{c}{\omega}(k_z \mathbf{x} + k_x \mathbf{z})\right) e^{i(k_x x - k_z z - \omega t)}, \end{aligned}$$

for the reflected wave, where we have used that $k_x^{in} = -k_x^{ref}$ with obvious notation. The Cartesian unit vectors are represented by $\mathbf{x}, \mathbf{y}$ and $\mathbf{z}$ and we define $k_x = \frac{\omega}{c}\text{sin}\theta_i$ and $k_z = \frac{\omega}{c}\text{cos}\theta_i$, where θ_i is the angle of incidence. The problem consists in finding the relative amplitudes $A_\perp, A_\parallel$ and $R_\perp, R_\parallel$. Their quotients will define the entries of the reflection matrices (7.4). The second step is to solve Maxwell's equations inside the uniaxial material. Since there is translational invariance along the interface, k_x must be conserved so the transmitted wave can have the form:

$$\mathbf{E}_t = \mathbf{e} e^{i(qz + k_x x - \omega t)}, \quad \mathbf{H}_t = \mathbf{h} e^{i(qz + k_x x - \omega t)}, \tag{D.17}$$

where q is the transverse transmitted momentum to be determined by finding the dispersion relation. From the Maxwell equation $\boldsymbol{\nabla} \times \mathbf{E} = -\frac{1}{c}\frac{\partial \mathbf{B}}{\partial t}$, with $B_i = \mu_{ij} H_j$ one can obtain the

conditions for vectors $\mathbf{e}(z)$ and $\mathbf{h}(z)$ which are

$$h_z = \frac{ck_x}{\omega\mu_z}e_y, \quad h_x = -\frac{cq}{\omega\mu_\perp}e_y, \quad h_y = -\frac{c}{\omega\mu_\perp}\left(k_x e_z - q e_x\right). \tag{D.18}$$

From the Maxwell equation $\boldsymbol{\nabla}\times\mathbf{H} = \frac{1}{c}\frac{\partial\mathbf{D}}{\partial t}$ with $D_i = \epsilon_{ij}E_j$ one obtains

$$e_z = -\frac{ck_x}{\omega\epsilon_z}h_y, \quad e_x = \frac{cq}{\omega\epsilon_\perp}h_y, \quad e_y = \frac{c}{\omega\epsilon_\perp}\left(k_x h_z - q h_x\right). \tag{D.19}$$

From the sets (D.19) and (D.18), after a few steps one can see that if $e_y \neq 0$, $h_x \neq 0$ and $h_y = 0$ $e_x = 0$, q must satisfy $q^2 \equiv q'^2 = \left(\frac{\omega}{c}\right)^2 \mu_\perp\epsilon_\perp - k_x^2\frac{\mu_\perp}{\mu_z}$. This is just the transverse electric mode inside the material. Then, in this case

$$e_y = -\frac{\omega\mu_\perp}{cq'}h_x. \tag{D.20}$$

In a similar fashion if $e_y = 0$, $h_x = 0$ and $h_y \neq 0$ $e_x \neq 0$, q must satisfy $q^2 \equiv q''^2 = \left(\frac{\omega}{c}\right)^2 \mu_\perp\epsilon_\perp - k_x^2\frac{\epsilon_\perp}{\epsilon_z}$, and

$$h_y = \frac{\omega\epsilon_\perp}{cq''}e_x, \tag{D.21}$$

which corresponds to the transverse magnetic mode inside the uniaxial crystal.
It is now time to impose the boundary conditions. As mentioned above, tangential components of $\boldsymbol{E}$ and $\boldsymbol{H}$ must be continuous along the interface, thus

$$\begin{aligned}
(A_\parallel - R_\parallel)\frac{c}{\omega} &= e_x, && \text{(D.22)}\\
(A_\perp + R_\perp) &= e_y, && \text{(D.23)}\\
(A_\parallel + R_\parallel) &= h_y, && \text{(D.24)}\\
(R_\perp - A_\perp)\frac{c}{\omega} &= h_x. && \text{(D.25)}
\end{aligned}$$

The last two equations can be further simplified by using (D.21) and (D.20) to give:

$$\begin{aligned}
(A_\parallel + R_\parallel) &= \frac{\omega\epsilon_\perp}{cq''}e_x = \frac{\omega\epsilon_\perp}{cq''}(A_\parallel - R_\parallel)\frac{c}{\omega},\\
(R_\perp - A_\perp)\frac{c}{\omega} &= -\frac{cq'}{\omega\mu_\perp}e_y = -\frac{cq'}{\omega\mu_\perp}(A_\perp - R_\perp).
\end{aligned}$$

From these it is clear that the transverse electric and the transverse magnetic mode are decoupled, a well known result from ordinary electromagnetic theory [261]. One can now solve for the quotients $R_\perp/A_\perp$ and $R_\parallel/A_\parallel$ and find the ordinary reflection coefficients for a

uniaxial crystal, which in matrix form define the reflection matrix:

$$\begin{pmatrix} E_s^{(r)} \\ E_p^{(r)} \end{pmatrix} = \begin{pmatrix} \dfrac{\mu_\perp k_z - \sqrt{\dfrac{\omega^2}{c^2}\epsilon_\perp\mu_\perp - k_\parallel^2\dfrac{\mu_\perp}{\mu_z}}}{\mu_\perp k_z + \sqrt{\dfrac{\omega^2}{c^2}\epsilon_\perp\mu_\perp - k_\parallel^2\dfrac{\mu_\perp}{\mu_z}}} & 0 \\ 0 & \dfrac{\epsilon_\perp k_z - \sqrt{\dfrac{\omega^2}{c^2}\epsilon_\perp\mu_\perp - k_\parallel^2\dfrac{\epsilon_\perp}{\epsilon_z}}}{\epsilon_\perp k_z + \sqrt{\dfrac{\omega^2}{c^2}\epsilon_\perp\mu_\perp - k_\parallel^2\dfrac{\epsilon_\perp}{\epsilon_z}}} \end{pmatrix} \begin{pmatrix} E_s^{(i)} \\ E_p^{(i)} \end{pmatrix} \quad \text{(D.26)}$$

where $E_{s,p}^{(r)}$ and $E_{s,p}^{(i)}$ are reflected and transmitted electric field respectively for s and p polarizations.

Fresnel coefficients for uniaxial material plates with a topological magnetoelectric response (axion)

It is known from earlier works [77, 78] that topological insulators contain, together with a dielectric response, a topological contribution to the magnetoelectric effect originated in an axion type Lagrangian. The inclusion of this coupling into the reflection coefficients was discussed by [357] for the isotropic case. Their conclusion was that the tangential components of $\boldsymbol{E}$ and $\boldsymbol{H}$ were still conserved, although now $H = \mu^{-1}B + \bar{\alpha}E$ where $\bar{\alpha}$ is the topological magnetoelectric response or axion term and α is the fine structure constant ($\alpha = \frac{e^2}{c\hbar}$). Analogously the inclusion of the new term to the boundary conditions given by (D.22),(D.23),(D.24) and (D.25) is implemented by modifying the last two equations (D.24),(D.25) (which come from the continuity of the tangential component of H) to give:

$$(A_\parallel - R_\parallel)\frac{c}{\omega} = e_x, \quad \text{(D.27)}$$

$$A_\perp + R_\perp = e_y, \quad \text{(D.28)}$$

$$A_\parallel + R_\parallel = h_y + \bar{\alpha}e_y, \quad \text{(D.29)}$$

$$(R_\perp - A_\perp)\frac{c}{\omega} = h_x + \bar{\alpha}e_x, \quad \text{(D.30)}$$

with h_x given by (D.20) and h_y given by (D.21). It is now a matter of algebra to elucidate the reflection coefficients as in the last section. Inevitably, the relations become more messy. The reflection coefficients can be written in matrix form as

$$\frac{1}{\Delta_{an}}\begin{pmatrix} (\mu_\perp k_z - q')(\epsilon_\perp k_z + q'') - q''k_z\mu_\perp\bar{\alpha}^2 & 2\bar{\alpha}q''\mu_\perp k_z \\ 2\bar{\alpha}q''\mu_\perp k_z & (\epsilon_\perp k_z - q'')(\mu_\perp k_z + q') + q''k_z\mu_\perp\bar{\alpha}^2 \end{pmatrix} \quad \text{(D.31)}$$

where $\Delta_{an} = (\mu_\perp k_z + q')(\epsilon_\perp k_z + q'') + q''k_z\mu_\perp\bar{\alpha}^2$, $k_z^2 = \dfrac{\omega^2}{c^2} - k_\parallel^2$, $q'^2 = \dfrac{\omega^2}{c^2}\epsilon_\perp\mu_\perp - k_\parallel^2\dfrac{\mu_\perp}{\mu_z}$, $q''^2 = \dfrac{\omega^2}{c^2}\epsilon_\perp\mu_\perp - k_\parallel^2\dfrac{\epsilon_\perp}{\epsilon_z}$ and $\bar{\alpha} = \alpha\theta/\pi$.

To compute the Casimir energy, one should define these in the imaginary frequency axis and turn all the frequencies to $\omega = i\xi$. Note as well that these reduce to the ordinary anisotropic coefficients presented in the last section when $\bar{\alpha} = 0$. They also reduce to the isotropic reflection coefficients (7.9) when μ and ϵ are isotropic.

E. Finite frequency response of a topological insulator: Technical details

E.1. Calculation of $\Pi_5(p_0, \mu = 0)$

As described in the main text $\Pi_5(p_0, \mu)$ determines the finite frequency response of the topological insulator system. In this appendix we provide details of how to compute it for $\mu = 0$ leaving the $\mu \neq 0$ for the last appendix.

As shown in Ref. [77] the quantized DC magnetoelectric response of topological insulator system can be described as descending from a five dimensional analogue of the quantized integer quantum Hall effect [283]. The work of Refs. [284–286] for finite chemical potential can be understood as arising from the corresponding anomalous quantum Hall effect analogue in five dimensions. Similarly, it is possible to reinterpret the results presented in the main text as descending from a five dimensional finite frequency quantum Hall effect at finite chemical potential. The function $\Pi_5(p, q)$ is generated from the Feynman diagrams shown in Fig. 8.3 (a) and can be regarded as arising from the antisymmetric part of the tensor (8.41)

$$\Pi_5^{\mu\nu\rho}(p,q) = -ie^2 \int \frac{d^5k}{(2\pi)^5} \mathrm{Tr}\left[G_{k-p}\Gamma^\mu G_k \Gamma^\nu G_{k-q}\Gamma^\rho + G_{k+p-q}\Gamma^\nu G_k \Gamma^\mu G_{k-q}\Gamma^\rho\right]. \tag{E.1}$$

The electronic Green's function is a function of a five-momentum vector $k = (k_0, \mathbf{k})$ given by $G(k) = (k_0 - H(\mathbf{k}))^{-1}$. For our model with one massive Dirac fermion in $D = 4+1$ dimensions [77] the low energy propagator is of the form $G(k) = \frac{k_0 + \Gamma^a k_a}{k_0^2 - \mathbf{k}^2}$.

Using that the Γ_a matrices satisfy $\mathrm{Tr}\left[\Gamma_a\Gamma_b\Gamma_c\Gamma_d\Gamma_e\right] = -4\epsilon_{abcde}$ one can isolate in (E.1) the antisymmetric term with five Γ_a matrices to obtain, in terms of the Feynman parameters α, β, γ [301]:

$$\begin{aligned}
\Pi_5^{(a)\mu\nu\rho}(p,q) &= -16ie^2 m\epsilon^{\mu\nu\rho\sigma\tau} p_\sigma q_\tau \int \frac{d^5k}{(2\pi)^5} \int_0^1 d\alpha d\beta d\gamma \; \frac{\delta(1-\alpha-\beta-\gamma)}{\left(k^2 - m^2 + p^2\alpha\beta + q^2\gamma\alpha + (p+q)^2\beta\gamma\right)^3}, \\
&= -\frac{e^2 m}{8\pi^2}\epsilon^{\mu\nu\rho\sigma\tau} p_\sigma q_\tau \int_0^1 d\alpha d\beta d\gamma \; \frac{\delta(1-\alpha-\beta-\gamma)}{\sqrt{m^2 - p^2\alpha\beta - q^2\gamma\alpha - (p+q)^2\beta\gamma}} \\
&\equiv \epsilon^{\mu\nu\rho\sigma\tau} p_\sigma q_\tau \Pi_5(q,p).
\end{aligned}$$

To compute it, it is possible to numerically evaluate the integrals on the Feynman parameters and find $\Pi_5(q, p)$. As shown in the main text, to calculate the finite frequency response to an external time dependent but spatially uniform electric field, only the external frequency

p_0 is kept finite while all the rest are sent to zero. The integrals in Feynman parameters are analytic and give the logarithmic dependence shown in (8.44).

E.2. Finite chemical potential: $\Pi_5(p_0, \mu)$

In this appendix we discuss the details of the computation of the response at finite frequency p_0 and chemical potential μ. The integral to be computed in this case above with the replacement $k_0 \to k_0 + \mu$:

$$\Pi_5(p,q) = -16ie^2m \int \frac{d^5k}{(2\pi)^5} \int_0^1 d\alpha d\beta d\gamma \; \frac{\delta(1-\alpha-\beta-\gamma)}{\left((k_0+\mu)^2 - \mathbf{k}^2 - m^2 + p^2\alpha\beta + q^2\gamma\alpha + (p+q)^2\beta\gamma\right)^3}.$$

Following the arguments in the main text the relevant case is where all external momenta are zero except p_0. The integral in k_0 has two third order poles at $k_0^{\pm}$. The position of the poles in the complex plane is determined by the relative magnitude of m^2, μ, α, p_0 and $\mathbf{k}^2$. When $p_0 \to 0$ and following the procedure in chapter 6, there is a pole which is always has a negative imaginary part, no matter what value of $\mathbf{k}$ it has. The other pole however depending on $\mathbf{k}$ will change semi planes and so for certain values of $\mathbf{k}$ the integral should be split into two. At this point it is possible to identify several cases:
$|\mu| \leq m$: In this case there are always both poles in different semiplanes and the integral is proportional to $\text{sign}(m)$.
$|\mu| \geq m$: In this case it is necessary split the integral on $\mathbf{k}$ into two parts. One from 0 to k^* and the other one from k^* to ∞ where k^* is the value of $\mathbf{k}$ at which the pole changes semiplane, namely $\sqrt{\mu^2 - m^2}$. The first integral gives zero since both poles are on the same side. The second one is

$$\Pi_5(\mu) = 16e^2m \int \frac{dk_0}{2\pi} \int_{k^*}^{\infty} k^3 \frac{dk}{(2\pi)^4} 2\pi^2 \; \frac{1}{\left((k_0+\mu)^2 - k^2 - m^2\right)^3}. \tag{E.2}$$

We calculate first the k_0 integral with the residue theorem. It is a third order pole so closing the contour from above and restoring $\hbar$ we find

$$\Pi_5(\mu) = \frac{1}{2}\frac{1}{8\pi^2}\left[-\frac{3m}{|\mu|} + \frac{m^3}{|\mu|^3}\right]\frac{e^2}{\hbar}. \tag{E.3}$$

Since we need $\sigma(\mu) \equiv 2\pi\Pi_5(\mu)$ we finally obtain (9.35)

$$\sigma(\mu) = 2\pi\Pi_5(\mu) = \frac{1}{4}\left[-\frac{3m}{|\mu|} + \frac{m^3}{|\mu|^3}\right]\frac{e^2}{h}, \tag{E.4}$$

which reduces to the familiar $\frac{1}{2}\frac{e^2}{h}\text{sign}(m)$ contribution of a $2+1$ massive Dirac fermion when $m = \mu$, and has an extra term $\dfrac{m^3}{|\mu|^3}$ compared to the $D = 2+1$ case (see chapter 6).
For finite p_0 and $|\mu| \geq m$ one can generalize the same arguments and find that for $p_0 << 2m$ we have

$$\sigma(p_0 < 2m, \mu) = \frac{1}{4}\left[-\frac{3m}{|\mu|} + \frac{m^3}{|\mu|^3} - \frac{mp_0^2}{6|\mu|^3}\right]\frac{e^2}{h}. \tag{E.5}$$

F. Matrix definitions for the theory of Weyl semi-metals

F.1. Matrix definitions

In this appendix, all the definitions for the matrices used in the main text are reviewed. The Hamiltonian matrices are defined to be:

$$\begin{aligned}
\alpha_1 &= \tau_z \otimes \sigma_y \\
\alpha_2 &= -\tau_z \otimes \sigma_x \\
\alpha_3 &= \tau_y \otimes 1_\sigma \\
\beta &= \tau_x \otimes 1_\sigma \\
\alpha_5 &= -\tau_z \otimes \sigma_z = \beta\alpha_1\alpha_2\alpha_3.
\end{aligned}$$

To construct a low energy effective field theory action the following dictionary can be used, following the usual convention for the γ matrices.

$$\begin{aligned}
H_0(\mathbf{k}) &= \psi^\dagger_{\mathbf{k}}\alpha^i k_i \psi_{\mathbf{k}} = \bar{\psi}_{\mathbf{k}}\beta\alpha^i k_i \psi_{\mathbf{k}} \equiv \bar{\psi}_{\mathbf{k}}\gamma^i k_i \psi_{\mathbf{k}} \\
H_m(\mathbf{k}) &= m\psi^\dagger_{\mathbf{k}}\beta\psi_{\mathbf{k}} \equiv m\bar{\psi}_{\mathbf{k}}\psi_{\mathbf{k}} \\
H_{m_{1c}}(\mathbf{k}) &= m_{1c}\psi^\dagger_{\mathbf{k}} 1_\tau \otimes \sigma_z \psi_{\mathbf{k}} \\
&= m_{1c}\psi^\dagger_{\mathbf{k}} i\beta\alpha_3\alpha_5\psi_{\mathbf{k}} \equiv b_3\bar{\psi}_{\mathbf{k}}\gamma_3\gamma_5\psi_{\mathbf{k}} \\
H_\lambda(\mathbf{k}) &= \lambda\psi^\dagger_{\mathbf{k}}\tau_y \otimes \sigma_z \psi_{\mathbf{k}} \\
&= -\lambda\psi^\dagger_{\mathbf{k}} i\beta\alpha_5\psi_{\mathbf{k}} \equiv -b_0\bar{\psi}_{\mathbf{k}}\gamma_0\gamma_5\psi_{\mathbf{k}}
\end{aligned}$$

which define $\gamma_i = \beta\alpha_i$, $\gamma_0 = \beta$ and $\gamma_5 = -i\beta\alpha_5$, $b_3 = m_{c1}$ and $b_0 = \lambda$.

Bibliography

[1] Y. Nambu. *Quarks* (World Scientific Pub., 1985). (cited on pages vii and 41)

[2] A. Zee. *Quantum Field Theory in a Nutshell* (Princeton University press, 2003). (cited on pages 1, 18, and 100)

[3] P. A. M. Dirac. *The Quantum Theory of the Electron*. Proceedings of the Royal Society of London. Series A **117**, 610 (1928). (cited on p. 1)

[4] A. A. Abrikosov and S. D. Beneslavskii. *Possible existence of substances intermediate between metals and dielectrics*. Zh. Eksp. Teor. Fiz. **59**, 1280 (1971). (cited on p. 1)

[5] D. H. Kim, P. A. Lee, and X.-G. Wen. *Massless Dirac fermions, gauge Fields, and underdoped Cuprates*. Phys. Rev. Lett. **79**, 2109 (1997). (cited on p. 1)

[6] A. W. W. Ludwig, M. P. A. Fisher, R. Shankar, and G. Grinstein. *Integer quantum Hall transition: An alternative approach and exact results*. Phys. Rev. B **50**, 7526 (1994). (cited on pages 1 and 14)

[7] A. H. C. Neto, F. Guinea, N. M. R. Peres, K. S. Novoselov, and A. K. Geim. *The electronic properties of graphene*. Rev. Mod. Phys. **81**, 109 (2009). (cited on pages 1, 2, 3, 4, 5, 65, 71, 119, 131, and 183)

[8] M. Z. Hasan and C. L. Kane. *Colloquium: Topological insulators*. Rev. Mod. Phys. **82**, 3045 (2010). (cited on pages 1, 10, 11, 117, 139, 159, 175, and 185)

[9] X.-L. Qi and S.-C. Zhang. *Topological insulators and superconductors*. Rev. Mod. Phys. **83**, 1057 (2011). (cited on pages 1, 10, 11, 92, 117, 159, and 185)

[10] K. S. Novoselov, A. K. Geim, S. V. Morozov, D. Jiang, Y. Zhang, S. V. Dubonos, I. V. Gregorieva, and A. A. Firsov. *Electric Field Effect in Atomically Thin Carbon Films*. Science **306**, 666 (2004). (cited on pages 2, 5, and 52)

[11] N. M. R. Peres. *Colloquium : The transport properties of graphene: An introduction*. Rev. Mod. Phys. **82**, 2673 (2010). (cited on pages 2, 4, and 62)

[12] M. Vozmediano, M. Katsnelson, and F. Guinea. *Gauge fields in graphene*. Physics Reports **496**, 109 (2010). (cited on p. 2)

[13] S. Das Sarma, S. Adam, E. H. Hwang, and E. Rossi. *Electronic transport in two-dimensional graphene*. Rev. Mod. Phys. **83**, 407 (2011). (cited on pages 2 and 62)

[14] D. R. Cooper, B. D'Anjou, N. Ghattamaneni, B. Harack, M. Hilke, A. Horth, N. Majlis, M. Massicotte, L. Vandsburger, E. Whiteway, and V. Yu. *Experimental review of graphene*. ArXiv e-prints (2011). (cited on pages 2 and 4)

[15] V. N. Kotov, B. Uchoa, V. M. Pereira, F. Guinea, and A. H. Castro Neto. *Electron-Electron Interactions in Graphene: Current Status and Perspectives*. Rev. Mod. Phys. **84**, 1067 (2012). (cited on pages 2, 23, 29, 51, 60, 62, and 66)

[16] A. Cortijo, F. Guinea, and M. A. H. Vozmediano. *Geometrical and topological aspects of graphene and related materials*. Journal of Physics A: Mathematical and Theoretical **45**, 383001 (2012). (cited on p. 2)

[17] P. R. Wallace. *The Band Theory of Graphite*. Phys. Rev. **71**, 622 (1947). (cited on p. 3)

[18] J. C. Slonczewski and P. R. Weiss. *Band Structure of Graphite*. Phys. Rev. **109**, 272 (1958). (cited on pages 4 and 52)

[19] R. Winkler and U. Zulicke. *Invariant expansion for the trigonal band structure of graphene*. Phys. Rev. B **82**, 245313 (2010). (cited on pages 4 and 52)

[20] T. L. Linnik. *Effective Hamiltonian of strained graphene*. Journal of Physics: Condensed Matter **24**, 205302 (2012). (cited on pages 4 and 52)

[21] K. S. Novoselov, A. K. Geim, S. V. Morozov, D. Jiang, M. I. Katsnelson, I. V. Grigorieva, S. V. Dubonos, and A. A. Firsov. *Two-dimensional gas of massless Dirac fermions in graphene*. Nature **438**, 197 (2005). (cited on pages 4, 52, 65, and 72)

[22] A. K. Geim and K. S. Novoselov. *Two-dimensional gas of massless Dirac fermions in graphene*. Nature Mat. **6**, 183 (2007). (cited on pages 4 and 28)

[23] A. Bostwick, T. Ohta, T. Seyller, K. Horn, and E. Rotenberg. *Quasiparticle dynamics in graphene*. Nature Physics **3**, 36 (2007). (cited on pages 4, 5, 31, 32, and 64)

[24] J. L. Mañes, F. Guinea, and M. A. H. Vozmediano. *Existence and topological stability of Fermi points in multilayered graphene*. Physical Review B **75**, 155424 (2007). (cited on pages 4, 83, and 119)

[25] I. F. Herbut. *Explanation for the isotropy of the Dirac cone in graphene*. Phys. Rev. B **79**, 193405 (2009). (cited on p. 4)

[26] J. González, F. Guinea, and M. A. H. Vozmediano. *Non-Fermi Liquid behavior of electrons in the half-filled honeycomb lattice. A renormalization group approach*. Nucl. Phys. B **424 [FS]**, 595 (1994). (cited on pages 5, 28, 32, 52, 57, 58, 60, 61, 67, and 71)

[27] N. W. Ashcroft and N. D. Mermin. *Solid state physics* (Saunders College, 1976). (cited on pages 5 and 75)

[28] E. Fradkin. *Field Theories of Condensed Matter System* (Perseus Books, 1997). (cited on pages 5, 75, 76, and 117)

[29] E. McCann and V. I. Falko. *Landau-Level Degeneracy and Quantum Hall Effect in a Graphite Bilayer*. Phys. Rev. Lett. **96**, 086805 (2006). (cited on pages 5 and 6)

[30] E. McCann. *Asymmetry gap in the electronic band structure of bilayer graphene*. Phys. Rev. B **74**, 161403 (2006). (cited on pages 5 and 6)

[31] E. V. Castro, K. S. Novoselov, S. V. Morozov, N. M. R. Peres, J. M. B. L. dos Santos, J. Nilsson, F. Guinea, A. K. Geim, and A. H. C. Neto. *Biased Bilayer Graphene: Semiconductor with a Gap Tunable by the Electric Field Effect*. Phys. Rev. Lett. **99**, 216802 (2007). (cited on pages 5, 6, and 131)

[32] J. Nilsson, A. H. Castro Neto, F. Guinea, and N. M. R. Peres. *Electronic properties of bilayer and multilayer graphene*. Phys. Rev. B **78**, 045405 (2008). (cited on pages 5 and 6)

[33] L. M. Zhang, Z. Q. Li, D. N. Basov, M. M. Fogler, Z. Hao, and M. C. Martin. *Determination of the electronic structure of bilayer graphene from infrared spectroscopy*. Phys. Rev. B **78**, 235408 (2008). (cited on p. 6)

[34] T. Ohta, A. Bostwick, T. Seyller, K. Horn, and E. Rotenberg. *Controlling the Electronic Structure of Bilayer Graphene*. Science **313**, 951 (2006). (cited on pages 6 and 7)

[35] A. S. Mayorov, D. C. Elias, M. Mucha-Kruczynski, R. V. Gorbachev, T. Tudorovskiy, A. Zhukov, S. V. Morozov, M. I. Katsnelson, V. I. Fal'ko, A. K. Geim, and K. S. Novoselov. *Interaction-Driven Spectrum Reconstruction in Bilayer Graphene*. Science **333**, 860 (2011). (cited on p. 6)

[36] J. Velasco, L. Jing, W. Bao, Y. Lee, P. Kratz, V. Aji, M. Bockrath, C. N. Lau, C. Varma, R. Stillwell, D. Smirnov, F. Zhang, J. Jung, and A. H. MacDonald. *Transport spectroscopy of symmetry-broken insulating states in bilayer graphene*. Nature Nanotechnology **7**, 156 (2012). (cited on p. 6)

[37] J. Martin, B. E. Feldman, R. T. Weitz, M. T. Allen, and A. Yacoby. *Local Compressibility Measurements of Correlated States in Suspended Bilayer Graphene*. Phys. Rev. Lett. **105**, 256806 (2010). (cited on p. 6)

[38] O. Vafek and K. Yang. *Many-body instability of Coulomb interacting bilayer graphene: Renormalization group approach*. Phys. Rev. B **81**, 041401 (2010). (cited on p. 6)

[39] F. Zhang, H. Min, M. Polini, and A. H. MacDonald. *Spontaneous inversion symmetry breaking in graphene bilayers*. Phys. Rev. B **81**, 041402 (2010). (cited on p. 6)

[40] Y. Lemonik, I. Aleiner, and V. I. Fal'ko. *Competing nematic, antiferromagnetic, and spin-flux orders in the ground state of bilayer graphene*. Phys. Rev. B **85**, 245451 (2012). (cited on p. 6)

[41] L. D. Landau and E. M. Lifshitz. *Statistical Physics*, volume 5, chapter VIII (John Wiley and Sons, 1987). (cited on pages 7, 87, 211, and 212)

[42] H. Bruus and K. Flensberg. *Many-Body Quantum Theory in Condesed Matter Physics* (Oxford Graduate Texts, 2004). (cited on pages 7, 23, 25, 26, 32, 41, 42, and 74)

[43] W. N. Cottingham and D. A. Greenwood. *An introduction to the standard model of particle physics* (Cambridge University Press, 2007). (cited on pages 7 and 177)

[44] C. Coll. *Observation of a new boson at a mass of 125 GeV with the CMS experiment at the LHC*. Phys. Lett. B **716**, 30 (2012). (cited on p. 7)

[45] C. Coll. *Observation of a new particle in the search for the Standard Model Higgs boson with the ATLAS detector at the LHC*. Phys. Lett. B **716**, 1 (2012). (cited on p. 7)

[46] K. v. Klitzing, G. Dorda, and M. Pepper. *New Method for High-Accuracy Determination of the Fine-Structure Constant Based on Quantized Hall Resistance*. Phys. Rev. Lett. **45**, 494 (1980). (cited on pages 7 and 93)

[47] D. C. Tsui, H. L. Stormer, and A. C. Gossard. *Two-Dimensional Magnetotransport in the Extreme Quantum Limit*. Phys. Rev. Lett. **48**, 1559 (1982). (cited on pages 7 and 93)

[48] R. E. Prange and S. M. Girvin. *The Quantum Hall Effect* (Springer, New York, 1987). (cited on pages 7 and 93)

[49] M. Nakahara. *Geometry, topology, and physics* (CRC Press, 2003). (cited on pages 8 and 18)

[50] D. J. Thouless, M. Kohmoto, M. P. Nightingale, and M. den Nijs. *Quantized Hall Conductance in a Two-Dimensional Periodic Potential*. Phys. Rev. Lett. **49**, 405 (1982). (cited on pages 8, 10, 94, 118, 121, and 122)

[51] Q. Niu, D. J. Thouless, and Y. S. Wu. *Quantized Hall conductivity as a topological invariant*. Phys. Rev. B **31**, 3372 (1985). (cited on pages 8, 10, 94, and 101)

[52] J. E. Avron, R. Seiler, and B. Simon. *Homotopy and Quantization in Condensed Matter Physics*. Phys. Rev. Lett. **51**, 51 (1983). (cited on pages 8 and 10)

[53] S. Ryu, A. P. Schnyder, A. Furusaki, and A. W. W. Ludwig. *Topological insulators and superconductors: tenfold way and dimensional hierarchy*. New Journal of Physics **12**, 065010 (2010). (cited on p. 8)

[54] N. Nagaosa, J. Sinova, S. Onoda, A. H. MacDonald, and N. P. Ong. *Anomalous Hall effect*. Rev. Mod. Phys. **82**, 1539 (2010). (cited on pages 9 and 73)

[55] F. D. M. Haldane. *Berry Curvature on the Fermi Surface: Anomalous Hall Effect as a Topological Fermi-Liquid Property*. Phys. Rev. Lett. **93**, 206602 (2004). (cited on pages 9, 72, 84, 86, 91, and 125)

[56] M. V. Berry. *Quantal Phase Factors Accompanying Adiabatic Changes*. Royal Society of London Proceedings Series A **392**, 45 (1984). (cited on p. 9)

[57] D. Xiao, M.-C. Chang, and Q. Niu. *Berry phase effects on electronic properties*. Rev. Mod. Phys. **82**, 1959 (2010). (cited on pages 9 and 84)

[58] S. Murakami, N. Nagaosa, and S.-C. Zhang. *Dissipationless Quantum Spin Current at Room Temperature*. Science **301**, 1348 (2003). (cited on p. 10)

[59] M. Onoda and N. Nagaosa. *Spin Current and Accumulation Generated by the Spin Hall Insulator*. Phys. Rev. Lett. **95**, 106601 (2005). (cited on p. 10)

[60] C. L. Kane and E. J. Mele. *Quantum Spin Hall Effect in Graphene*. Phys. Rev. Lett. **95**, 226801 (2005). (cited on pages 10, 117, 118, 119, 120, 122, 124, 126, 127, 131, 134, 174, and 222)

[61] C. Kane and E. J. Mele. *Z2 topological order and the quantum spin Hall effect*. Phys. Rev. Lett. **95**, 146802 (2005). (cited on pages 10, 11, 12, 13, 117, 118, 122, 125, and 130)

[62] X.-L. Qi, Y.-S. Wu, and S.-C. Zhang. *Topological quantization of the spin Hall effect in two-dimensional paramagnetic semiconductors*. Phys. Rev. B **74**, 085308 (2006). (cited on p. 10)

[63] B. A. Bernevig and S.-C. Zhang. *Quantum Spin Hall Effect*. Phys. Rev. Lett. **96**, 106802 (2006). (cited on pages 10, 11, and 122)

[64] C. Kane and E. J. Mele. *Quantum spin Hall effect in graphene*. Phys. Rev. Lett. **95**, 226801 (2005). (cited on pages 10, 11, 12, and 13)

[65] G. W. Semenoff. *Condensed-Matter Simulation of a Three-Dimensional Anomaly*. Phys. Rev. Lett. **53**, 2449 (1984). (cited on pages 11, 72, 124, and 190)

[66] F. D. M. Haldane. *Model for a Quantum Hall Effect without Landau Levels: Condensed-Matter Realization of the "Parity Anomaly"*. Phys. Rev. Lett. **61**, 2015 (1988). (cited on pages 11, 72, 93, 118, 120, and 126)

[67] B. A. Bernevig, T. L. Hughes, and S. C. Zhang. *Quantum spin Hall effect and topological phase transition in HgTe quantum wells*. Science **314**, 1757 (2006). (cited on pages 11, 12, and 118)

[68] B. M. Askerov. *Electron Transport Phenomena in Semiconductors* (World Scientific Publishing, 1985). (cited on p. 11)

[69] M. König, S. Wiedmann, C. Brüne, A. Roth, H. Buhmann, L. W. Molenkamp, X.-L. Qi, and S.-C. Zhang. *Quantum Spin Hall Insulator State in HgTe Quantum Wells*. Science **318**, 766 (2007). (cited on pages 11, 13, and 118)

[70] G. E. Volovik. *The universe in a helium droplet* (Clarendon Press, Oxford, 2003). (cited on pages 12, 124, 178, and 183)

[71] H. Nielsen and M. Ninomiya. *Absence of neutrinos on a lattice I. Proof by homotopy theory*. Nucl. Phys. B **185**, 20 (1981). (cited on pages 12 and 52)

[72] H. Nielsen and M. Ninomiya. *Absence of neutrinos on a lattice II. Intuitive topological proof*. Nucl. Phys. B **193**, 173 (1981). (cited on pages 12 and 52)

[73] H. Ochoa, A. H. Castro Neto, V. I. Fal'ko, and F. Guinea. *Spin-orbit coupling assisted by flexural phonons in graphene*. Phys. Rev. B **86**, 245411 (2012). (cited on pages 12 and 120)

[74] L. Fu, C. Kane, and E. J. Mele. *Topological insulators in three dimensions*. Phys. Rev. Lett. **98**, 106803 (2007). (cited on pages 13 and 15)

[75] M. E. Peskin and D. V. Schroeder. *An introduction to quantum field theory* (Westview Press, 1995). (cited on pages 13, 14, 42, 43, 45, 47, 48, 50, 57, 61, 121, 162, 180, and 183)

[76] S. Weinberg. *The Quantum Theory of Fields Vol. 1* (Cambridge University Press, 2005). (cited on pages 14, 45, and 46)

[77] X.-L. Qi, T. L. Hughes, and S.-C. Zhang. *Topological field theory of time-reversal invariant insulators*. Phys. Rev. B **78**, 195424 (2008). (cited on pages 14, 15, 17, 139, 142, 159, 160, 161, 162, 167, 170, 173, 176, 192, 234, and 237)

[78] A. M. Essin, J. E. Moore, and D. Vanderbilt. *Magnetoelectric Polarizability and Axion Electrodynamics in Crystalline Insulators*. Phys. Rev. Lett **102**, 146805 (2009). (cited on pages 14, 139, 142, 159, and 234)

[79] R. Jackiw and C. Rebbi. *Solitons with fermion number one-half*. Phys. Rev. D **13**, 3398 (1976). (cited on pages 14, 160, and 164)

[80] D. Hsieh and et al. *A topological Dirac insulator in a quantum spin Hall phase*. Nature **452**, 970 (2008). (cited on p. 15)

[81] H. Zhang and et al. *Topological insulators in Bi2Se3, Bi2Te3 and Sb2Te3 with a single Dirac cone on the surface*. Nature Phys. **5**, 438 (2009). (cited on pages 15 and 16)

[82] Y. Xia and et al. *Observation of a large-gap topological-insulator class with a single Dirac cone on the surface*. Nature Phys. **5**, 398 (2009). (cited on pages 15, 16, 151, and 168)

[83] Y. L. Chen and et al. *Experimental realization of a three-dimensional topological insulator, Bi2Te3*. Science **325**, 178 (2009). (cited on pages 15 and 151)

[84] W. Feng and Y. Yao. *Three-dimensional topological insulators: A review on host materials*. Science China Physics, Mechanics and Astronomy **55**, 2199 (2012). (cited on pages 15 and 16)

[85] K. Fujikawa. *Path integral for gauge theories with fermions*. Phys. Rev. D **21**, 2848 (1980). (cited on pages 16 and 182)

[86] F. Wilczek. *Two applications of axion electrodynamics*. Phys. Rev. Lett. **58**, 1799 (1987). (cited on pages 17 and 192)

[87] X.-L. Qi, R. Li, J. Zang, and S.-C. Zhang. *Inducing a Magnetic Monopole with Topological Surface States*. Science **323**, 1184 (2009). (cited on pages 17 and 193)

[88] Y. L. Chen, J.-H. Chu, J. G. Analytis, Z. K. Liu, K. Igarashi, H.-H. Kuo, X. L. Qi, S. K. Mo, R. G. Moore, D. H. Lu, M. Hashimoto, T. Sasagawa, S. C. Zhang, I. R. Fisher, Z. Hussain, and Z. X. Shen. *Massive Dirac fermion on the surface of a magnetically doped topological insulator*. Science **329**, 659 (2010). (cited on pages 18, 142, 144, 147, 151, and 188)

[89] S.-Y. Xu, M. Neupane, C. Liu, D. Zhang, A. Richardella, L. A. Wray, N. Alidoust, M. Leandersson, T. Balasubramanian, J. Sánchez-Barriga, O. Rader, G. Landolt, B. Slomski, J. H. Dil, J. Osterwalder, T.-R. Chang, H.-T. Jeng, H. Lin, A. Bansil, N. Samarth, and M. Z. Hasan. *Hedgehog Spin-texture and Berry's Phase tuning in a Magnetic Topological Insulator*. arXiv:1212.3382 (2012). (cited on pages 18 and 142)

[90] L. Oroszany and A. Cortijo. *Gap generation in topological insulator surface states by nonferromagnetic magnets*. Phys. Rev. B **86**, 195427 (2012). (cited on pages 18, 142, and 158)

[91] X.-G. Wen. *Quantum Field Theory of Many-body Systems* (Oxford University Press, 2007). (cited on pages 18, 94, 99, 100, and 102)

[92] S. L. Boersma. *A maritime analogy of the Casimir effect*. Am. J. Phys. **64**, 539 (1996). (cited on pages 18 and 137)

[93] A. Abanov and P. Wiegmann. *Theta-terms in nonlinear sigma-models*. Nucl. Phys. B **570**, 685 (2000). (cited on pages 18 and 162)

[94] A. A. Abrikosov, L. P. Gorkov, and I. E. Dzyaloshinski. *Methods of quantum field theory in statistical physics* (Dover, 1975). (cited on pages 23 and 24)

[95] G. Giuliani and G. Vignale. *Quantum Theory of the Electron Liquid* (Cambirdge Univ. Press, 2005). (cited on pages 23 and 32)

[96] G. D. Mahan. *Many-Particle Physics* (Plenum Press, New York, 1990). (cited on pages 23 and 27)

[97] D. Pines and P. Nozières. *The Theory of Quantum Liquids* (Adv. Book Classics, 1966). (cited on pages 24 and 32)

[98] T. Giamarchi. *Quantum Physics in One Dimension* (Clarendon Press, 2003). (cited on p. 24)

[99] C. Varma, P. Littlewood, S. Schmitt-Rink, E. Abrahams, and A. Ruckenstein. *Phenomenology of the normal state of Cu-O High-Temperature superconductors*. Phys. Rev. B **63**, 1996 (1989). (cited on pages 24, 33, 35, 40, and 206)

[100] C. Varma, Z. Nussinov, and V. W. Saarloos. *Singular or non-Fermi Liquids*. Phys. Reports **361**, 0370 (2002). (cited on pages 24, 32, and 40)

[101] D. Baeriswyl and L. Degiorg. *Strong interactions in low dimensions* (Springer, 2005). (cited on pages 24, 25, and 27)

[102] N. M. R. Peres. *Colloquium : The transport properties of graphene: An introduction*. Rev. Mod. Phys. **82**, 2673 (2010). (cited on p. 28)

[103] A. K. Geim and K. S. Novoselov. *The rise of graphene*. Nature Materials **6**, 183 (2007). (cited on p. 28)

[104] Y.-W. Tan, Y. Zhang, K. Bolotin, Y. Zhao, S. Adam, E. H. Hwang, S. Das Sarma, H. L. Stormer, and P. Kim. *Measurement of Scattering Rate and Minimum Conductivity in Graphene*. Phys. Rev. Lett. **99**, 246803 (2007). (cited on p. 28)

[105] A. C. Ferrari, J. C. Meyer, V. Scardaci, C. Casiraghi, M. Lazzeri, F. Mauri, S. Piscanec, D. Jiang, K. S. Novoselov, S. Roth, and A. K. Geim. *Raman Spectrum of Graphene and Graphene Layers*. Phys. Rev. Lett. **97**, 187401 (2006). (cited on p. 29)

[106] B. Shastry and B. Shraiman. *Theory of Raman scattering in Mott-Hubbard systems*. Phys. Rev. Lett. **65**, 1068 (1990). (cited on p. 29)

[107] T. P. Devereaux and R. Hackl. *Inelastic light scattering from correlated electrons*. Rev. Mod. Phys. **79**, 175 (2007). (cited on pages 29 and 30)

[108] O. Kashuba and V. I. Fal'ko. *Signature of electronic excitations in the Raman spectrum of graphene*. Phys. Rev. B **80**, 241404 (2009). (cited on p. 29)

[109] A. A. Kordyuk, S. V. Borisenko, A. Koitzsch, J. F. andM. Knupfer, and H. Berger. *Bare electron dispersion from experiment: Self-consistent self-energy analysis of photoemission data*. Phys. Rev. B **71**, 214513 (2005). (cited on p. 30)

[110] A. Kaminski and H. M. Fretwell. *Bare electron dispersion from experiment: Self-consistent self-energy analysis of photoemission data*. New Journal of Physics **6**, 98 (2004). (cited on p. 30)

[111] A. S. Mayorov, D. C. Elias, I. S. Mukhin, S. V. Morozov, L. A. Ponomarenko, K. S. Novoselov, A. K. Geim, and R. V. Gorbachev. *How Close Can One Approach the Dirac Point in Graphene Experimentally?* Nano Letters **12**, 4629 (2012). (cited on pages 31 and 66)

[112] S. D. Sarma, E. H. Hwang, and W.-K. Tse. *Many-body interaction effects in doped and undoped graphene: Fermi liquid versus non-Fermi liquid*. Phys. Rev. B **75**, 121406 (2007). (cited on p. 31)

[113] J. González, F. Guinea, and M. A. H. Vozmediano. *Unconventional quasiparticle lifetime in graphite*. Phys. Rev. Lett. **77**, 3589 (1996). (cited on pages 32 and 52)

[114] G. Li, E. Henriksen, Z. Jiang, Z. Hao, M. Martin, P. Kim, H. L. Stormer, and D. N. Basov. *Dirac charge dynamics in graphene by infrared spectroscopy*. Nature Phys. **4**, 532 (2008). (cited on pages 33, 40, and 65)

[115] N. M. R. Peres, T. Stauber, and A. H. C. Neto. *The infrared conductivity of graphene on top of silicon oxide*. Europhys. Lett. **84**, 38002 (2008). (cited on pages 35 and 40)

[116] T. Stauber, N. M. R. Peres, and A. H. Castro Neto. *Conductivity of suspended and non-suspended graphene at finite gate voltage*. Phys. Rev. B **78**, 085418 (2008). (cited on pages 35 and 40)

[117] K. F. Mak, M. Y. Sfeir, Y. Wu, C. H. Lui, J. A. Misewich, and T. F. Heinz. *Measurement of the Optical Conductivity of Graphene*. Phys. Rev. Lett. **101**, 196405 (2008). (cited on pages 35 and 40)

[118] N. M. R. Peres, R. M. Ribeiro, and A. H. Castro Neto. *Excitonic Effects in the Optical Conductivity of Gated Graphene*. Phys. Rev. Lett. **105**, 055501 (2010). (cited on p. 35)

[119] D. N. Basov and T. Timusk. *Electrodynamics of High-Tc superconductors*. Rev. Mod. Phys. **77**, 721 (2005). (cited on pages 35 and 40)

[120] G. Li, A. Luican, and E. Y. Andrei. *Scanning tunneling spectroscopy of graphene on graphite*. Phys. Rev. Lett. **102**, 176804 (2009). (cited on pages 35 and 36)

[121] K. R. Knox, A. Locatelli, M. B. Yilmaz, D. Cvetko, T. O. Mente, M. A. Niño, P. Kim, A. Morgante, and R. M. Osgood. *Making angle-resolved photoemission measurements on corrugated monolayer crystals: Suspended exfoliated single-crystal graphene*. Phys. Rev. B **84**, 115401 (2011). (cited on p. 36)

[122] T. Stauber, N. M. R. Peres, and A. H. C. Neto. *Conductivity of suspended and non-suspended graphene at finite gate voltage*. Phys. Rev. B **78**, 085418 (2008). (cited on p. 37)

[123] L. Ren, Q. Zhang, J. Yao, Z. Sun, R. Kaneko, Z. Yan, S. Nanot, Z. Jin, I. Kawayama, M. Tonouchi, J. M. Tour, and J. Kono. *Terahertz and Infrared Spectroscopy of Gated Large-Area Graphene*. Nano Letters **12**, 3711 (2012). (cited on p. 40)

[124] C.-F. Chen, C.-H. Park, B. W. Boudouris, J. Horng, B. Geng, C. Girit, A. Zettl, M. F. Crommie, R. A. Segalman, S. G. Louie, and F. Wang. *Controlling inelastic light scattering quantum pathways in graphene*. Nature **471**, 617 (2011). (cited on p. 40)

[125] A. A. Abrikosov, L. P. Gorkov, and I. E. Dzialoshinski. *Methods of quantum field theory in statistical physics* (Courier Dover Publications, 1975). (cited on pages 41 and 42)

[126] P. Ramond. *Field theory* (Perseus Books, 1997). (cited on pages 41, 42, 43, 45, 179, and 219)

[127] A. Altland and B. Simons. *Condensed matter field theory* (Cambridge University Press, 2006). (cited on pages 41 and 42)

[128] J. C. Collins. *Renormalization* (Cambridge University Press, 1985). (cited on pages 42, 43, 45, 48, 51, and 60)

[129] D. J. Amit and V. Martin-Mayor. *Field Theory, the Renormalization Group and Critical Phenomena* (World Scientific Publishing, 2005). (cited on pages 42, 43, and 45)

[130] R. Shankar. *Renormalization-group approach to interacting fermions*. Reviews of Modern Physics **66**, 129 (1994). (cited on pages 42 and 45)

[131] H. Georgi. *Effective field theory*. Annu. Rev. Nucl. Part. Sci. **43**, 209 (1993). (cited on pages 42 and 45)

[132] J. Polchinski. *Effective Field Theory and the Fermi Surface*. hep-th/9210046 (1992). (cited on p. 46)

[133] S. Weinberg. *New Approach to the Renormalization Group*. Phys. Rev. D **8**, 3497 (1973). (cited on p. 50)

[134] G. 't Hooft. *Dimensional regularization and the renormalization group*. Nucl. Phys. B **61**, 455 (1973). (cited on p. 50)

[135] M. L. Bellac. *Quantum and statistical field theory* (Oxford University Press, 1991). (cited on p. 51)

[136] D. Hanneke, S. Fogwell, and G. Gabrielse. *New Measurement of the Electron Magnetic Moment and the Fine Structure Constant*. Phys. Rev. Lett. **100**, 120801 (2008). (cited on p. 51)

[137] T. Aoyama, M. Hayakawa, T. Kinoshita, and M. Nio. *Revised Value of the Eighth-Order Contribution to the Electron* $g-2$. Phys. Rev. Lett. **99**, 110406 (2007). (cited on p. 51)

[138] V. Gerginov, K. Calkins, C. E. Tanner, J. J. McFerran, S. Diddams, A. Bartels, and L. Hollberg. *Optical frequency measurements of transitions in 133Cs and their impact on the fine-structure constant*. Phys. Rev. A **73**, 032504 (2006). (cited on p. 51)

[139] I. F. Herbut. *Interactions and Phase Transitions on Graphene's Honeycomb Lattice*. Phys. Rev. Lett. **97**, 146401 (2006). (cited on pages 52 and 60)

[140] E. V. Gorbar, V. P. Gusynin, and V. A. Miransky. *Dynamical chiral symmetry breaking on a brane in reduced QED*. Phys. Rev. D **64**, 105028 (2001). (cited on pages 52 and 67)

[141] E. Mishchenko. *Effect of electron-electron interactions on the conductivity of clean graphene*. Phys. Rev. Lett. **98**, 216801 (2007). (cited on pages 58, 60, 61, 62, 63, and 182)

[142] J. González. *Higher-order renormalization of graphene many-body theory*. Journal of High Energy Physics **2012**, 1 (2012). (cited on p. 60)

[143] J. González, F. Guinea, and M. A. H. Vozmediano. *Marginal Fermi liquid behavior from two-dimensional Coulomb interaction*. Phys. Rev. B **59**, R2474 (1999). (cited on pages 61 and 62)

[144] *The influence of morphology and long range interactions on the electronic properties of graphene*. Ph. D. Thesis (2010). (cited on p. 61)

[145] O. Vafek and M. J. Case. *Renormalization group approach to two-dimensional Coulomb interacting Dirac fermions with random gauge potential*. Physical Review Letters **77**, 033410 (2008). (cited on p. 61)

[146] D. E. Sheehy and J. Schmalian. *Quantum Critical Scaling in Graphene*. Phys. Rev. Lett. **99**, 226803 (2007). (cited on pages 62, 63, and 182)

[147] I. F. Herbut, V. Juricic, and O. Vafek. *Coulomb Interaction, Ripples, and the Minimal Conductivity of Graphene*. Phys. Rev. Lett. **100**, 046403 (2008). (cited on pages 62, 63, and 182)

[148] E. G. Mishchenko. *Minimal conductivity in graphene: Interaction corrections and ultraviolet anomaly*. Europhys. Lett. **83**, 17005 (2008). (cited on pages 62, 63, and 182)

[149] D. E. Sheehy and J. Schmalian. *Why is the optical transparency of graphene determined by the fine structure constant?* Phys. Rev. B **78**, 085418 (2008). (cited on pages 62, 63, and 182)

[150] S. H. Abedinpour, G. Vignale, A. Principi, M. Polini, W.-K. Tse, and A. H. MacDonald. *Drude weight, plasmon dispersion, and ac conductivity in doped graphene sheets*. Phys. Rev. B **84**, 045429 (2011). (cited on pages 62, 63, and 182)

[151] B. Rosenstein, M. Lewkowicz, and T. Maniv. *Chiral anomaly and strength of the electron-electron interaction in graphene*. arXiv:1210.3345 (2012). (cited on pages 62, 63, and 182)

[152] A. L. Walter, A. Bostwick, F. Speck, M. Ostler, K. S. Kim, Y. J. Chang, L. Moreschini, D. Innocenti, T. Seyller, K. Horn, and E. Rotenberg. *Small scale rotational disorder observed in epitaxial graphene on SiC(0001)*. arXiv:1209.4744 (2012). (cited on p. 64)

[153] C. Hwang, C.-H. Park, D. A. Siegel, A. V. Fedorov, S. G. Louie, and A. Lanzara. *Direct measurement of quantum phases in graphene via photoemission spectroscopy*. Phys. Rev. B **84**, 125422 (2011). (cited on p. 64)

[154] C. Hwang, D. A. Siegel, S.-K. Mo, W. Regan, A. Ismach, Y. Zhang, A. Zettl, and A. Lanzara. *Fermi velocity engineering in graphene by substrate modification*. Sci. Rep. **2**, 590 (2012). (cited on p. 64)

[155] D. C. Elias, R. V. Gorbachev, A. S. Mayorov, S. V. Morozov, A. A. Zhukov, P. Blake, L. A. Ponomarenko, I. V. Grigorieva, K. S. Novoselov, F. Guinea, and A. K. Geim. *Dirac cones reshaped by interaction effects in suspended graphene*. Nature Physics **7**, 701 (2011). (cited on pages 64, 65, and 66)

[156] Y. Zhang, V. W. Brar, C. Girit, A. Zettl, and M. F. Crommie. *Origin of spatial charge inhomogeneity in graphene*. Nat Phys **5**, 722 (2009). (cited on p. 65)

[157] R. S. Deacon, K.-C. Chuang, R. J. Nicholas, K. S. Novoselov, and A. K. Geim. *Cyclotron resonance study of the electron and hole velocity in graphene monolayers*. Phys. Rev. B **76**, 081406 (2007). (cited on p. 66)

[158] J. Hubbard. *Electron Correlations in Narrow Energy Bands*. Proceedings of the Royal Society of London. Series A. Mathematical and Physical Sciences **276**, 238 (1963). (cited on p. 71)

[159] K. Sun and E. Fradkin. *Time-reversal symmetry breaking and spontaneous anomalous Hall effect in Fermi fluids*. Phys. Rev. B **78**, 245122 (2008). (cited on pages 72 and 91)

[160] R. Peierls. *On the theory of diamagnetism of conduction electrons*. Z. Phys **30**, 763 (1933). (cited on p. 72)

[161] S. Raghu, X.-L. Qi, C. Honerkamp, and S.-C. Zhang. *Topological Mott Insulators*. Phys. Rev. Lett. **100**, 156401 (2008). (cited on pages 73, 89, 90, 91, and 92)

[162] G. Parisi. *Statistical Field Theory* (1988). (cited on p. 74)

[163] J. L. Alonso, L. A. Fernandez, F. Guinea, V. Laliena, and V. Martin-Mayor. *Variational mean-field approach to the double-exchange model*. Phys. Rev. B **63**, 054411 (2001). (cited on p. 74)

[164] J. M. Luttinger. *Fermi Surface and Some Simple Equilibrium Properties of a System of Interacting Fermions*. Phys. Rev. **119**, 1153 (1960). (cited on pages 75, 76, 77, and 207)

[165] B. Valenzuela and M. A. H. Vozmediano. *Pomeranchuk instability in doped graphene*. New Journal of Physics **10**, 113009 (2008). (cited on pages 75, 87, and 91)

[166] I. I. Pomeranchuk. Sov. Phys. JETP **8**, 361 (1959). (cited on p. 75)

[167] C.-Y. Hou, C. Chamon, and C. Mudry. *Electron Fractionalization in Two-Dimensional Graphenelike Structures*. Phys. Rev. Lett. **98**, 186809 (2007). (cited on pages 81, 87, and 120)

[168] D. J. Thouless. *Wannier functions for magnetic sub-bands*. Journal of Physics C: Solid State Physics **17**, L325 (1984). (cited on p. 83)

[169] C. Brouder, G. Panati, M. Calandra, C. Mourougane, and N. Marzari. *Exponential Localization of Wannier Functions in Insulators*. Phys. Rev. Lett. **98**, 046402 (2007). (cited on p. 83)

[170] C. M. Varma. *Theory of the pseudogap state of the cuprates*. Phys. Rev. B **73**, 155113 (2006). (cited on p. 84)

[171] H. B. Callen. *Thermodynamics and an introduction to thermostatics*, chapter 8 (John Wiley and Sons, 1988). (cited on pages 87 and 211)

[172] K. Huang. *Statistical Mechanics*, chapter 2 (John Wiley and Sons, 1987). (cited on pages 87 and 211)

[173] A. C. Rahul Nandkishore, Leonid Levitov. *Chiral superconductivity from repulsive interactions in doped graphene*. Nat. Phys. **8**, 158 (2012). (cited on pages 91 and 92)

[174] R. Nandkishore, G.-W. Chern, and A. V. Chubukov. *Itinerant Half-Metal Spin-Density-Wave State on the Hexagonal Lattice*. Phys. Rev. Lett. **108**, 227204 (2012). (cited on p. 91)

[175] R. B. Laughlin. *Anomalous Quantum Hall Effect: An Incompressible Quantum Fluid with Fractionally Charged Excitations*. Phys. Rev. Lett. **50**, 1395 (1983). (cited on pages 94 and 99)

[176] D. Yoshioka, B. I. Halperin, and P. A. Lee. *Ground State of Two-Dimensional Electrons in Strong Magnetic Fields and 1/3 Quantized Hall Effect*. Phys. Rev. Lett. **50**, 1219 (1983). (cited on p. 94)

[177] F. D. M. Haldane and E. H. Rezayi. *Finite-Size Studies of the Incompressible State of the Fractionally Quantized Hall Effect and its Excitations*. Phys. Rev. Lett. **54**, 237 (1985). (cited on pages 94 and 98)

[178] F. D. M. Haldane. *Fractional Quantization of the Hall Effect: A Hierarchy of Incompressible Quantum Fluid States*. Phys. Rev. Lett. **51**, 605 (1983). (cited on p. 94)

[179] B. I. Halperin. *Statistics of Quasiparticles and the Hierarchy of Fractional Quantized Hall States*. Phys. Rev. Lett. **52**, 1583 (1984). (cited on pages 94 and 100)

[180] J. K. Jain. *Composite Fermions* (Cambridge University Press, 2012). (cited on p. 94)

[181] S. Zhang. *The Chern Simons Landau Ginzburg theory of the Fractional Quantum Hall Effect*. Int. J. Mod. Phys. B **6**, 25 (1992). (cited on pages 94 and 99)

[182] T. Neupert, L. Santos, C. Chamon, and C. Mudry. *Fractional Quantum Hall States at Zero Magnetic Field*. Phys. Rev. Lett. **106**, 236804 (2011). (cited on pages 94, 95, and 97)

[183] E. Tang, J.-W. Mei, and X.-G. Wen. *High-Temperature Fractional Quantum Hall States*. Phys. Rev. Lett. **106**, 236802 (2011). (cited on p. 94)

[184] K. Sun, Z. Gu, H. Katsura, and S. Das Sarma. *Nearly Flatbands with Nontrivial Topology*. Phys. Rev. Lett. **106**, 236803 (2011). (cited on p. 94)

[185] D. Sheng, Z.-C. Gu, K. Sun, and L. Sheng. *Fractional quantum Hall effect in the absence of Landau levels*. Nat Commun **2**, 389 (2011). (cited on p. 95)

[186] J. W. F. Venderbos, M. Daghofer, and J. van den Brink. *Narrowing of Topological Bands due to Electronic Orbital Degrees of Freedom*. Phys. Rev. Lett. **107**, 116401 (2011). (cited on pages 95 and 113)

[187] X.-L. Qi. *Generic Wave-Function Description of Fractional Quantum Anomalous Hall States and Fractional Topological Insulators*. Phys. Rev. Lett. **107**, 126803 (2011). (cited on pages 95 and 113)

[188] N. Regnault and B. A. Bernevig. *Fractional Chern Insulator*. Phys. Rev. X **1**, 021014 (2011). (cited on pages 95, 102, 103, 105, 106, and 113)

[189] Z. Liu and E. J. Bergholtz. *From fractional Chern insulators to Abelian and non-Abelian fractional quantum Hall states: adiabatic continuity and orbital entanglement spectrum*. arXiv:1209.5310 (2012). (cited on pages 95, 111, and 113)

[190] A. M. Lauchli, Z. Liu, E. J. Bergholtz, and R. Moessner. *Hierarchy of fractional Chern insulators and competing compressible states*. arXiv:1207.6094 (2012). (cited on pages 95, 111, and 113)

[191] T. Neupert, L. Santos, C. Chamon, and C. Mudry. *Elementary formula for the Hall conductivity of interacting systems*. Phys. Rev. B **86**, 165133 (2012). (cited on pages 95, 107, 108, and 113)

[192] A. Sterdyniak, C. Repellin, B. A. Bernevig, and N. Regnault. *Series of Abelian and Non-Abelian States in C>1 Fractional Chern Insulators*. arXiv:1207.6385 (2012). (cited on pages 95, 103, and 113)

[193] B. A. Bernevig and N. Regnault. *Thin-Torus Limit of Fractional Topological Insulators*. arXiv:1204.5682 (2012). (cited on pages 95, 103, 108, and 113)

[194] Y. Wu, B. A. Bernevig, and N. Regnault. *Zoology of Fractional Chern Insulators*. Phys. Rev. B **85**, 075116 (2012). (cited on pages 95, 103, 104, 105, 112, and 113)

[195] B. A. Bernevig and N. Regnault. *Emergent Many-Body Translational Symmetries of Abelian and Non Abelian Fractionally Filled Topological Insulators*. Phys. Rev. B **85**, 075128 (2012). (cited on pages 95, 103, and 113)

[196] T. Liu, C. Repellin, B. A. Bernevig, and N. Regnault. *Fractional Chern Insulators beyond Laughlin states*. arXiv:1206.2626 (2012). (cited on pages 95, 104, 112, and 113)

[197] C. H. Lee, R. Thomale, and X.-L. Qi. *Pseudopotential Formalism for Fractional Chern Insulators*. arXiv:1207.5587 (2012). (cited on pages 95 and 113)

[198] Y.-F. Wang, H. Yao, C.-D. Gong, and D. N. Sheng. *Fractional quantum Hall effect in topological flat bands with Chern number two*. Phys. Rev. B **86**, 201101 (2012). (cited on pages 95, 104, 112, and 113)

[199] C. Fang, M. J. Gilbert, and B. A. Bernevig. *Entanglement Spectrum Classification of C_n-invariant Noninteracting Topological Insulators in Two Dimensions*. arXiv:1208.4603 (2012). (cited on pages 95 and 113)

[200] H. Fehske, R. Schneider, and A. W. (Eds.). *Computational Many-Particle Physics* (Springer, 2008). (cited on p. 98)

[201] E. H. Rezayi and F. D. M. Haldane. *Laughlin state on stretched and squeezed cylinders and edge excitations in the quantum Hall effect*. Phys. Rev. B **50**, 17199 (1994). (cited on pages 98, 102, and 108)

[202] X. G. Wen and Q. Niu. *Ground state degeneracy of the fractional quantum Hall states in the presence of random potential and on high genus Riemann surfaces*. Phys. Rev. B **41**, 9377 (1990). (cited on p. 99)

[203] P. L. Taylor and O. Heinonen. *A quantum approach to Condensed Matter Physics* (Cambridge, 2002). (cited on p. 99)

[204] J. Frohlich and U. M. Studer. *Gauge invariance and current algebra in nonrelativistic many-body theory*. Rev. Mod. Phys. **65**, 733 (1993). (cited on pages 99 and 100)

[205] J. Frohlich and U. M. Studer. *Integral quadratic forms, Kac-Moody algebras, and fractional quantum Hall effect. AnADE-O classification*. J. Stat. Phys. **76**, 209 (1994). (cited on p. 100)

[206] X. G. Wen and A. Zee. *Classification of Abelian quantum Hall states and matrix formulation of topological fluids*. Phys. Rev. B **46**, 2290 (1992). (cited on p. 100)

[207] X. G. Wen. *Vacuum degeneracy of chiral spin states in compactified space*. Phys. Rev. B **40**, 7387 (1989). (cited on p. 100)

[208] X. G. Wen. *Topological Orders and Chern-Simons Theory in strongly correlated quantum liquid*. Int. J. Mod. Phys. **B5**, 1641 (1991). (cited on p. 100)

[209] R. Tao and D. J. Thouless. *Gauge invariance and fractional quantum Hall effect*. Phys. Rev. B **30**, 1097 (1984). (cited on p. 101)

[210] D. J. Thouless. *Level Crossing and the fractional quantum Hall effect*. Phys. Rev. B **40**, 12034 (1989). (cited on p. 101)

[211] R. B. Laughlin. *Quantized Hall conductivity in two dimensions*. Phys. Rev. B **23**, 5632 (1981). (cited on p. 101)

[212] H. Li and F. D. M. Haldane. *Entanglement Spectrum as a Generalization of Entanglement Entropy: Identification of Topological Order in Non-Abelian Fractional Quantum Hall Effect States*. Phys. Rev. Lett. **101**, 010504 (2008). (cited on p. 103)

[213] M. Haque, O. Zozulya, and K. Schoutens. *Entanglement Entropy in Fermionic Laughlin States*. Phys. Rev. Lett. **98**, 060401 (2007). (cited on p. 103)

[214] A. Sterdyniak, N. Regnault, and B. A. Bernevig. *Extracting Excitations from Model State Entanglement*. Phys. Rev. Lett. **106**, 100405 (2011). (cited on p. 103)

[215] Z. Liu, E. J. Bergholtz, H. Fan, and A. M. Lauchli. *Fractional Chern Insulators in Topological Flat Bands with Higher Chern Number*. Phys. Rev. Lett. **109**, 186805 (2012). (cited on pages 104 and 112)

[216] R. Tao and D. J. Thouless. *Fractional quantization of Hall conductance*. Phys. Rev. B **28**, 1142 (1983). (cited on p. 108)

[217] J. W. F. Venderbos, S. Kourtis, J. van den Brink, and M. Daghofer. *Fractional Quantum-Hall Liquid Spontaneously Generated by Strongly Correlated t2g Electrons*. Phys. Rev. Lett. **108**, 126405 (2012). (cited on p. 113)

[218] Y.-L. Wu, N. Regnault, and B. A. Bernevig. *Bloch Model Wavefunctions and Pseudopotentials for All Fractional Chern Insulators*. arXiv:1210.6356 (2012). (cited on p. 113)

[219] Y.-L. Wu, N. Regnault, and B. A. Bernevig. *Bloch Model Wavefunctions and Pseudopotentials for All Fractional Chern Insulators*. ArXiv e-prints (2012). (cited on p. 113)

[220] M. Nakahara. *Geometry, topology, and physics* (CRC Press, 2003). (cited on pages 118 and 124)

[221] A. Rycerz, J. Tworzydło, and C. Beenakker. *Valley filter and valley valve in graphene*. Nature Physics **3**, 172–175 (2007). (cited on pages 118 and 122)

[222] A. R. Akhmerov and C. W. J. Beenakker. *Detection of Valley Polarization in Graphene by a Superconducting Contact*. Phys. Rev. Lett. **98**, 157003 (2007). (cited on pages 118 and 122)

[223] J. Tworzydlo, I. Snyman, A. R. Akhmerov, and C. W. J. Beenakker. *Valley-isospin dependence of the quantum Hall effect in a graphene p-n junction*. Phys. Rev. B **76**, 035411 (2007). (cited on pages 118 and 122)

[224] J. Li, I. Martin, M. Buttiker, and A. F. Morpurgo. *Topological origin of subgap conductance in insulating bilayer graphene*. Nature Physics **7**, 38 (2011). (cited on pages 118, 122, and 133)

[225] M. Gmitra, S. Konschuh, C. Ertler, C. Ambrosch-Draxl, and J. Fabian. *Band-structure topologies of graphene: Spin-orbit coupling effects from first principles*. Phys. Rev. B **80**, 235431 (2009). (cited on p. 120)

[226] S. Ryu, C. Mudry, C.-Y. Hou, and C. Chamon. *Masses in graphenelike two-dimensional electronic systems: Topological defects in order parameters and their fractional exchange statistics*. Phys. Rev. B **80**, 205319 (2009). (cited on pages 120, 121, and 126)

[227] A. P. Schnyder, S. Ryu, A. Furusaki, and A. W. W. Ludwig. *Classification of topological insulators and superconductors in three spatial dimensions*. Phys. Rev. B **78**, 195125 (2008). (cited on p. 121)

[228] D. A., V. K. Dugaev, and J. Barnas. *Spin Hall effect in a system of Dirac fermions in the honeycomb lattice with intrinsic and Rashba spin-orbit interaction*. Phys. Rev. B **80**, 155444 (2009). (cited on pages 125, 128, 130, and 223)

[229] F. Guinea. *Spin–orbit coupling in a graphene bilayer and in graphite*. New Journal of Physics **12**, 083063 (2010). (cited on pages 131 and 133)

[230] E. McCann and M. Koshino. *Spin-orbit coupling and broken spin degeneracy in multilayer graphene*. Phys. Rev. B **81**, 241409 (2010). (cited on pages 131 and 134)

[231] W. Li and R. Tao. *Edge States of Monolayer and Bilayer Graphene Nanoribbons*. Journal of the Physical Society of Japan **81**, 024704 (2012). (cited on pages 132 and 134)

[232] S. Konschuh, M. Gmitra, D. Kochan, and J. Fabian. *Theory of spin-orbit coupling in bilayer graphene*. Phys. Rev. B **85**, 115423 (2012). (cited on p. 132)

[233] E. Prada, P. San-Jose, L. Brey, and H. Fertig. *Band topology and the quantum spin Hall effect in bilayer graphene*. Solid State Communications **151**, 1075 (2011). (cited on pages 133 and 135)

[234] A. Dyrdał and J. Barnaś. *Intrinsic contribution to spin Hall and spin Nernst effects in a bilayer graphene*. Journal of Physics: Condensed Matter **24**, 275302 (2012). (cited on p. 135)

[235] P. Carmier, O. Shevtsov, C. Groth, and X. Waintal. *Competing topological phases in few-layer graphene*. arXiv:1211.6628 (2012). (cited on p. 135)

[236] Z. Qiao, W.-K. Tse, H. Jiang, Y. Yao, and Q. Niu. *Two-Dimensional Topological Insulator State and Topological Phase Transition in Bilayer Graphene*. Phys. Rev. Lett. **107**, 256801 (2011). (cited on p. 135)

[237] Z. Qiao, X. Li, W.-K. Tse, H. Jiang, Y. Yao, and Q. Niu. *Topological phases in gated bilayer graphene: Effects of Rashba spin-orbit coupling and exchange field*. arXiv:1211.3802 (2012). (cited on p. 135)

[238] H. B. G. Casimir. Proc. Kon. Neder. Akad. Wet. **51**, 793 (1948). (cited on pages 137 and 138)

[239] M. Bordag, G. Klimchitskaya, U. Mohideen, and V. Mostepanenko. *Advances in the Casimir Effect* (Oxford University Press, 2009). (cited on pages 137, 138, 139, 140, 146, 147, 148, 152, and 157)

[240] M. Bordag, U. Mohideen, and V. M. Mostepanenko. *New developments in the Casimir effect*. Phys. Rept. **353**, 1 (2001). (cited on p. 137)

[241] H. B. G. Casimir and D. Polder. *The influence of retardation on the London-van der Waals forces*. Phys. Rev. **73**, 360 (1948). (cited on p. 138)

[242] I. Dzyaloshinskii, E. M. Lifshitz, and L. P. Pitaevskii. Adv. Phys. **10**, 165 (1961). (cited on pages 138 and 140)

[243] S. J. Rahi, T. Emig, N. Graham, R. L. Jaffe, and M. Kardar. *Scattering theory approach to electrodynamic Casimir effect*. Phys. Rev. D **80**, 085021 (2009). (cited on pages 138, 139, 140, and 146)

[244] S. K. Lamoreaux. *Demonstration of the Casimir Force in the 0.6 to 6 micrometer Range*. Phys. Rev. Lett. **78**, 5 (1997). (cited on p. 138)

[245] J. Munday, F. Capasso, and V. A. Parsegian. Nature **457**, 170 (2009). (cited on p. 138)

[246] G. L. Klimchitskaya, U. Mohideen, and V. M. Mostepanenko. *The Casimir force between real materials: experiment and theory*. Rev. Mod. Phys. **81**, 1827 (2009). (cited on pages 138 and 144)

[247] T. H. Boyer. *Comment on the sign of the Casimir force*. Phys. Rev. A **9**, 2078 (1974). (cited on p. 139)

[248] F. S. S. Rosa, D. A. R. Dalvit, and P. W. Milonni. *Comment on the sign of the Casimir force*. Phys. Rev. Lett. **100**, 183602 (2008). (cited on pages 139 and 141)

[249] U. Leonhardt and T. G. Philbin. *Quantum levitation by left-handed metamaterials*. New J.Phys. **9**, 254 (2007). (cited on pages 139 and 141)

[250] R. Z. et al. *Repulsive Casimir Force in Chiral Metamaterials*. Phys. Rev. Lett. **103**, 103602 (2009). (cited on pages 139 and 141)

[251] M. Levin, A. P. McCauley, A. W. Rodriguez, M. T. H. Reid, and S. G. Johnson. *Casimir Repulsion between Metallic Objects in Vacuum*. Phys. Rev. Lett. **105**, 090403 (2010). (cited on p. 139)

[252] O. Kenneth and I. Klich. *Opposites Attract: A Theorem about the Casimir Force*. Phys. Rev. Lett. **97**, 160401 (2006). (cited on pages 139 and 156)

[253] C. P. Bachas. *Comment on the sign of the Casimir force*. Journal of Physics A: Mathematical and Theoretical **40**, 9089 (2007). (cited on pages 139 and 156)

[254] S. J. Rahi, M. Kardar, and T. Emig. *Constraints on stable equilibria with fluctuation-induced forces*. Phys. Rev. Lett **105**, 070404 (2010). (cited on pages 139 and 156)

[255] J. E. Moore. *The birth of Topological Insulators*. Nature **464**, 194 (2010). (cited on p. 139)

[256] D. Hsieh, D. Qian, L. Wray, Y. Xia, Y. Hor, R. J. Cava, and M. Hasan. *A (3D) Topological Dirac insulator (Bi-Sb semiconductors) in a quantum spin Hall phase*. Nature **452**, 970 (2008). (cited on p. 139)

[257] D. Hsieh, Y. Xia, L. Wray, D. Qian, A. Pal, J. H. Dil, F. Meier, J. Osterwalder, C. Kane, G. Bihlmayer, Y. S. Hor, R. J. Cava, and M. Hasan. *Observation of unconventional quantum spin-textures (non-trivial Berry's phase) in topological insulators Bi-Sb*. Science **323**, 919 (2009). (cited on p. 139)

[258] G. Deng, Z.-Z. Liu, and J. Luo. *Attractive-repulsion transition of the Casimir force between anisotropic plates*. Phys. Rev. A **78**, 062111 (2008). (cited on p. 139)

[259] F. Rosa, D. A. R. Dalvit, and P. W. Milonni. *Casimir interactions for anisotropic magnetodielectric metamaterials*. Phys. Rev. A **78**, 032117 (2008). (cited on pages 139 and 232)

[260] M. T. Jaekel and S. Reynaud. *Casimir force between partially transmitting mirrors*. Journal de Physique I **1**, 1395 (1991). (cited on p. 140)

[261] M. Born, E. Wolf, and A. B. Bhatia. *Principles of optics* (Cambridge University Press, 1993), seventh edition. (cited on pages 140, 143, and 233)

[262] J. D. Jackson. *Classical Electrodynamics* (Wiley, 1998). (cited on pages 140, 178, and 180)

[263] F. Wilczek. *Two applications of axion electrodynamics*. Phys. Rev. Lett **58**, 1799 (1987). (cited on p. 142)

[264] X.-L. Qi and et al. *Seeing the magnetic monopole through the mirror of topological surface states*. Science **323**, 1184 (2009). (cited on p. 142)

[265] P. Bruno. *Long Range Magnetic interaction due to the Casimir effect*. Phys. Rev. Lett **88**, 240401 (2002). (cited on p. 143)

[266] L. D. Landau and E. M. Lifshitz. *Electrodynamics of Continous Media* (Pergamon Press, 1984), second edition. (cited on pages 143 and 151)

[267] Y. N. Obukhov and F. W. Hehl. *On the boundary-value problems and the validity of the Post constraint in modern electromagnetism*. Optik 120 418-421 (2009). (cited on p. 143)

[268] M.-C. Chang and M.-F. Yang. *Optical signature of topological insulators*. Phys. Rev. B. **80**, 113304 (2009). (cited on p. 143)

[269] C. Mitsas, D. Siapkas, and J. Luo. *Phonon and electronic properties of TlBiSe2 thin films*. Solid State Comm. **83**, 857 (1992). (cited on pages 144 and 229)

[270] Y. Xia, L. Wray, D. Qian, D. Hsieh, A. Pal, H. Lin, A. Bansil, D. Grauer, Y. Hor, R. Cava, and M. Hasan. *Observation of a large-gap topological-insulator class (Bi2Se3 class) with a single Dirac cone on the surface*. Nat. Phys. **5**, 398 (2009). (cited on p. 147)

[271] F. Brown, R. Hornreich, and S. Shtrikman. *Upper bound on the magnetic susceptibility*. Phys. Rev. **168**, 574 (1968). (cited on p. 149)

[272] F. W. Hehl, Y. N. Obukhov, J.-P. Rivera, and H. Schmid. *Relativistic analysis of magnetoelectric crystals: extracting a new 4-dimensional P odd and T odd pseudoscalar from Cr2 O3 data*. Phys. Lett. A **372**, 1141 (2008). (cited on pages 151 and 158)

[273] A. M. Essin, A. M. Turner, J. E. Moore, , and D. Vanderbilt. *Orbital magnetoelectric coupling in band insulators*. Phys. Rev. B **81**, 205104 (2010). (cited on p. 151)

[274] B. Yan. *Theoretical Prediction of Topological Insulators in Thallium-based III-V-VI$_2$ Ternary Chalcogenides*. arXiv: 1003.0074 (2010). (cited on p. 151)

[275] H. Lin, R. Markiewicz, L. Wray, L. Fu, M. Hasan, and A. Bansil. *Single-Dirac-Cone topological surface states on pseudo-IV-VI-semimetal/semiconductors: Thallium-based III-V-VI2 Ternary Chalcogenides*. arXiv:1003.2615 (2010). (cited on pages 151 and 175)

[276] H. Lin, R. Markiewicz, L. Wray, L. Fu, M. Hasan, and A. Bansil. *Single-Dirac-Cone topological surface states in TlBiSe2 class of Topological Insulators*. Phys. Rev. Lett. **105**, 036404 (2010). (cited on p. 151)

[277] F. Rosa, D. A. R. Dalvit, and P. W. Milonni. *Casimir-Lifshitz theory and Metamaterials*. Phys. Rev. Lett. **100**, 183602 (2008). (cited on p. 157)

[278] W.-K. Tse and A. MacDonald. *Giant Magneto-Optical Kerr Effect and Universal Faraday Effect in Thin Film Topological Insulators*. Phys. Rev. Lett. **105**, 057401 (2010). (cited on pages 157, 159, 175, and 176)

[279] J. Maciejko, X.-L. Qi, H. D. Drew, and S.-C. Zhang. *Topological Quantization in Units of the Fine Structure Constant*. Phys. Rev. Lett. **105**, 166803 (2010). (cited on pages 157, 159, 175, and 176)

[280] E. D. Palik. *Handbook of Optical constants of solids, Vol.1 and 2.* (Academic Press, 1998). (cited on p. 157)

[281] J. F. Hulliger edited by K. A. Gschneidner and L. Eyring. *Handbook on the Physics and Chemistry of Rare Earths*, volume 4 (North-Holland Publishing, Amsterdam, 1978). (cited on p. 157)

[282] J. Q. Xiao and C. L. Chien. *Proximity Effects in Superconductor/Insulating-Ferromagnet NbN/GdN Multilayers*. Phys. Rev. Lett. **76**, 1727 (1996). (cited on p. 157)

[283] S.-C. Zhang and J. Hu. *A Four-Dimensional Generalization of the Quantum Hall Effect*. Science **294**, 823 (2001). (cited on pages 160 and 237)

[284] M. Barkeshli and X.-L. Qi. *Topological response theory of doped topological insulators*. Phys. Rev. Lett. **107**, 206602 (2011). (cited on pages 160, 162, 168, 169, 170, 174, and 237)

[285] D. L. Bergman. *Axion response in gapless systems*. Phys. Rev. Lett. **107**, 176801 (2011). (cited on pages 160, 168, 174, and 237)

[286] D. L. Bergman and G. Refael. *Topological response theory of doped topological insulators*. arXiv:1201.3042 (2012). (cited on pages 160, 174, and 237)

[287] W. E. Thirring. *A soluble relativistic field theory*. Annals of Physics **3**, 91 (1958). (cited on p. 160)

[288] J. Schwinger. *Gauge Invariance and Mass. II*. Phys. Rev. **128**, 2425 (1962). (cited on p. 160)

[289] C. M. Naon. *Abelian and non-Abelian bosonization in the path-integral framework*. Phys. Rev. D **31**, 2035 (1985). (cited on p. 160)

[290] J.-N. Chazalviel. *Spin-dependent Hall effect in semiconductors*. Phys. Rev. B **11**, 3918 (1975). (cited on p. 160)

[291] W. P. Su, J. R. Schrieffer, and A. J. Heeger. *Solitons in Polyacetylene*. Phys. Rev. Lett. **42**, 1698 (1979). (cited on p. 160)

[292] W. P. Su, J. R. Schrieffer, and A. J. Heeger. *Soliton excitations in polyacetylene*. Phys. Rev. B **22**, 2099 (1980). (cited on p. 160)

[293] W. P. Su and J. R. Schrieffer. *Fractionally Charged Excitations in Charge-Density-Wave Systems with Commensurability 3*. Phys. Rev. Lett. **46**, 738 (1981). (cited on p. 160)

[294] W. P. Su. *Fractionally charged kinks in a 1: 3 Peierls system*. Phys. Rev. B **27**, 370 (1983). (cited on p. 160)

[295] J. Goldstone and F. Wilczek. *Fractional Quantum Numbers on Solitons*. Phys. Rev. Lett. **47**, 986 (1981). (cited on pages 160, 162, and 164)

[296] D. M. Basko. *Calculation of the Raman G peak intensity in monolayer graphene: role of Ward identities*. New Journal of Physics **11**, 095011 (2009). (cited on pages 163 and 170)

[297] A. Hill, A. Sinner, and K. Ziegler. *Optical Hall Conductivity for gapped graphene*. arXiv:1005.3211v1 (2010). (cited on p. 165)

[298] C.-X. Liu, X.-L. Qi, H. Zhang, X. Dai, Z. Fang, and S.-C. Zhang. *Model Hamiltonian for topological insulators*. Phys. Rev. B **82**, 045122 (2010). (cited on p. 168)

[299] Y. L. Chen, J.-H. Chu, J. G. Analytis, Z. K. Liu, K. Igarashi, H.-H. Kuo, X. L. Qi, S. K. Mo, R. G. Moore, D. H. Lu, M. Hashimoto, T. Sasagawa, S. C. Zhang, I. R. Fisher, Z. Hussain, and Z. X. Shen. *Massive Dirac Fermion on the Surface of a Magnetically Doped Topological Insulator*. Science **329**, 659 (2010). (cited on pages 168, 173, and 176)

[300] L. A. Wray, S. Y. Xu, Y. Xia, Y. S. Hor, D. Qian, A. V. Fedorov, H. Lin, A. Bansil, R. Cava, and M. Z. Hasan. *Observation of topological order in a superconducting doped topological insulator* . (cited on pages 168, 173, and 176)

[301] R. Delbourgo and A. B. Waites. *Induced Parity Violation in Odd Dimensions*. Austral.J.Phys. **47**, 465 (1994). (cited on pages 172 and 237)

[302] A. A. Schafgans, B. C. Chapler, K. W. Post, D. N. Basov, A. A. Taskin, Y. Ando, and X.-L. Qi. arXiv:1202.4029 (2012). (cited on p. 176)

[303] R. Li, J. Wang, X.-L. Qi, and S.-C. Zhang. Nature **6**, 284 (2010). (cited on p. 176)

[304] S. M. Carroll, G. B. Field, and R. Jackiw. *Limits on a Lorentz- and parity-violating modification of electrodynamics*. Phys. Rev. D **41**, 1231 (1990). (cited on pages 176, 178, 180, 192, and 194)

[305] L. Balents. *Weyl electrons kiss*. Physics **4**, 36 (2011). (cited on p. 176)

[306] A. A. Zyuzin and A. A. Burkov. *Topological response in Weyl semimetals and the chiral anomaly*. arXiv:1206.1868 (2012). (cited on p. 176)

[307] J. Polchinski. *String Theory Vol. 1 and 2* (Cambridge University Press, 1998). (cited on p. 178)

[308] B. Zwiebach. *A First Course in String Theory* (Cambridge University Press, 2009). (cited on p. 178)

[309] B. Altschul. *Perspectives on Lorentz and CPT Symmetry Violation*. Journal of Physics: Conference Series **335**, 012010 (2011). (cited on pages 178 and 181)

[310] A. Einstein. *Zur Elektrodynamik bewegter Körper*. Annalen der Physik **17**, 891 (1905). (cited on pages 178 and 179)

[311] L. D. Landau and E. M. Lifshitz. *The Classical Theory of Fields* (Butterworth-Heinemann, 19980). (cited on pages 178, 179, and 180)

[312] V. A. Kostelecky and N. Russell. *Data tables for Lorentz and CPT violation*. Rev. Mod. Phys. **83**, 11 (2011). (cited on p. 178)

[313] D. Colladay and V. A. Kostelecký. *Lorentz-violating extension of the standard model*. Phys. Rev. D **58**, 116002 (1998). (cited on pages 178, 181, and 182)

[314] R. Jackiw and V. A. Kostelecký. *Radiatively Induced Lorentz and CPT Violation in Electrodynamics*. Phys. Rev. Lett. **82**, 3572 (1999). (cited on pages 178, 182, and 190)

[315] S. Coleman and S. L. Glashow. *High-energy tests of Lorentz invariance*. Phys. Rev. D **59**, 116008 (1999). (cited on pages 178, 182, and 190)

[316] J.-M. Chung. *Radiatively-induced Lorentz and CPT violating Chern Simons term in QED*. Phys. Lett. B **461**, 138 (1999). (cited on pages 178, 182, and 190)

[317] M. Pérez-Victoria. *Exact Calculation of the Radiatively Induced Lorentz and CPT Violation in QED*. Phys. Rev. Lett. **83**, 2518 (1999). (cited on pages 178, 182, 189, and 190)

[318] G. Volovik. *On induced CPT-odd Chern-Simons terms in the 3+1 effective action*. JETP Letters **70**, 1 (1999). (cited on pages 178, 179, 182, 183, 184, and 190)

[319] W. F. Chen. *Issues on radiatively induced Lorentz and CPT violation in quantum electrodynamics*. AIP Conference Proceedings **601**, 242 (2001). (cited on pages 178, 182, and 190)

[320] A. A. Andrianov, P. Giacconi, and R. Soldati. *Lorentz and CPT violations from Chern-Simons modifications of QED*. Journal of High Energy Physics **2002**, 030 (2002). (cited on pages 178, 182, and 190)

[321] J. R. Nascimento, E. Passos, A. Y. Petrov, and F. A. Brito. *Lorentz-CPT violation, radiative corrections and finite temperature*. Journal of High Energy Physics **2007**, 016 (2007). (cited on pages 178 and 182)

[322] M. Gomes, J. R. Nascimento, E. Passos, A. Y. Petrov, and A. J. da Silva. *Induction of the four-dimensional Lorentz-breaking non-Abelian Chern-Simons action*. Phys. Rev. D **76**, 047701 (2007). (cited on pages 178 and 182)

[323] W. Chen. *A Note on the Radiatively Induced Lorentz and CPT Violated Chern-Simons-like Term in the Extended Quantum Electrodynamics*. arXiv:0712.2557 (2007). (cited on pages 178, 182, and 190)

[324] O. M. D. Cima, J. M. Fonseca, D. H. Franco, and O. Piguet. *Lorentz and CPT violation in QED revisited: A missing analysis*. Phys. Lett. B **688**, 258 (2010). (cited on pages 178, 182, and 190)

[325] F. R. Klinkhamer and G. E. Volovik. *Emergent CPT violation from the splitting of Fermi Points*. Int. J. Mod. Phys. A **20**, 2795 (2005). (cited on pages 178, 183, and 194)

[326] R. Jackiw. *When radiative corrections are finite but undetermined*. AIP Conference Proceedings **14**, 2011 (2000). (cited on pages 178 and 182)

[327] F. A. Brito, L. S. Grigorio, M. S. Guimaraes, E. Passos, and C. Wotzasek. *Induced Chern-Simons-like action in Lorentz-violating massless QED*. Phys. Rev. D **78**, 125023 (2008). (cited on pages 178, 182, and 190)

[328] G. Bonneau. *Regularisation: many recipes, but a unique principle: Ward identities and normalisation conditions. The case of CPT violation in QED*. Nucl. Phys. B **593**, 398 (2001). (cited on pages 178 and 182)

[329] C. Adam and F.R. Klinkhamer. *Causality and radiatively induced CPT violation*. Phys. Lett. B **513**, 245 (2001). (cited on pages 178 and 182)

[330] P. Goswami and S. Tewari. *Axion field theory and anomalous non-dissipative transport properties of (3+1)-dimensional Weyl semi-metals and Lorentz violating spinor electrodynamics*. arXiv:1210.6352 (2012). (cited on p. 180)

[331] F. Wilczek. *Two applications of axion electrodynamics*. Phys. Rev. Lett. **58**, 1799 (1987). (cited on p. 180)

[332] D. Colladay and V. A. Kostelecký. *CPT Violation and the Standard Model*. Phys. Rev. D **55**, 6760 (1997). (cited on p. 181)

[333] A. A. Burkov and L. Balents. *Weyl Semimetal in a Topological Insulator Multilayer*. Phys. Rev. Lett. **107**, 127205 (2011). (cited on pages 183, 184, 185, 188, 191, and 193)

[334] A. A. Burkov, M. D. Hook, and L. Balents. *Topological nodal semimetals*. Phys. Rev. B **84**, 235126 (2011). (cited on pages 183 and 191)

[335] L. Balents. *Weyl electrons kiss*. Physics **4**, 36 (2011). (cited on p. 183)

[336] X. Wan, A. M. Turner, A. Vishwanath, and S. Y. Savrasov. *Topological semimetal and Fermi-arc surface states in the electronic structure of pyrochlore iridates*. Phys. Rev. B **83**, 205101 (2011). (cited on pages 183, 184, and 193)

[337] A. A. Zyuzin, S. Wu, and A. A. Burkov. *Weyl semimetal with broken time reversal and inversion symmetries*. Phys. Rev. B **85**, 165110 (2012). (cited on pages 183 and 188)

[338] C.-X. Liu, P. Ye, and X.-L. Qi. *Chiral gauge field and axial anomaly in a Weyl semi-metal*. arXiv:1204.6551 (2012). (cited on pages 183 and 193)

[339] P. Delplace, J. Li, and D. Carpentier. *Topological Weyl semi-metal from a lattice model*. EPL (Europhys. Lett.) **97**, 67004 (2012). (cited on pages 183, 184, and 193)

[340] K.-Y. Yang, Y.-M. Lu, and Y. Ran. *Quantum Hall effects in a Weyl semimetal: Possible application in pyrochlore iridates*. Phys. Rev. B **84**, 075129 (2011). (cited on pages 183, 184, and 193)

[341] C. Herring. *Accidental Degeneracy in the Energy Bands of Crystals*. Phys. Rev. **52**, 365 (1937). (cited on p. 183)

[342] H. Nielsen and M. Ninomiya. *Absence of neutrinos on a lattice I Proof by homotopy theory*. Nucl. Phys. B **185**, 20 (1981). (cited on p. 183)

[343] H. Nielsen and M. Ninomiya. *Absence of neutrinos on a lattice II Intuitive topological proof*. Nucl. Phys. B **193**, 173 (1981). (cited on p. 183)

[344] G. Y. Cho. *Possible topological phases of bulk magnetically doped Bi2Se3: turning a topological band insulator into the Weyl semimetal*. arXiv:1110.1939 (2011). (cited on p. 184)

[345] J.-H. Jiang. *Tunable topological Weyl semimetal from simple-cubic lattices with staggered fluxes*. Phys. Rev. A **85**, 033640 (2012). (cited on p. 184)

[346] K. Nakayama, K. Eto, Y. Tanaka, T. Sato, S. Souma, T. Takahashi, K. Segawa, and Y. Ando. *Manipulation of Topological States and Bulk Band Gap Using Natural Heterostructures of a Topological Insulator*. arXiv:1206.7043 (2012). (cited on p. 185)

[347] M. Kohmoto, B. I. Halperin, and Y.-S. Wu. *Quantized Hall effect in 3D periodic systems*. Physica B: Condensed Matter **184**, 30 (1993). (cited on p. 191)

[348] L. D. Landau and E. M. Lifshitz. *Electrodynamics of continuous media* (Pergamon Press, Oxford, 1984). (cited on p. 192)

[349] G. Y. Cho. *Possible topological phases of bulk magnetically doped Bi2Se3: turning a topological band insulator into the Weyl semimetal*. arXiv:1110.1939 (2011). (cited on p. 193)

[350] G. Xu, H. Weng, Z. Wang, X. Dai, and Z. Fang. *Chern Semimetal and the Quantized Anomalous Hall Effect in HgHr2He4*. Phys. Rev. Lett. **107**, 186806 (2011). (cited on p. 193)

[351] J.-H. Jiang. *Tunable topological Weyl semimetal from simple-cubic lattices with staggered fluxes*. Phys. Rev. A **85**, 033640 (2012). (cited on p. 193)

[352] G. B. Arfken and H. J. Weber. *Mathematical Methods for Physicists* (Academic Press, 2001). (cited on p. 205)

[353] R. Zhao, J. Zhou, T. Koschny, E. N. Economou, and C. M. Soukoulis. *Repulsive Casimir Force in Chiral Metamaterials*. Phys. Rev. Lett. **103**, 103602 (2009). (cited on p. 228)

[354] F. S. S. Rosa, D. A. R. Dalvit, and P. W. Milonni. *Casimir-Lifshitz Theory and Metamaterials*. Phys. Rev. Lett. **100**, 183602 (2008). (cited on p. 228)

[355] F. S. S. Rosa, D. A. R. Dalvit, and P. W. Milonni. *Casimir interactions for anisotropic magnetodielectric metamaterials*. Phys. Rev. A **78**, 032117 (2008). (cited on p. 228)

[356] G. Deng, Z.-Z. Liu, and J. Luo. *Attractive-repulsive transition of the Casimir force between anisotropic plates*. Phys. Rev. A **78**, 062111 (2008). (cited on p. 228)

[357] Y. N. Obukhov and F. W. Hehl. *Measuring a piecewise constant axion field in classical electrodynamics*. Phys. Lett. A **341**, 357 (2005). (cited on p. 234)